

**Full Vehicle Simulation and Exploration of a Range Extended
Electric Vehicle Battery Pack and Thermal Management
System in Diurnal Operating Environments**

by

Lokendra Ramotar

A Thesis Submitted in Partial Fulfillment of the Requirements for the Degree of
Doctor of Philosophy in Mechanical Engineering

Supervisor: Dr. Greg Rohrauer

Faculty of Engineering and Applied Science
University of Ontario Institute of Technology
Oshawa, Ontario, Canada

December 2018

© Lokendra Ramotar, 2018

THESIS EXAMINATION INFORMATION

Submitted by: **Lokendra Ramotar**

Doctor of Philosophy in Mechanical Engineering

Thesis title: Full Vehicle Simulation and Exploration of a Range Extended Electric Vehicle Battery Pack and Thermal Management System in Diurnal Operating Environments

An oral defense of this thesis took place on December 10th, 2018 in front of the following examining committee:

Examining Committee:

Chair of Examining Committee	Dr. Xianke Lin
Research Supervisor	Dr. Greg Rohrauer
Examining Committee Member	Dr. Martin Agelin-Chaab
Examining Committee Member	Dr. Sheldon Williamson
University Examiner	Dr. Edward Waller
External Examiner	Dr. Roydon Fraser, University of Waterloo - Engineering

The above committee determined that the thesis is acceptable in form and content and that a satisfactory knowledge of the field covered by the thesis was demonstrated by the candidate during an oral examination. A signed copy of the Certificate of Approval is available from the School of Graduate and Postdoctoral Studies.

ABSTRACT

A full vehicle model is created in Autonomie to represent a production extended range electric vehicle (EREV), specifically including the high voltage battery pack which is validated in dynamic operation against experimental data. Vehicle data is utilized as comparative input to a thermal equivalent circuit model developed analytically which aims to capture and understand the heat propagation from the cells through the entire pack, to and from the environment. The inclusion of production hardware and the liquid battery thermal management system components into the physical model considers detail geometric properties to calculate thermal resistances of components (conduction, convection and radiation) along with their associated thermal capacitances. Analog equivalent circuit simulations using PSPICE are compared to experimental results in order to validate internal temperature nodes and the heat rate through various elements with heat flux sensors; all used to refine the model. The solar data, diurnal temperature and terrain are included in the simulations to model the effects of gradient, convection and road radiation on the battery pack; both stationary and through drive cycles.

The thermal equivalent circuit accurately quantifies the heat flow dynamics of the battery. Convection and radiation sources primarily influenced the baseplate and underbody shield components whereas cell heat propagation was closely linked to cell retention frame hardware details. The distribution of cooling indicated close to 90% was directed to the cell while the remaining 10% went to the surrounding hardware. Modeling a quiescent background cooling showed the ability to reduce the diurnal temperature effects on the battery pack at the 50 watt level. The addition of insulation in key areas delineated the ability to reduce initial cell temperatures for all drive cycles, while a miniscule amount added between the cell and retention frame interface showed increased cooling capacity directed towards the cells nearing 100%. The models developed incorporated many elements which were neglected or highly simplified in all previous works and the methodology developed highlights an ability to generate accurate dynamic results with little computational power. This is a prerequisite to enable predictive controls and accurate onboard system diagnostics to extend the pack's operational life.

ACKNOWLEDGMENTS

I'd like to thank my supervisor Dr. Greg Rohrauer for his support and guidance throughout this research. Without his help I would not have gained the deep insight into electric vehicle design and the importance of battery thermal management systems. This research was also made possible by the funding provided by Automotive Partnerships Canada, Grant APCPJ 386787 – 09.

I would also like to thank my friends and labmates, Ryan and Kathryn, who helped carry out experiments that supported this research and making the lab a great environment to work in. A special thanks also goes to Shawn and Stuart who I started graduate studies with. Their support as friends and colleagues helped me through some tough times during my research journey.

Finally, I would like to thank my family for supporting me and being there when I needed them the most.

TABLE OF CONTENTS

THESIS EXAMINATION INFORMATION	ii
ABSTRACT	iii
AKNOWLEDGMENTS	iv
TABLE OF CONTENTS	v
LIST OF TABLES	x
LIST OF FIGURES	xi
NOMENCLATURE	xvii
CHAPTER 1 - INTRODUCTION & MOTIVATIONS	20
1.1 Introduction.....	20
1.2 Objectives and Motivation	22
CHAPTER 2 - LITERATURE REVIEW	26
2.1 Mathematical Models.....	28
2.2 Computer Simulation Models.....	33
2.3 Thermal Equivalent Circuits.....	43
2.4 Capacity Fade and Increased Resistance with Aging	58
2.5 Effects of Cold Temperatures on Li-Ion cells.....	62
2.6 Summary	63
CHAPTER 3 - JUSTIFICATION AND RATIONALE	64
3.1 Software	64
3.1.1 Vehicle Simulation Software	64
3.1.2 Thermal Equivalent Circuit Analysis Tools	66
3.2 Thermal System Architectures.....	68
3.3 Lithium-Ion Electrochemistry.....	71

3.3.1	Capacity and Power Fade.....	71
3.3.2	Safety	72
3.4	Projected Life of System.....	75
3.5	Summary	75
CHAPTER 4 - AUTONOMIE MODEL DEVELOPMENT		77
4.1	Production EREV Vehicle	77
4.2	Autonomie.....	79
4.2.1	Autonomie EREV Model.....	80
4.2.2	Vehicle Specific Files	84
4.2.3	Simulation Performance.....	90
4.3	Drive Cycles.....	93
4.3.1	US06 Drive Cycle	93
4.3.2	UDDS Drive Cycle	95
4.3.3	LA92 Drive Cycle.....	96
4.3.4	EPA 5-Cycle Test Procedure	97
4.3.5	Creating New Drive Cycles	101
4.3.6	Drive Cycle Heat Generation.....	103
4.4	Vehicle Testing.....	105
4.4.1	Thermal Chamber Testing	105
4.4.2	Vehicle Road Testing.....	107
4.5	Heat Generation Equations	109
4.5.1	Cell Heat Generation.....	110
4.5.2	Liquid Cooling Heat Exchanger System.....	112
4.6	Summary of Autonomie Model Development.....	115

CHAPTER 5 - THERMAL EQUIVALENT CIRCUIT MODEL	
DEVELOPMENT	116
5.1	Cell and Thermal System Equivalent Circuit 119
5.2	Heat Transferred to External Environment 121
5.2.1	Nylon Frame Sections 121
5.2.2	Heat Flow Path through the Cover 125
5.2.3	Heat Flow through the Baseplate 127
5.2.4	Endplate and Bulkhead Heat Flow Paths 130
5.3	Complete Thermal Equivalent Circuit 132
5.3.1	Simplified Thermal Equivalent Circuit and Experiments 138
5.4	Thermal Equivalent Circuit Validation 142
5.5	Cooling System Logic Controls 146
5.6	Liquid Cooling Control Validation 148
5.7	Summary of Thermal Equivalent Circuit Development 150
CHAPTER 6 - DEVELOPMENT OF ENVIRONMENTAL CONDITIONS 151	
6.1	Road Temperature Modeling 151
6.2	Environmental and Initial Conditions 152
6.2.1	Environmental Test Regions 152
6.2.2	Determination of Initial Conditions 157
6.2.3	Identifying Initial Conditions for Drive Cycle Simulations 162
6.2.4	Ambient and Road Surface Temperatures 166
6.3	Summary of Environmental Conditions 169
CHAPTER 7 - FULL VEHICLE SIMULATION RESULTS 170	
7.1	Model Validations 170
7.1.1	Autonomie Validation Using Vehicle Test Data 170

7.2	Drive Cycle Effects on Cell Temperature.....	177
7.2.1	US06 Drive Cycles	178
7.2.2	UDDS Drive Cycles.....	180
7.2.3	LA92 Cycle.....	182
7.2.4	Davis Dam Cycle	184
7.3	Heat Flow through the Battery Pack.....	186
7.3.1	US06 Heat Flows	186
7.3.2	UDDS Heat Flows	196
7.3.3	Summary of Heat Flow Results	198
7.4	Cooling Performance	199
7.4.1	Drive Cycle Cooling Events	200
7.4.2	Summary of Cooling Performance	204
7.5	Effects of the ICE on Cell Temperature.....	205
7.6	Battery Aging.....	208
7.7	Workday and Weeklong Analysis	210
7.8	System Improvements.....	213
7.8.1	Thermal Set Point Simulations	214
7.8.2	Addition of Insulation for the Battery Pack	216
7.8.3	Cold Weather Simulations	230
7.9	Summary of System Improvements.....	232
CHAPTER 8 - SUMMARY AND CONCLUSIONS.....		234
8.1	Summary	234
8.2	Conclusions.....	234
CHAPTER 9 - CONTRIBUTIONS AND FUTURE WORK.....		239
9.1	Contributions.....	239

9.2	Directions for Future Work.....	246
REFERENCES.....		249
APPENDIX		260
	APPENDIX A – Data for Autonomie Model	260
	APPENDIX B – Sample Calculations	267
	APPENDIX C – Error Analysis.....	276
	APPENDIX D – Drive Cycle Heat Flow.....	281
	APPENDIX E – Cooling Performance	307
	APPENDIX F – Battery Aging.....	310
	APPENDIX G – Insulation Addition.....	314
	APPENDIX H – Cold Weather Drive Cycle Simulations	318

LIST OF TABLES

Table 4.1 – EREV Technical Specifications [74].....	79
Table 4.2 – Vehicle Reported SOC vs Actual SOC.....	88
Table 4.3 – INL Dyno Test and Autonomie Vehicle Comparisons.....	92
Table 4.4 – US06 Drive Cycle Parameters [81].....	94
Table 4.5 – UDDS Drive Cycle Parameters [81].....	95
Table 4.6 – LA92 Drive Cycle Parameters [81].....	96
Table 4.7 – Key Features of 5-Cycle Testing [83].....	98
Table 4.8 – FTP Drive Cycle Parameters [83].....	99
Table 3.9 – HWFET Drive Cycle Parameters.....	100
Table 4.10 – SC03 Drive Cycle Parameters.....	100
Table 4.11 – Davis Dam Cycle Parameters.....	102
Table 4.12 – Liquid Cooling Sample Calculations.....	115
Table 5.1 – Thermal and electrical analogies.....	117
Table 5.2 – Cell and Thermal System Elements.....	120
Table 5.3 – Frame Resistance and Capacitance Elements.....	125
Table 5.4 – Internal Air Gap Resistance and Capacitance Elements.....	127
Table 5.5 – Bottom Heat Flow Path Elements.....	129
Table 5.6 – Bulkhead Elements.....	132
Table 5.7 – Cell and thermal system definitions.....	135
Table 5.8 – Modified Components (balance of values as per Table 5.7).....	140
Table 7.1 – Trace Errors for EPA Standardized Drive Cycles.....	177
Table 7.2 – US06 Average Heat Flow (mW/cell).....	187
Table 7.3 – UDDS Average Heat Flow (W/cell).....	196
Table 7.4 – US06 Mesa Average Heat Flow Comparison.....	227
Table 7.5 – Cell Temperatures on Simulated Cold Drive Cycles.....	231
Table 7.6 - Cell Temperatures on Simulated Cold Drive Cycles with CF insulation.....	231
Table 7.7 – Cell Temperatures on Simulated Cold Cycles with BP-OC-CF insulation.....	232

LIST OF FIGURES

Figure 2.1 – Three dimensional cell stack by Chen and Evans [19].....	30
Figure 2.2 – Hypothetical lead acid HEV battery with air cooling [22].....	33
Figure 2.3 – (Top) Finite element model after 100A discharge, (Bottom) Thermal image after 100A discharge [23]	34
Figure 2.4 – Cylindrical SAFT Li-Ion cells [24]	35
Figure 2.5 – Parallel cell cooling system [3]	35
Figure 2.6 – Conceptual MSMD model domains [29]	36
Figure 2.7 – Temperature contours in separate planes for each cell design a) ND cell, b) CT cell, c) ST cell, d) WS cell [26].....	37
Figure 2.8 – T-shaped battery schematic [31].....	38
Figure 2.9 – Battery pack thermal model used in the Chevrolet Volt EREV [31]	38
Figure 2.10 – US06 heat generation [31].....	39
Figure 2.11 – Gokce et. al. series-parallel hybrid schematic [34]	40
Figure 2.12 – Series-parallel HEV Simulink model [34]	41
Figure 2.13 – Series-parallel HEV Simulink model for battery pack [34]	42
Figure 2.14 – Voltage (top) and temperature (bottom) comparisons between and actual and simulation data for a given drive cycle [36].....	43
Figure 2.15 – Resistance network with multiple heat generation points [39]	44
Figure 2.16 – Equivalent circuit model schematic [41]	45
Figure 2.17 – Thermal model schematic [41]	46
Figure 2.18 – Voltage and temperature readings under charge depleting [41].....	47
Figure 2.19 – Voltage and temperature readings under charge sustaining [41]	47
Figure 2.20 – Three RC equivalent circuit model [42]	48
Figure 2.21 – Voltage prediction results [42]	48
Figure 2.22 – Temperature prediction results [42]	49
Figure 2.23 – Pouch cell heat generation results [42].....	49
Figure 2.24 – Conceptual thermal management system by Saw et. al. [43].....	50
Figure 2.25 – Simplified model with a cell on the heat pipe [44].....	51
Figure 2.26 – Transient electrothermal model [44].....	51

Figure 2.27 – Maximum cell temperatures for the various simulations [44].....	52
Figure 2.28 – Equivalent circuit model presented by Baghdadi et. al. [45].....	53
Figure 2.29 – Simulation and experimental results of varying C-rate at 25°C [45]	54
Figure 2.30 – Centred prismatic cell in a battery pack with a cooling base (grey) [46]..	55
Figure 2.31 – Lumped thermal model by Damay et. al. [46].....	56
Figure 2.32 – Equivalent circuit used by Zhang et. al. [47].....	57
Figure 2.33 – Battery test setup [47].....	57
Figure 2.34 – Comparison between experimental and simulation results [47].....	58
Figure 2.35 – Four-seasons sample test resistance increase [50].....	59
Figure 2.36 – Four-seasons sample test capacity fade [50]	60
Figure 2.37 – Capacity fade as a function of estimated aging [51]	61
Figure 2.38 – Estimation and predictions of resistance with aging [51]	61
Figure 3.1 – Passive air thermal strategy	69
Figure 3.2 – Active air thermal strategy	69
Figure 3.3 – Chevrolet Volt thermal loops	70
Figure 4.1 – 1 st generation Chevrolet Volt component layout [74]	78
Figure 4.2 – EREV vehicle configuration elements in the Autonomie environment	82
Figure 4.3 – EREV expanded VPA	83
Figure 4.4 – Second order dual polarization model [77]	87
Figure 4.5 – Vehicle SOC operating range in relation to cell SOC range	89
Figure 4.6 – INL MY2013 Volt pack charge and discharge resistance	89
Figure 4.7 – Cell internal resistance as a function of temperature and SOC [80]	90
Figure 4.8 – US06 driving trace [81]	94
Figure 4.9 – UDDS driving trace [81]	96
Figure 4.10 – LA92 drive trace [81]	97
Figure 4.11 – FTP driving trace [83]	98
Figure 4.12 – HWFET driving trace [83]	99
Figure 4.13 – SC03 driving trace	100
Figure 4.14 – Davis Dam elevation (top) and driving trace (bottom)	102
Figure 4.15 – Heat generation of drive cycles (from simulations)	104
Figure 4.16 – Trunk left open while on the dynamometer for recording purposes	106

Figure 4.17 – Heat flux and temperature sensor placement on the baseplate	108
Figure 4.18 – Profile of cell	111
Figure 4.19 – Multiple fluid flow paths through cooling plate [31]	112
Figure 4.20 – Alternating pattern of foam and cooling plates [31].....	113
Figure 5.1 – Electrical and heat flow [88]	117
Figure 5.2 – Electrical topographies	118
Figure 5.3 – Resistance network for liquid cooling system (Section A)	120
Figure 5.4 – Cell edge heat flow paths (red lines) to nylon frame.....	122
Figure 5.5 – Li-Ion pouch layer construction [89].....	122
Figure 5.6 – Division of nylon frame sections.....	123
Figure 5.7 – Resistance network for frame elements (Section B)	124
Figure 5.8 – Chassis structure and battery adapted from GM [90].....	126
Figure 5.9 – Resistance network for air gaps and cover (Section C).....	126
Figure 5.10 – Nylon frame and cell attached to steel baseplate.....	128
Figure 5.11 – Convection flow under vehicle.....	128
Figure 5.12 – Resistance network for underbody elements and effects (Section D)	129
Figure 5.13 – Front bulkhead, dashed line depicts exhaust heat shield (removed)	130
Figure 5.14 – Position of steel endplates	131
Figure 5.15 – Resistance network for the engine, bulkhead and endplates (Section E)	131
Figure 5.16 – Thermal equivalent circuit delineating physical regions within the battery pack.....	133
Figure 5.17 – Cross-section of cell packaging showing placement of equivalent resistances in sections A, B and C. R5 from Section A is surface area portioned to respective branches	137
Figure 5.18 – Simplified thermal equivalent circuit used for validation experiments and predictive modeling	139
Figure 5.19 – Fluid conditioning cart and pre-heating reservoir setup (a), front bulkhead with heat flux sensors (b), pack with regions identified (c), manifold path sensor placement (d)	141
Figure 5.20 – Simulation and experimental frame and baseplate temperatures (circuit Section B and D)	144

Figure 5.21 – Simulation and experimental frame and baseplate heat flows (circuit Section B and D)	145
Figure 5.22 – Compressor power during cooling cycle collected from vehicle testing.	147
Figure 5.23 – Simulink cooling control strategy (A) and expanded Stateflow cooling.	148
Figure 5.24 – Cooling control comparison of inlet fluid temperature	149
Figure 6.1 – Mesa, Arizona test week ambient data	154
Figure 6.2 – Toronto, Ontario test week ambient data.....	155
Figure 6.3 – San Francisco, California test week ambient data.....	156
Figure 6.4 – Cell initial condition test cases for Toronto test week.....	158
Figure 6.5 – Mesa test week component analysis.....	160
Figure 6.6 – Toronto test week component analysis.....	161
Figure 6.7 – San Francisco test week component analysis	162
Figure 6.8 – Mesa test day component analysis	163
Figure 6.9 – Toronto test day component analysis	164
Figure 6.10 – San Francisco test day component analysis.....	165
Figure 6.11 – Toronto test day US06 cell temperature comparisons.....	166
Figure 6.12 – Mesa test day ambient and road temperatures.....	167
Figure 6.13 – Toronto test day ambient and road temperatures.....	168
Figure 6.14 – San Francisco test day ambient and road temperatures	168
Figure 7.1 – Test 1 pack voltage	171
Figure 7.2 – Test 1 SOC	172
Figure 7.3 – Test 2 pack voltage	173
Figure 7.4 – Test 2 SOC	174
Figure 7.5 – Test 3 pack voltage	175
Figure 7.6 – Test 3 SOC	176
Figure 7.7 – US06 cell temperatures.....	178
Figure 7.8 – Consecutive US06 cycle pack resistance and SOC	179
Figure 7.9 – UDDS cell temperatures.....	181
Figure 7.10 – Consecutive UDDS cycle pack resistance and SOC	182
Figure 7.11 – LA92 cell temperatures	183
Figure 7.12 – Consecutive LA92 cycle pack resistance and SOC.....	184

Figure 7.13 – Davis Dam cell temperatures.....	185
Figure 7.14 – US06 component heat flow values (top) and percentage (bottom)	188
Figure 7.15 – HC US06 shield heat flow percentage (left) and heat flow value (right)	189
Figure 7.16 – HC US06 shield heat flow percentage (left) and heat flow value (right) at peak solar position.....	191
Figure 7.17 – Mesa HC component comparison, different times of day	192
Figure 7.18 – US06 cycle frame side heat flow comparison for HC battery simulation	193
Figure 7.19 – US06 shield heat flows	194
Figure 7.20 – Toronto US06 external component heat flow	195
Figure 7.21 – UDDS component heat flow values (top) and percentage (bottom)	197
Figure 7.22 – US06 Toronto FC cooling effects.....	201
Figure 7.23 – US06 Toronto FC cooling percentages	202
Figure 7.24 – Davis Dam FC cooling.....	203
Figure 7.25 – Davis Dam FC cooling percentages	204
Figure 7.26 – UDDS San Francisco cell surface and bulkhead heat flows	206
Figure 7.27 – LA92 San Francisco cell surface and bulkhead heat flows	207
Figure 7.28 – Resistance values for aging simulations.....	209
Figure 7.29 – US06 Toronto resistance simulations	210
Figure 7.30 – 24 hour soak period with various cooling rates.....	211
Figure 7.31 – Simulated workday with cell heat generation and quiescent cooling.....	212
Figure 7.32 – 7 day static simulation with various cooling rates.....	213
Figure 7.33 – Cell temperatures for the Toronto US06 thermal setpoint simulations ...	215
Figure 7.34 – Cell temperatures for the Toronto LA92 thermal setpoint simulations...	216
Figure 7.35 – Underbody insulation in the thermal circuit.....	217
Figure 7.36 – Outside cover insulation implementation	217
Figure 7.37 – Inside cover insulation implementation.....	218
Figure 7.38 – Inside and outside cover insulation	218
Figure 7.39 – Cell and frame cross-section [97].....	219
Figure 7.40 – Frame compression tabs	220
Figure 7.41 – Frame compression tab profile	220

Figure 7.42 – Modified frame section with added insulation	221
Figure 7.43 – Example of foam around the cell edge	222
Figure 7.44 – Cell to frame isolation resistance and capacitance added to thermal circuit.....	222
Figure 7.45 – Mesa, AZ test day cell temperatures with added pack insulation	224
Figure 7.46 – US06 regional simulations with insulation implementation, A: Toronto, B: San Francisco, C: Mesa	225
Figure 7.47 – US06 TO simulation with CF insulation	228
Figure 7.48 – US06 Mesa simulation with CF insulation.....	229
Figure 7.49 – 24hr workday simulation with CF insulation and quiescent cooling	230
Figure 7.50 – Toronto US06 external component heat flow for fully charged (FC) cold simulation	231

NOMENCLATURE

A	Area (m ²)
A _c	Cross-sectional area (m ²)
A _s	Surface area (m ²)
Bi	Biot number
C _p	Specific heat (kJ/kgK)
D _h	Hydraulic diameter (m)
<i>f</i>	Friction factor
g	gravitational acceleration (m/s ²)
h	Heat transfer coefficient (W/m ² K)
H	Height (m)
I	Current (A)
I _A	Current per unit area (A/m ²)
k	Thermal conductivity (W/mK)
k _{eff}	Effective thermal conductivity (W/mK)
L _c	Characteristic length (m)
L	Length (m)
\dot{m}	Mass flow rate (kg/s)
N	Number of components
Nu	Nusselt number
p	Perimeter (m)
P	Pressure (Pa)
Pr	Prantl number
Q	Heat generation (W)
Q _A	Heat generation per unit area (W/m ²)
Re	Reynolds number
T	Temperature (K)
t	time (sec)
U	Open circuit voltage (V)
V _{avg}	Average velocity (m/s)

V	Volume (m ³)
\dot{V}	Volumetric flow rate (m ³ /s)
\dot{W}_{pump}	Work of the pump (W)
W	Width (m)

Greek Letters

α	Thermal diffusivity (m ² /s)
Δ	Difference
ε	Surface emissivity
ρ	Density (kg/m ³)
σ	Stefan–Boltzmann constant (5.6703e ⁻⁸ W/m ² K ⁴)
τ	Dimensionless heat transfer coefficient
Θ	Dimensionless temperature
ν	Kinematic viscosity (m ² /s)
μ	Dynamic viscosity (kg/ms)

Subscripts

ag	air gap
ce	cell edge
cf	cell face
cp	cooling plate
fs	foam spacer
i	initial
in	inlet
nh	nylon holder
out	outlet

Acronyms

BTMS	Battery thermal management system
CAE	Computer aided engineering

CFD	Computational fluid dynamics
EV	Electric vehicle
EREV	Electric range extended vehicle
FC	Fully charged
GUI	Graphical user interface
HC	Half charged
HEV	Hybrid electric vehicle
ICE	Internal combustion engine
Li-Ion	Lithium Ion
NiMH	Nickel metal hydride
RMS	Root Mean Squared
SOC	State of charge
VPA	Vehicle propulsion architecture
VPC	Vehicle propulsion controller
VRLA	Valve regulated lead-acid

CHAPTER 1 - INTRODUCTION & MOTIVATIONS

1.1 Introduction

While hybrid and electric vehicles are not a new technology, they have received increased attention over the past decade as a solution to help reduce the dependency on fossil fuels in the transportation sector. Over the previous two decades such vehicles constituted limited production models from General Motors (GM), Chrysler, Ford, Toyota, Honda and Nissan. Most automotive manufactures today produce and/or have plans to produce hybrids, plug-in hybrids, and full electric vehicles in mass quantities. With an increased push from manufacturers, the price of these vehicles will reduce over time as they are currently more expensive to purchase compared to a conventional vehicle featuring comparable specifications.

The higher prices for these vehicles resides in the battery technology. Early hybrids (HEVs) and electric vehicles (EVs) used battery chemistries that were very expensive to manufacture and maintain. The Toyota Prius and Honda Insight were the first commercially successful mass produced hybrids which implemented the use of nickel metal hydride (NiMH) cells. NiMH cells were first applied in full electric passenger vehicles such as GM's EV1, Ford Ranger EV pickup, Chrysler's EPIC minivan and Toyota's RAV4 EV. NiMH cells provided the required power for these vehicles and a variety of cell sizes were developed. One drawback of NiMH cells is the evolution of heat especially while charging, substantially more than from valve regulated lead acid (VRLA) and lithium ion (Li-Ion) cells [1]. This caused researchers to focus even more on battery thermal management systems (BTMS). Keeping the battery operating in a safe temperature range is vital to the general performance of the cell's life span and safety.

Today's HEVs and EVs have moved away from NiMH and currently use Li-Ion cells. Even though the preferred chemistry in the batteries has evolved, the need for a well-designed BTMS still exists. Li-Ion cells require stricter temperature regulation as colder temperatures can permanently damage cells and operating temperatures above 50°C can drastically reduce the lifespan and put the cells at risk for thermal runaway. There are four basic types of cooling/heating methods that can be implemented in HEVs and EVs which

can be summarized as: passive or active systems using either air or liquid as the coolant. Passive air systems are most commonly employed for their simplicity with a fan/blower moving air from the passenger compartment or from the outside through the battery pack. This method is inexpensive but not as consistent as an indirect active liquid cooling system at regulating the battery temperature. Liquid systems are complex and expensive however they have been shown to be substantially better than air systems [1, 2, 3].

Selecting the appropriate BTMS requires an understanding of how much heat must be removed from the battery. System selection also depends on packaging and budgetary requirements for the project. Within the industry, there is a focus on the engineering details (packaging and geometry) and cost. Most studies in academia consider the relevant physics in detail while neglecting the engineering intricacies necessary to execute a design. To build a better BTMS, engineering detail needs to be combined with a full comprehension of how and where heat is generated within the battery system based on the relevant physics. Both industry and academia have implemented the use of computer software to analyze heat dissipation concerns, particularly Finite Element Analysis approaches. Computational fluid dynamics (CFD) in combination with computer aided engineering/design (CAE/CAD) programs are aiding in the development of better battery and thermal models. Programs such as ANSYS Fluent and NX Nastran have the ability to take relevant geometry and packaging to analyze multiphysic interactions between fluids and surfaces. This is beneficial to battery and BTMS development due to the ability to visualize heat propagation within a cell and how that heat flow affects surrounding components. When relevant thermal models are developed and integrated into full vehicle simulations, it provides the best combination to improve the BTMS.

However from a design optimization perspective and broadly testing out new concepts, or for implementing controls or diagnostics routines, much simpler battery systems models are needed. To this end a more useful approach is a system model that can execute much faster than realtime yet capture all essential aspects and accurately predict the dynamic response of all key elements within. For such purposes MATLAB and Simulink are two commonly used programs due to their versatility. MATLAB is a code based environment that can be employed to simulate systems and Simulink uses predefined input blocks to simplify the system building process. MATLAB and Simulink can be

integrated into other automotive based analysis software such as Advisor, GT Power, AMESim and CARsim. The automotive programs named above investigate vehicle dynamics, engine performance, and other mechatronic systems. The models contained in the program libraries are primarily for conventional gasoline vehicles. New models are starting to be implemented into these programs for HEVs and EVs, however there is no emphasis on the battery or BTMS.

There is a learning curve that exists with all new technology. HEVs and EVs evolve to become better over time with advanced engineering research, and the initial designs improve. Creating new vehicle systems that break the conventional mould must have proper design methodology in place. This ensures development for next generation vehicles which build upon the successes, and learn from the failures and shortcomings of past designs.

The analysis and experiments being performed in this thesis aim to enhance the development of BTMS and provide a new approach to designing thermal models by utilizing the appropriate combination of engineering intricacies, relevant physics, and computer simulations. The reduced models developed are amenable to modifications for utilization within predictive control strategies and system diagnostics routines integral to on board vehicle controls.

1.2 Objectives and Motivation

With the increased attention globally for EVs and HEVs, there exists the need for advanced development tools with this new powertrain technology. A greater understanding of the technologies to be implemented in such vehicles is also crucial from a manufacturer and consumer perspective. From the manufacturer's point of view, building a safe, energy efficient vehicle that is cost effective and marketable are key. Consumers want to ensure they purchase a quality vehicle that is safe, economical to operate and suits their personal needs.

There have been numerous studies where the effects of heat generation in single cells and modules are described. Some studies have simulated real world drive cycles with mathematical and experimental models. While these simulations help describe the battery and the associated temperature rise, they do not fully reflect the environment that a battery

would be subjected to on a production vehicle. It is important to understand how heat propagates through a cell and the amount of heat it generates or absorbs from the surroundings. An appropriate thermal management system can be designed once the level of heat generation and flux to and from the environment is known. This can alleviate potential issues associated with cell degradation due to excessively hot or cold climates and mitigate safety concerns with thermal runaway. However, a battery in an EV or HEV is just a subsystem that interacts with many other components within the vehicle. The automotive industry already widely implements simulation tools that help analyze full scale vehicles before production, or as a proof of concept. These tools tend to be very proprietary in nature and sometimes they employ simplified models neglecting interactions with associated components. There is still much to be gained from using physics based modeling and full scale vehicle simulations. This can lead to faster development and a reduction in costs during the design process.

There have been few if any studies that have tried to simulate, validate, and modify a current production vehicle to examine thermal management system effects on the battery without the use of CFD/CAD. Such analysis can reveal if the current thermal management strategy is sufficient, over designed or inadequate to keep the battery within an optimal operating temperature range. However, this requires an innovative approach to reduce computational times while maintaining a high degree of accuracy. The main objective of this research is to understand how key components within the battery pack which restrain the cells from moving, affect the design and operation of a BTMS as current models in existence and simulations performed to date have not addressed this. Therefore, this research will develop a full production vehicle simulation and integrate the results generated into a thermal equivalent circuit model which is developed to represent a production EREV BTMS. Key environmental parameters often neglected in previous studies are also incorporated into the thermal equivalent circuit model. This combined approach will allow for a complete transient modeling of a vehicle while capturing the temperature and heat flow profile of the internal cells in various driving conditions with minimal computational resources and time. To ensure a high degree of accuracy, the models developed were validated against experimental data acquired from the production vehicle.

The sub- objectives to meet the overall objective of this research pursue the following:

1. Develop the simulation of a production EREV in Autonomie which is subjected to various drive cycles.
 - Vehicle components are selected from the available libraries and altered to match the production EREV specifications.
 - The vehicle controllers are modified and tuned to resemble the production EREV operation.
 - Conduct various drive cycles simulations in which to validate against experimental data:
 - i. Battery characteristics (voltage, current, SOC, energy used)
 - ii. Battery thermal performance/operation
 - iii. Battery state when vehicle enters Charge Sustaining (CS) mode
2. Compile data from an instrumented production EREV for model validation
 - Instrument data compiled on IPETronik and VehicleSpy data acquisition systems installed within a production vehicle.
 - Various additional sensors are incorporated into the vehicle to record operational parameters.
 - The instrumented vehicle is subjected to elevated ambient temperatures and various driving conditions.
 - Compile results for the battery system in operation.
 - Validate baseline vehicle operation between simulation and experimental data.
3. Develop a thermal equivalent circuit model to incorporate all internal battery components of the production EREV and validate against experimental data
 - Identify key internal components to be modeled in the circuit.
 - Structure the circuit to have multiple heat flow paths into and out of the system.
 - Incorporate convective, conductive, and radiation environmental elements.

- Integrate battery output data from Autonomie drive cycles to be used as the internal cell heat generation input.
4. Examine battery system thermal performance under different environmental scenarios to understand and hence improve upon the design
- Simulate changes in the environment that reflect important world regions.
 - Analyze whether the current thermal management system can maintain the optimal battery operating conditions even for aged cells, and at what efficiency level.
 - Examine possible areas of improvement and alternate designs.
 - i. Changes to the BTMS control set points
 - ii. Evaluation of a of quiescent background cooling strategy
 - iii. Addition of insulation in different locations

From the objectives stated, this research aims to address the absence of complete vehicle simulations with an integrated and comprehensively modeled BTMS. In addition, analysis to date has not included the effects of diurnal ambient conditions and road solar radiation, which are included in the present research endeavor. One key overall objective is to definitively elicit the worst time of day for initiating a drive cycle. A further quest is to comprehensively understand where gains in packaging efficiency are possible and achieved most effectively from the battery thermal management perspective.

CHAPTER 2 - LITERATURE REVIEW

The mobile electronic market has adopted Li-Ion as the battery technology of choice [4] and these cells have made their way into HEVs and EVs. To better understand these cells, models developed showcase the effects of anode/cathode material properties, electrolytes, and separator materials; but often it can be difficult to interpret or verify the origin of the data and its applicability to automotive scale battery formats. This decreases the credibility of many simulations for practical use. Uncertainty can be greatly reduced when models are developed through a combination of theoretical concepts and experimental models [5]. Model developers tend to reside in academia whereas battery system designers work for industry. There exists a separation between the two disciplines because battery system developers working for automotive OEM's generally regard all design information as proprietary. This leads to many assumptions being made by model developers, due in part to the inability to access accurate data [5, 6, 7, 8, 9, 10], especially regarding automotive scale cells and their packaging details.

The models developed by researchers cover various aspects of battery behavior, which can be classified into four different categories [11]:

- Physical Models – Details the physical process occurring with the battery
- Empirical Models – Comprised of ad hoc equations which are matched to experimental data
- Abstract Models – Batteries are modeled as electrical circuits or other process
- Mixed Models – Simplified view of physical and empirical aspects

Given the four model categories, each category can then be evaluated using four basic criteria:

- Accuracy – How well do predicted values match experimental data and whether other criteria such as time constraints are implemented into the model
- Computational Complexity – Length of time to complete simulation
- Configuration Effort – The number of parameters incorporated into the model

- Analytical Insight – The type of results the model generates (ie. thermal behavior, battery performance, etc)

Thermal characteristics intrinsic to materials used in battery designs are important to understanding the spatial heat generation within batteries, which has been the focus of numerous studies. Heat is generated internally within the cells and then transferred to the exterior surfaces where it is dissipated, through conduction to the surroundings [12]. Within Li-ion batteries, heat is produced in the cells during the charge/discharge cycle. Thermal modeling for Li-Ion batteries is important due to their sensitivity to temperature, which may cause irreversible damage or run-away reactions beginning with decomposition of the organic electrolyte. If excessive thermal energy is released within a Li-ion cell, it will eventually enter thermal runaway and/or explode causing a safety concern [13]. Battery module and pack designs will determine how effective the heat transfer is and which type of thermal management strategy is optimally selected [14].

Since Li-Ion cells have a higher energy density compared to previous cell chemistries utilized in EVs and HEVs, there are added safety and operational concerns with these cells, especially at extreme temperatures. New materials used in Li-Ion cells have produced a longer life, good abuse tolerance, and material costs are slowly decreasing [15]. Despite recent developments, a proper thermal management system selection is important to improve driving range, safety, longevity, warranty costs, and overall customer satisfaction of vehicles employing Li-ion cell technology. Present lithium ion cells are derived from earlier lithium polymer technology. The early generation lithium polymer cells used a solid polymer electrolyte between the anode and cathode. The use of a solid polymer resulted in higher internal resistance as well as requiring elevated operating temperatures, between 60°C to 100°C, to develop sufficient power output for practical use. Current generation lithium ion cells operate at room temperature and have moved away from the solid polymer electrolyte in favour of a liquid electrolyte that saturates a porous polymer membrane separator. The organic solvent mix of ethylene dicarbonate/ethylene carbonate holding a lithium fluoride salt (LiPF_6) in solution is very flammable, and a root cause of the inherent danger.

Computer simulations have the potential for cost savings and provide information that cannot be obtained with ease experimentally. Bandhauer et al. [16] conducted a critical review of thermal issues associated with Li-Ion cells. The review focused on capacity/power fade, thermal runaway, pack imbalances and how temperature affects those areas. Some current thermal systems are investigated as well as a few heat generation models.

2.1 Mathematical Models

One of the first battery heat generation models was created in 1985 by Bernardi et al. [17], who developed a general energy balance for LiAl/FeS battery chemistry. The cell model is assumed to be uniform throughout but varies with time. The energy balance is derived from the First Law of Thermodynamics looking at different processes which contribute to heat generation. Due to the complexities of heat generation in cells, a modeling equation is valuable. Equation 2.1 is a generic equation of heat generation within a cell. This equation represents a single cell reaction, referenced and modified in various papers.

$$q = IV + I \left(T \frac{dU_{avg}}{dT} \right) + mC_p \frac{dT}{dt} \quad 2.1$$

where:

q – Heat transfer rate (W)

I – Cell current (A)

V – Cell potential (V)

T – Absolute temperature (K)

U_{avg} – Open-circuit potential at the average composition relative to a reference electrode (V)

m – Mass of cell (g)

C_p – Mean heat capacity at constant pressure (J/gK)

t – Time (s)

U_{avg} is the theoretical open-circuit potential at the average chemical composition relative to a reference electrode, and T is the absolute temperature. The equation is considered valid if the effects of phase change, mixing, and simultaneous reactions are excluded as those effects are not easily modeled.

Fan and White [8, 18] created a mathematical model for a sealed nickel-cadmium (Ni-Cd) cell during charging and discharge back in 1991. While Ni-Cd cells are not used in current HEVs and EVs, the authors concluded their model predictions fit very well with experimental data, given the existence of transport properties within the electrolyte as well as the cycling performance and the effects of the electrode reactions on cell performance, which were all studied.

Chen and Evans [19] in 1994 were the first to create a three dimensional model that simulated the heat generation in a lithium polymer cell (Li|PEO-LiX|TiS₂) under constant galvanostatic discharge. The battery model was also simulated under the Simplified Federal Urban Driving Schedule (SFUDS). The authors placed importance on maintaining operational temperature and temperature uniformity which can lead to a better designed thermal management system. The heat transport equation was defined in each direction as:

$$\rho C_p \frac{\partial T}{\partial t} = k_x \frac{\partial^2 T}{\partial x^2} + k_y \frac{\partial^2 T}{\partial y^2} + k_z \frac{\partial^2 T}{\partial z^2} + q \quad 2.2$$

where:

ρ – average density of battery (kg/m³)

C_p – average specific heat of battery (J/kgK)

T – temperature of battery (K)

k_x – average thermal conductivity in X direction (W/mK)

k_y – average thermal conductivity in Y direction (W/mK)

k_z – average thermal conductivity in Z direction (W/mK)

q – rate of heat generation per unit volume (W/cm³)

Where k_x, k_y, k_z are the effective thermal conductivities in the respective directions. The heat generation per unit volume is defined as:

$$q = \frac{N_{\text{cell}} \left(E_{\text{oc}} - E - T \frac{dE_{\text{oc}}}{dt} \right)}{LX} \quad 2.3$$

where:

q – rate of heat generation per unit volume (W/cm^3)

N_{cell} – cell number in a stack

i – superficial current density (A/cm^2)

E_{oc} – open-circuit voltage of one cell (V)

E – voltage of one cell (V)

T – temperature of battery (K)

LX – thickness of cell stack (cm)

E_{oc} is the open circuit voltage and $i > 0$ for discharge and $i < 0$ for charge. Figure 2.1 is a schematic of the three dimensional cell stack.

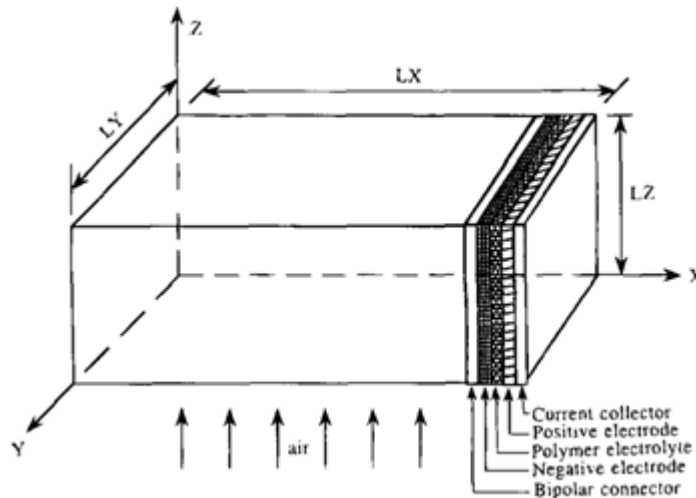


Figure 2.1 – Three dimensional cell stack by Chen and Evans [19]

The thermal management system here was comprised of various arrangements which included the use of air cooling channels, electric heaters, and insulation. The heat

generation from the cell is taken to be uniform with the thermal conductivities in the X direction assumed in the range of 0.16-2.0 W/mK, and the Y and Z directions were assumed in the range 20-60 W/mK. Under low discharge rates it was shown no cooling is necessary and thermal insulation was capable of holding the cell stacks at a uniform temperature distribution. Under the SFUDS power profile, the heat generation rate is low enough that a high-performance insulation material is all that was required to maintain the operating temperature which needed to be approximately 95°C for this legacy technology. Investigation into the warm-up time and heating intensity demonstrated the external surface of the cell stack should have limited heating intensity as the external surface reached operating temperature before the center of the cell. Here it should clearly be noted again that early lithium polymer technology posed a different thermal dilemma, keeping the cells warm enough to produce sufficient power, and required warm-up. Their internal resistance at ambient temperature was too high for useful output.

A three dimensional model created by Newman and Tiedemann [20] in 1995, using the model originally outlined by Chen and Evans [19], can be used on modules comprised of lithium polymer, nickel metal hydride, nickel cadmium or lead acid cells. The work focuses on the temperature rise in a battery module which is placed in a constant temperature environment. The battery module is taken as a composite in which separators, battery plates, and partitions are all part of a layered structure with parameters uniform and independent of time. There are also non-dimensionalized quantities that include temperature with respect to the direction of the greatest heat transfer rate. Furthermore, the model can be extended by a superposition integral, to incorporate a time dependent heat generation rate based on a specific driving profile.

Pals and Newman [13] provided a two part study which created a comprehensive thermal model for a single cell and cell stack of a lithium/polymer battery. In Part I of their work, a single cell model is developed with uniform temperature distribution assumed within the cell that allows temperature to vary with time. Unlike the Bernardi model, this model considered reactions within the cell, changes in the heat capacity of the system, phase changes, mixing, electrical work, and heat transfer with the surroundings [13]. The author's main focus was to study the effects of temperature rise on the charge/discharge characteristics of the battery. Various temperatures can be "tested" with this model as well

as finding the optimal operating temperature. The heat release by the cell is predicted which aids in the design of the thermal management system for the battery. The Pals and Newman model is different from previous studies because they let the salt diffusion coefficient and ionic conductivity vary with temperature. The one dimensional model presented is a combination of previous works which includes the energy balance from Bernardi et al. [17] and properties that vary with temperature. The simplified equation for the cell heat generation rate is defined in Equation 2.4.

$$Q_a = I_A \left(U - V - T \frac{dU}{dt} \right) = h_s (T - T_a) + M_a C_p \frac{dT}{dt} \quad 2.4$$

Here the $I_A(U - V)$ term results in the heat produced and the $-IT(dU/dT)$ term is due to the reversible entropy change within the cell. The dU/dT term is considered as zero in these simulations, with the cell mass per unit area (M_A) and the specific heat set to 460 g/m^2 and 0.7467 J/gK respectively in the modeling. Operating temperatures examined a range between 80°C to 120°C with air as the heat transport medium. The convective heat transfer coefficients ranged from $6\text{-}30 \text{ W/m}^2$ and forced convection values between $30\text{-}300 \text{ W/m}^2$ were used for air. The results showed that with an 11 A/m^2 discharge rate, the cell potential and temperature decreases with increased values of the heat transfer coefficient. A stack of 300 cells with a convective heat transfer coefficient of 24 W/m^2 and varying heat transfer coefficients on the surface of the stack showed the center of the stack to be hotter than the outer edges.

In Part II of the Pals and Newman model [21], they apply the heat generated from the single cell model to help find the temperature profiles in cell stacks. The proposed electric vehicle battery simulated in this paper was designed for a 40 kWh capacity. The model in Part II is a one dimensional model oriented perpendicular to the cell layers with half the cell stack modeled because symmetry is assumed. This model is capable of calculating temperature profiles since it approximates the time and position dependent variable heat generation rate, and is able to assess the battery performance.

2.2 Computer Simulation Models

Computer aided engineering (CAE) and computational fluid dynamics (CFD) are currently widely used in the automotive industry. With advancements in software and computer hardware, it is becoming more feasible to simulate complex systems and also cutting down on the simulation times. Batteries and thermal systems can benefit from CAE and CFD analysis to help understand thermal characteristics within cells/modules.

Pesaran outlined issues relating to batteries and thermal management in 2001 [1]. In his team they tested 3 different types of cell chemistries to show the difference in heat generation at varying discharge rates. Results showed the effects on cell surface temperature and fluid temperature for various thermal systems and the author concluded that air systems, while simple in design, were not as effective at reducing cell temperatures when compared to liquid based systems.

Pesaran et al. continued investigation on battery thermal management in another publication [22] where a lead acid battery pack was subjected to air cooling. The steady state results showed the 30 cell battery pack to have a 1.3°C increase with each row the air passes through. Figure 2.2 depicts the temperature distribution within the pack.

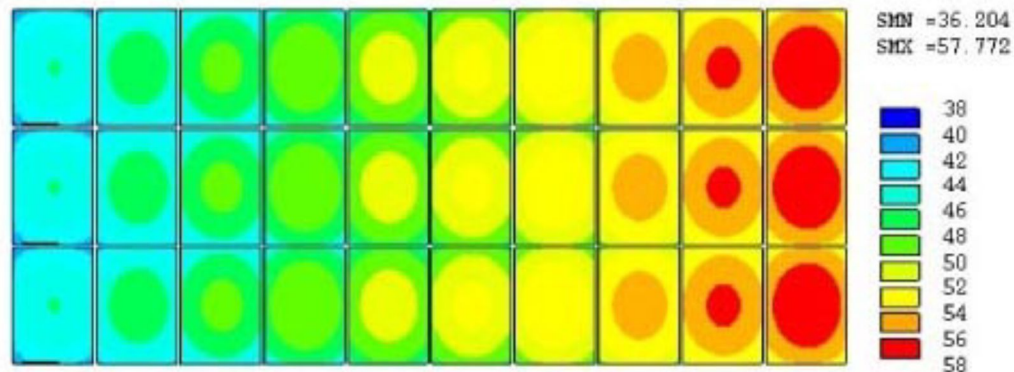


Figure 2.2 – Hypothetical lead acid HEV battery with air cooling [22]

The National Renewable Energy Laboratory (NREL) utilized finite element analysis tools in 2005 to predict the thermal performance of cells [23]. Panasonic prismatic Ni-MH from the 2001 Toyota Prius were used as an example showing comparable results between

the finite element model and photos captured by thermal imaging. Figure 2.3 depicts the comparison between the model developed and thermal images.

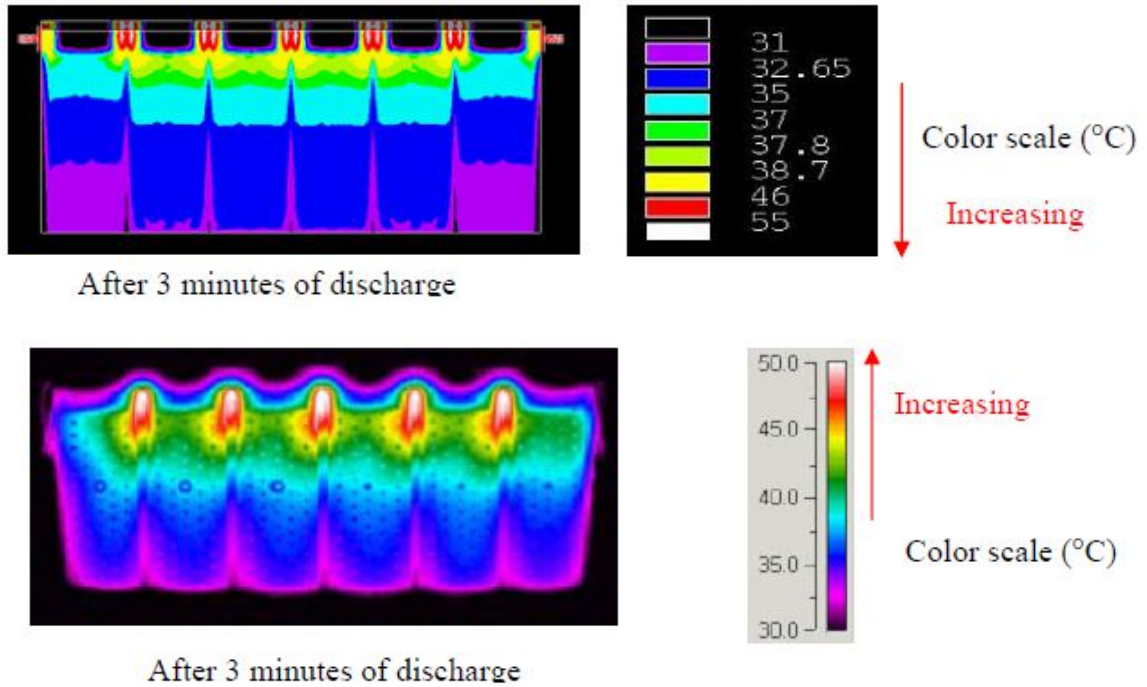


Figure 2.3 – (Top) Finite element model after 100A discharge, (Bottom) Thermal image after 100A discharge [23]

In 2006, NREL continued finite element simulations of cells turning their focus to SAFT cylindrical Li-Ion cells using ANSYS [24]. Thermal performance was investigated based on two cell design iterations to identify areas of improvement. The two designs were cylindrical cells with terminals on opposite, and on the same sides. Heat generated within the cell was calculated by ohmic heating and the model assumed air cooling on all exterior surfaces. Figure 2.4 shows the CAD images of the cells being analyzed.

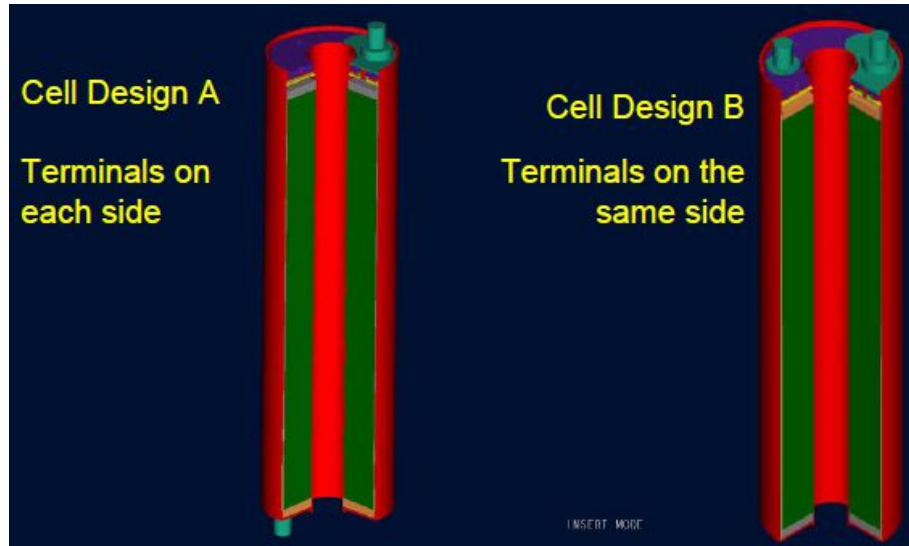


Figure 2.4 – Cylindrical SAFT Li-Ion cells [24]

The effects of various cooling strategies around cylindrical Li-Ion cells were studied by NREL in 2006 [3]. A parallel cell cooling system was investigated in this study with parameters such as pressure loss in the coolant channel, inlet and outlet temperatures, and temperature differences incorporated into the model. Three different coolants were simulated; air, mineral oil, and water/glycol, with the mass flow rate of the coolant and the hydraulic diameter of the coolant channel set as the controlling parameters. The schematic of the cell and cooling channel are shown in Figure 2.5.

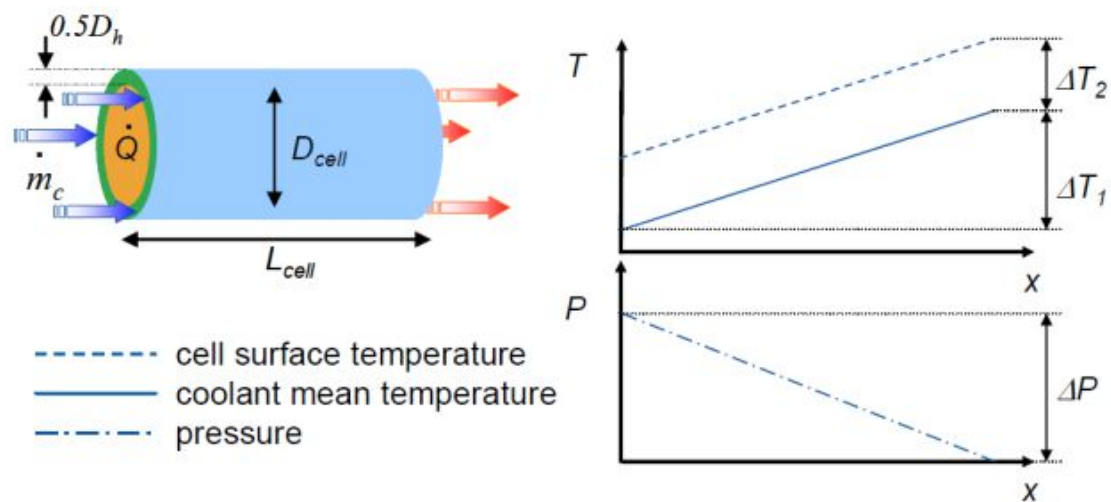


Figure 2.5 – Parallel cell cooling system [3]

Kim et al. [25] [26] [27] [28] investigated multiphysics CAE models in 2010 and 2011. The Multi-Scale Multi-Dimensional (MSMD) model was developed to address the interaction among physics at different scales as shown in Figure 2.6. Various geometries of Li-Ion cells with distinct tab designs were modeled and the total heat generation, volumetric heat generation and temperature contours are analyzed. Figure 2.7 shows the temperature contours for the cell geometries modeled.

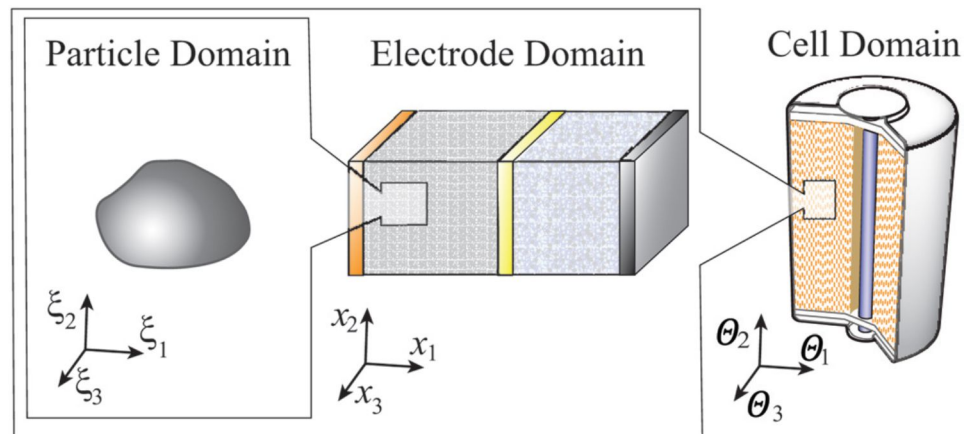


Figure 2.6 – Conceptual MSMD model domains [29]

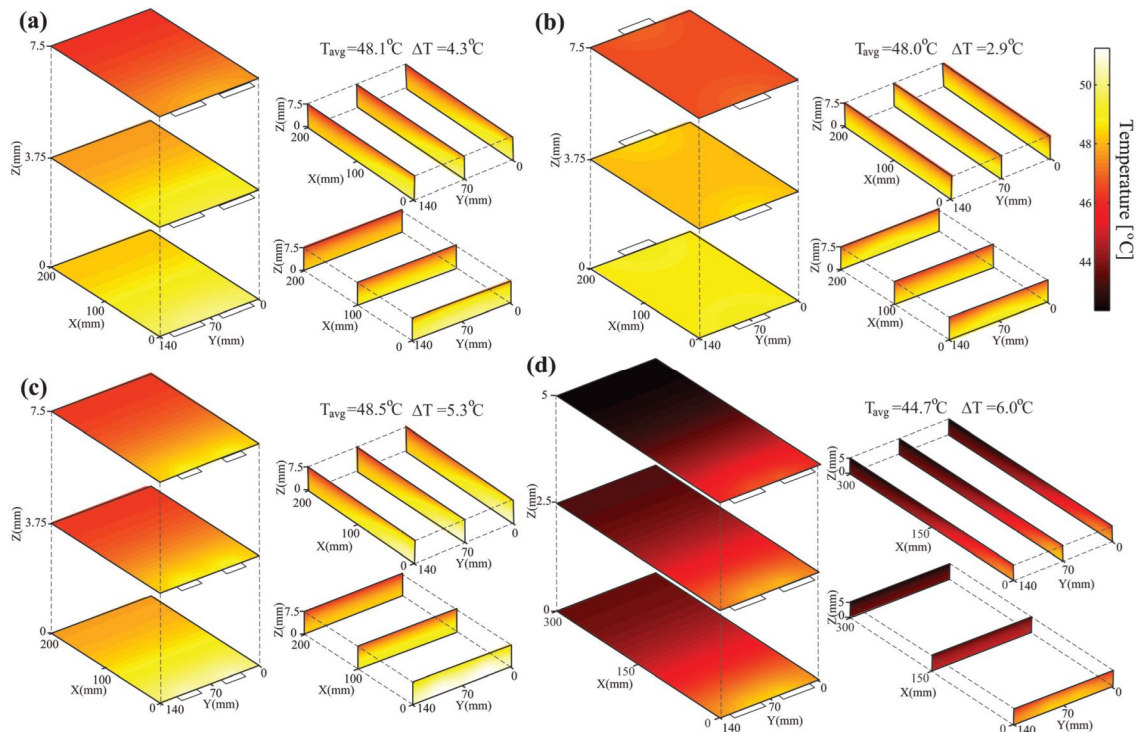


Figure 2.7 – Temperature contours in separate planes for each cell design a) ND cell, b) CT cell, c) ST cell, d) WS cell [26]

Teng [30] developed a finite element model (FEM) in ABAQUS which studied the temperature rise for 8 different Li-Ion cells. Cylindrical, pouch and prismatic cells of various sizes and capacity were analyzed. Air cooling was implemented in the simulations and the author concluded that cylindrical cells are easier to package but their higher internal resistance results in higher heat generation. For prismatic and pouch cells, they are easier to keep isothermal in their thickness direction but for adequate cooling, cell spacing must be taken into consideration.

General Motors published information relating to their Chevrolet Volt EREV vehicle [31]. CFD analysis was employed for the large liquid cooled T-shaped battery pack in the vehicle, shown in Figure 2.8. The fluid pressure drop within the pack was compared between the actual system and CFD simulations with closely matching results. Cell and coolant heat transfer also agreed between experiments and simulations. General Motors proprietary software, Unified Vehicle Model (UVM) and e-Thermal, incorporate a detailed battery thermal model depicted in Figure 2.9, which also outlines the basic equations used. Results summarized by the GM authors are the temperature rise and time averaged heat generation over 3.5 consecutive US06 drive cycles without the cooling system active

shown in Figure 2.10. The approach followed here inspired a more detailed analysis to elicit a fuller understanding, and brought forth the research work detailed within this thesis.

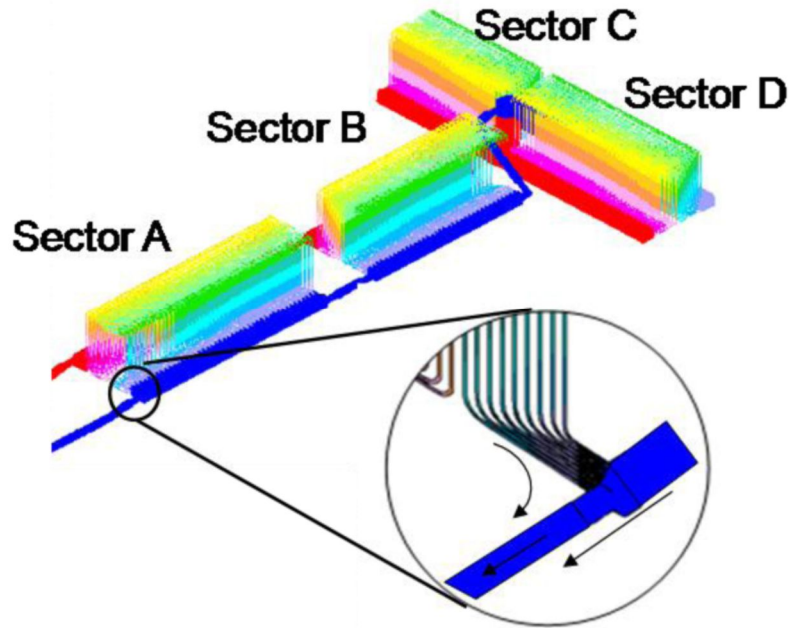
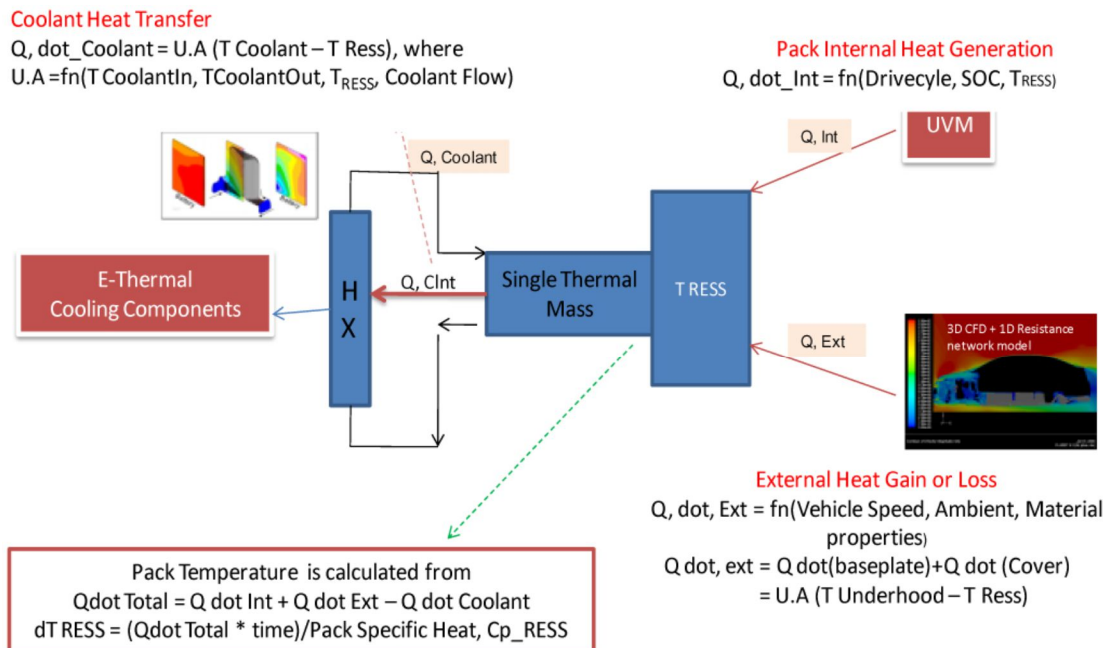


Figure 2.8 – T-shaped battery schematic [31]



**U.A is the Overall heat transfer coefficient between the battery pack and coolant or ambient.

Figure 2.9 – Battery pack thermal model used in the Chevrolet Volt EREV [31]

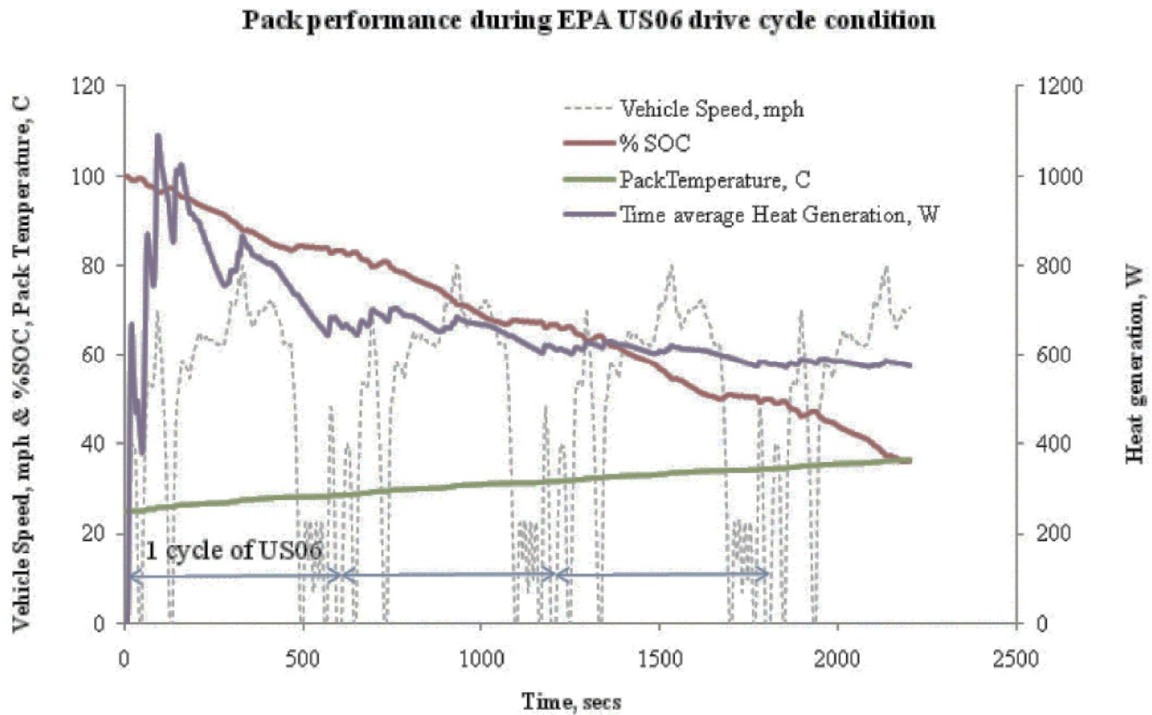


Figure 2.10 – US06 heat generation [31]

Sun et al. [32] from General Motors of Canada used various CFD packages and code based software to analyze an HEV air-cooled battery pack with pouch cells. A multi-physics model was created then incorporated into a FLUENT CFD model. The codes are generated in FORTRAN, iSIGHT, and DEP MORPHER. This allows for various cooling flow paths, pressures, and geometry to be modeled on virtual battery packs under different drive cycles. FLUENT is used to find the heat transfer coefficients of the cell holders at various flow rates which aids in finding the lumped temperature change for the individual cells. Simulations showed how increased air flow with better air manifold designs improved the results.

The Penn State EcoCAR team in 2011 illustrated the development of their EREV vehicle as part of the EcoCAR competition [33]. The team utilized the Powertrain Selection and Assessment Tool (PSAT) from Argonne National Laboratories to quantify the vehicle’s performance. CFD and CAD were used for various parts and a passive air cooled battery pack was employed. However, the focus remained on the design methodology for the entire vehicle with little information detailing the thermal model for the battery.

Gokce et. al. developed a series-parallel HEV in Simulink and simulated the vehicle on different drive cycles [34]. The internal combustion engine, main traction motor, generator, battery, gearbox, and vehicle control logic are all modeled in MATLAB and Simulink, and they investigated the improvements that HEVs can gain over conventional vehicles. Figure 2.11, Figure 2.12 and Figure 2.13 shows a schematic of the series-parallel HEV and the Simulink model developed. They did not however reference a specific battery thermal model for the series-parallel hybrid outlined.

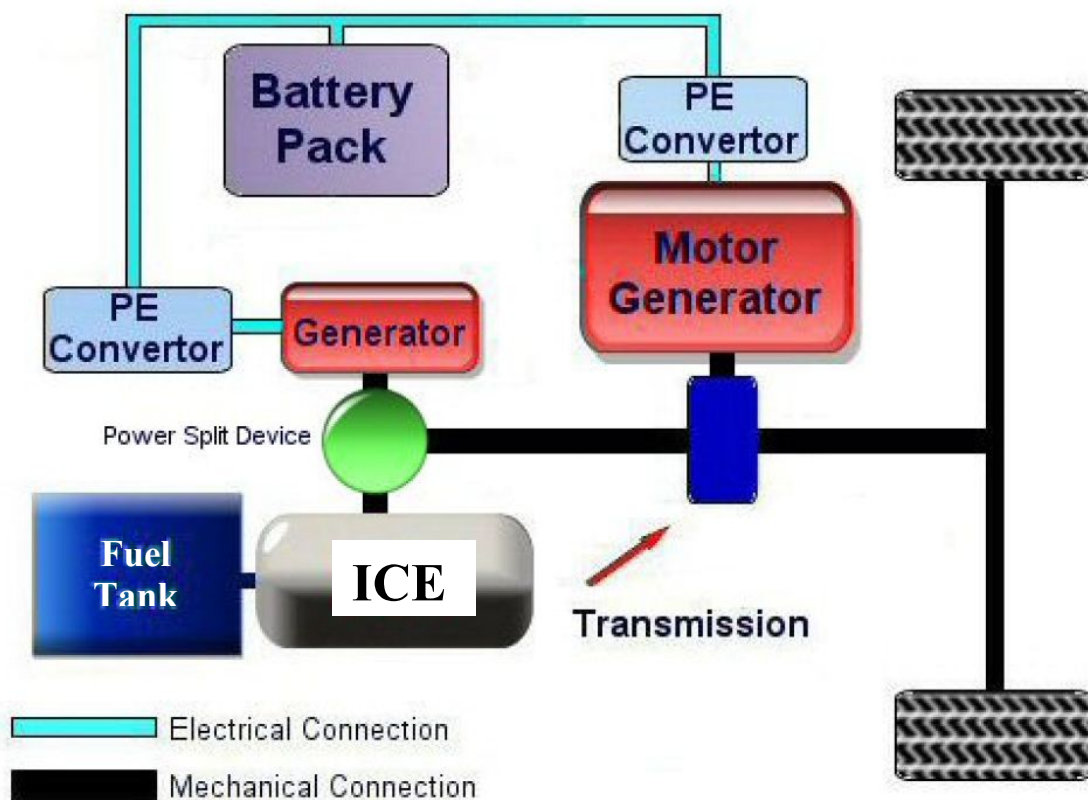


Figure 2.11 – Gokce et. al. series-parallel hybrid schematic [34]

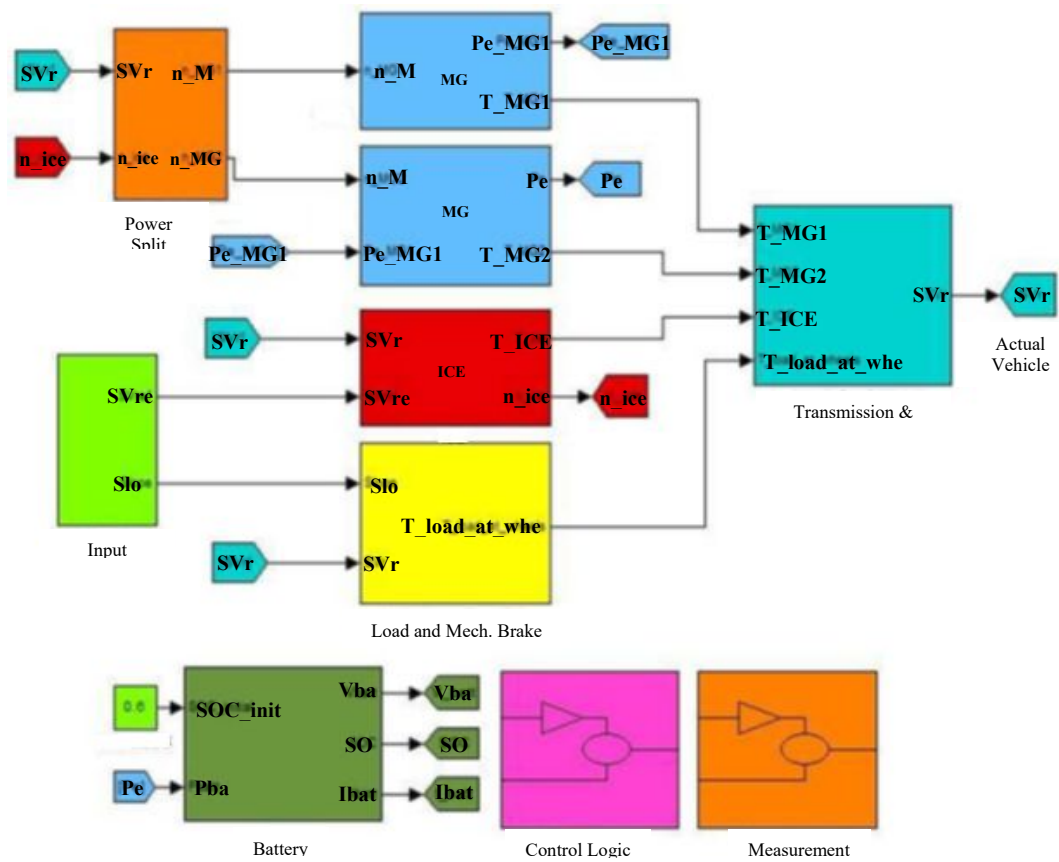


Figure 2.12 – Series-parallel HEV Simulink model [34]

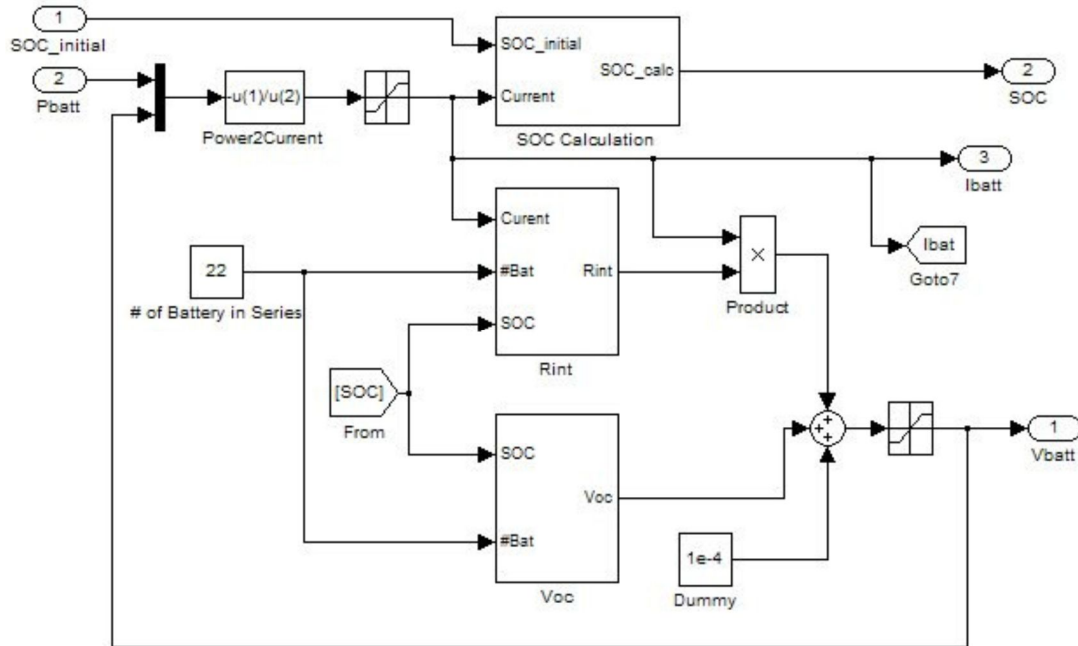


Figure 2.13 – Series-parallel HEV Simulink model for battery pack [34]

Damodaran et al. [35] in 2011, from General Motors of India, investigate solutions for inexpensive EVs. A generic model is created for a worst case scenario that a thermal management system might encounter. City driving conditions on a 7-8% grade with a 4 passenger payload are test conditions for the model developed and results are generated from vehicle simulation software. The CFD simulations employed heat transfer correlations for lead acid cells to determine the bulk cell temperature and the coolant requirements needed to keep the battery thermally stable. Even though the model developed in this paper used lead acid cells, the general methodology can be applied to Ni-MH and Li-Ion chemistries.

Panchal et al. in [36] 2018 developed a battery model using a neural network and validated it using vehicle data under various driving conditions and ambient temperatures. The developed model effectively captured the charge and discharge behaviour over the range of ambient conditions. The drive cycles consisted of aggressive, moderate and light driving characteristics with Figure 2.14 demonstrating the voltage and temperature results for a drive cycle in 2°C ambient conditions.

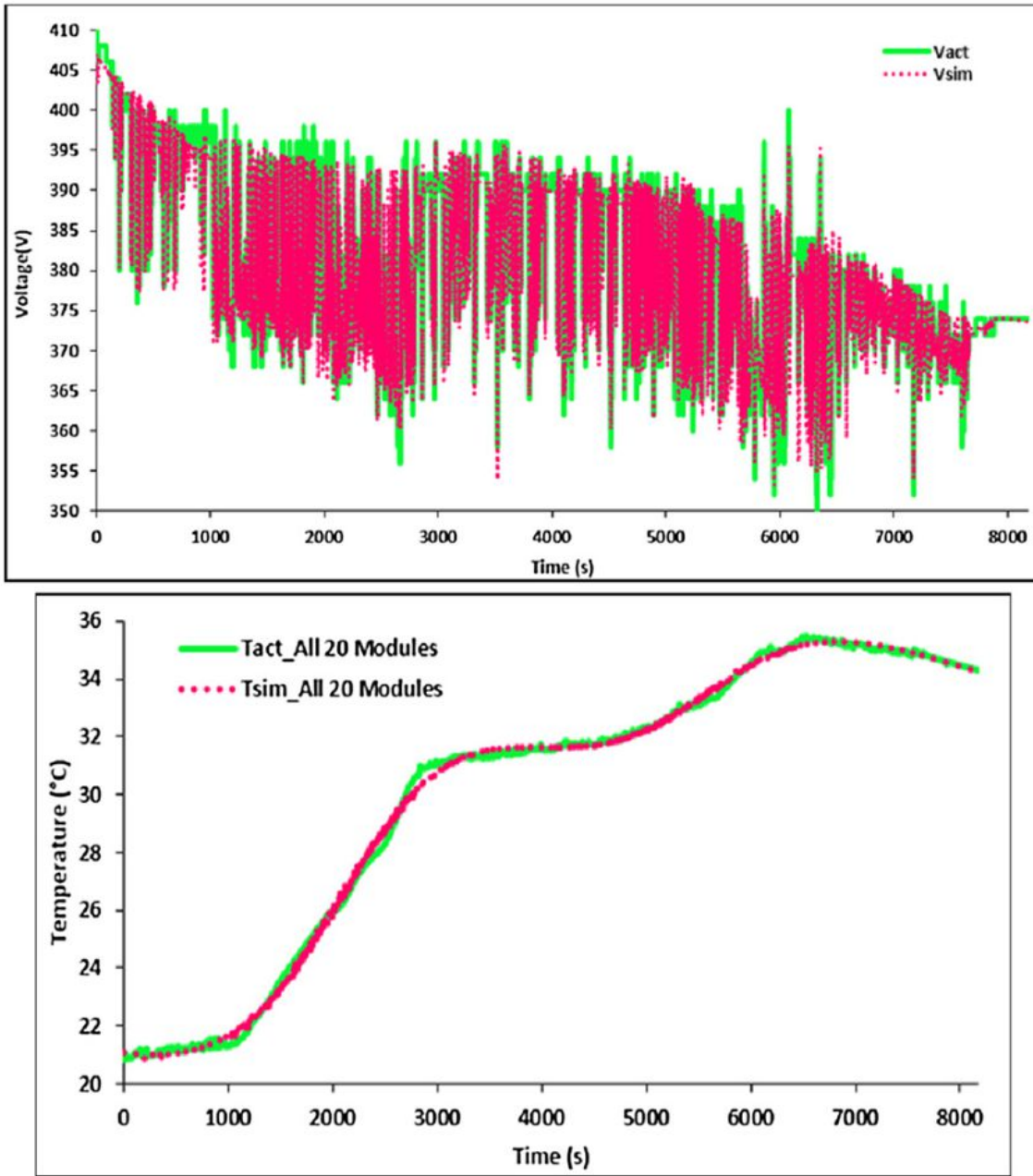


Figure 2.14 – Voltage (top) and temperature (bottom) comparisons between and actual and simulation data for a given drive cycle [36]

2.3 Thermal Equivalent Circuits

Thermal equivalent circuits, also called electrothermal models, take a geometric based approach where components are divided into simplified regions/elements to find the thermal resistance and capacitance of the various constituent parts. Many industries utilize

thermal equivalent circuits as detailed thermal models are difficult to design and compute in standard CFD/CAE environments. An accurate thermal simulation can help reduce computational times and create more accessible models. These networks also allow for the temperature at specific points within the system to be analyzed in both steady-state and transient conditions.

Karagol et. al. generated equivalent circuit models based on simulation data in 2010 and 2011 [37, 38]. The paper looked to bridge the gap between smaller thermal networks and large scale accurate thermal models developed with finite element software which required large computational times. Mathematical equations for the resistance, capacitance and heat flux were derived to satisfy the model created. Steady-state and transient scenarios were compared in which the results between finite element simulations and the electrothermal model developed yielded an average relative error in temperature rise of less than 7%. The authors concluded the error could be reduced with further model refinement.

Jain et. al. in 2010 [39] implemented an electrothermal model to predict the thermal performance of three dimensional integrated circuits. The significant thermal resistances and heat generation elements were identified and simulated through equations developed. Figure 2.15 shows the general thermal resistance network.

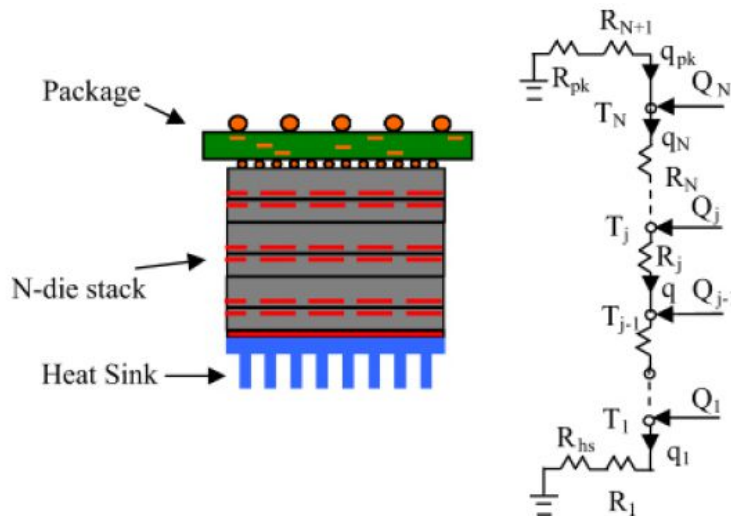


Figure 2.15 – Resistance network with multiple heat generation points [39]

Results for the model were not compared to experimental results, however, it lead to an enhanced understanding of heat transfer issues in three dimensional microelectronics. With an ability to better understand heat generation, propagation and dissipation the authors concluded that thermal and electrical co-design of three dimensional integrated circuits can potentially alleviate thermal management problems with better circuit board planning.

Hu et. al. used a Foster thermal model for HEV/EV battery modeling and compared it to CFD analysis in 2011 [40]. A Foster thermal network is a set of RC thermal elements in series. However, in the model developed, the resistors do not represent traditional thermal network components. In this case, they represent the transfer function of the battery thermal system. This meant the way the circuits were constructed are slightly different than in traditional thermal circuits. The idea behind this approach is to couple the Foster network with temperature dependent battery electrical models in order to replace the simple thermal model. This would lead to more accurate results and improved computational time. The authors concluded that battery cooling systems can be represented by a matrix of Foster networks as the results showed a maximum error of 2% between the CFD work and the Foster matrix.

Lin et. al. investigated a lumped parameter electrothermal model for A123's cylindrical LiFePO₄/graphite li-ion cells in 2014 [41]. The electrothermal model captured the battery SOC, voltage, and surface and core temperatures. Results were validated against electrochemical impedance spectroscopy. Experiments were conducted to find the open circuit voltage, capacity and ohmic resistance for the equivalent circuit shown in Figure 2.16.

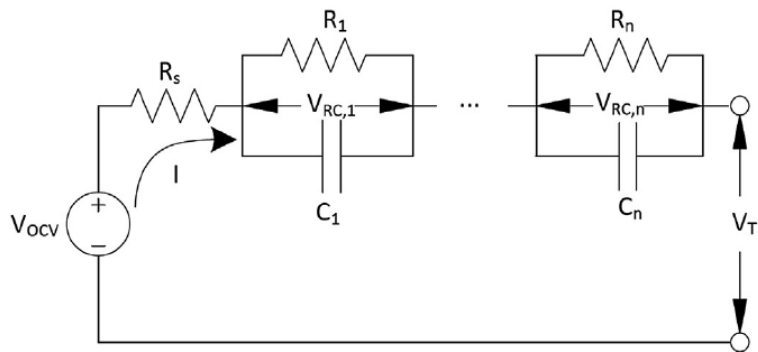


Figure 2.16 – Equivalent circuit model schematic [41]

The cross-section for the cylindrical cell is shown in Figure 2.17 with key parameters identified. The heat conduction resistance is used to model the heat flow from the core to the surface. Convective resistance is modeled from the surface of the cell to show convective cooling. The temperatures of the core, surface, cooling fluid, heat capacity of the core and surface casing are also shown. Many of the parameters were dependent on geometry and convective fluid properties.

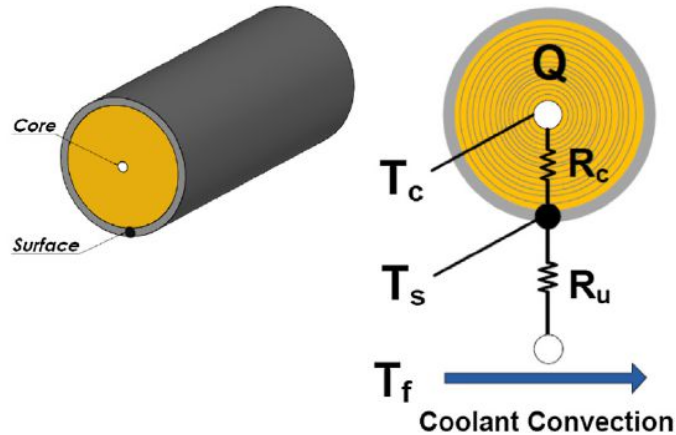


Figure 2.17 – Thermal model schematic [41]

The results given showed little error between the measured and estimated voltage and temperatures. The root mean square errors (RMSE) indicated the voltage varied by 20mV and temperature deviation was less than 1°C. The model was also simulated on a UDDS and FUDS drive cycle which confirmed the same range of errors for the voltage and temperatures. Figure 2.18 and Figure 2.19 give the voltage and temperature results during charge depleting and charge sustaining modes. For charge depleting, the maximum current was 10C and the average current was 4C. In charge sustaining, the maximum current was 20C with the average around 0.03C.

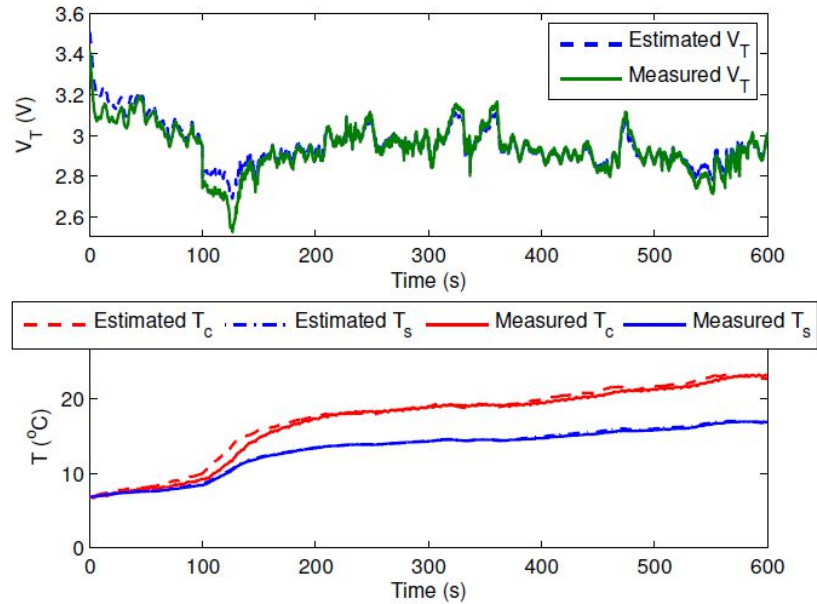


Figure 2.18 – Voltage and temperature readings under charge depleting [41]

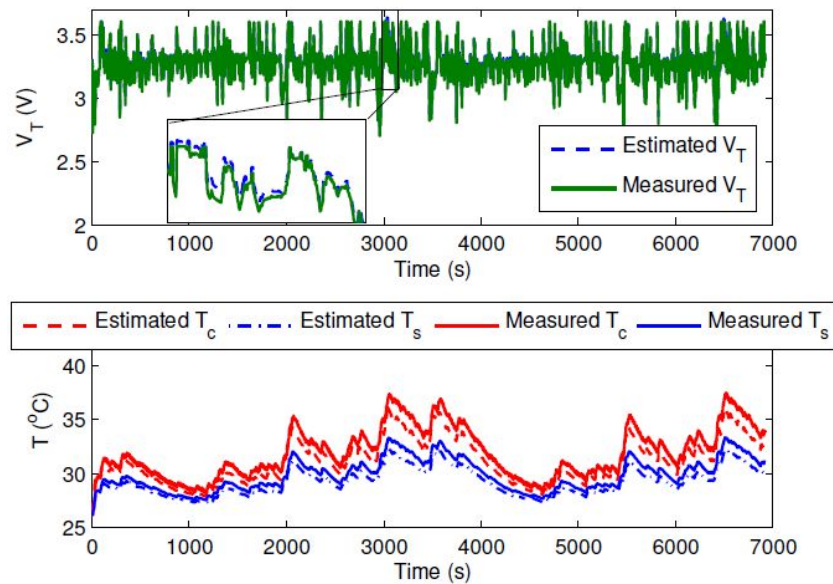


Figure 2.19 – Voltage and temperature readings under charge sustaining [41]

Saw et. al. used the equivalent circuit model of a LiFePO_4 cell for electrothermal characterization in 2014 and 2015 [42, 43]. The thermal model was based on the Hyundai Trajet electric vehicle which utilized a 19.5 kWh battery pack. The battery pack consisted of twenty eight modules with twenty four 10 Ah cells per module. Figure 2.20 shows the equivalent circuit model used by the authors. Results indicated the proposed battery model

is capable of accurately predicting the electrical and thermal responses. The voltage and temperature over a wide range of ambient temperatures and SOCs also showed good agreement. Figure 2.21 through Figure 2.23 depicts results between the experimental and model developed for the voltage, temperature and heat generation given various discharge tests.

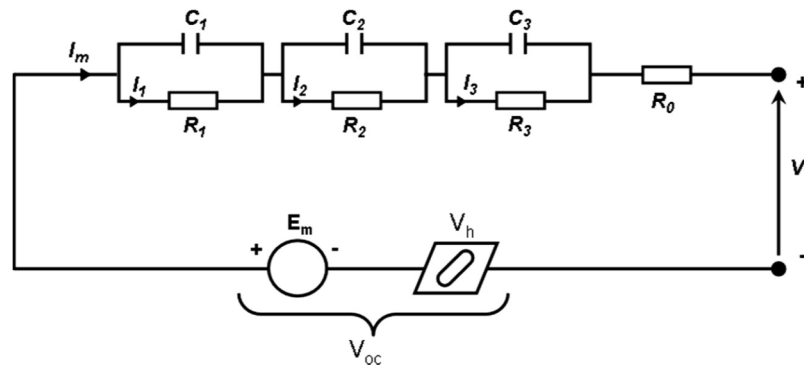


Figure 2.20 – Three RC equivalent circuit model [42]

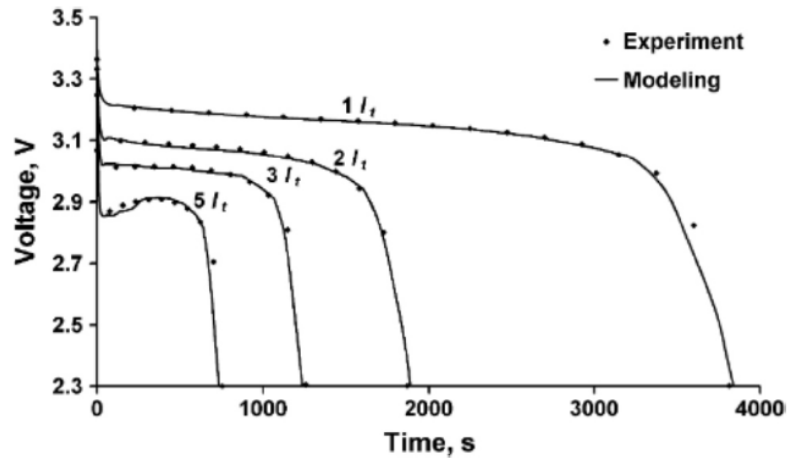


Figure 2.21 – Voltage prediction results [42]

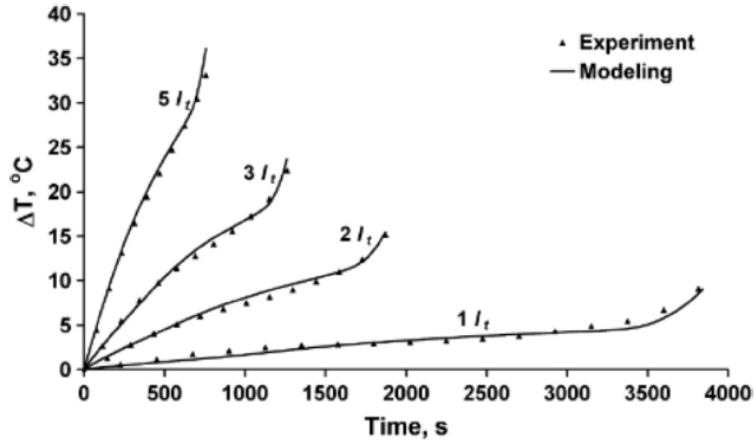


Figure 2.22 – Temperature prediction results [42]

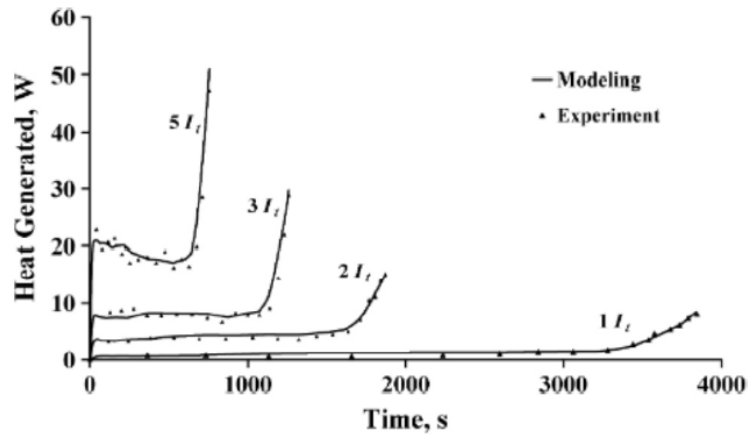


Figure 2.23 – Pouch cell heat generation results [42]

The thermal management system was based on a battery pack comprised of 50, 10 Ah, pouch cells. The cells are sandwiched between heat spreaders with cold plates on either side of the pack as the authors describe. Figure 2.24 shows a diagram of the conceptual design.

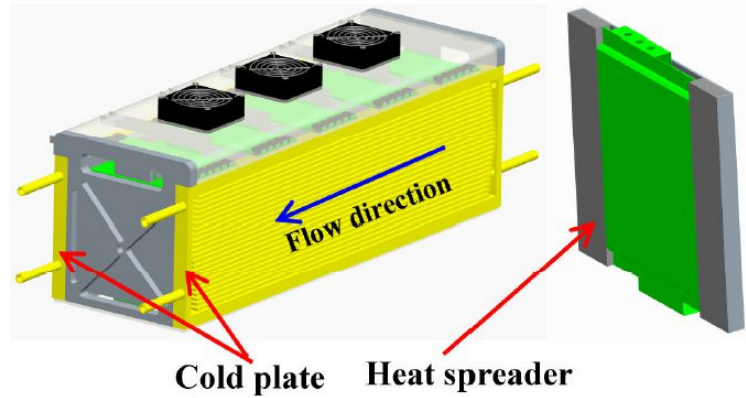


Figure 2.24 – Conceptual thermal management system by Saw et. al. [43]

From numerical solutions, the authors found a maximum heat generation in the cells at a 5C discharge rate and 90% SOC to be 20 W. Fluid properties for the cooling system using 50/50 percentage of ethylene glycol and water with an inlet temperature of 30°C and flow rate of 4.5 L/min, was found to be 36.5°C average surface temperature with the internal cell temperature being 43°C.

Greco et. al. developed a one dimensional transient computational model of a prismatic cell in 2014 using a thermal circuit approach for the thermal modeling of a passive heat pipe thermal management system [44]. The model was compared to an analytical solution as well as CFD simulations. For the design of the heat pipes, the authors chose a maximum heat transfer capacity of 400 W for a single heat pipe to reflect 41 W of heat generated by the battery. The heat pipe was over designed to reflect the conservative estimate of battery heat generation by the authors. Figure 2.25 shows the heat pipe and cell model together with Figure 2.26 depicting the associating electrothermal model.

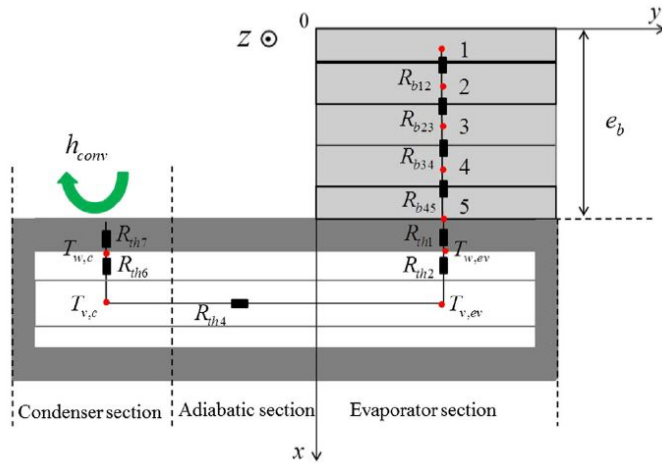


Figure 2.25 – Simplified model with a cell on the heat pipe [44]

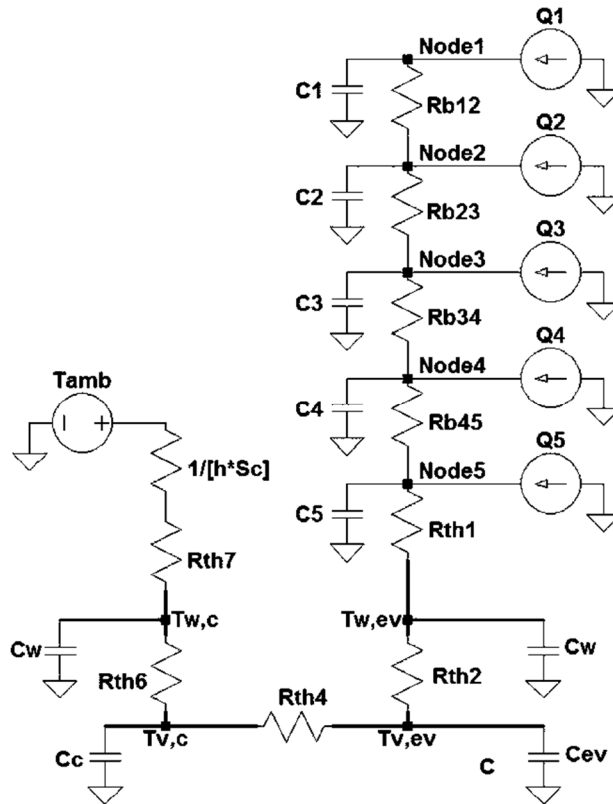


Figure 2.26 – Transient electrothermal model [44]

The simulation results showed good agreement between the electrothermal, analytical and CFD models. Figure 2.27 recounts the maximum temperature rise of the cell using the different approaches. The authors do note the CFD model was computationally intensive

and therefore the thermal equivalent model offers a feasible solution for the design and analysis of battery cooling systems during the preliminary design stages.

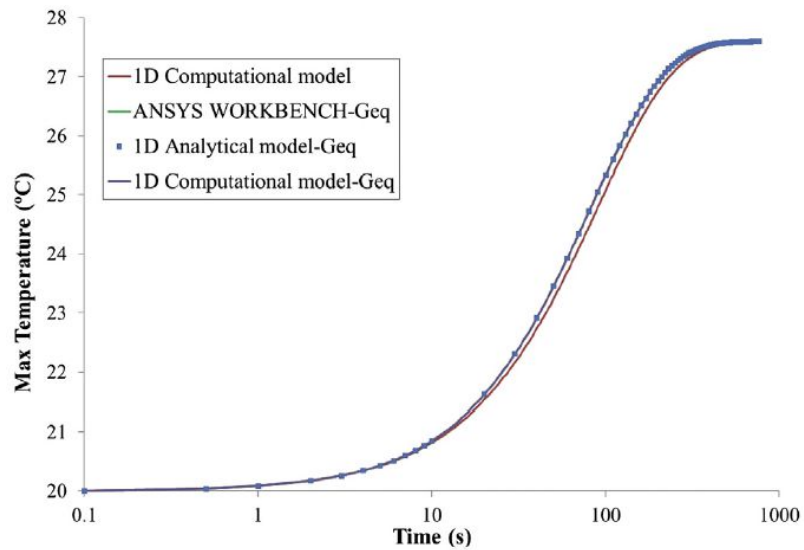


Figure 2.27 – Maximum cell temperatures for the various simulations [44]

Baghdadi et. al. used experimental results to obtain parameters to be implemented in MATLAB/Simulink to create a dynamic electrothermal model for li-ion batteries in 2015 [45]. The authors modeled a 12 Ah Nickel Manganese Cobalt cell from Kokam using non-linear parameters such as open circuit voltage and battery resistances. The accuracy of the model was tested under static and dynamic current profiles for different operating conditions. Figure 2.28 is the equivalent circuit model developed by Baghdadi et. al.

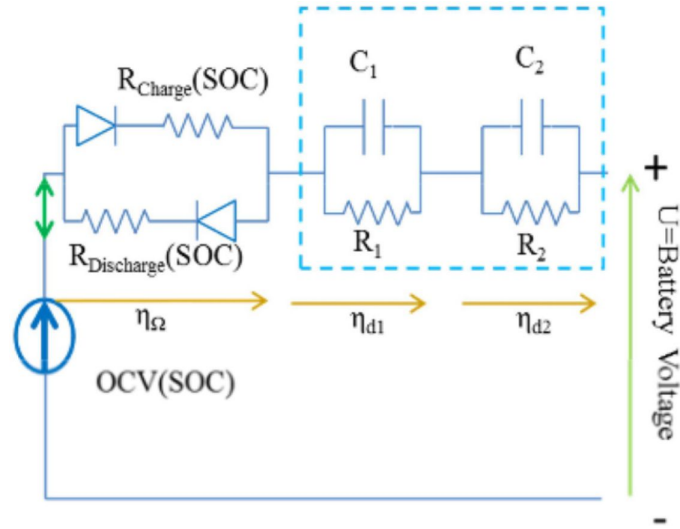


Figure 2.28 – Equivalent circuit model presented by Baghdadi et. al. [45]

The model in Figure 2.28 is different than other equivalent circuit models due to the bidirectional structure of the model. Diodes are used to account for voltage polarization and the difference in charge and discharge resistances. The heat generation governing equation for the thermal model developed is given by:

$$mC_p \frac{dT}{dt} = Q_{\Omega} + Q_{rev} + Q_{env} \quad 2.5$$

Where m is the mass of the battery (kg), C_p is the specific heat (J/kgK), Q_{Ω} is the ohmic heat generated, Q_{rev} is the reversible heat due to the electrochemical dynamics of the battery and Q_{env} is the heat loss to the surrounding environment by convection. Simulations for the electrothermal model were compared to various experimental test (varying SOC, temperature, and current profiles). It should be noted that no official drive cycles or vehicle data was used to validate the model, only simulated driving profiles were created. Figure 2.29 shows the results of a varying C-rate at 25°C ambient test condition. The temperature predicted follows the experimental profile with some variation resulting in a precision better than 0.5°C. The authors conclude their electrothermal model is in agreement with the various experimental tests at different operating conditions. While the results were favourable, they recommend the electrothermal model should be able to model battery

geometry and be coupled with an aging model that updates the battery capacity and resistance.

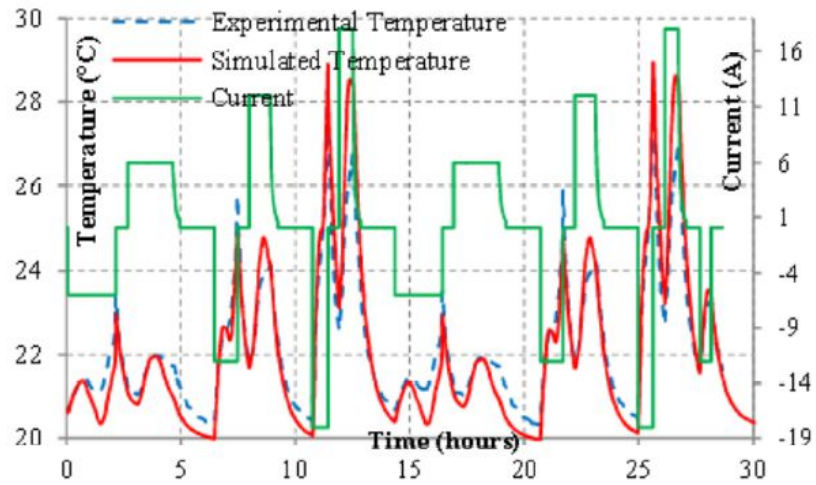


Figure 2.29 – Simulation and experimental results of varying C-rate at 25°C [45]

Damay et. al. created an electrothermal model of a large prismatic LiFePO₄/graphite cell in 2015 [46]. This model combined the heat flux through the battery, external casing, to the atmosphere and also integrated a cooling system at the base of the cells. Most of the parameters were determined analytically using the physical and geometric properties of the cells. The model developed is based off a 40 Ah centralized cell in a battery pack as shown in Figure 2.30 and a difference of 0.2°C was measured between the neighboring cells.

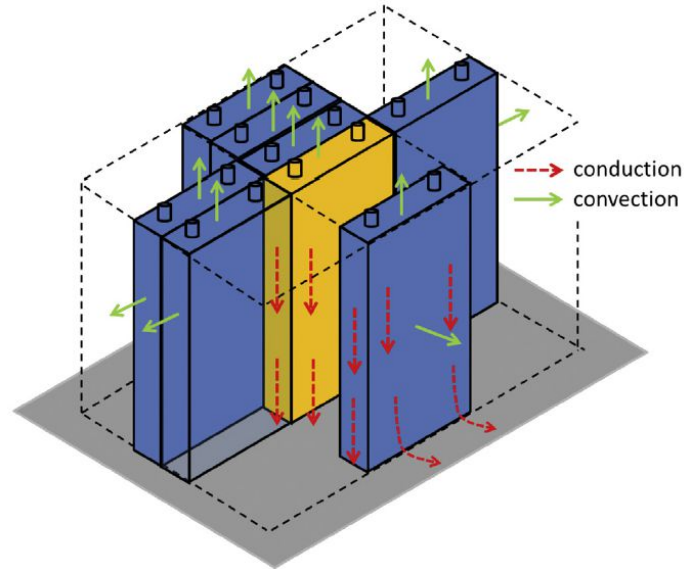


Figure 2.30 – Centred prismatic cell in a battery pack with a cooling base (grey) [46]

A detailed equivalent circuit for the central cell was created which outlines the heat generation internally, the heat capacity and resistive elements around the external casing, resistive elements to the surrounding atmosphere and to the cooling plate. It is a detailed three dimensional equivalent circuit with the values of each resistance in the model summarized in a table. The table also identified which equations were used to calculate the resistance value and which were derived mathematically or experimentally. Figure 2.31 is a diagram of the lumped thermal model developed.

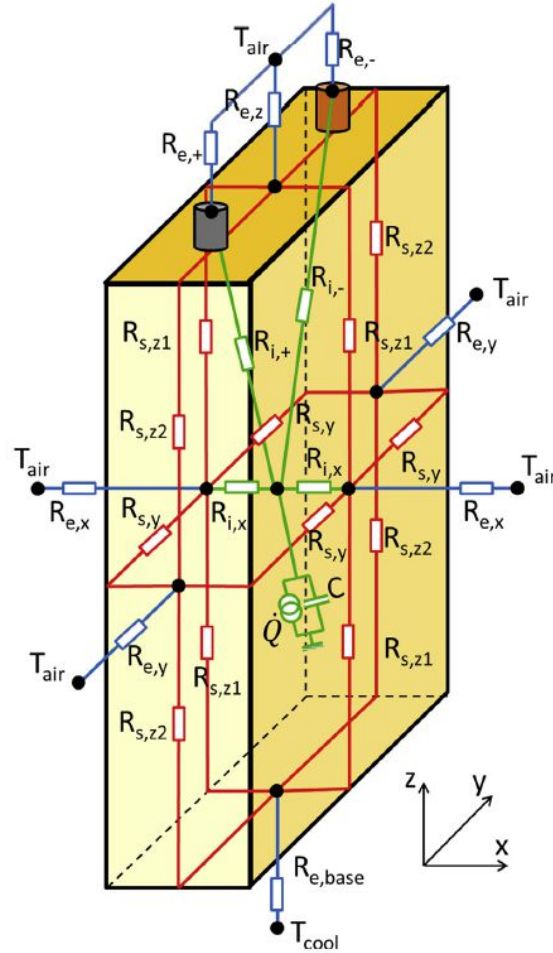


Figure 2.31 – Lumped thermal model by Damay et. al. [46]

While the authors state the model is fairly accurate and have used some experimental values there isn't a full validation between simulation and experimental results, only a combination of simulation and experimental results for various nodes. While the design approach is very detailed, it is still lacking a direct validation between the experimental and simulation of external casing temperatures given the number of resistance elements they have outlined, the majority of which were determined analytically.

Zhang et. al. used a simplified electrothermal model to estimate the battery internal temperature in real-time in 2016 [47]. The authors adopted the most popular equivalent circuit model as the basis for their electrothermal model shown in Figure 2.32. Various equations were developed to solve parameters relating to the equivalent circuit. The battery thermal model was then developed with derived equations and combined with the

equivalent circuit for an integrated model. Experimental data for a prismatic LiFePO₄ cell was used to validate the model with the setup shown in Figure 2.33. They used 3 cells and thermocouples at various locations to measure cell surface temperature.

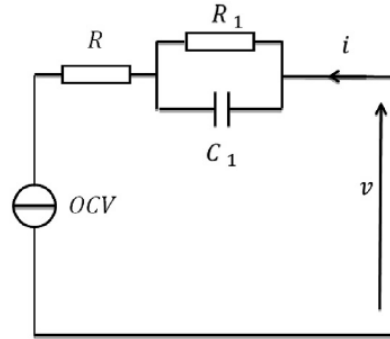


Figure 2.32 – Equivalent circuit used by Zhang et. al. [47]

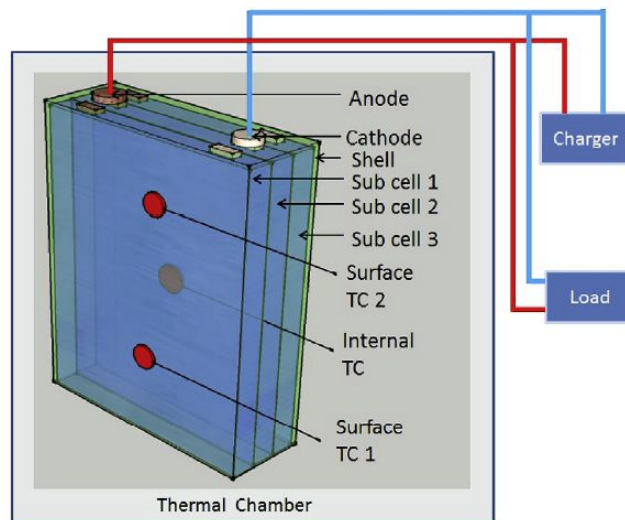


Figure 2.33 – Battery test setup [47]

Results for the model showed good agreement between the experimental and simulation data for the surface and internal temperature of the cells. As seen in Figure 2.34, T_{in} is the interior temperature of the cell and T_{sh} is the surface temperature of the cell. The authors state that for T_{in} , there is an average error of 0.37°C with a maximum error of 1.28°C . For T_{sh} , the average error was 0.36°C with a maximum error of 1.43°C . They concluded the combined model created is capable of predicting the internal temperature of the cell effectively.

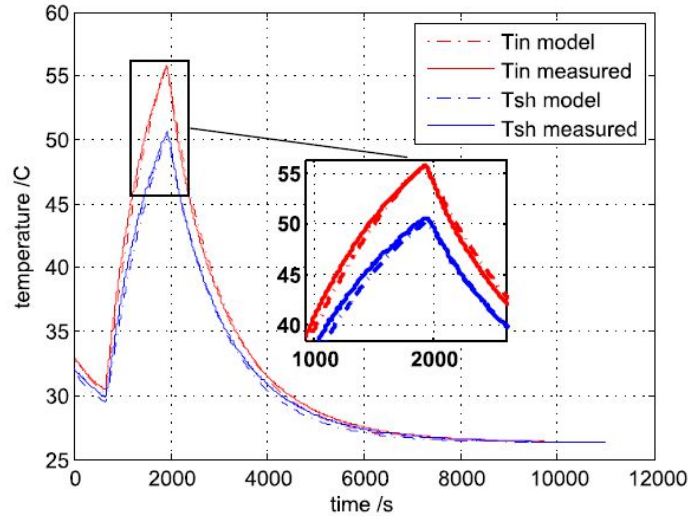


Figure 2.34 – Comparison between experimental and simulation results [47]

2.4 Capacity Fade and Increased Resistance with Aging

As cells are charged and discharged, the available capacity decreases due to an increase in resistance at the anode and cathode. This leads to faster discharge times, reduction of available power and increased internal heat generation. These are important factors for HEVs and EVs as battery aging leads to a reduction in available driving range and develops potential safety hazards. Understanding how cells increase in resistance and decrease in capacity over time can aid in the design of thermal systems to ensure they can continue to regulate the cell temperature as the battery pack reaches end-of-life.

In 2000, Zhang et. al. investigated the effects of increased resistance on the surface of the positive and negative electrodes and associated capacity fade in Sony 18650S li-ion cells [48]. The author’s model showed after 800 cycles, the available capacity decreased 30% from 1200 mAh to 840 mAh and the resistance increased three times the original value.

Lam and Bauer used empirical and experimental models to gauge the capacity fade in EV cells under most operating conditions [49]. They tested A123 Systems’ APR18650m1 LiFePO₄ cells with test conditions of 90% initial SOC, 25% depth of discharge, and 25°C with discharging and regenerative braking C-rates of 0.67 C and 0.22 C respectively. From the models developed, the authors concluded that capacity fade was small for a low average SOC and SOC deviation. However, high temperature rise due to

ohmic heating would accelerate capacity fading. They also concluded for temperatures of 0°C and below, capacity fade is accelerated by high recharging C-rates.

Steffke et. al of General Motors developed a test methodology for Li-Ion batteries in automotive applications in 2013 [50]. One of objectives were to verify a battery pack was capable of performing for the entire service period which was 10 years/150000 miles. The two other objectives of the research was to provide data to optimize battery pack design and to verify performance of the battery pack correlated with simulated cell data. The authors determined the Beginning of Life (BOL) performance, simulated four-season accelerated life use, simulated battery packs in elevated environmental conditions, and determined End of Life (EOL) performance. The results concluded the resistance increased 105% at the 10 year mark and capacity faded by 46%. Figure 2.35 and Figure 2.36 illustrate the resistance increase and capacity fade respectfully for the authors sample four-season accelerated test. The 10 year operational target is indicated on each figure.

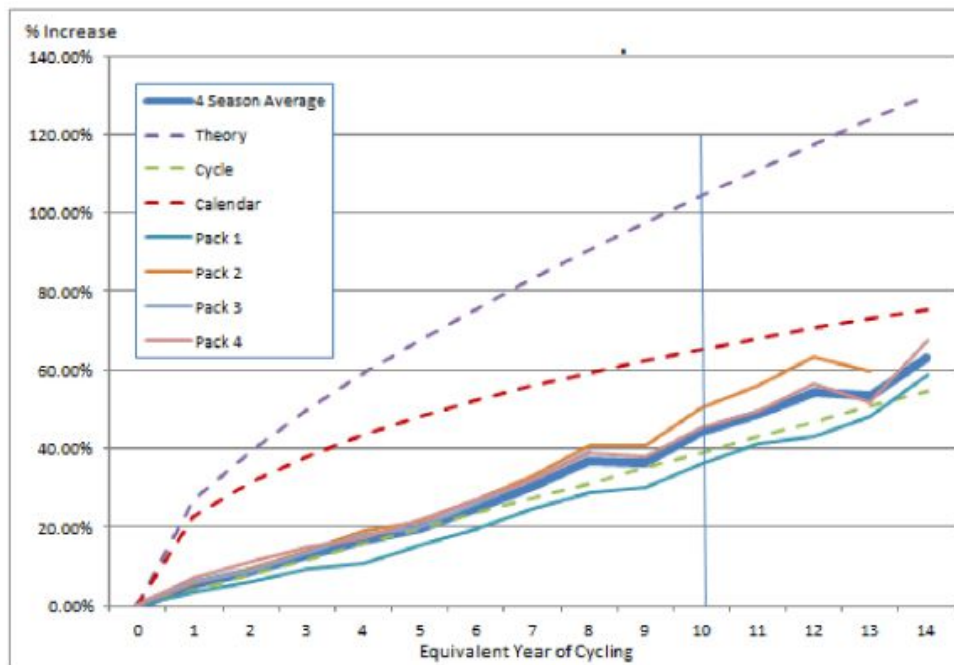


Figure 2.35 – Four-seasons sample test resistance increase [50]

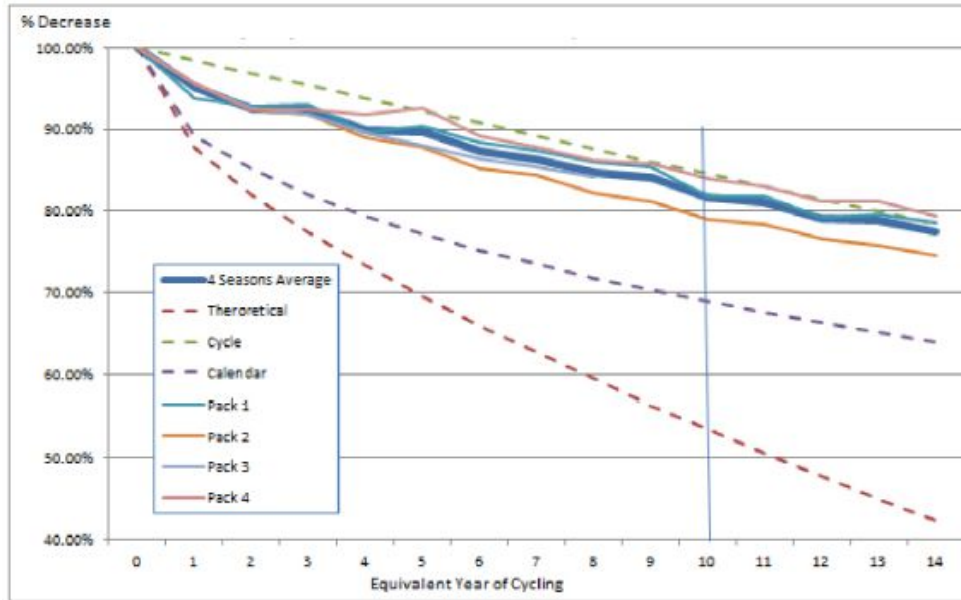


Figure 2.36 – Four-seasons sample test capacity fade [50]

Baek et. al. in 2015 developed a 2D model to simulate the loss of active material on the anode and cathode resulting in capacity fade and increased resistance for Li-ion cells used in EVs. The model established, when compared to experimental results, showed the capacity linearly decreased with the number of cycles and saw a 34% decrease after 3000 cycles. The resistance also increased linearly and quadrupled in value after 2000 cycles.

Daigle and Kulkarni predicted end-of-discharge and end-of-life in li-ion batteries with an electrochemical based aging model with research sponsored by NASA in 2016 [51]. The cell chemistry being tested was a lithium cobalt oxide which the authors developed in a previous study [52]. The results for the capacity fade and increase in resistance showed a linear trend for 1000 cycles. Figure 2.37 recounts the capacity fade estimation after each discharge cycle. Figure 2.38 shows the increase in resistance with increased aging.

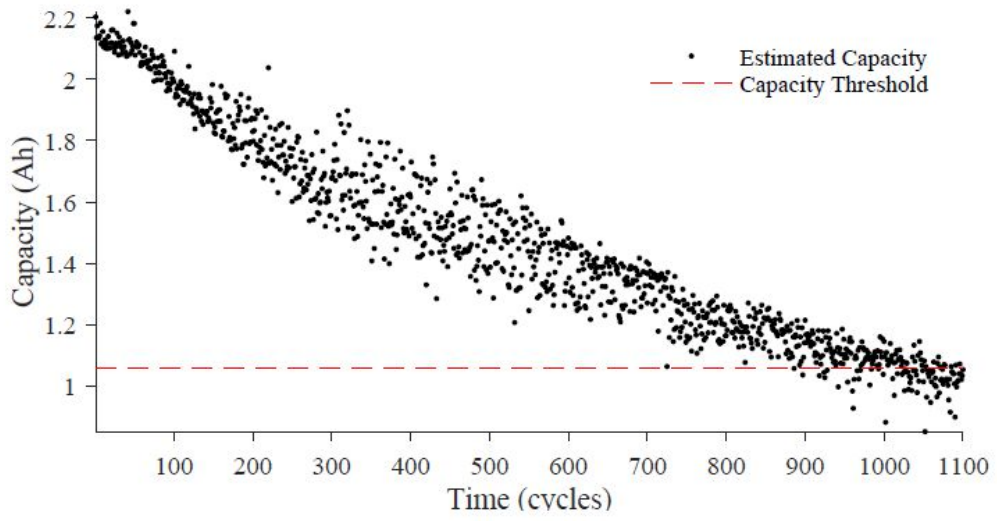


Figure 2.37 – Capacity fade as a function of estimated aging [51]

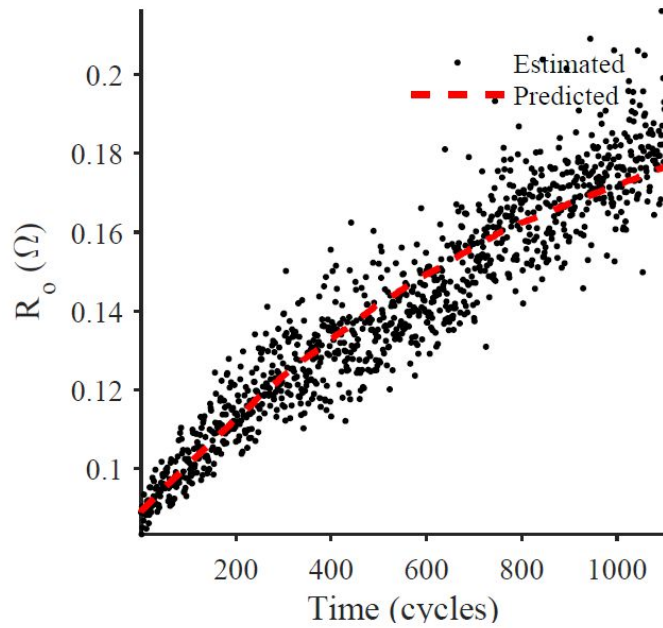


Figure 2.38 – Estimation and predictions of resistance with aging [51]

2.5 Effects of Cold Temperatures on Li-Ion cells

Numerous studies investigate Li-Ion cells at room temperatures or to study the safety concerns of cells at elevated temperatures. Fewer studies investigate cells at low environmental temperatures to determine the effects on resistance and capacities. These studies are imperative as hybrid and electric vehicles can experience a wide range of temperatures. Vehicles need to be equipped with a heater as part of the thermal management system, however, this can't be achieved unless the effects of cold temperatures are known and understood.

In 2013, Yi et. al. modeled a Li-ion cell discharge behaviour in low temperature environments [53]. The cell modeled and simulated by the authors was 14.6 Ah pouch cell with a cell chemistry of LiMn_2O_4 . The discharge rates were 0.5 to 5 C at -20, -10 and 0°C. The results showed at 1 C discharge, the cell had decreased capacity at temperatures below 0°C. As the discharge rate increased, the low temperature results showed the cells have substantial capacity reduction and in some cases became inoperable.

Idaho National Laboratory (INL) conducted on-road cold weather testing in a MY12 Chevrolet Volt in 2014 [54]. INL observed temperatures at or below -3°C results in the vehicle's control system periodically starting the engine. The colder the ambient temperature, the more frequent the engine cycled on and off. In charge depleting mode, the range decreased from 68 km at 21°C to 32 km when the temperature was -26°C, a range decrease of 53%. The authors also observed in extreme cold conditions, the engine cycling slowed the rate of battery depletion.

Jaguemont et. al. in 2015 [55] conducted low temperature aging tests for a 100 Ah prismatic LiFeMnPO_4 cell. The cell was studied at three operating temperatures (25°C, 0°C, -20°C). However, only one SOC was tested (50%) due to time and material constraints. Various test procedures were outlined by the authors to represent different vehicle situations such as workday usage, home charging and overnight parking. The authors concluded there is a strong connection with low temperatures and cell degradation. A severe degradation at low temperatures called lithium plating occurs. The long term effects of lithium plating are a loss of capacity and power efficiency and a rise in impedance. The authors also concluded a thermal management strategy for HEVs and EVs is crucial to preventing or reducing degradation by lithium plating.

Jaguemont et. al. in 2016 investigated thermal management strategies for HEVs and EVs in cold weather conditions [56]. At the selected temperatures (0°C, -10°C, -20°C), the ambient condition was held at a constant value. The authors utilized the same 100 Ah cell from their previous studies and used MATLAB/Simulink and an electro-thermal model. However, the model developed used an initial temperature of 20°C for the cells in all test conditions. The two strategies tested were keeping the cells at approximately 21.2°C and raising the cell temperature to 25°C when the vehicle is started. The authors concluded there were trade-offs to various scenarios given the size of the cell being tested. The overall consensus was a proper thermal management system strategy is necessary for cold weather situations. While this method allows for the implementation of a cold weather thermal management system, it is limited by the initial temperature conditions and static ambient temperature. The authors noted future work is needed to account for the varying nature of ambient temperatures to simulate a real world application.

2.6 Summary

A few mathematical, computer simulation, and thermal equivalent circuit models have been discussed in this chapter. The mathematical models use a common equation to calculate the heat generation within a cell. The heat generation of individual cells and cell stacks employing the earlier lithium polymer cell chemistry were also reviewed. Computer simulations have been deployed by many to model heat generation within different cell geometries and chemistries. CFD analysis and MATLAB approaches appear to be popular though the former are computationally extensive. Thermal equivalent circuits have shown the ability to offer results comparative to CFD with far less computational time and offering more system design flexibility. The effects of battery aging on the cell capacity and resistance were also reviewed, with results concluding a linear increase in resistance of between 2-4x as the capacity decreases proportionately by about 30%; a point generally defined as “End of Life” for the battery pack.

CHAPTER 3 - JUSTIFICATION AND RATIONALE

This chapter discusses software selection considerations to complete the full vehicle simulations which enable the creation of a thermal equivalent circuit. Information is also provided with regards to the electrochemical phenomena that reduces battery capacity and power over time. Safety aspects of the electrochemistry are taken into account as well providing rationale to why investigations into thermal management systems are ever more important.

3.1 Software

Various software suites can be used examine the proposed objectives. The capabilities and cost are some important factors to consider as well as if the software will see continued development to support future versions. This section will outline the reasoning for selecting Autonomie and PSpice for vehicle and thermal equivalent circuit simulations.

3.1.1 Vehicle Simulation Software

Depending on the level of fidelity needed, there are many options for vehicle simulation software. Some software suites specialize only in analysis while others offer the capabilities to test the model in the real world through controls development or Hardware in the Loop (HIL) testing. This leads some software into being forward-facing, backward-facing or a mix of both. To understand forward and backward facing models, drive cycles will be use to explain the concepts.

Forward-facing vehicle models feature a driver model which provides the correct amount of power to meet a speed trace on a drive cycle. Based on the driver response, this input is propagated through the powertrain all the way to the wheels and then fed back to the driver controller. This results in changes to pedal demand affecting the output of the powertrain components so the torque demand is adjusted to follow the speed trace. Backward-facing models do not have a driver model and use the speed trace to calculate the required force at the wheels which is then propagated back to the powertrain components. The ability of the vehicle to meet the drive cycle demands is the key

assumption of a backward-facing model, something easily violated. Forward-facing models do not impose a speed trace on the vehicle model (but can output the degree to which the trace was missed) and more closely represent a test driver in a real vehicle. Forward-facing model are thus better for development of predictive controls and generally having low margins of error between the simulation and actual speed of the vehicle on a given drive cycle.

3.1.1.1 ADVISOR

ADVISOR (ADvanced VehIcle SimulatOR) was a powertrain analysis tool built by NREL from 1994-2004. It created a set of data and model files to be used in the MATLAB/Simulink environment for the rapid analysis of the performance and fuel economy of vehicles (including electric/hybrid powertrains). The models in ADVISOR are mostly empirical and rely on powertrain component relationships measured in a laboratory. The models are also quasi-static, collecting data (ie. torque and speed) from steady state and then modifying those inputs for transient effects like rotational inertia. Predictive or forward-facing simulations are not possible in ADVISOR so it's considered backward-facing. The software has transitioned to open-source since NREL ended support.

3.1.1.2 GT-SUITE

GT-SUITE is an industry focused simulation tool with libraries aimed at various applications. Some of the software highlights are summarized below from the GT-Suite website [57]:

GT-SUITE is a multi-physics platform for creating models of general systems based on many underlying fundamental:

- Flow, thermal, mechanical and electrical libraries
- Controls library (signal processing)
- Performs embedded 3D CFD and 3D FE thermal/structural modeling with all boundary conditions provided by the simulated surrounding complete system
- Performs component design, system integration, controls, HIL and calibration, and even to on-board CPU model based control

While there is a benefit to using an industry focused tool for development that is forward-facing, the costs associated to licensing such a program may be out of budget for most academic research purposes.

3.1.1.3 PSAT/Autonomie

In response to engineers needing to develop the next generation of HEVs and EVs without costly prototypes Argonne National Laboratory (ANL) developed the Powertrain System Analysis Toolkit (PSAT). PSAT was developed in conjunction with US automotive manufacturers and the US DOE. The use of MATLAB/Simulink allowed for results to be generated much quicker in PSAT. Some capabilities for PSAT are described below:

- Forward-facing model
- Can simulate light to heavy duty vehicle applications
- Ease of implementation of data, component models and control strategies
- HIL/SIL integration

In 2012, ANL transitioned PSAT into Autonomie which they continue to support. The underlying backbone of the software remained (ie. MATLAB/Simulink based) with updates to the GUI and the ability to link to third party tools such as GTPower and SimScape. The benefit of Autonomie is its ability to be forward-facing and integrate third party tools that increases its versatility relative to other software suites which tend to be proprietary in nature. Autonomie also offers licenses for academic purposes for a cost which is lower compared to other tools.

3.1.2 Thermal Equivalent Circuit Analysis Tools

To analyze the thermal equivalent circuit model which was developed, there are various tools which may be used. Voltage and current in electrical representation of thermal systems are temperature and heat flow respectively. Each of the tools described in this section can perform the analysis with the benefits and drawbacks discussed.

3.1.2.1 Maple

Maple (Maplesoft) was created by the University of Waterloo which can input mathematical expressions in traditional notation for computations. In relation to circuit analysis, Maple can solve expressions developed from Kirkoff's voltage and current laws (KVL and KCL) to find the current and voltage at various nodal points. If the mathematical expressions are known for the circuit being analyzed, Maple can compute the output with low computational resources. However, this method works well for simple circuits and the limitations of Maple become apparent when trying to analyze more complex circuits as the mathematical computations become increasingly complex.

3.1.2.2 MATLAB and Simulink

MATLAB and Simulink are well known mathematical tools which allow for scalability and flexibility in model complexities. Unlike Maple, MATLAB cannot process mathematical expressions. Like all programming languages, everything must be defined for the expressions to be solved. Like Maple, simple circuit equations can be solved but complex equations also result with solving issues. Simulink is a graphical representation of mathematical expressions and systems. It also has specific toolboxes to help with various mechanical and electrical systems. The SimScape toolbox enables the rapid creation of models of physical systems. Models are built using physical component sub-models based on physical connections that directly integrate with block diagrams and other modeling paradigms. The electrical blocksets allow for a circuit to be built with RLC components and various sinks/sources. The simulation times depend on the complexity and it takes time to add/modify all the required circuit components (for the system being simulated). SimScape toolboxes also allow for HIL simulations which aid in forward-facing applications.

3.1.2.3 SPICE Software

Simulation Program with Integrated Circuit Emphasis (SPICE) is an open source analog electric circuit simulation tool. It is often used to develop integrated circuits so as to check their integrity if it's not practical to build prototypes before manufacturing. There are companies who have commercialized SPICE software under different names (ISPICE,

PSPICE, XSPICE, LTspice). The programs are graphical based allowing for RLC elements to be added to the workspace by selecting from the parts library. The libraries are also more extensive than what is offered by SimScape. Semi-conductor manufactures offer SPICE models for their components which can be added to the SPICE library. This allows for production components to be added to a circuit already developed with only the element values needing adjustment. This allows for faster tuning of circuits. Since SPICE is targeted towards the development and tuning of integrated circuits, it appeared as the best solution to define/develop/tune a thermal equivalent circuit alongside experiments. There are no explicit equations to generate first, and simulation times are extremely quick, even on the most complex circuit designs.

Given the user friendly design and capabilities, PSPICE was selected for the thermal circuit analysis in the Chevrolet Volt. It also allows for integration into Simulink which further enhances its capabilities. What need be understood to build a circuit model are the various paths of heat flow within the battery pack, and to/from the environment. This makes the circuit developed here within specific to the Voltec platform; however, the underlying principles for developing the circuit are applicable to other vehicle architectures/layout (air or liquid systems). New heat flow paths as well as the resistance, capacitance and source values will need to change but the graphical interface of PSPICE allows for a rapid reconfiguration of elements through a drag and drop method.

3.2 Thermal System Architectures

Depending on the size of the high voltage battery pack and vehicle architecture type, the thermal management strategy will be either air or liquid based. Air cooling is the most cost effective thermal strategy as it required fewer parts, however, this battery pack design requires space between the cells/modules for airflow which can cause packaging constraints. When using air in a battery module, forced convection adds/removes heat through forced convection. The air system can either be classified as passive or active. A passive system means that only the ambient environment is used to supply air, which is either from outside the vehicle, or from within the cabin of the vehicle as seen in Figure 3.1. An active system utilizes the vehicle's refrigeration system to cool the supplied air to a specific temperature target, whereas for heating there is specific high voltage battery

heater to warm the air as seen in Figure 3.2. Conditioning the air into the pack is ideal as environmental/cabin has limits regarding the amount of heat/cooling is directed towards the cells.

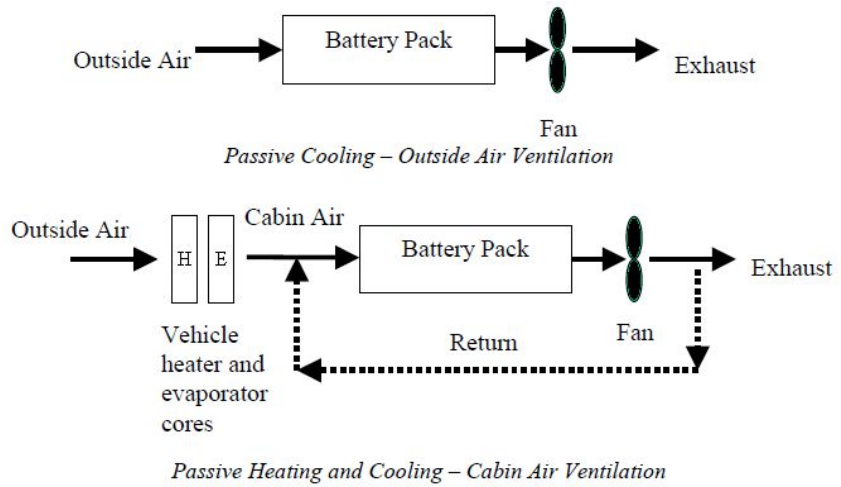


Figure 3.1 – Passive air thermal strategy [1]

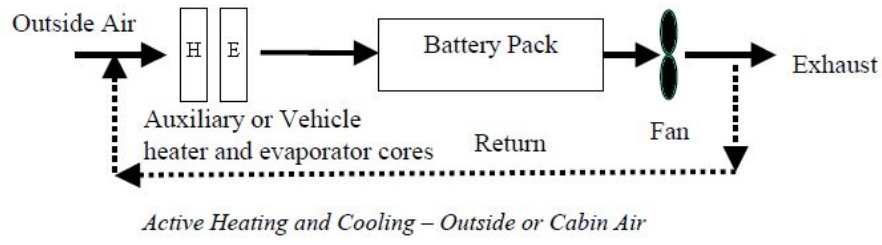


Figure 3.2 – Active air thermal strategy [1]

Liquid thermal systems on production vehicles utilize an active indirect arrangement which consists of liquid flowing through jackets which cool/heat the cells by way of conduction. The fluid that enters the module can be cooled by flowing it through the automotive radiator or by using the AC and a secondary heat exchanger to cool the fluid further. For heating, the fluid would pass through a resistive heater module which warms the fluid before entering the pack. In both cases, a pump is required to circulate fluid through the battery pack. In the case of the Chevrolet Volt, the vehicle selected for this research, it supports the later complex liquid thermal management system. Cooling/heating plates are sandwiched between cells such that each cell has one face in direct contact. It is an

expensive pack arrangement due to the hardware required. To better comprehend how the system works, Figure 3.3 outlines the flows of fluid possible.

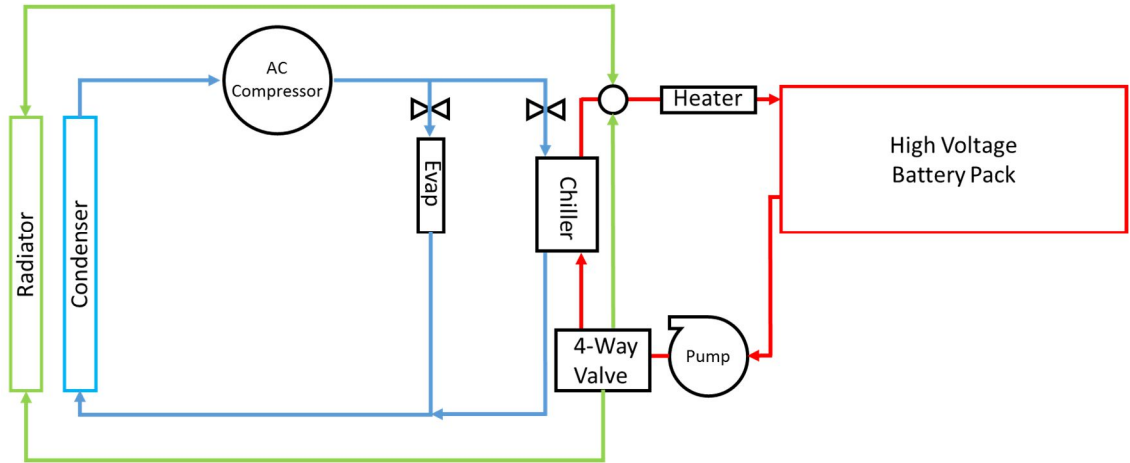


Figure 3.3 – Chevrolet Volt thermal loops with HV electric compressor and heater.

The refrigeration side operates as normal with a forward mounted condenser and cabin evaporator that has the refrigerant passing through a thermal expansion valve (TXV). The addition here is a parallel path for the refrigerant to flow through the chiller device (and the associated TXV). The chiller is classified as a two fluid non-mixing crossflow plate heat exchanger. The secondary loop is the glycol fluid flowing thorough the battery pack. It is circulated by a low voltage pump and enters the chiller where the colder refrigerant extracts heat from the hotter glycol. When the refrigerant passes through the condenser, the heat gained through the chiller is rejected to atmosphere. The 4 way valve can also be positioned to recirculate fluid within the pack to a dedicated radiator, rather than the chiller, for opportunity cooling or temperature equalization within the pack should the necessary conditions materialize. For heating, the AC is not operational so fluid passing through the chiller has no real effect. When the fluid passes through the resistive heater (1.8 kW), the warmed fluid enters the battery pack. Basically the AC compressor's output is approximately split in half, between the cabin requirements and the chiller to the battery. When operating at a higher output, over 3 kW of cooling can be directed towards the battery side, but typically the compressor runs at a moderate (quiet) and efficient speed and less than half this amount is normally directed towards the battery. The refrigerant side of this

architecture is not really within the scope of this research as it requires through understanding of the hardware limitations of the compressor and the associated components/controls. This research primarily considers how the inlet fluid to the pack changes temperature for a normal compressor operation profile (experimentally recorded) to see how effectively the cells are cooled over various drive cycles. Given the complexity of this arrangement, being able to simulate the entire vehicle with such a complex thermal management layout means other systems, including air based, can also be effectively modeled using this same approach as they all have reduced or simpler layouts.

3.3 Lithium-Ion Electrochemistry

This section will discuss various aspects of Li-Ion electrochemistry in relation to capacity/power fade, life expectancy and safety. These areas identify the need for better thermal management systems and expected temperature limits.

3.3.1 Capacity and Power Fade

Capacity fade refers to the loss of discharge energy capacity over time which also reduces the amount of power available. Available energy is lost when the active material inside the battery has been transformed into inactive phases, which reduces capacity at any discharge rate. Power reduction occurs when the cell internal impedance augments, which leads to a reduction in operating voltage at any discharge rate. The causes of these phenomena are different given the cell chemistry and its usage. It is clear however, that temperature plays a pivotal role in the capacity/power fade mechanisms, and Arrhenius relationships (logarithmic) govern such that small temperature changes have powerful influence. Various studies have shown the capacity fade to be far more significant with temperatures above 50°C [58, 59, 60]. Cold temperatures, below -20°C, will markedly reduce power due to the inability to transfer ions, and particularly charging under cold conditions (below 0°C) lead to a significant amount of plating on the anode (dendrites) [61, 62], that damages the separators, eventually causing internal shorts. At best these dendrites cause self-discharge, and at worst they lead up to “thermal runaway”, a euphemism for violent fire/explosion.

Power fade can be attributed primarily to the thickening of the solid electrolyte interface (SEI) and side reactions, all of which consume lithium. The SEI is carefully and purposefully formed during the initial charging cycles by the manufacturer. It acts as a porous insulator that allows electrons to flow without ions themselves crossing. This layer may also fracture slightly over time and thus needs to be reformed as a consequence. Also, unwanted side reactions continue and produce deposits that accumulate during cycling over a long period of time [63, 64]. Accumulation of deposits results in a thickening of the SEI, increasing the internal resistance across that layer, which leads to power fade. Since formation of both side reaction deposits and SEI are lithium ion consuming, energy capacity is also affected. The deposits are all electronic isolators so the number of particles available to combine with electrons are permanently reduced, and active material is “lost”. In essence this causes the capacity fade to become permanent [64]. Since increased internal resistance causes heating, and the whole process is accelerated in an exponential fashion via heat generation, the situation worsens over time until it gets out of hand.

The capacity and power fade phenomena helps to identify an upper threshold for battery temperatures when cells are used for automotive applications. Hotter environments as typified in the southern US in conjunction with demanding drive cycles will push battery temperatures well above 50°C; this over time reduces the available driving range due to capacity/power fade. A properly size and designed thermal system should be able to mitigate cell temperature towards the mid to low 30’s where the life expectancy is adequate. A thermal system cannot fully prevent these reactions from happening; however it can still maintain the battery temperature against any increases in heat generation due to augmented internal resistance, mitigate against hot spots surrounding areas of internal cell shorting, and help equalize cell temperature distribution between tabs (current collectors) and the cell body, all which increase lifespan and performance.

3.3.2 Safety

Safety of vehicles powered with Li-Ion cells is important due to their extreme combustibility. There have been a variety of high profile incidents, some of which have led to fatalities [65, 66]. Understanding the events and mechanisms that cause uncontrolled combustion are important.

3.3.2.1 Abuse of Cells

Collisions or other impacts to the battery pack (ie. road debris) are events that may not be preventable and depending on how severe the damage is catastrophic failures can occur. When a battery pack is damaged in an accident, the following events can result [62]:

1. The battery separator gets torn and an internal short circuit (ISC) occurs.
2. The flammable electrolyte leaks and potentially causes a subsequent fire.

Advanced simulations of potential crashes and their prediction capability can help understand how a Li-Ion cell would deform. CAE modeling can provide a partial solution considering design cost and protection capabilities. Further research is still required to improve the accuracy of these studies while reducing computational load [67].

3.3.2.2 Thermal Runaway

Thermal runaway is a process in which an exothermic reaction becomes uncontrollable. The chemical reaction rate in the cells increase due to a rise in temperature, which leads to a feedback loop of accelerating reaction rates and consequent further heating, until in the end this accelerates to the point where the heat released cannot adequately be absorbed by any external cooling mechanism. Thermal runaway can be caused by unexpected events such as an internal/external short circuit or other thermal abuse scenarios.

Overcharging/discharging can lead to thermal runaway events. Overcharging will result in excessive energy accumulating within the battery; this can be attributed to a failure of the battery management system (BMS) to stop charging as the upper voltage limit is reached. Due to the complexities and inherent variabilities inside a large battery pack, the cell with the highest voltage is the first overcharged cell, followed by others. Heat and gas generation are by-products of overcharging cells, and manifest as new reactions once the design energy storage capacity of the cell has been exceeded. Unlike precedent battery technologies like NiMH, NiCd or PBA, no energy consuming re-dox shuttles are designed into the lithium chemistry that would otherwise consume excess energy allowing cell to

cell equalization and consequent equilibrium to exist at “trickle charge” rates. Lithium-ion as a class is intolerant of overcharge, and the damage is permanent. Over discharging also eventually produces heat and gas generation because the BMS may not be catching a cell with too low of a voltage and limiting current draw. When too high of a current is drawn the polarity of the lowest charged/highest internal resistance cell will be forced into reverse. This phenomenon can be envisioned easily if one remembers that at no load there exists an open circuit voltage E at the cell terminal. As current i is drawn this voltage drops to $V = (E - i \cdot R_{internal})$ until it hits zero at short circuit conditions. At this point the cell is outputting its maximum current. Should a greater amount of current be flowing as a result of other cells in the string having the ability to liberate a higher level current output, then the worst cell sees a reversal in cell polarity. The chemical reactions initiated by reversed polarity quickly damage the cell. It leads to a rapid increase in internal resistance, hence heat.

An ISC is the most common cause leading to thermal runaway. ISC occurs when the cathode and anode come in contact with each other. This could be due to a failure in the SEI layer due to age or excessive amounts of heat. SEI decomposition can occur as low as 57°C [68], this depends on the cell chemistry. Cold weather charging will also lead to an ISC due to lithium plating on the anode as a result of improper ion transfer. It causes a growth of lithium dendrites (sharp pointed crystals) on the anode which can pierce the SEI layer and short circuit with the cathode [69]. Once an ISC is triggered, the electrochemical energy stored in the materials releases spontaneously with local heat generation. In these cases, a proper thermal management system should be able to keep the cell exterior at a low enough temperature while the internal cell separators melt and attempt to shut down the cell operation as a whole. The idea is to prevent the trouble from spreading to other cells. Controllers also need to be designed properly to catch overcharged/discharged cells before they happen through better sensors and load balancing techniques. Also electrolyte leakage detection is important since it is so flammable and it can catch a problem in the making, and a means of measuring the swelling in cells as they age (another predictor of trouble ahead) are complementary techniques aimed towards intrinsic safety. At times, like with severe impacts that totally compromise the structure and tear/penetrate through the cells where massive heat release is inevitable; the thermal management strategy might

simply be to delay/contain the cell to cell heat propagation and resulting fire long enough for vehicle occupants to escape.

3.4 Projected Life of System

Manufacturers incur a lot of cost through warranty claims; the goal is to minimize those losses due to claims, while at the same time satisfying customers with trouble free products. In an EV, the battery pack is the most expensive part and it takes considerable amount of time and effort to remove the pack to effect repairs. It's up to the manufacturer to ensure the design of their pack meets or exceeds the warranty provided to the customer. Chevrolet and Nissan electrified vehicles have an 8 year/160,000 km warranty [70, 71] whereas Tesla has an 8 year warranty with kilometer limit between 160,000 – 200,000 (depending on the vehicle model) [72]. All warranties also advise customers of battery pack degradation to anywhere between 10 – 40% during the warranty period.

The previous section outlined how hot and cold temperatures affect the battery pack, as well as charging. Gross et. al. [73] concluded the use of a thermal management system does improve the battery life. The authors also concluded that use of the thermal system during fast charging will help extend the battery life. Liquid cooling has also been shown to be much more effective at cooling the battery pack compared to air cooling [1, 2, 22, 29]. At the time of this writing, it will be a few more years before the first generation Chevrolet Volt, Nissan Leaf and Tesla customer battery packs can be fully studied for real world end of life performance. What is known is that although thermal management systems might incur an incremental energy penalty on the vehicle while driving, the future benefits probably outweigh those penalties when it tends towards a longer lasting pack with lower degradation. This leads to more a satisfied customer who won't experience an excessive decrease in driving range over time and a reduction in warranty costs for manufacturers, along with a safer vehicle.

3.5 Summary

In this chapter, the decision and reasoning for the use of Autonomie and PSPICE software suites were outlined. The Li-Ion electrochemistry and life expectancy

considerations were discussed to highlight the benefits of a well-designed battery thermal management system.

Autonomie is a forward-facing simulation tool with the ability to incorporate data from third party software. The user friendly interface and MATLAB/Simulink integration make it a powerful tool for vehicle simulations and analysis. PSPICE is an integrated circuit design program which is more user friendly compared to SimScape. The drag and drop nature of added RLC elements allows for faster reconfiguration thermal equivalent circuits and the integration with Simlink adds to its versatility. Though there are many avenues here, and preferences naturally exist among researchers, the path chosen was rationalized.

Temperature plays a major role in cell capacity and power fade. Temperatures in excess of $\sim 60^{\circ}\text{C}$ can start to degrade the SEI layer which may eventually lead to ICS and initiate thermal runaway events. At minimum higher temperatures will accelerate side reactions and deplete lithium (energy capacity loss) while causing a thicker SEI layer that augments internal resistance and consequent heating, hence accelerated aging of the cells. In cold weather, the transfers of ions is reduced which leads to lithium plating. Excessive plating is a leading cause of ICS, at minimum causing self-discharge and unbalanced packs, at worst an initiator for thermal runaway events during charging. Given the safety implications at both ends of the temperature spectrum, it's important to have a thermal management strategy to reduce the detrimental effects of hot and cold temperatures. This can aid in reducing warranty costs for manufactures and provide customers with vehicles that are safe while providing consistent driving range for many years.

CHAPTER 4 - AUTONOMIE MODEL DEVELOPMENT

There are many elements to consider when simulating a full vehicle. Having all the components modeled correctly is essential to integrating a battery thermal model into the simulations. Employing specific vehicle simulation software helps streamline the design process leveraging on vehicle focused interfaces and libraries. However, before the simulations are built, the production vehicle being replicated must be well understood.

4.1 Production EREV Vehicle

The EREV that is studied and simulated in this research is the MY2011 Chevrolet Volt, the first generation of the vehicle. It is classified as a 5-door compact vehicle which is capable of traveling approximately 60 km on pure battery power before the engine turns on to extend the range of the vehicle. The total available travel range is 640 km (380 miles). The vehicle architecture is a series-parallel powersplit drivetrain with 2 electric machines. To model the EREV in Autonomie, key technical specifications must be identified which include the battery pack configuration, electric machines powersplit device, ICE and chassis parameters. The key technical specifications of the EREV are reviewed in Table 4.1. Figure 4.1 shows the component layout of the Chevrolet Volt [74].

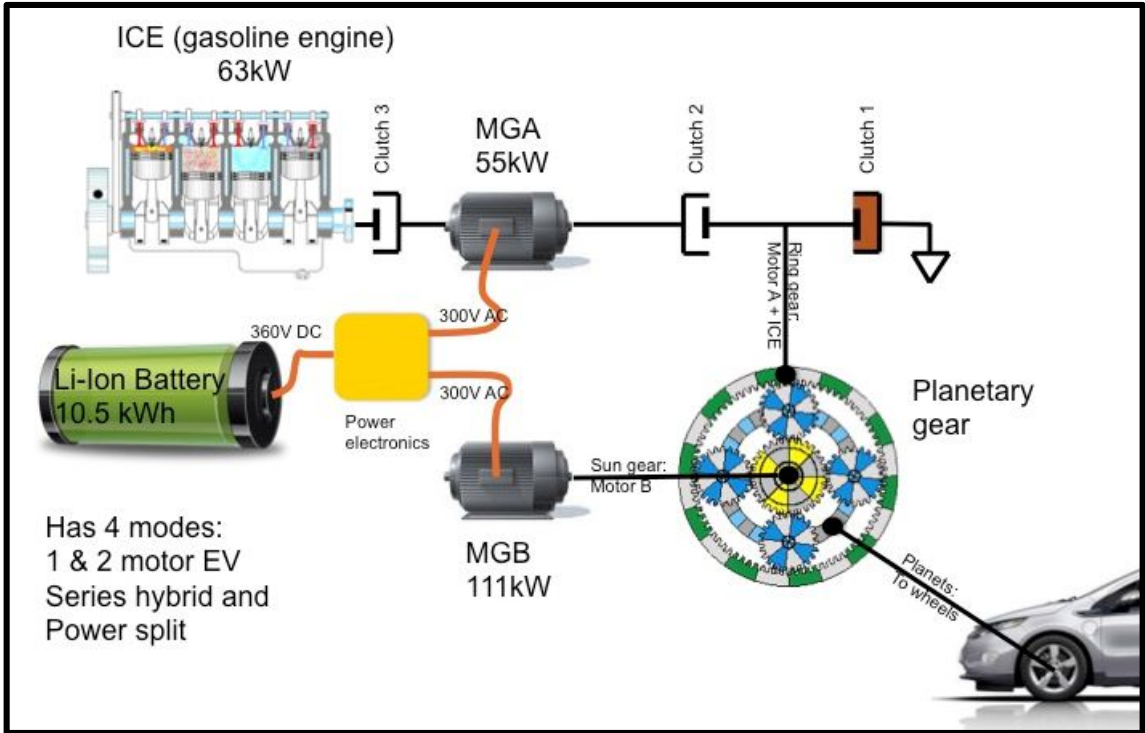


Figure 4.1 – 1st generation Chevrolet Volt component layout [74]

Table 4.1 – EREV Technical Specifications [74]

Component	Value
Battery Chemistry	Li-Ion
Number of Cells	288 (3p3s)
Cell Nominal Voltage	3.7 V
Cell Maximum Voltage	4.1 V
Thermal System	Active Liquid Cooling
Energy	16 kWh
Cell Capacity	15 Ah
Total Capacity	45 Ah
Engine	1.4L DOHC I4
Compression Ratio	10.5:1
Engine Power (HP / kW)	63 / 84
Electric Drive Motor (MG _B)	111 kW
Drive Motor Max Speed (rpm)	9500
Drive Motor Max Torque (Nm)	370
Electric Generator (MG _A)	54 kW
Generator Max Speed (rpm)	6000
Generator Max Torque (Nm)	200
Transmission	Planetary Powersplit
Ring Gear (# of teeth)	83
Sun Gear (# of teeth)	37
Planet Gear (# of teeth)	25
Ring to Sun Gear Ratio	2.24
Final Drive Ratio	2.16
Wheelbase (in / mm)	106 / 2685
Track Width (in / mm)	62 / 1578
Curb Weight (lb / kg)	3800 / 1720
Coefficient of Drag	0.28
Tire size	215/55/17

The vehicle parameters above were used as inputs and modeled in Autonomie.

4.2 Autonomie

Autonomie started out as PSAT (Powertrain System Analysis Toolkit), a software developed by Argonne National Laboratory (2003-present) [75]. It is a MATLAB based full vehicle simulation tool meant to study conventional and alternative drivetrains in the context of government mandated fuel economy and emissions targets. PSAT was later

marketed as Autonomie beginning in later 2011 and soon after Siemens PLC took over support functions as the endeavor became more commercialized and market oriented. The use of math based simulation environments allow for more rapid deployment of vehicle propulsion architectures and technologies through virtual designs and analysis which can accelerate the product development cycle. Autonomie key features and utility are:

- Plug-and-play model environment – GUI interface allows for vehicle components to be easily added/removed and modified
- Model reusability
- Vehicle model and data customization
- Powertrain customization
- Evaluate fuel consumption benefits (technology, size, powertrain configuration)
- Evaluate Fuel Economy, Emissions & Drivability
- Develop component requirements
- Develop vehicle production controls
- SIL and HIL (software-in-the-loop, hardware-in-the-loop) interfaces
- Incorporate inputs from other models specialty software (CarSim, GTPower, Amesim)
- Capable of performing forward-facing simulations

4.2.1 Autonomie EREV Model

To simulate the EREV architecture in Autonomie requires the creation of several configuration files for the entire vehicle and its components. The following steps were taken to create the vehicle in Autonomie:

1. Create the Vehicle Propulsion Architecture (VPA) – The physical layout of the components in the Autonomie environment
2. Add associated plant and controller models to the components in the VPA
3. Add the propulsion and brake controllers

4. Debug issues related to missing/broken links between the component models and the controller
5. Compile the completed model in MATLAB and simulate selected drive cycles

To simplify the design process for creating the EREV, Autonomie has developed a series-parallel vehicle architecture in the VPA library. Component models are taken from the Autonomie library, by selecting models that closely resemble a production EREV specification and modified accordingly. With the release of Autonomie Rev12, a complete transmission and propulsion controller has been provided in the software library for an EREV. Once the vehicle is completed and it can simulate a selected drive cycle, the component models are then modified to match the production vehicle specification. This approach is taken because it is easier to verify existing model elements and tuning them rather than starting from scratch. Therefore, when parameters are modified to resemble the production EREV, the debugging process becomes much simpler. All library files have been created in the MATLAB and Simulink environment, streamlining modifications. Figure 4.2 shows the completed vehicle configuration in the Autonomie environment.

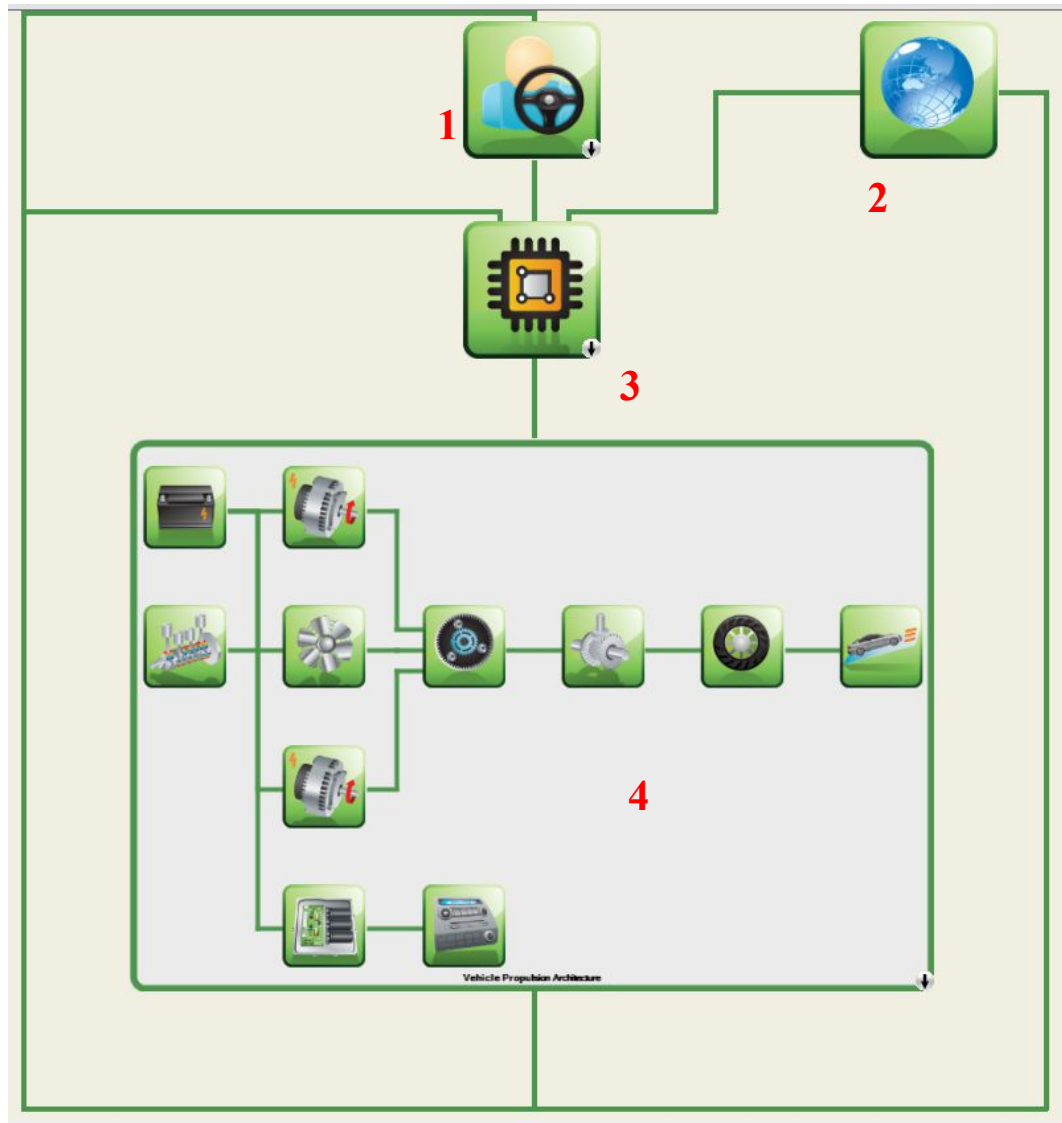


Figure 4.2 – EREV vehicle configuration elements in the Autonomie environment

The key components of the configuration are numbered with an explanation below:

1. Driver – Selects the type of driver (bus, truck, car) and specific driving profiles
2. Environment – The external environmental conditions the modeled vehicle will be subjected to
3. Vehicle Propulsion Controller (VPC) – Represents the high level vehicle controller for the compiled model
4. Vehicle Propulsion Architecture (VPA) – Represents the vehicle powertrain configuration and all associated sub models

Figure 4.3 presents an expanded view of the VPA within Figure 3.2, a brief explanation of each component follows.

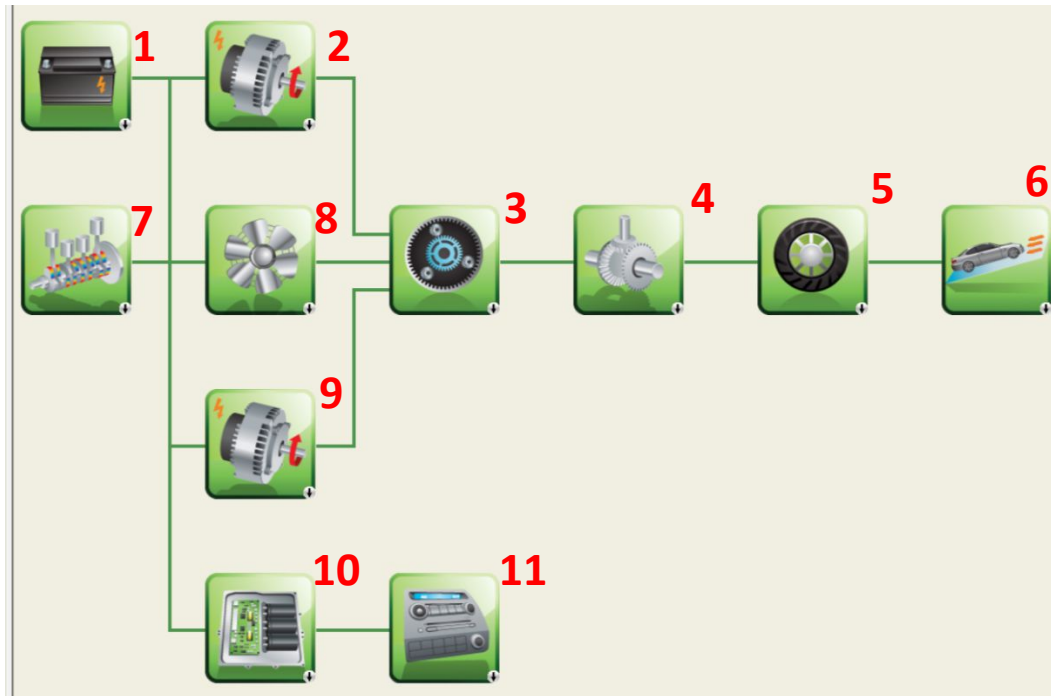


Figure 4.3 – EREV expanded VPA

1. Energy Storage System (ESS) – Battery system used for vehicle propulsion and to power the auxiliary electronics
2. Motor – Powered by the energy storage system to propel the vehicle
3. Electric Variable Transmission (EVT) – Planetary gearbox that takes the input power from the motor and transmits it to the driving wheels
4. Final Drive – Final drive gear reduction
5. Wheels – Power supplied to the road
6. Chassis – Overall vehicle size, weight and aerodynamics
7. Internal Combustion Engine (ICE) – Engine which is operational when the ESS is depleted to provide extended range driving capabilities
8. Mechanical Accessory – Power consumed by mechanical accessories (engine driven)

9. Generator – Supplies the ESS with power under regenerative braking and when in the ICE is active
10. Power Converter – Calculates losses associated with the electrical accessories based on constant efficiency
11. Electrical Accessory – Power consumed by the electrical accessories

4.2.2 Vehicle Specific Files

The vehicle controllers are required for the vehicle model to operate. They are based on Simulink and Stateflow in the MATLAB environment. Signals from various components and initialization values are used as the input commands to the controllers. Other important files for the specific EREV being simulated is the ESS and the motor/generator. The ESS cell information was obtained from GM and LG Chem resources [53] and motor/generator specifications are from Remy (now BorgWarner) [58]. Data used for the motor/generator can be found in the figures shown in Appendix A.1 and A.2. The mathematical equations used to create component models and a part of the MATLAB initialization codes can also be found in Appendix A.

4.2.2.1 Propulsion Controller

The propulsion controller monitors input signals such as the accelerator pedal input, battery SOC, motor speeds, and chassis speed. The Chevrolet Volt EREV is different than other hybrids on the market because the series-parallel architecture uses 3 separate clutches in the transmission which determine the various operating modes (Figure 4.1). Implementation of the logic for the propulsion controller is complex and was developed by the team at Argonne and is included in the software package as a proprietary file in the software library. The two modes being simulated by the controller is Charge Depleting (CD) and Charge Sustaining (CS). In CD mode, the vehicle will solely utilize electric power until the battery SOC reaches a defined minimum level which is set as 20%. In this mode, the controller engages clutch #1 which locks the ring gear in the transmission as seen in Figure 4.1 and allows transfer of power from the main traction motor (MG_B) to the final drive unit. Thus the battery and MG_B power the vehicle transferring power from the sun

gear to the final drive via the carrier. Once the minimum SOC level has been reached, the vehicle enters CS where the controller engages clutch #3 between the engine and generator so that the engine spins the generator which supplies power to maintain the battery SOC. This is the series mode utilized typically for intermediate speeds. It should be noted that while in charge sustaining mode, the generator will not charge the battery to maximum SOC. Instead, the generator will supply the battery with power to maintain 20% SOC cycling the engine on and off to achieve this. The engine will operate at various speeds, adjusting to varying road load demands. If the sustained demand is low over a period of time, the engine will turn off and cycle back on when needed. At higher speeds in charge sustaining mode, the majority of the power is typically transmitted mechanically from the engine to the final drive via the ring gear in a powersplit mode whereby clutch #2 is also engaged while clutch #1 is released. The exact vehicle road requirements for torque and output speed are met by adjusting the circulating power between the electric generator (MG_A) and MG_B acting through the sun and carrier. In this case the engine torque to the ring gear is moderated by MG_A and the generated power is circulated to MG_B which provides both the counter balancing torque and speed to meet the net requirements at the carrier for the final drive. Lastly, a parallel 2 motor electric only mode is engaged when the vehicle is travelling over 70 mph (113 km/h) to maximize the efficiency of both electric machines. In this mode, only clutch #2 is engaged. The speed of MG_B is now lowered by reacting it's torque against MG_A . MG_A turns at a moderate speed to create the combined output, but this mode is essentially limited by the reaction torque capacity of MG_A .

4.2.2.2 Brake Controller

The braking control strategy is incorporated in the propulsion controller for the EREV. The braking force is determined by the brake pedal input, motor speed and torque, chassis speed, and regenerative capabilities of the ESS. The logic for braking takes three scenarios into consideration which are outlined below:

- Full mechanical/frictional braking
 - Used when the driver demands excessive/quick stopping power (eg. emergency maneuver situation)

- Full regenerative
 - Dependent on the generator size as well as the battery SOC
 - At full SOC, regenerative braking is not available because the battery cannot accept additional charge
 - Once SOC decreases to a set value, regenerative braking will again become active
- Blend state which uses both mechanical and regenerative
 - Balances frictional and regenerative braking based on the National Highway Traffic Safety Association (NHTSA) regulations concerning permissible front to rear ratio's
 - The control strategy monitors how much frictional braking is needed based on the difference between the total braking force required and the regenerative braking provided by the generator/motor on the front wheels

4.2.2.3 Motor/Generator

The motor and generator in the EREV, or any HEV/EV, is specific to the vehicle. Information about the motor's general characteristics were sourced online [76], and some detailed information was additionally made available through the GM research partnership. The motor model in Autonomie uses three look-ups which are continuous torque as a function of speed, maximum torque as a function of speed, and a four-quadrant efficiency map as a function of speed and torque. The Speed vs. Efficiency contour plot was converted into the required maps for the motor/generator models. Having the appropriate electric machine models allows for accurate calculations of the motor currents and output torques. This is critical as the motor/generator provides the demand torque requested by the vehicle controller to propel the vehicle. If the motor is not producing the correct torque and efficiency based the demand, then the simulated vehicle will not be able to follow the profile of drive cycles nor mimic the energy consumption. The output of the motor affects the demand on the ESS in regards to the current and voltage. This impacts the calculation of heat generation in the ESS which is used in other models developed for the thermal system discussed in later sections.

4.2.2.4 Energy Storage System

The ESS model for the EREV is a second order dual polarization representation which has long been the basis of the battery model in PSAT and now Autonomie. The dynamics of this model shown in Figure 4.4 [77] entail two time constants describing the dynamic voltage sag of the source as a function of the load current I_L .

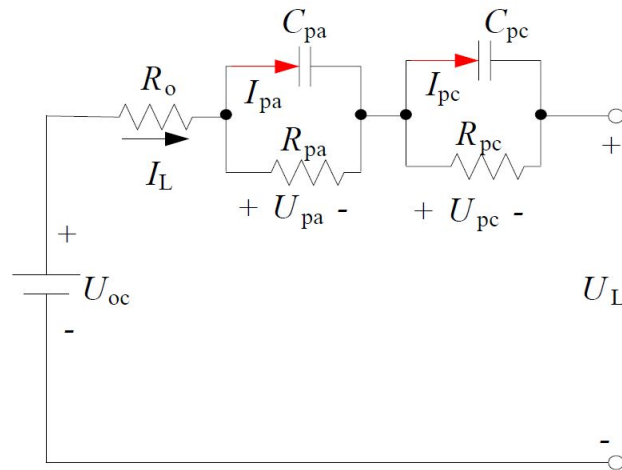


Figure 4.4 – Second order dual polarization model [77]

The second order model is comprised of the open circuit voltage, the internal resistance, and the effective polarization capacitances. The internal resistances are the ohmic resistance (R_o), the electrochemical resistance (R_{pa}), and the concentration polarization (R_{pc}). The corresponding capacitances C_{pa} and C_{pc} characterize the latter two resistances which materialize over a period of time (seconds to minutes). Results have shown the dual polarization model has good dynamic performance and SOC estimation capabilities [77, 78]. To make the Autonomie battery model resemble the production EREV, the following parameters need to be entered:

- Capacity (per cell and entire battery pack)
- Number of cells in series and parallel
- Nominal voltage
- Cell Voltage vs. SOC map
- Resistance vs. SOC maps
- Time constants

The first three points listed above are known from the technical specifications of the vehicle. The voltage and resistance maps are matrices constructed against the SOC from 0-100% at 10% SOC increments. The voltage map was determined from vehicle acquired data and compared to lab experiments conducted by a Masters student on the research team. The results from the vehicle data indicate a linearization of the voltage vs. SOC. This does not reflect the data provided by cell manufacturer which gives the voltage and SOC more accurately.

While examining recorded vehicle data, what the vehicle defines as “fully charged” and “fully depleted” must be deciphered. Using the LG Chem cell data and testing data from NREL on an isolated pack subject to testing on a battery cycler, the vehicle reported SOC was correlated to open cell voltage and summarized in Table 4.2. Figure 4.5 plots the vehicle operating range versus cell manufacture data.

Table 4.2 – Vehicle Reported SOC vs Actual SOC

Vehicle SOC	Cell Voltage	Actual SOC
100%	4.02	80%
Enter CS Mode	3.54	20%
Lowest SOC	3.29	10%

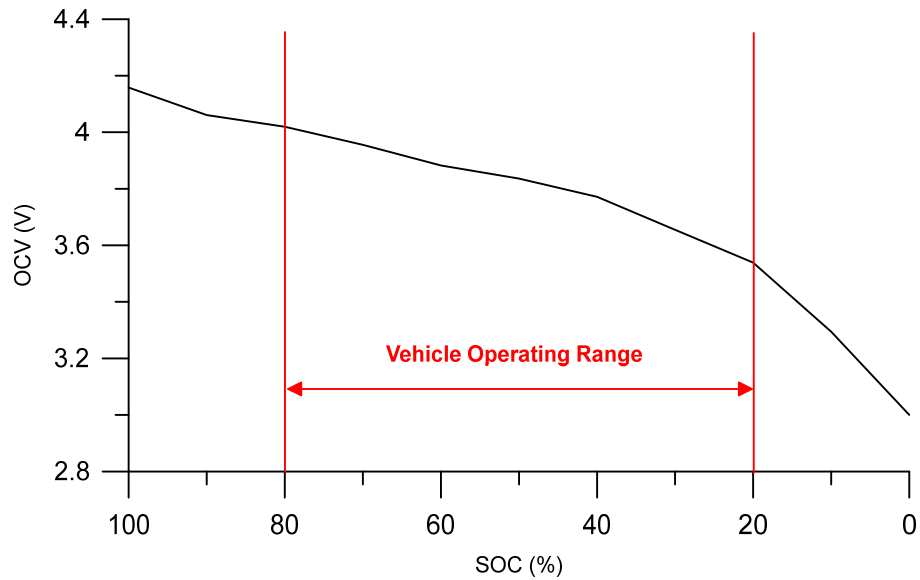


Figure 4.5 – Vehicle SOC operating range in relation to cell SOC range

The internal resistance map requires values representative of the production EREV as it will affect the simulation’s calculation of SOC as well as the heat generation rate which is needed for the thermal model. For the production EREV, Idaho National Laboratory (INL) published battery data on the MY2013 Volt. The pack charge and discharge resistance was studied for three years over 125,000 miles [79]. The INL tested charge and discharge resistance for the battery at the beginning of test (BOT) is shown in Figure 4.6.

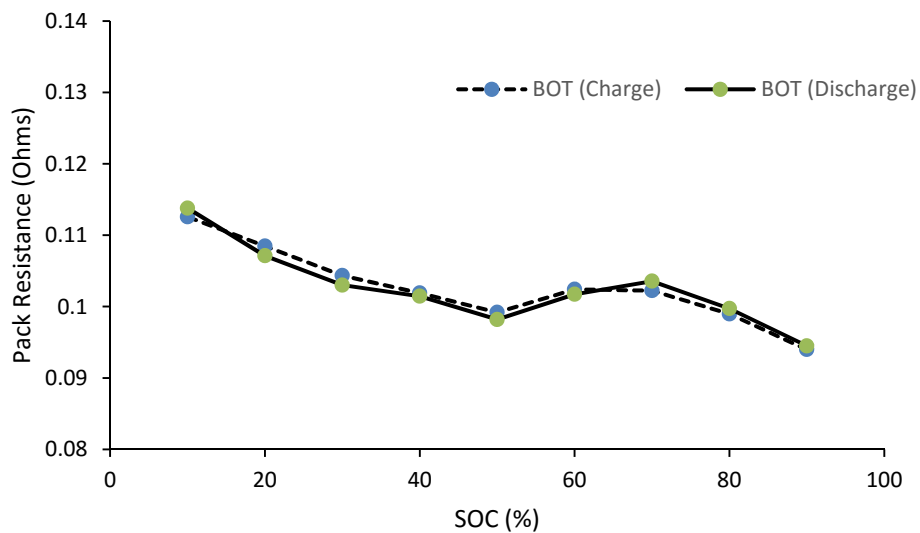


Figure 4.6 – INL MY2013 Volt pack charge and discharge resistance

The pack resistance data is for the 10-90% SOC range which satisfies the operation range of the production vehicle. Based on the test procedure INL used to find the pack resistance (constant charge and discharge rate), the polarization resistances are already included in the values they presented. This means the Autonomie model defaults to one resistance map, the internal resistance vs. SOC. Polarization resistance through concentration gradient and electrochemical effects is thus fully developed. Heat generation would decrease slightly according to the battery model if the capacitive effect were fully considered. It should also be noted internal resistance is affected by the cell temperature, not just the state of charge, especially at cold temperatures. Gong in 2016 presented the correlation of internal cell resistance with temperatures and SOC [80] seen in Figure 4.7 using Electrochemical Impedance Spectroscopy (EIS). For the research presented in this thesis, the cell temperature range is between 15-32°C and the SOC is between 20-100%. Therefore, the effects of the internal resistance at different temperatures are negligible for the simulations conducted and the INL internal resistance map is used in the Autonomie model.

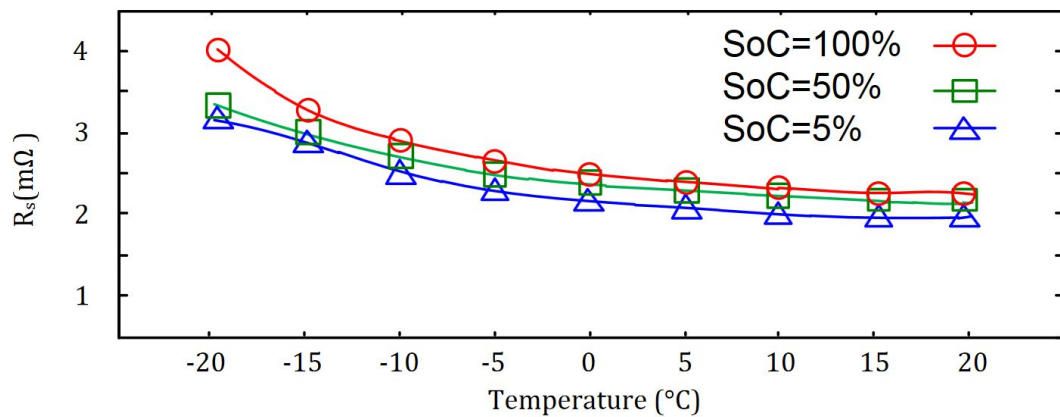


Figure 4.7 – Cell internal resistance as a function of temperature and SOC [80]

4.2.3 Simulation Performance

Part of examining the performance of the thermal management system is the ability to calculate the heat generation within the cell over the various drive cycles. Heat

generation is the product of I^2R , and the current draw is known via Autonomie model outputs. In the ESS Simulink model, the calculated pack voltage is based on resistance and current values subtracted from the open circuit voltage. Higher resistances lower the pack voltage over the course of a drive cycle thus leading to the faster depletion of the battery pack in the simulation. When the resistance values are correct, power and energy consumption on the drive cycles follows. To help identify if the Autonomie simulation is producing results similar to the production vehicle, Idaho National Laboratory (INL) published data on a MY2011 Volt is used for US06, HWFET, and UDDS drive cycles. This independent data helps determine if the correct capacity, energy, power and current are being output by Autonomie for individual and cumulative cycles. The number of consecutive cycles simulated to battery depletion are seven UDDS, five HWFET and five US06. Charge depleting energy consumption values are calculated through consecutive cycles until the vehicle enters charge sustaining mode. Comparisons of the Autonomie simulations with the INL data are summarized in Table 4.3. Positive error values signify an overestimation by Autonomie and negative values are underestimations of the parameter in question.

Table 4.3 – INL Dyno Test and Autonomie Vehicle

		Average Cycle Capacity Discharged in CD Mode (Ah)	Total Energy Discharged in CD Mode (kWh)	Total Capacity Discharged in CD Mode (Ah)	CD Max Drive Power – all cycles (kW)	CD Max Drive Current – all cycles (A)	Average Cycle Capacity Discharged in CS Mode (Ah)	Transition from CD to CS Pack Voltage (V)
UDDS	INL	4.54	8.72	27.67	55.70	147.60	0.16	345.20
	Sim	4.37	8.89	26.20	52.20	148.40	0.16	346.80
	Deviation	-1.74	+0.17	-1.47	-3.50	+0.80	+0.00	+1.60
HWFET	INL	6.51	8.88	26.93	49.50	135.80	0.23	345.70
	Sim	6.58	9.24	26.32	48.50	140.20	0.24	351.10
	Deviation	+0.07	+0.36	-0.61	-1.00	+4.40	+0.01	+5.40
US06	INL	6.94	8.97	26.75	79.30	212	0.61	337.70
	Sim	6.84	9.45	26.65	80.10	225.20	0.63	335.50
	Deviation	-0.10	+0.48	-0.10	+1.80	+13.20	+0.02	-2.20

The Autonomie model has produced accurate results compared to the production vehicle tested by INL. Therefore, Autonomie can adequately simulate any drive cycle and the values generated to calculate the heat generation on the various cycles will be valid. The next section will detail the standardized and custom drive cycles the Autonomie model was subjected to.

4.3 Drive Cycles

Standard drive cycles are used to calculate fuel economy under city and highway driving conditions. In the United States, the Environmental Protection Agency (EPA) has outlined 5 drive schedules [81] to simulate different driving conditions and styles. For simulations in Autonomie, each driveline component may be analyzed throughout the cycle to detail how the component is operating at any particular point. This offers an in depth view of the entire vehicle operation. In this research, thermal aspects of the battery system were analyzed in relation to the vehicle's operation as well as changes resulting from environmental ambient temperature exposure throughout the drive cycle. Drive cycles conducted using vehicle simulations should follow the drive cycle velocity profile trace with no more than 2% of the trace being missed by more than 2 mph, similar to the criteria used in the EPA laboratory on the chassis dynamometer [82]. If the simulated vehicle can satisfy these criteria, the results from the drive cycle analysis can be considered valid. If simulations deviate from the drive cycle trace by more than 2%, a different solving algorithm may be used to try and bring the error within acceptable values.

The drive cycles described in the subsequent sections detail key operative parameters as well as the average heat generation per cycle which depends on the average current values. Cycles with similar heat generation can be consolidated.

4.3.1 US06 Drive Cycle

The US06 drive cycle may be classified as an aggressive acceleration cycle. Total duration of this drive cycle is 600 seconds (10 minutes) and the vehicle will experience fast acceleration periods as well as sustained high speeds. The aggressive acceleration and high speed sections in the drive cycle are demanding, and contribute to a significant rise in

battery temperature. A summary of the US06 drive cycle can be seen in Table 4.4 and a speed graph of the cycle is shown in Figure 4.8.

Table 4.4 – US06 Drive Cycle Parameters [81]

Time for Cycle	600 sec (10 mins)
Maximum Speed	80 mph (128.7 km/h)
Average Speed	46 mph (74 km/h)
Total Distance Travelled	8 miles (13 km)
Max Acceleration	7.2 mph/s (3.2 m/s ²)

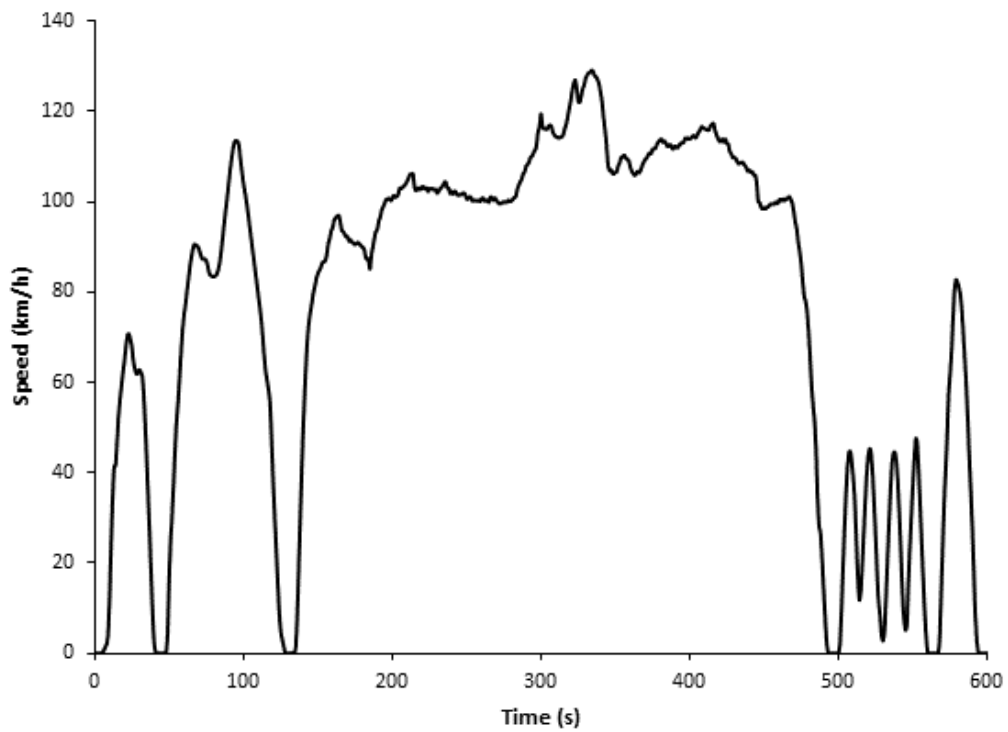


Figure 4.8 – US06 driving trace [81]

4.3.2 UDDS Drive Cycle

The Urban Dynamometer Driving Schedule (UDDS) represents city driving conditions. From Figure 4.9, it can be seen that there are many accelerating and braking sections that represent stop-and-go traffic in an urban environment. There are clearly more braking sections when compared to the US06 cycle which means the vehicle will be able to utilize regenerative braking capabilities. The duration for the UDDS cycle is approximately double the US06 drive cycle. Table 4.5 summarizes the parameters in the UDDS cycle.

Table 4.5 – UDDS Drive Cycle Parameters [81]

Time for Cycle	1369 sec (22.8 mins)
Maximum Speed	57 mph (91.7 km/h)
Average Speed	19.6 mph (31.5 km/h)
Total Distance Travelled	7.45 miles (12 km)
Max Acceleration	3.3 mph/s (1.5 m/s ²)

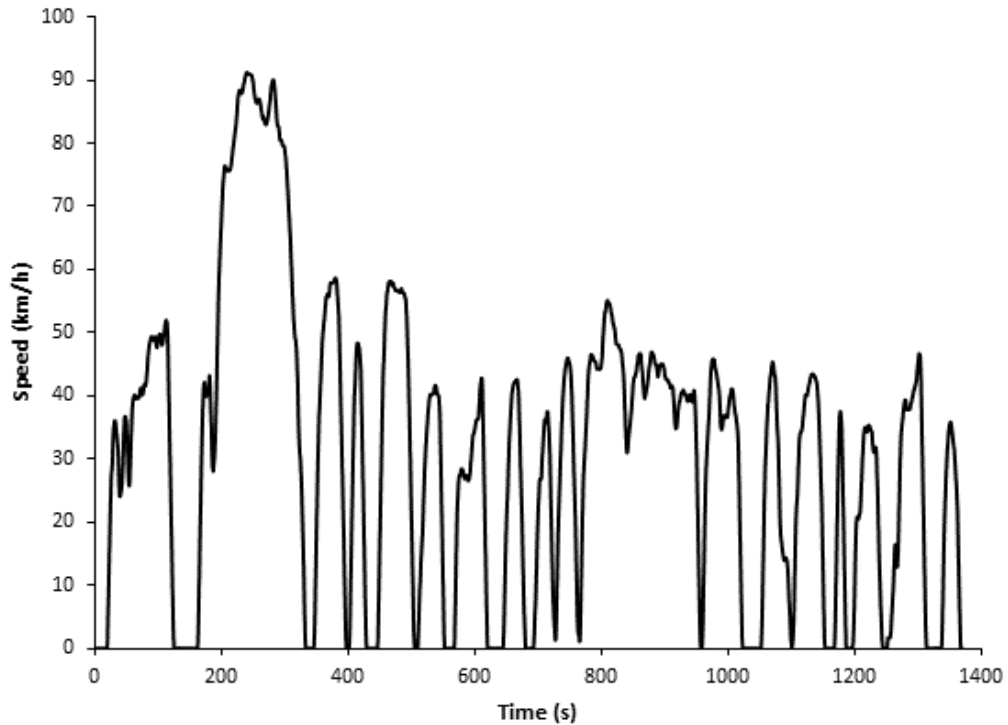


Figure 4.9 – UDDS driving trace [81]

4.3.3 LA92 Drive Cycle

The LA92 drive cycle, also known as Unified Cycle (UC), was developed in 1992 in California. The cycle is composed of high speeds and high acceleration. There are also some stops but with less idle time. A summary of the LA92 drive cycle parameters can be seen in Table 4.6 and the drive trace in Figure 4.10.

Table 4.6 – LA92 Drive Cycle Parameters [81]

Time for Cycle	1435 sec (23.9 mins)
Maximum Speed	66.7 mph (107.3 km/h)
Average Speed	24.61 mph (39.6 km/h)
Total Distance Travelled	9.82 miles (15.8 km)
Max Acceleration	6.3 mph/s (2.8 m/s ²)

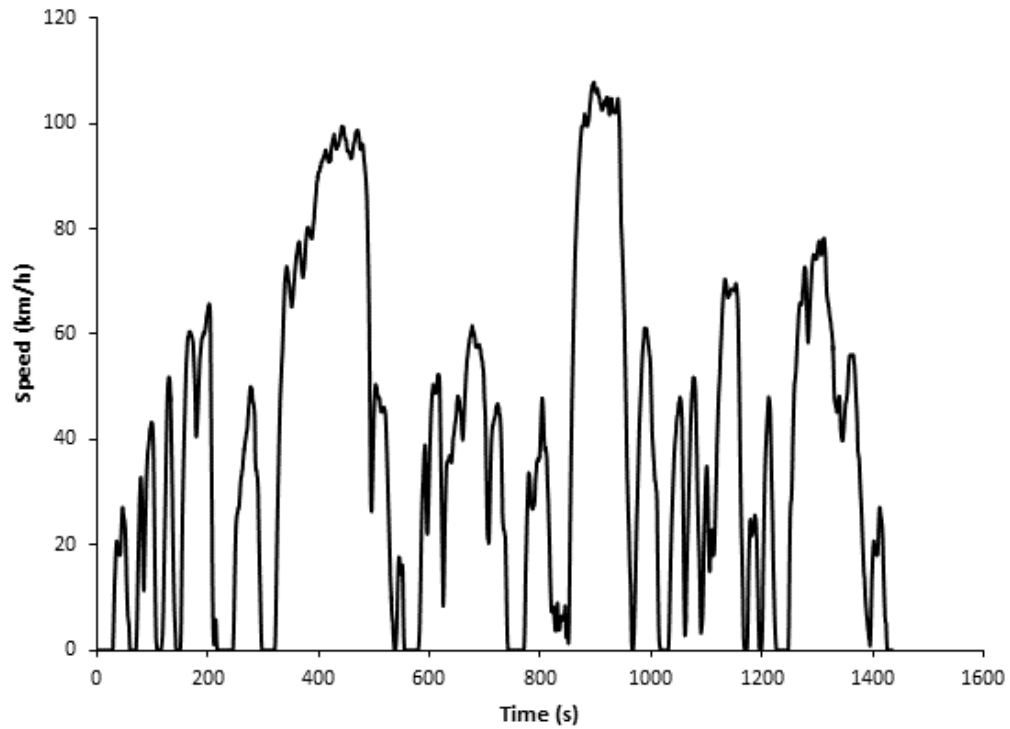


Figure 4.10 – LA92 drive trace [81]

4.3.4 EPA 5-Cycle Test Procedure

The EPA uses drive cycles as a method to measure the emissions and average fuel economy while driving. As of 2008, a new 5-cycle testing methodology was implemented to better calculate fuel economy based on more aggressive driving, air conditioner use, and hot and cold driving climates in addition to the tests conducted prior. For consumers, this change in methodology means fuel economy ratings from 2008 onwards cannot be compared to vehicles using the previous methodology. Table 4.7 shows the key features of the 5 drive cycles used in the 5-cycle testing methodology.

Table 4.7 – Key Features of 5-Cycle Testing [83]

EPA Test	Driving Speed	Ambient Temperature	Engine Starting Condition	Accessories
FTP	Low Speed	24°C	Cold and Hot	None
HWFET	Mid-Speed	24°C	Hot	None
US06	Aggressive (low and high speeds)	24°C	Hot	None
SC03	Low Speed	35°C	Hot	A/C on
Cold FTP	Low Speed	-7°C	Cold and Hot	None

The Federal Test Procedure (FTP) represents urban driving. The vehicle is started with the engine cold and driven in stop-and-go rush hour traffic. This cycle is the same as the primary UDDS, except it repeats the first 505 seconds when the engine is hot after a period where the vehicle is stopped with the engine idling. Figure 4.11 shows the FTP drive trace with Table 3.8 summarizing the key parameters. The Cold FTP test is the same as the standard FTP test with the exception of a lower ambient starting temperature of -7°C.

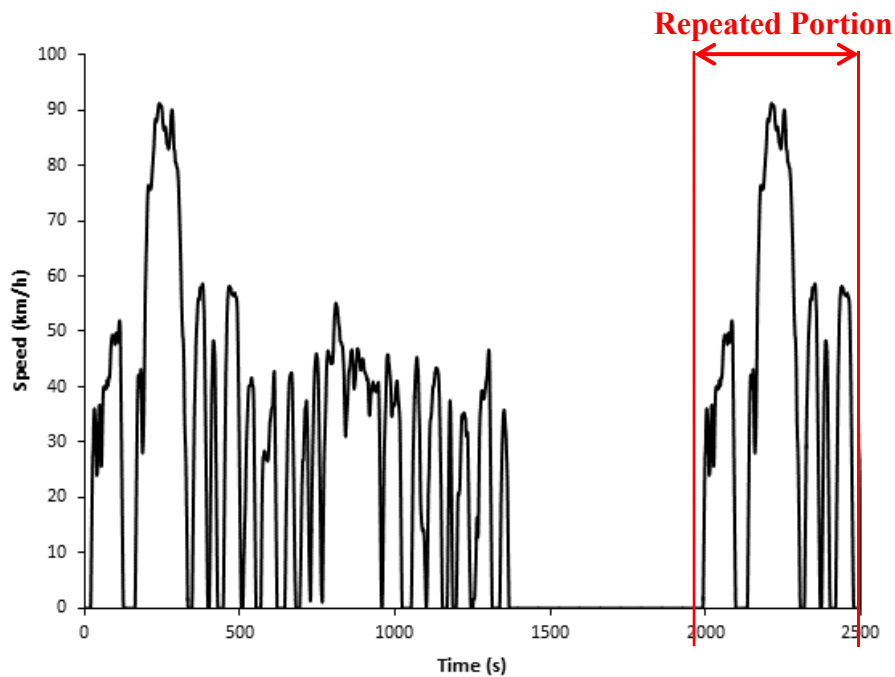


Figure 4.11 – FTP driving trace [83]

Table 4.8 – FTP Drive Cycle Parameters [83]

Time for Cycle	2500 sec (41.7 mins)
Maximum Speed	56 mph (90.1 km/h)
Average Speed	21.2 mph (34.1 km/h)
Total Distance Travelled	11 miles (17.7 km)
Max Acceleration	3.3 mph/s (1.5 m/s ²)

The Highway Fuel Economy Test (HWFET) represents a mixture of rural and highway driving with free flowing traffic. The test is completed with a warmed up engine and no accessories on. Figure 4.12 shows the HWFET drive trace and Table 3.9 summarizes the parameters in the drive cycle.

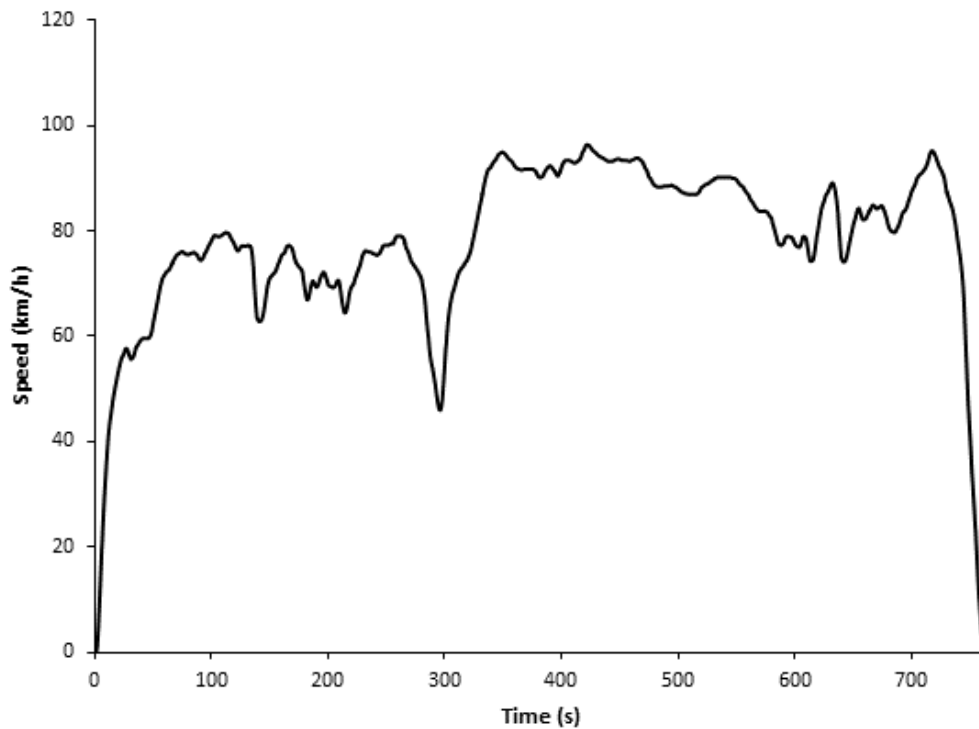


Figure 4.12 – HWFET driving trace [83]

Table 3.9 – HWFET Drive Cycle Parameters

Time for Cycle	765 sec (12.75 mins)
Maximum Speed	60 mph (96.6 km/h)
Average Speed	48.3 mph (77.7 km/h)
Total Distance Travelled	10.3 miles (16.6 km)
Max Acceleration	3.2 mph/s (1.4 m/s ²)

The SC03 test represents urban driving with the air conditioning turned on maximum, at an elevated ambient temperature of 35°C. Figure 4.13 and Table 4.10 show the driving trace and parameters for the SC03 cycle.

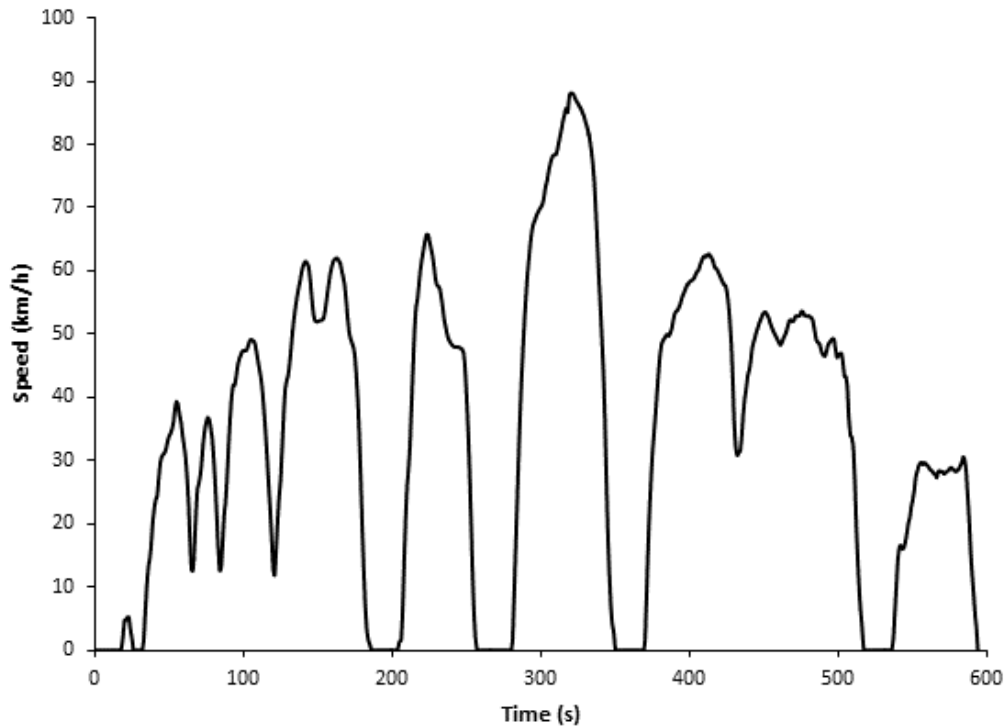


Figure 4.13 – SC03 driving trace

Table 4.10 – SC03 Drive Cycle Parameters

Time for Cycle	596 sec (9.93 mins)
Maximum Speed	54.8 mph (88.2 km/h)
Average Speed	21.6 mph (34.8 km/h)
Total Distance Travelled	3.6 miles (5.8 km)

4.3.5 Creating New Drive Cycles

Aside standardized drive cycles customized drive cycles can be created and imported into Autonomie. This allows investigation of more demanding or unique driving scenarios not captured by current EPA schedules. The time and speed data can defined in Microsoft Excel for simplicity and then imported into Autonomie. However, Autonomie requires three data sets for the drive cycle to be recognized. This comprises:

- Speed vs. Time
- Grade vs. Time
- Key On vs. Time

The SAE J2807 Tow Standard (Davis Dam test) [84] is used to calculate the gross vehicle weight of light truck, minivan, sport utility and crossover vehicles in Arizona near the Davis Dam. The test is comprised of various acceleration launches leading into an elevated climb averaging 5% grade. This grade test begins at the intersection of JL McCormick and AZ-68 and ends at Union Pass on AZ-68. For the EREV, the grading test portion of the J2807 was created as a separate cycle to examine how the constant grade and elevated Arizona temperatures affect the battery and operation of the thermal management system. It should be noted the production EREV is not meant to tow any type of trailer as per the owner's manual. Figure 4.14 shows Davis Dam elevation and driving trace. Table 4.11 shows the cycle parameters.

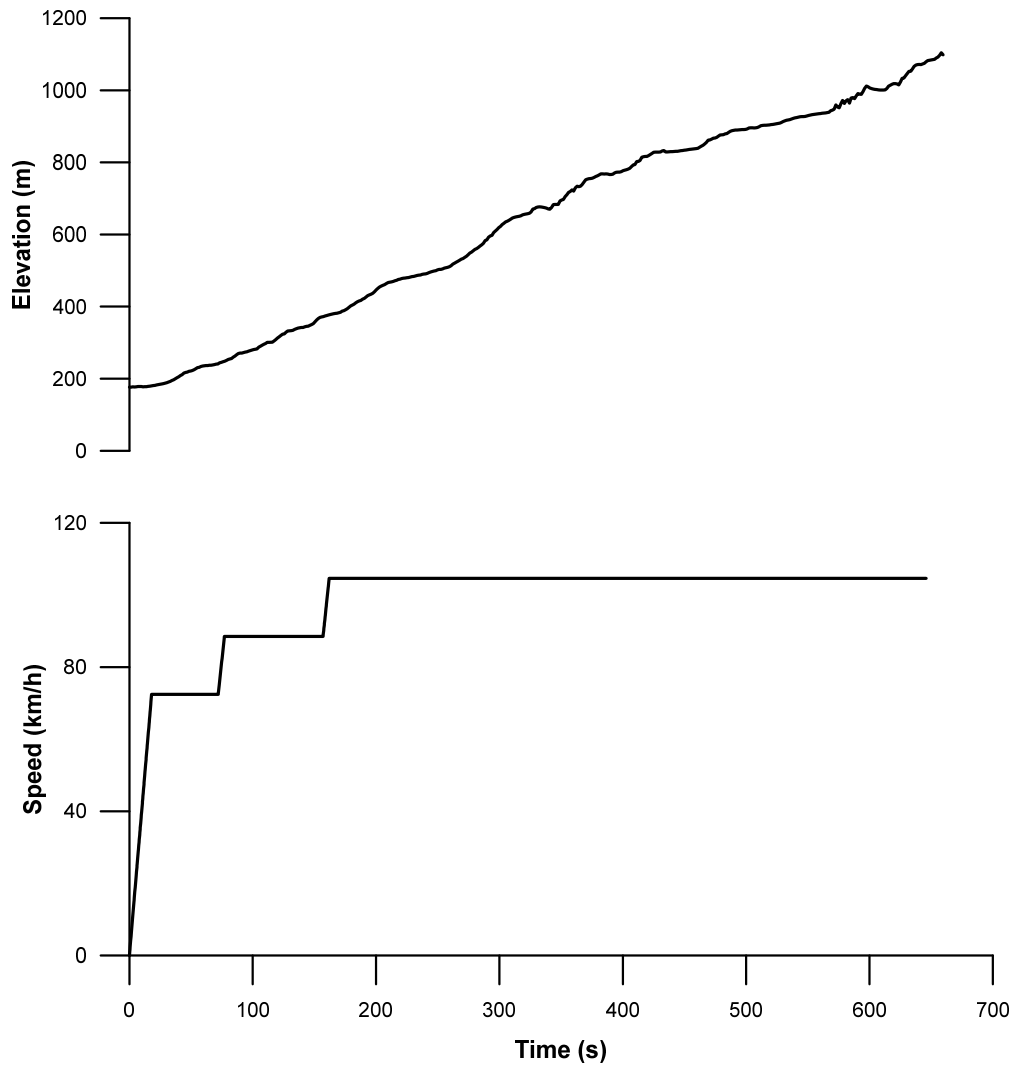


Figure 4.14 – Davis Dam elevation (top) and driving trace (bottom)

Table 4.11 – Davis Dam Cycle Parameters

Time for Cycle	646 sec (10.8 mins)
Maximum Speed	65 mph (104.6 km/h)
Average Speed	60.8 mph (97.8 km/h)
Total Distance Travelled	11.7 miles (18.8 km)
Max Acceleration	2.9 mph/s (1.3 m/s ²)

To obtain the grade versus time trace, the grade profile is mapped using available tools online and then fit to the time scale. Unlike the EPA standardized drive cycles which measure the percentage of the drive trace missed to evaluate the success of the test, the Davis Dam test does not follow the same procedure. The vehicle is meant to (try) and maintain the posted speed limit and complete the drive cycle. If the vehicle does not travel the entire distance or completes the cycle with a lower speed, it is still considered a completed test.

4.3.6 Drive Cycle Heat Generation

Determining the heat generated during a drive cycle allows for a comparison of the effects different drive cycles have on the battery pack. The heat generation is equal to the ohmic heating in the cell, plus the transitory effects of concentration polarization and electrochemical resistance contribution which is explained in Section 3.5. For this research, it helps to determine which drive cycles have similar operating characteristics in an effort to consolidate the various drive cycles and separately evaluate ones which show high, moderate and low internal heat generation. The amount of heat generated by the battery through the course of a drive cycle can be calculated by averaging the instantaneous heat generation over the length of the schedule. Furthermore, dividing the average heat generation by 288 gives the per cell value over the duration assuming each cell contributes the same amount of heat. For each drive cycle in Autonomie, simulation starts with a fully charged vehicle. As explained in previous sections, a fully charged vehicle is when the battery SOC is at 80%. The current and resistance outputs from Autonomie are exported for calculating the instantaneous and average heat generation driving the cycle. Such results are shown in Figure 4.15.

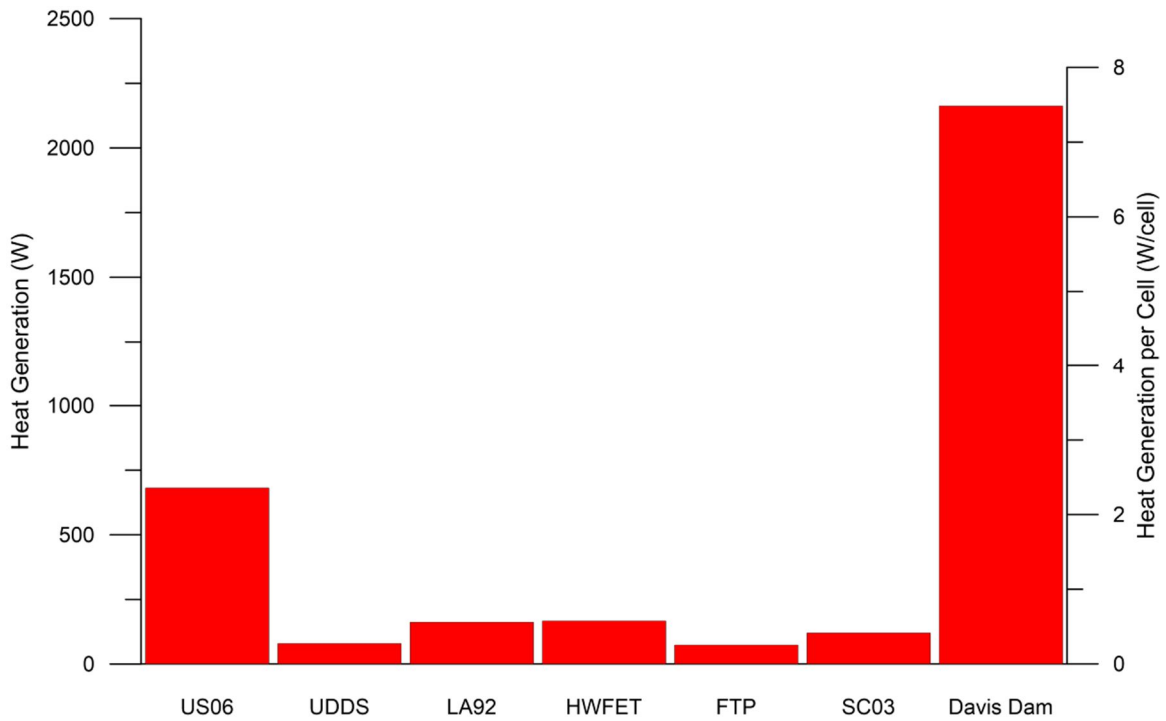


Figure 4.15 – Heat generation of drive cycles (from simulations)

The analysis clearly shows the US06 cycle is the most aggressive of the standardized EPA cycles generating the most heat at 679 W in the pack and 2.35 W/cell. The LA92 and HWFET have similar pack and cell heat generation values around 160 W and 0.57 W/cell respectively. The UDDS and FTP cycles are also similar to another with pack and cell heat generation values around 78 W and 0.27 W/cell. The SC03 cycle sits inbetween the two with pack and cell values of 119 W and 0.41 W/cell. In the analysis to follow, UDDS, LA92, and US06 were taken as the representative low-medium-high cases for test consolidation purposes. The Davis Dam scenario is treated separately as an extreme random occurrence.

Figure 4.15 also shows the motivation for testing the Davis Dam cycle. It may be a one off cycle a vehicle could experience while vacationing in the region. This highlights the importance of real life regional testing and not only dynamometer standardized testing. The Davis Dam drive generates 2155 W of heat in the pack and 7.5 W/cell, approximately three times the amount of heat of generated in the US06 cycle in the same amount of time, both cycles are approximately ten minutes long.

4.4 Vehicle Testing

Theoretical mathematical models describing the battery thermal system are a key element for understanding and improving present designs. Controlled experiments can help validate theoretical models and establish proof of concept for new designs. While most thermal management models, either theoretical or experimentally derived, look at the cells/battery individually or as a system there are many implicit assumptions that can be difficult to verify. There have only been a handful of models presented in the academic literature that take the entire vehicle into consideration, but not to the extent of a full scale vehicle simulation over terrain and ambient exposures. Part of the reason stems from the availability of an instrumented vehicle with said characteristics to verify findings, or the costs associated with purchasing and making incremental changes to its configuration.

When building a simulation model, validating the simulated results with a production vehicle is imperative. Even though the Autonomie model was “tested” against INL’s published data, further validation with an instrumented production vehicle and a battery pack in the lab leads to further insight.

4.4.1 Thermal Chamber Testing

Actual testing at elevated temperatures in a climatic chamber allows investigation of the stock battery cooling system performance through means of onboard data systems and querying the vehicle’s CAN bus. Figure 4.16 shows the first test vehicle on the dynamometer.

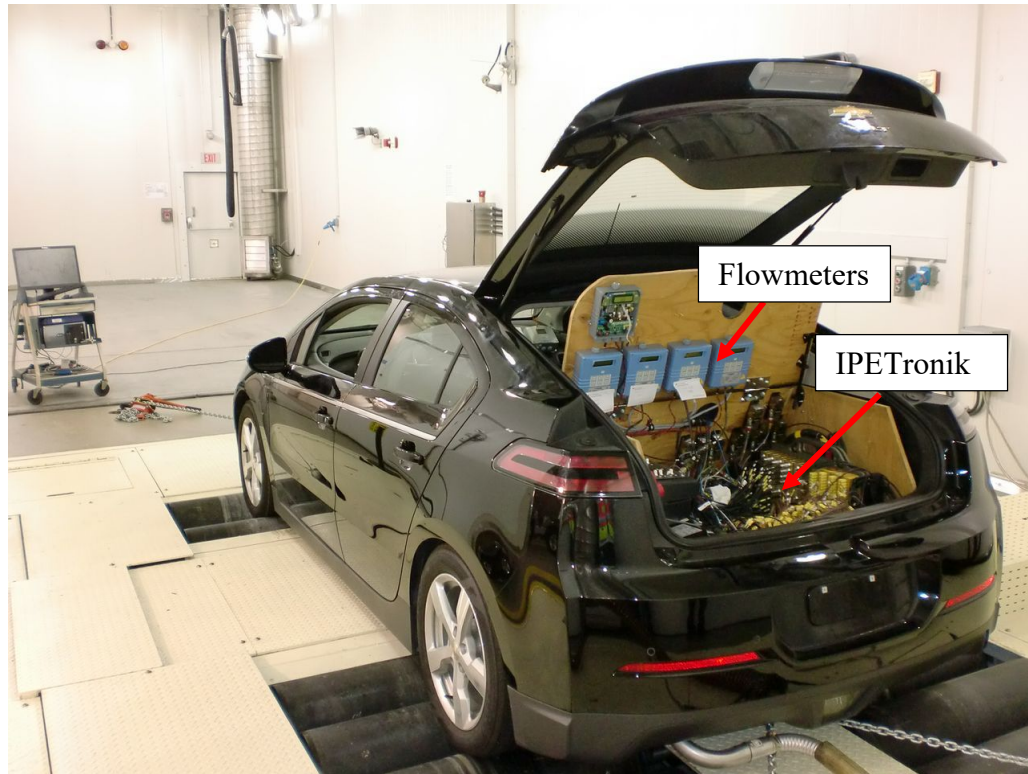


Figure 4.16 – Trunk left open while on the dynamometer for recording purposes

The test procedure for the vehicle in the climatic chamber was as follows:

- Vehicle is plugged in (120 V, 20 Amp circuit)
- Thermal chamber set to +50°C
- Vehicle soaked at +50°C for 68 hours with all data acquisition systems recording over this period
- Chamber temperature brought down to +45°C
- With chamber at +45°C, constant load dynamometer test starts with a driver in the vehicle
- Vehicle speed brought up to 91.7 km/h (57 mph) corresponding to ~10 kW constant load and cruise control is activated
- Vehicle runs for a total of 45 minutes
 - 0-10 mins with the AC turned on full
 - Vehicle driven until it enters charge sustaining mode with AC off
 - 10 mins after driving in charge sustaining mode AC turned back on full
 - At 45 mins, cruise and AC turned off and vehicle brought to a full stop

High parasitic losses at low vehicle speeds on the simple 4WD absorption dyno within the ACE thermal chamber at UOIT meant that real world drive cycles could not be run. Thus the vehicle was tested at a constant load of 10 kW, which corresponds to 92 km/h. It represents approximately the UDDS cycle average load. The thermal chamber was first set to +50°C to activate the BTMS. This exposure condition mimics the worst case scenario envisioned for regions such as Arizona's Death Valley in the sun. Information on the vehicle's CANbus shows the BTMS turns on when the bulk pack temperature reaches +32°C. Soaking the entire vehicle at +50°C allows the battery bulk temperature to exceed the +32°C threshold. Holding the chamber at such elevated temperature forces a worst case operating scenario for the vehicle. Acquiring data on how the vehicle functions under sustained operating load while in extreme heat helped identify how key components of the BTMS functioned when there was a large demand. In the particular soak test run, the vehicle was also plugged in to the charge port. As such it might replicate a vehicle getting charged in an enclosed and sun soaked garage or car port.

4.4.2 Vehicle Road Testing

Thermal chamber testing was helpful in revealing how the EREV operates under elevated temperatures conditions. Testing the vehicle on the road reveals how the vehicle operates normally with the ability to capture more information on additional systems within the vehicle through the CANbus. A rented vehicle was used for road tests, in place of the one shown in the previous section, but it was the same MY2011 Chevrolet Volt. For the road tests, heat flux, temperature, and air flow sensors were placed underneath the vehicle. The majority of these sensors were placed on the metal baseplate of the battery pack to help capture the temperature profile and record heat flowing in/out of the pack. Temperature sensors were also placed behind the engine, in front of the battery pack and in the cavity between the battery cover and chassis metal. The placement of the sensors help identify the following parameters:

- Influence of the engine operation on the underbody temperature
- Temperature between the top cover and chassis air gap

- Influence of hot pavement on the battery baseplate temperature
- Air speed under the car and in the cavities surrounding the battery

Figure 4.17 shows a heat flux and thermocouple attached to the bottom of the baseplate. The heat flux sensors have integrated thermocouples and there were a total of two heat flux sensors and nine thermocouples placed on the baseplate.

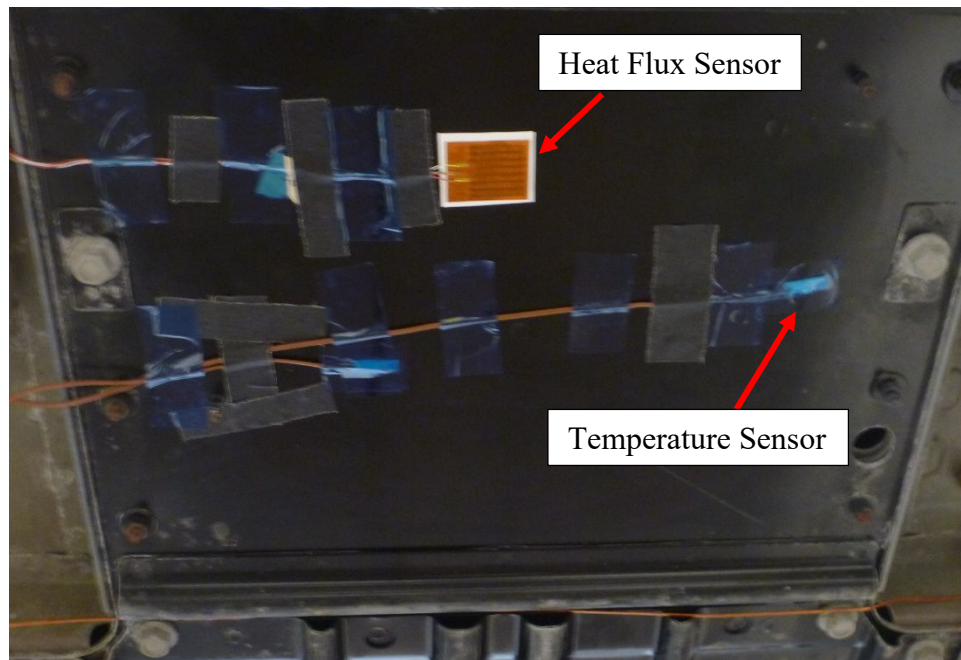


Figure 4.17 – Heat flux and temperature sensor placement on the baseplate

All sensors were connected to an IPEtroniks acquisition system and VehicleSpy [software] was used to connect to the CANbus. The CANbus data provided information within the battery, chassis and recorded key parameters such as:

- Battery pack voltage and current
- Cell voltage
- Cell temperatures
- SOC value
- Inlet and outlet pack fluid temperature
- Vehicle, engine and electric machine speeds
- Engine and electric machine torque outputs

- AC compressor voltage, current and power
- Electrical accessories power consumption

A variety of road tests were conducted over a week in the middle of August 2015 in the Durham Region which coincided with the hottest week of the summer. The vehicle routes were mapped and the appropriate grade profile for the routes were created. Testing times varied and were meant to replicate an average driver. The tests capture vehicle data for the following conditions:

- CD and CS operation modes
- The transition from CD to CS mode
- City and highway driving
- Thermal system operation while driving
- Thermal system operation when parked

The CANbus data for the battery and vehicle aid in further validating the Autonomie model to strengthen the results, as this data was not available through any publication. For the thermal system, it aids in the development of the cooling system model in conjunction with the thermal chamber operation to determine the threshold, cut off points and durations of operation. The thermocouples under the vehicle and airspeed sensor under the vehicle helps in the development and validation of a thermal equivalent circuit for the battery system.

4.5 Heat Generation Equations

The total heat generation for the battery is given below:

$$\dot{Q}_{total} = \dot{Q}_{gen} - \dot{Q}_{cooling} \pm \dot{Q}_{external} \quad 4.1$$

Where:

\dot{Q}_{gen} = Ohmic heating (I^2R). Other forms of heat generation or absorption, such as entropy changes are neglected [1, 2]. Ohmic heating is the predominate contributor to heat

generation at the discharge C-rates typically seen while driving [1-4 C → 45-180 Amps].

$\dot{Q}_{cooling}$ = Amount of heat transferred from the cell to the cooling fluid when the thermal management system is active and represents heat leaving the system.

$\dot{Q}_{external}$ = Heat is either added to or removed from the system depending on the environmental conditions. If the ambient temperature is lower than the surface temperature of the cells, heat will be removed from the battery through natural convection and conduction.

4.5.1 Cell Heat Generation

Ohmic heating is a squared function of current multiplied by internal resistances. Current is dependent on the power demand while driving. The battery internal resistance is a function of SOC and cell temperature, with the resistance profile typically a little different for charging and discharging. \dot{Q}_{gen} , is the instantaneous heat generation given the current and resistance at any particular point in time. To find the total heat generation over a period of time, the instantaneous values are summed on a second by second basis.

$$\dot{Q}_{gen} = \sum_t I^2(t) \times R(t) = Watts \quad 4.2$$

4.5.1.1 Heat generation at center of cell

Finding the core temperature of the cell allows the surface temperature to be calculated. With a known surface temperature, the cooling system model can be developed.

Assumptions:

- Cell assumed to be a flat uniform plate
- Symmetry along the center plane
- Volume of cell has uniform heat generation

- T_∞ is taken as the air temperature surrounding the cells within the battery pack, a constant.

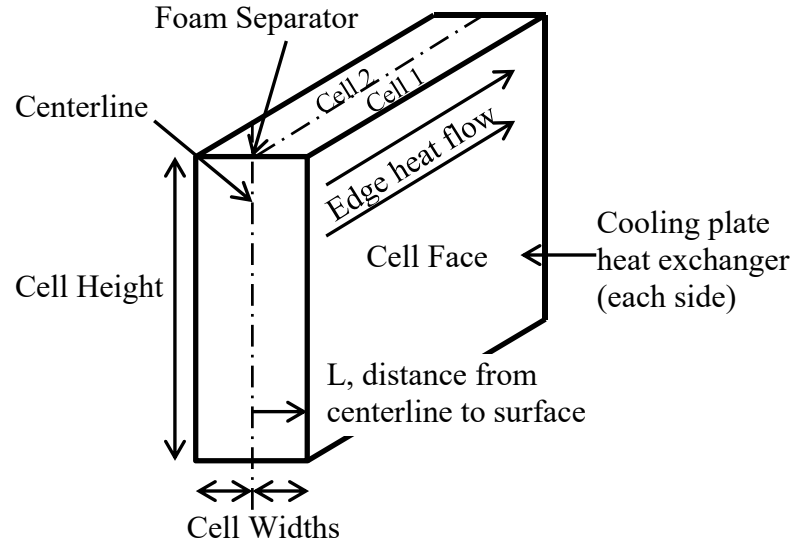


Figure 4.18 – Profile of cell

From Newton's Law of Cooling:

$$\dot{Q}(t) = hA_s [T(t) - T_\infty] \quad 4.3$$

where $T(t) = T_{core}(t)$

Substituting \dot{Q}_{gen} into the above equation and rearranging to solve for $T_{core}(t)$ the equation becomes:

$$\dot{Q}(t) = \dot{Q}_{gen}(t) \quad 4.4$$

$$hA_s [T_{core}(t) - T_\infty] = I^2(t) \times R(t) \quad 4.5$$

$$T_{core}(t) = T_\infty + \frac{I^2(t) \times R(t)}{hA_s} \quad 4.6$$

4.5.2 Liquid Cooling Heat Exchanger System

The liquid cooling system incorporates cooling plates sandwiched between cells resulting in indirect contact cooling. These plates exist between every other cell and foam is placed in the alternating spaces to exert light pressure, ensuring contact. The amount of heat transferred to the cooling fluid can be mathematically stated as:

$$\dot{Q}_{\text{total}} = \dot{Q}_{\text{gen}} - \dot{Q}_{\text{cooling}} \pm \dot{Q}_{\text{external}} \quad 4.7$$

The cooling plate is made from two stamped sheets of aluminum brazed together to form passages. Figure 4.19 shows the flow paths for the fluid. The total length and cross-sectional areas for the flow paths were found through measurements of the plate. Figure 4.20 is a schematic of the alternating pattern of the foam and cooling plates sandwiched between the cells.

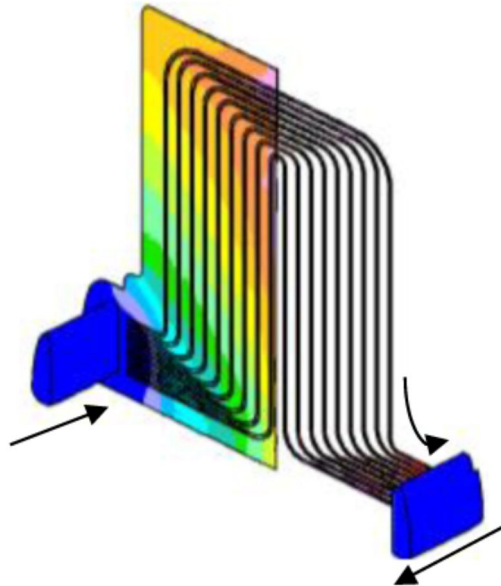


Figure 4.19 – Multiple fluid flow paths through cooling plate [31]

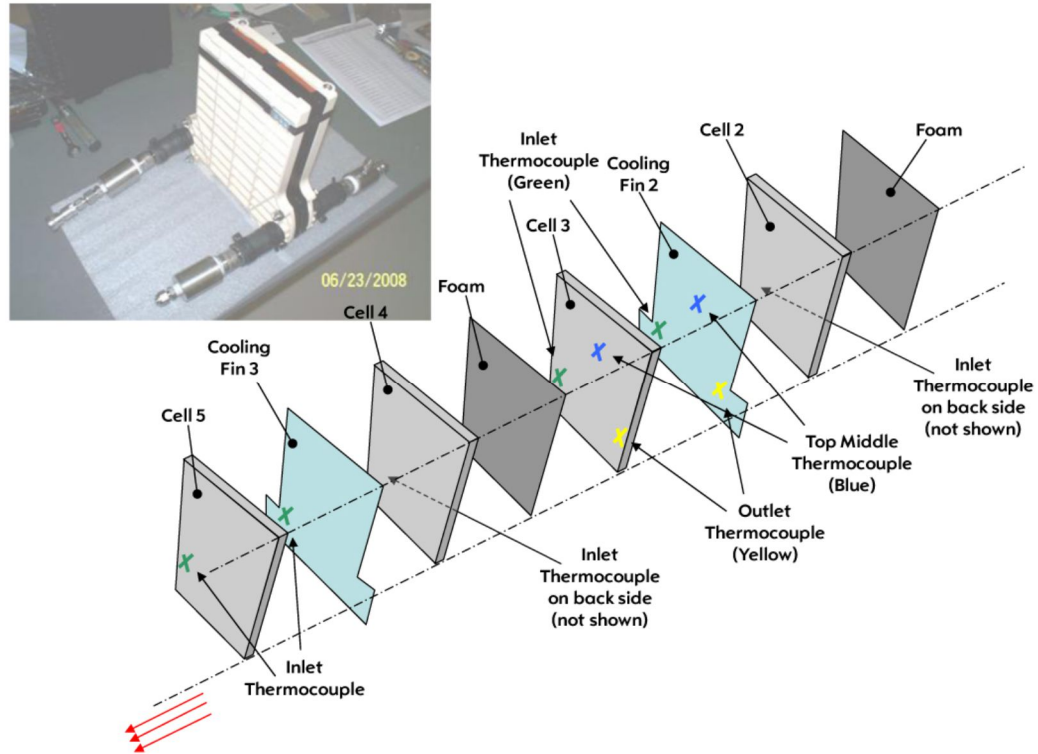


Figure 4.20 – Alternating pattern of foam and cooling plates [31]

The total amount of heat transferred from the cell surface to the fluid is defined by:

$$\dot{Q}_{fluid} = (hA_s \Delta T_{ln}) N_{plates} \quad 4.8$$

Where \dot{Q}_{fluid} is the amount of heat transferred to the moving fluid by internal forced convection. The following simplifying assumptions are made for this system:

- Temperature of the coolant entering all cooling plates is the same
- Temperature distribution across cooling plates is uniform when the thermal system is active
- Each flow path on an individual cooling plate has the same mass flow rate
- Constant fluid properties due to the small temperature change involved
- Uniform contact pressure between the cooling plate and cells

The Reynolds number, Nusselt number, heat transfer coefficient, exit temperature of the fluid and pressure drop needs to be calculated. There are nine flow paths per cooling plate. The cross-sectional area for each flow path is the same and the lengths have been verified to be approximately the same as well. The necessary computations are:

$$Re_{liquid} = \frac{V_{avg,liquid} D_h}{\mu_{liquid}} \quad 4.9$$

$$D_h = \frac{4A_c}{p} \quad 4.10$$

$$\dot{V}_{avg,liquid} = \frac{\dot{V}_{liquid}}{A_c} \quad 4.11$$

$$Nu_{liquid} = \frac{h_{liquid} D_h}{k_{liquid}} = 0.023 Re_{liquid}^{0.8} Pr_{liquid}^{0.3} \quad Re > 10000 \text{ (turbulent flow)} \quad 4.12$$

$$Nu_{liquid} = \frac{h_{liquid} D_h}{k_{liquid}} = Constant \quad Re < 10000 \text{ (laminar flow)} \quad 4.13$$

$$T_{exit} = T_{surf} - (T_{surf} - T_{inlet}) e^{\left(\frac{-hA_s}{\dot{m}C_p}\right)} \quad 4.14$$

$$\Delta T_{ln} = \frac{T_{inlet} - T_{exit}}{\ln \frac{T_{surf} - T_{exit}}{T_{surf} - T_{inlet}}} \quad 4.15$$

$$\dot{Q}_{channel} = hA_s \Delta T_{ln} \quad 4.16$$

$$\dot{Q}_{cooling} = \dot{Q}_{channel} \times N_{flowpaths} \times N_{cooling\ plates} \quad 4.17$$

Table 4.12 is a summary of resultant values using the equations above for a condition where the inlet fluid temperature is 20°C and using a mixture of 50/50 ethylene glycol.

Table 4.12 – Liquid Cooling Sample Calculations

Parameter	Calculated Value
Re	34.94
D_h	6.623×10^{-4} (m)
V_{avg}	0.19 (m/s)
Nu	2.25
T_{exit}	25.90 (°C)
ΔT_{ln}	5.54 (°C)
$\dot{Q}_{channel}$	2.52 (W)
$\dot{Q}_{cooling}$	3266.22 (W)

4.6 Summary of Autonomie Model Development

In this chapter, models were identified and developed to simulate a production EREV in order to analyze the battery pack and BTMS. Simulating a production vehicle requires parameters and initial conditions that reflect real world conditions. The production vehicle was created in Autonomie and validated with data acquired from road tests and independently published battery data. Drive cycles to be simulated in Autonomie were selected and analyzed to determine the average heat generation. The analysis concluded the US06, LA92, and UDDS cycles should be simulated to capture aggressive, moderate and low heat generation scenarios. The cycle created for the Davis Dam showed it had three times the amount of heat generation as the US06 and can simulate an extreme cycle well beyond daily driving.

Details for the test vehicles were outlined and the acquired data recorded temperatures under the vehicle, behind the engine, and in front of the battery pack. Air speed was also measured under the vehicle and operation of the BTMS was captured. The liquid cooling system and the operation logic in MATLAB using the data from the test vehicles was described in detail. The next chapter outlines the thermal equivalent circuit model development.

CHAPTER 5 - THERMAL EQUIVALENT CIRCUIT MODEL DEVELOPMENT

Previous models available in the literature have taken the battery pack as a lumped system. Such simplification considers the system's interior temperature to remain uniform throughout the heat transfer process. The Biot modulus compares the relative magnitudes of surface convection and internal conduction resistances to heat transfer. A very low number means that the internal conduction resistance is negligible in comparison with the surface convection resistance, and implies that the temperature will be nearly uniform throughout the body, thus system behaviour can be accurately approximated by lumped analysis. For a system to be accepted as lumped, the Biot number should be less than 0.1 [85].

$$Bi \leq 0.1 = \frac{hL_c}{K_{eff}}$$

When the Biot number is less than 0.1, the difference in temperature between the body and the surrounding environment remains within 5% [85]. Biot numbers higher than 0.1 decrease the accuracy of the lumped system analysis. However, lumped thermal model analysis in the food processing industry uses a Biot number of 0.2 as a limit [86, 87]. Therefore, a Biot number between 0.1-0.2 might be acceptable for a simple lumped thermal model analysis. Calculations regarding the Biot number for the system in question are shown in Appendix B where each heat flow path has a value of over 0.2. However, an overall value of 0.23 still approaches the criteria set for the Biot number which means this system could in the limit be analyzed as a lumped thermal model, albeit a very borderline approximation. To better model the system, a thermal equivalent circuit is developed to capture the multi-path heat flow characteristics in a transient model. In effect the system is discretized into its key components.

The rate of heat loss/gain through a material or medium can be modeled as an equivalent electrical circuit. The comparisons between a thermal circuit and electrical circuit element is shown in Figure 5.1.

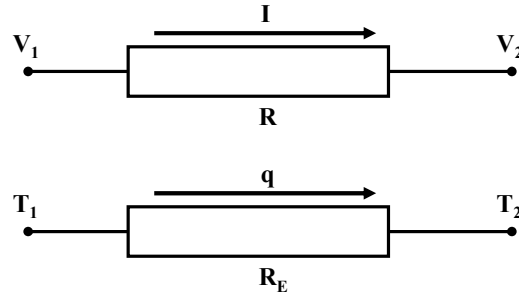


Figure 5.1 – Electrical and heat flow [88]

The rate of heat transfer corresponds to the electrical current and the temperature difference across the resistor corresponds to the voltage difference. Furthermore, voltage and current sources become temperature and heat generation sources in an equivalent thermal resistance network. Incorporating capacitors into the model represents a thermal mass in the system. Electrical capacitors increase in voltage as the current flow decreases until it cannot accept any more charge. For thermal systems, this represents a material increasing in temperature until it reaches steady state with the environment. Table 5.1 summarizes the thermal and electrical analogies.

Table 5.1 – Thermal and electrical analogies

Thermal Properties	Electrical Properties
R – resistance [K/W]	R – resistance [Ω]
C – capacitance [J/K]	C – capacitance [F]
T – temperature [K]	V – voltage [V]
\dot{Q} – heat rate [W]	I – current [A]
q – heat flux [W/m ²]	J – current density [A/m ²]

To calculate each of the components in the resistance network, the following equations are used:

Convection

$$R_{conv} = \frac{1}{hA_s} \text{ [K/W]} \tag{5.1}$$

Conduction

$$R_{cond} = \frac{L}{kA_s} \text{ [K/W]} \quad 5.2$$

Radiation

$$R_{rad} = \frac{1}{h_{rad} A_s} \text{ [K/W]} \quad 5.3$$

$$h_{rad} = \varepsilon\sigma(T_s^2 + T_{surr}^2)(T_s + T_{surr}) \quad 5.4$$

Capacitance

$$C = mC_p \text{ [J/K]} \quad 5.5$$

Thermal equivalent circuits may be constructed several ways. Some authors use the “L” half section topography for the RC elements, alternatively the “T” or “Π” sections as shown in Figure 5.2 may be employed to describe components of the system. Here the “L” half section was selected for model and computational simplicity.

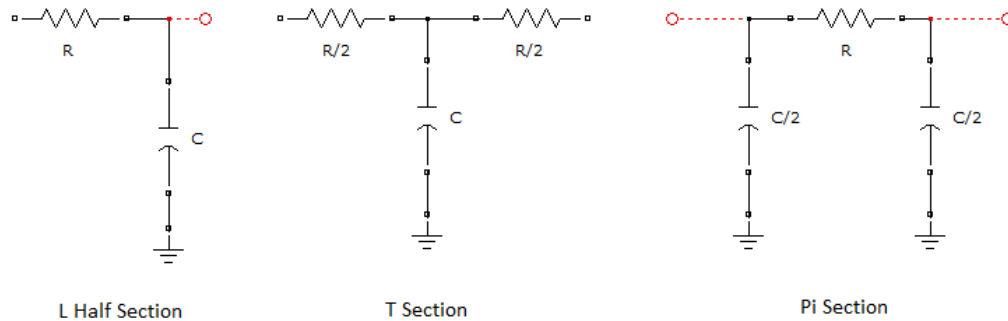


Figure 5.2 – Electrical topographies

The heat flow between the cells and the external environment is a combination of conduction, convection and radiation paths. While most previous models outlined in the literature have used a lumped model for the cells with simplified heat flow paths to the external environment, the present model takes into consideration the physical path of heat

flow through the cell pouch material, nylon frame, baseplate, cell retaining plates, internal air gaps and fibreglass cover. Heat sources emanate from the cells, the engine compartment at the front of the battery box, the chassis which surrounds the battery cover, the underbody of the vehicle and radiative heat from the road surface. A thermal equivalent circuit was created to represent the entire system's thermal capacitances, conduction, convection, radiation resistances and heat sources which are detailed in subsequent sections. These heat sources are represented by either voltage source or current source inputs using data interactively from Autonomie drive cycles. All resistance values used are equivalent resistances for various thermal paths which have been calculated and scaled down to a per cell value so as to represent the thermal path from a single cell to the environment. This approach helps quantify the contribution from the individual cells to the surrounding materials which comprise the entire battery and can then be scaled up to analyze an entire battery pack.

The ensuing analysis details the individual components and paths that form the thermal equivalent circuit. The complete circuit is then discussed, combining the sections into a representation of the whole battery pack as it sits in the vehicle complete with outside influences. It should be noted this methodology can be applied to any vehicle architecture and thermal management strategy. The process described in the preceding sections apply to the Chevrolet Volt but it provides insight on paths that could exist in other systems.

5.1 Cell and Thermal System Equivalent Circuit

The liquid cooling system coupled with the cell can also be modeled as a resistance network used in combination with the environmental model, as explained in the subsequent sections. Figure 5.3 depicts the resistive network for the liquid cooling system and Table 5.2 summarizes the elements.

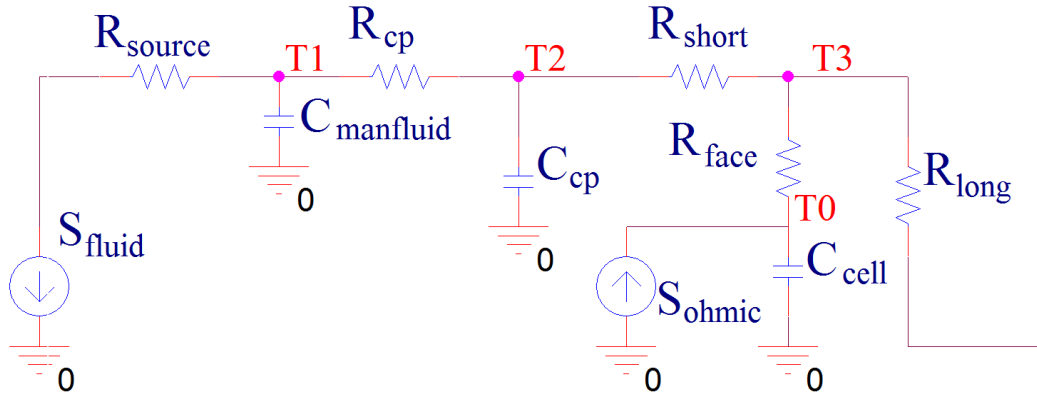


Figure 5.3 – Resistance network for liquid cooling system (Section A)

Table 5.2 – Cell and Thermal System Elements

Symbol	Definition
S_{liquid}	Liquid cooling system flow rate
S_{ohmic}	Heat input to the cells from ohmic effects
R_{source}	Resistance of the fluid moving through the plumbing to/from the battery inlet/outlet
R_{cp}	Resistance along the cooling plate channels
R_{short}	Resistance through the cooling plate to the face of the cell
R_{long}	Resistance from the center of the cell towards the edges
R_{face}	Resistance through the face direction of the cell
C_{manfluid}	Capacitance of the fluid in the manifold
C_{cp}	Capacitance of the cooling plate
C_{cell}	Capacitance of the cells

The cooling system is modeled as a current source which replicates the cooling rate experienced by the battery pack, denoted by S_{fluid} . R_{source} is the resistance of the cooling system in moving fluid from the compressor and its heat exchanger unit to/from the inlet/outlet. This resistance is calculated via the fluid plumbing between the compressor and the battery. Once the fluid enters the battery, it distributes/collects through the frame manifold. The thermal capacitance of the fluid which sits in the manifolds is C_{manfluid} . R_{cp} is the convection resistance along the cooling plate. The length of the cooling channels

and total surface area are found by physical measurement. C_{cp} is the thermal mass of the cooling plate, determined by weighing a cooling plate and the specific heat of aluminum. R_{short} represents the direct heat flow path across the cooling plate to the surface of the cell. R_{long} is the resistance of heat flowing through the cell to its edges, which are in contact with the nylon frame. This is an equivalent resistance because the rectangular shape of the cell effectively creates a 2D heat flow path going to the sides, top and bottom of the cell edges. R_{face} is the resistance across the face direction of the cell between its core and surface. C_{cell} is the thermal capacitance of the cell determined from its specific heat value and mass. Finally, S_{ohmic} is modeled as a current supply since it represents the heat input to the cells via ohmic heating.

5.2 Heat Transferred to External Environment

The cell and thermal system circuit is connected to other thermal paths which eventually lead to the external battery environment. When the battery is installed in the car, the battery cover is surrounded by the vehicle's chassis and the bottom plate is exposed to the fluid flow environment under the vehicle. Not only does the radiation from the hot pavement transmit into the battery, the EREV's radiator wash and exhaust system is in close proximity to the battery. These specific heat paths are examined in Section 5.2.3 and 5.2.4 detailing the method by which key equivalent resistances are calculated in these instances.

5.2.1 Nylon Frame Sections

The cell pouch edges are thermo-welded together and in contact with the nylon frame. This edge transfers heat from the cell to the nylon frame and continues to flow through the battery until it exits to the environment. The frame also contains two manifold channels which distribute the fluid throughout the system to the cooling plates and collect it again before exiting. To analyze how the frame interacts with the cells and fluid, the nylon frame was segmented into various parts. The flow of heat at the edge of the cell travels through the laminated aluminum/plastic pouch material and glue that seals it. Figure 5.4 depicts schematically the heat path (in red) emanating from the center of the cell,

flowing through the pouch material and out the edge of the cell which is touching the nylon frame. The cells have a much higher thermal conductivity in the planar direction compared to the face direction due their laminated construction. An aspect of this model is that one heat flow path is slightly longer. The heat flowing through the cell edge which is not in direct contact with the frame has to cross two pouch layers and the glue layer which seals the pouch material together. This arrangement creates parallel networks with some resistance elements in series.

Figure 5.5 depicts a cross-section of the pouch material and the typical associated thickness of each layer.

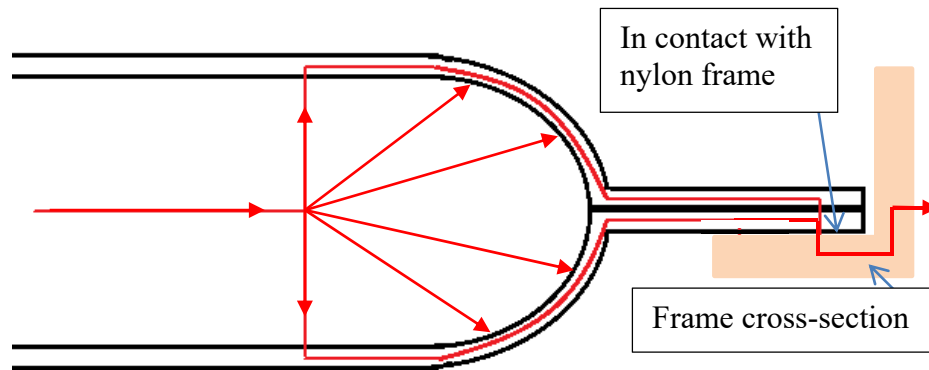


Figure 5.4 – Cell edge heat flow paths (red lines) to nylon frame


Construction	Material	Thickness
	Oriented Nylon	25 μm
	Adhesive	4 μm
	Foundation	–
	Aluminum Foil	40 μm
	Foundation	–
	Acid Modified Olefin	5 μm
	Sealant	30 μm

Figure 5.5 – Li-Ion pouch layer construction [89]

Figure 5.6 shows the nylon frame divided into regions so the heat transfer through the frame as a whole can be better estimated. Each region has an associated capacitance, which together totals to the thermal capacitance of the entire nylon frame.

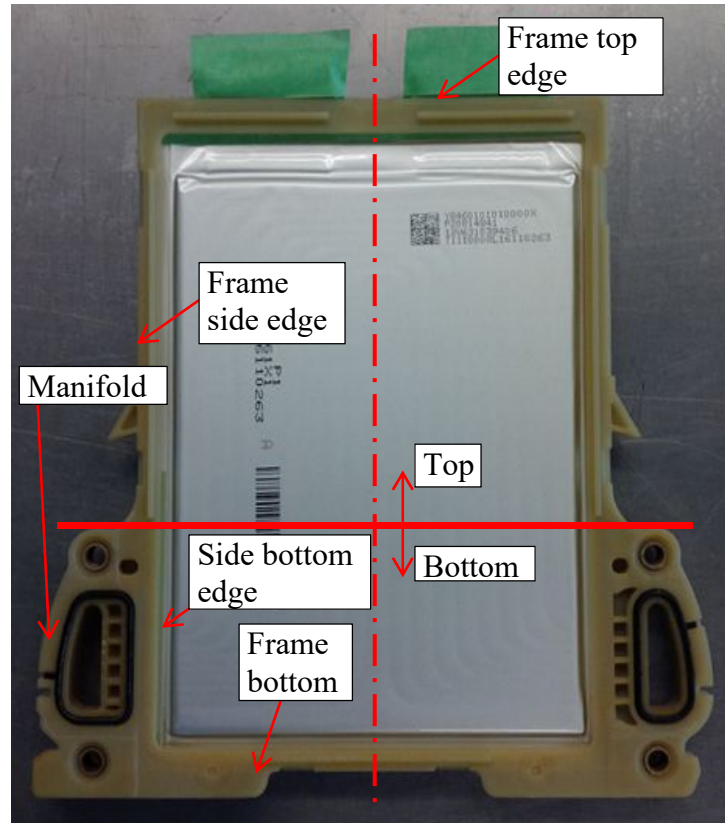


Figure 5.6 – Division of nylon frame sections

In the completed battery pack assembly, the top, side, and manifold portions of the frame are surrounded by an air gap to the battery cover, and then another air gap to the vehicle's chassis. Whereas the bottom portion of the frame experiences a different heat flow path due to its steel baseplate being exposed more directly to the underbody air flow and road surface radiation. Figure 5.7 represents the resistance network of the frame elements. Table 5.3 shows the keys resistance and capacitance elements for the nylon frame regions.

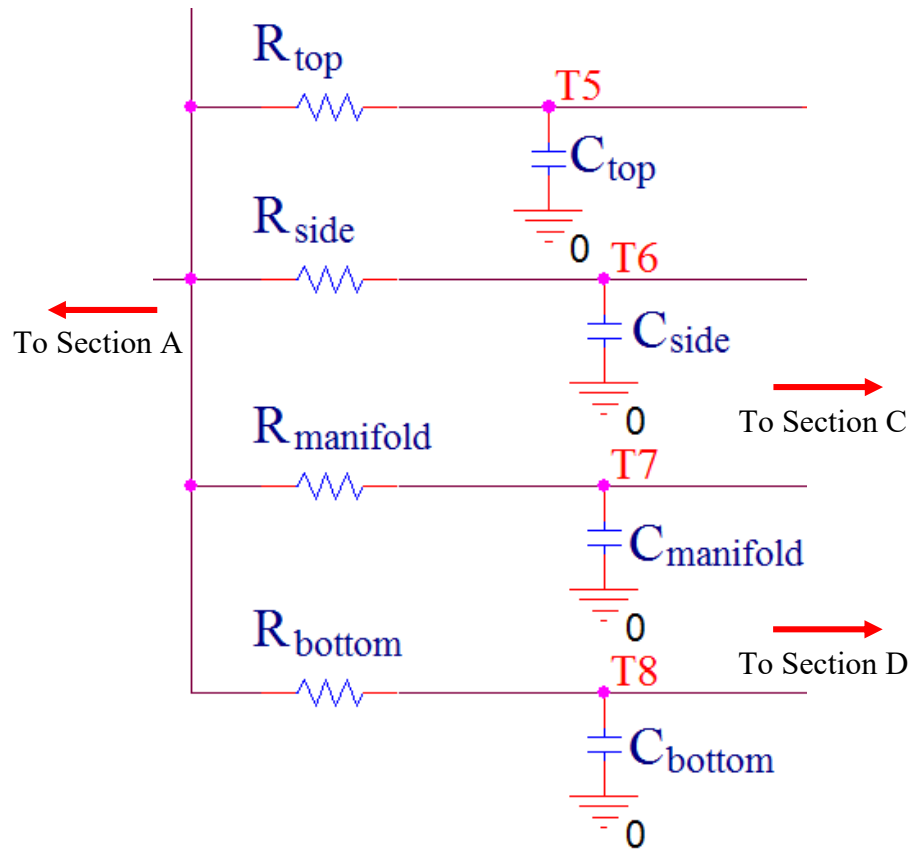


Figure 5.7 – Resistance network for frame elements (Section B)

Table 5.3 – Frame Resistance and Capacitance Elements

Symbol	Definition
R_{top}	Resistance through the top
R_{side}	Resistance through the sides
R_{bottom}	Resistance through the bottom
$R_{manifold}$	Resistance through the manifolds
C_{top}	Capacitance of the top
C_{side}	Capacitance of the sides
C_{bottom}	Capacitance of the bottom
$C_{manifold}$	Capacitance of the manifolds

The various sections of the frame geometry were physically measured in order to calculate the resistance and capacitance values. As seen from Figure 5.4 the frame cross section is L-shaped. Area calculations for the sides and manifolds are multiplied by two due to symmetry. The bottom frame is affected by the heat generation of the cells and by the manifold fluid temperature.

5.2.2 Heat Flow Path through the Cover

As stated previously, there exists an air gap between the frame and battery cover. The cover is again surrounded by an (external) air gap to the chassis as shown in Figure 5.8. For the internal air gap, the air is divided into local sections around the manifold, side and top. The purpose of dividing the air gap into sections is to account for the non-uniform heat distribution in the frame sections. Figure 5.9 shows the resistance network for the internal and external air gaps as well as the cover with the key elements defined in Table 5.4

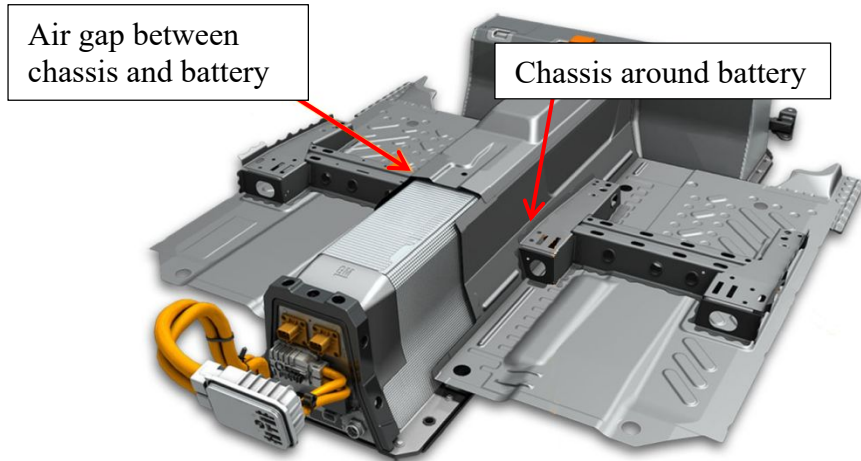


Figure 5.8 – Chassis structure and battery adapted from GM [90]

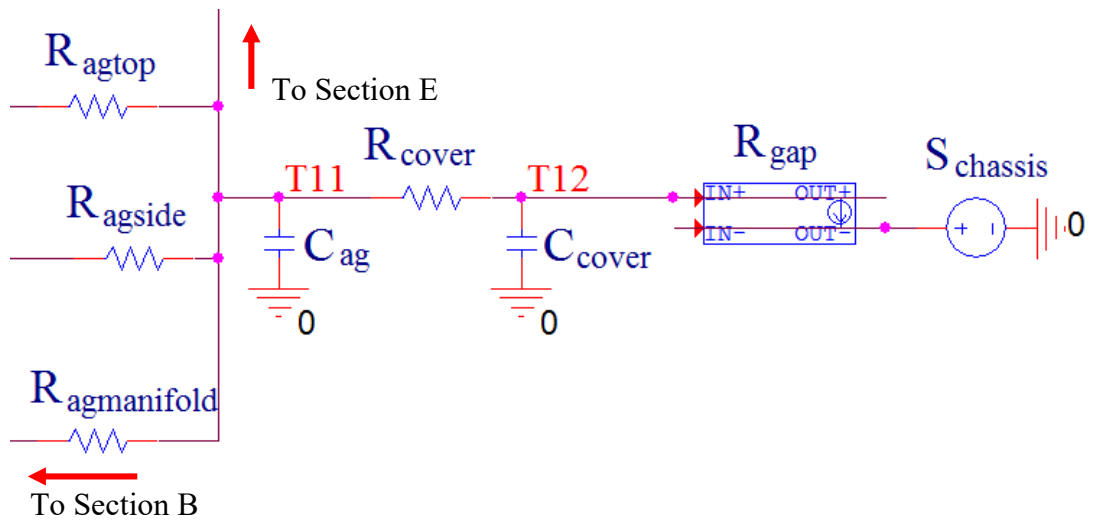


Figure 5.9 – Resistance network for air gaps and cover (Section C)

Table 5.4 – Internal Air Gap Resistance and Capacitance Elements

Symbol	Definition
$S_{chassis}$	Heat from surrounding chassis to battery
R_{agtop}	Resistance through the top air gap
R_{agside}	Resistance through the sides air gap
$R_{agmanifold}$	Resistance through the manifold air gap
R_{gap}	Variable resistance combining conduction and radiation resistance in the air gap
R_{cover}	Resistance through the cover
C_{ag}	Capacitance of total air gap
C_{cover}	Capacitance of the cover

The cover is made from a fiberglass composite and the external air gap between the chassis and cover is taken as the combination of conduction and radiation resistances. To determine if there is any significant convective heat transfer in the air gap, the air flow will need to be measured for the model to be as accurate as possible, rather than assuming a value. This experimental work was carried out by another Master’s student [91]. The electrical source represents the heat being emitted from the chassis into the battery due to elevated cabin temperatures when the latter is heated by the sun (greenhouse effect).

5.2.3 Heat Flow through the Baseplate

The heat flow through the bottom section of the frame is a series resistance path which starts at the frame then flows through the baseplate to the environment under the car shown in Figure 5.10 and Figure 5.11. Figure 5.12 depicts the resistance network of the underbody elements and effects. Table 5.5 summarizes the key elements in this heat flow path.

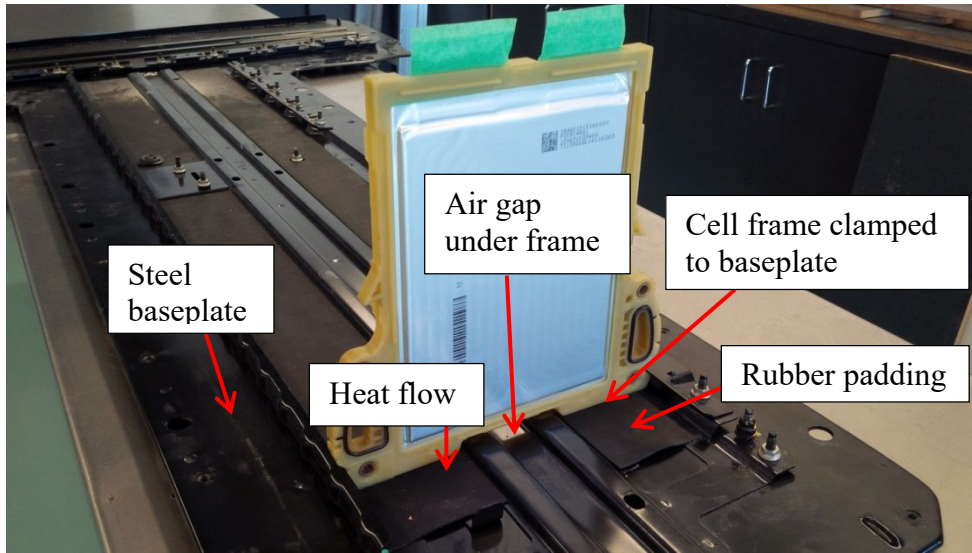


Figure 5.10 – Nylon frame and cell attached to steel baseplate

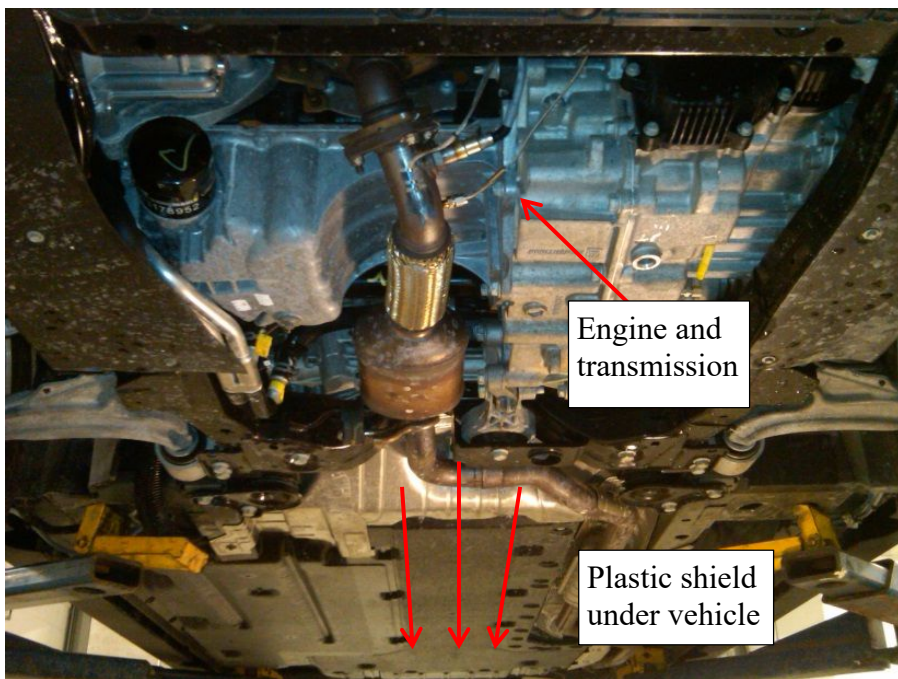


Figure 5.11 – Convection flow under vehicle

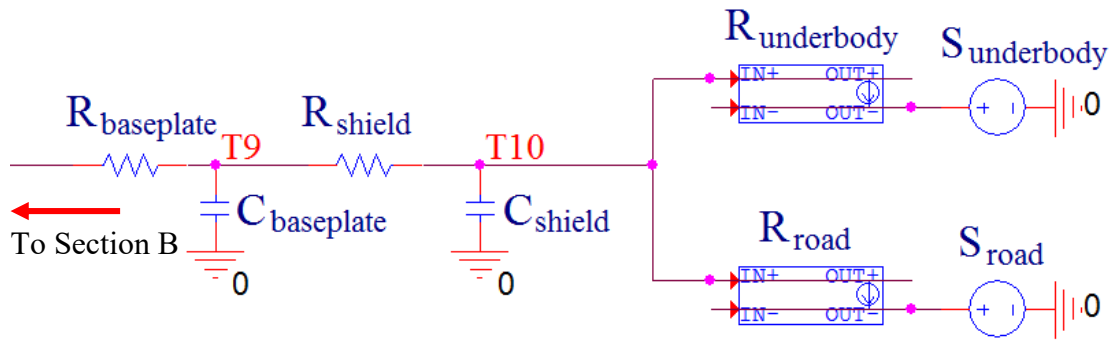


Figure 5.12 – Resistance network for underbody elements and effects (Section D)

Table 5.5 – Bottom Heat Flow Path Elements

Symbol	Definition
S_{road}	Radiant heat from the road surface
$S_{underbody}$	Heat from the underbody air stream temperature
$R_{underbody}$	Variable resistance through the underbody air gap
$R_{baseplate}$	Resistance through the baseplate material
R_{shield}	Resistance through the underbody shield assembly
R_{road}	Variable resistance of equivalent road radiation resistance
C_{shield}	Capacitance of the underbody shield
$C_{baseplate}$	Capacitance of baseplate

The road the vehicle is driving on may experience elevated temperatures due to radiant heating from the sun. The road surface will act as a radiant source, S_{road} , which transmits across air gap R_{road} . Underneath the vehicle, the hot air washing back from the engine and radiator through the ground clearance between the car and road acts as local ambient temperature source represented by $S_{underbody}$. $R_{underbody}$ is the combined conduction and convection resistances between the underbody air and the baseplate shield. $R_{baseplate}$ considers heat flow from the bottom edges of the cell retention frame in contact with the rubber padding/clamping arrangement, through the metal baseplate itself. R_{shield} is the resistance through the fiberglass underbody shielding (complete with its own local air gap). $C_{baseplate}$ and C_{shield} represents the thermal mass of the metal baseplate and underbody shielding respectively.

5.2.4 Endplate and Bulkhead Heat Flow Paths

Since the EREV has an ICE that is placed in front of the battery, as the ICE is in operation there is waste heat from the engine and exhaust system that will flow towards the battery. S_{engine} as a temperature source is determined from correlations to engine power output. From the vehicle road tests, the engine speed and torque is used to compute the engine power and correlated with the engine bay thermocouple readings above ambient. The front bulkhead of the battery pack, outlined in Figure 5.13, acts as a thermal sink, being it is situated directly behind the engine compartment. Figure 5.14 depicts the location of the steel endplates and BMS units; followed by Figure 5.15, which depicts the resistance network of the bulkhead, endplates and BMS unit. Table 5.6 summarizes the key elements of the resistance network.

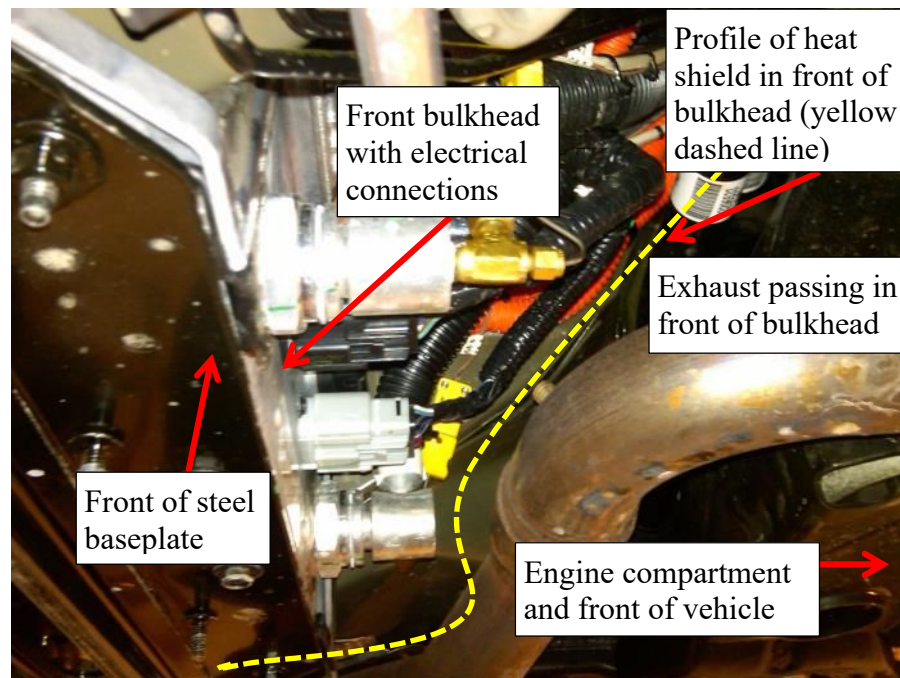


Figure 5.13 – Front bulkhead, dashed line depicts exhaust heat shield (removed)

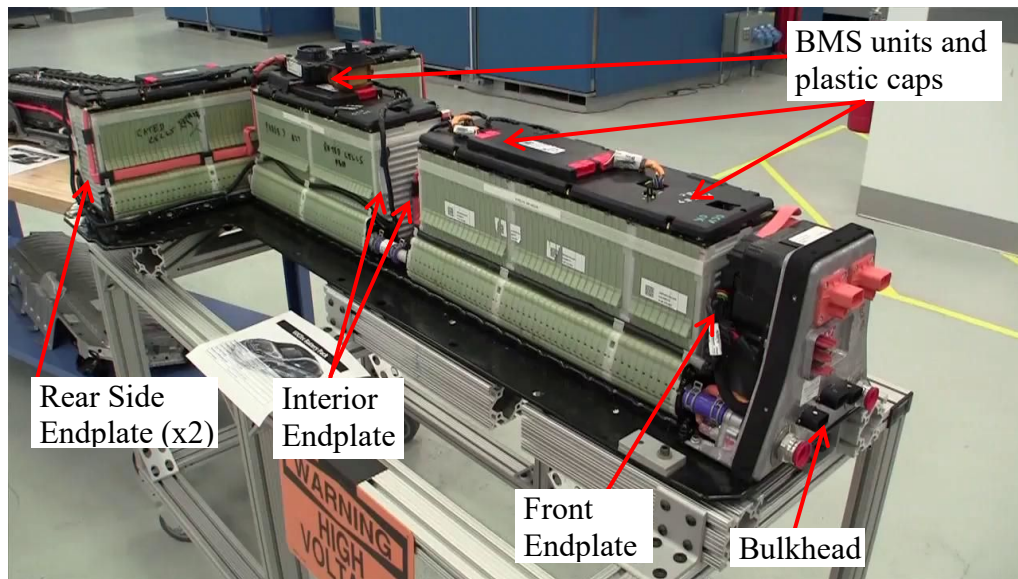


Figure 5.14 – Position of steel endplates

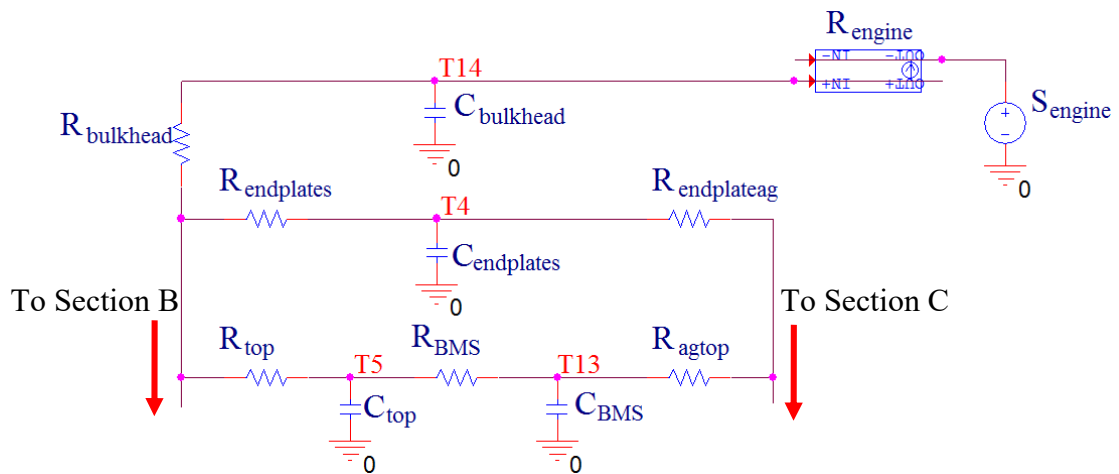


Figure 5.15 – Resistance network for the engine, bulkhead and endplates (Section E)

Table 5.6 – Bulkhead Elements

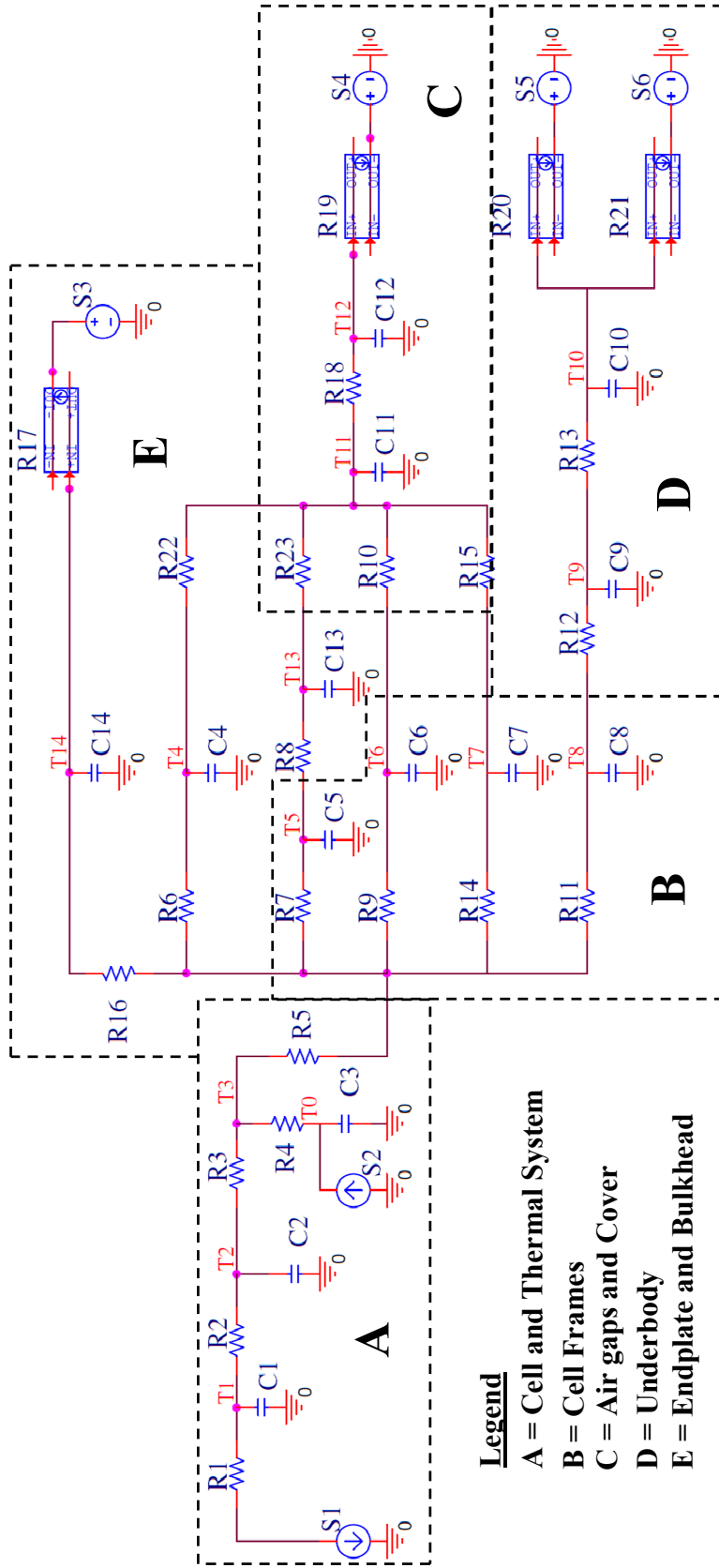
Symbol	Definition
S_{engine}	Heat from the engine compartment
R_{engine}	Variable resistance of the air gap between engine and bulkhead
R_{bulkhead}	Resistance through the bulkhead
$R_{\text{endplates}}$	Resistance of endplates
R_{BMS}	Resistance of the BMS and plastic caps
C_{bulkhead}	Capacitance of bulkhead
$C_{\text{endplates}}$	Capacitance of endplates
C_{BMS}	Capacitance of the BMS and plastic caps

R_{engine} represents the conductive/convective air in front the bulkhead. R_{bulkhead} is the resistance through the aluminum bulkhead and conductive air gap inside the front of the battery pack between the bulkhead and first cell. C_{bulkhead} represents the thermal mass of the bulkhead. Inside the battery, metal endplates are positioned at the ends of cell modules to compress and hold the frames together. These endplates constitute part of a cell module’s surface area. The endplates hold an internal air gap due to their layered construction and $R_{\text{endplates}}$ is an equivalent resistance to capture their construction. $C_{\text{endplates}}$ represents the thermal mass of the total endplates in the system. Because the endplates are conveying heat on a cell module basis, their resistance value as used in the circuit is scaled by (288/6) to allocate for their net contribution to an individual cell. The BMS units which are situated on top of the cells and mounted to the top frame are accounted for by R_{BMS} and C_{BMS} .

5.3 Complete Thermal Equivalent Circuit

Sections A-E from the previous resistance networks are connected to form an equivalent circuit in PSPICE to represent the system’s thermal capacitances, conduction properties, convection and radiation resistances, and sources / sinks shown in Figure 5.16. The latter are represented by either voltage or current inputs from Autonomie drive cycles, or they can be defined functions in MATLAB/Simulink. All simulations for the thermal equivalent circuit are conducted in MATLAB/Simulink with a PSPICE integration plugin.

This allows the developed cooling logic explained in Section 5.5 to be integrated. The resistances and capacitance values listed in Table 5.7 were calculated from geometrical considerations and used as initial values. Variables with an asterisk (*) indicate values that have been improved through experiments to produce outputs shown in the results section, and that process is described subsequently. The circuit component values reflect those attributable to a single cell as this represents the basic building block in any battery design. For the entire pack, the overall resistance values are to be divided, and capacitances multiplied, by 288 (the number of cells constituting the pack in this case), as each is considered an additional parallel path to the environment. This analysis method quantifies the thermal contribution of the individual cell and proportionate surrounding materials, which can then be more easily scaled to analyze the entire battery pack. Given that the model can be modified in specific areas to “explore” a new configuration, design alternatives are more readily quantifiable. The temperature nodes depicted in this circuit correspond to the bulk temperatures of their respective capacitances (thermal masses) and constitute validation test points where thermocouples can be installed. Figure 5.17 is the physical representation of Section A, B and C of the same thermal equivalent circuit shown in Figure 5.16.



Legend

- A = Cell and Thermal System
- B = Cell Frames
- C = Air gaps and Cover
- D = Underbody
- E = Endplate and Bulkhead

Figure 5.16 - Thermal equivalent circuit delineating physical regions within the battery pack

Table 5.7 – Cell and thermal system definitions

Symbol	Label	Definition	Values / Range
S ₁	S _{fluid}	Liquid system inlet cooling/heat flow rate	3.8 A
S ₂	S _{ohmic}	Heat input to the cells from ohmic heating	1-5 W
S ₃	S _{engine}	Temperature from the engine battery	100-350 V
S ₄	S _{chassis}	Temperature from chassis to cover	20-30 V
S ₅	S _{underbody}	Temperature from the underbody	20-40 V
S ₆	S _{road}	Temperature from the road	20-50 V
<hr style="border-top: 1px dashed black;"/>			
R ₁	R _{source}	Fluid through pipes to battery inlet	0.7 Ω
R ₂	R _{cp}	Cooling plate	0.3 Ω
R ₃	R _{short}	Cooling plate to the face of the cell	0.2 Ω
R ₄	R _{face}	Face direction of the cell	1 Ω
R ₅	R _{long}	Center of the cell towards the edges	1.8 Ω
R ₆ *	R _{endplates}	Endplates	26 Ω
R ₇ *	R _{top}	Frame top	160 Ω
R ₈ *	R _{BMS}	BMS units and plastic casing	100 Ω
R ₉ *	R _{side}	Frame sides	30 Ω
R ₁₀ *	R _{agside}	Sides air gap	90 Ω
R ₁₁ *	R _{bottom}	Frame bottom	123 Ω
R ₁₂ *	R _{baseplate}	Baseplate	35 Ω
R ₁₃ *	R _{shield}	Under vehicle fiberglass shielding	40 Ω
R ₁₄ *	R _{manifold}	Manifolds	40 Ω
R ₁₅ *	R _{agmanifold}	Manifold air gap	100 Ω
R ₁₆ *	R _{bulkhead}	Bulkhead	400 Ω
R ₁₇	R _{engine}	Air gap between engine and bulkhead	397 Ω
R ₁₈ *	R _{cover}	Cover	1.5 Ω
R ₁₉	R _{gap}	Air gap between battery and chassis	25 Ω
R ₂₀	R _{underbody}	Underbody air gap convective resistance	50 Ω
R ₂₁	R _{road}	Road radiation equivalent resistance	130 Ω
R ₂₂	R _{endplateag}	Endplate air gap	88 Ω
R ₂₃ *	R _{agtop}	Top air gap	130 Ω

C ₁	C _{manfluid}	Fluid in the manifold	3.8 F
C ₂	C _{cp}	Cooling plate	28 F
C ₃	C _{cell}	Cells	338 F
C ₄	C _{endplates}	Endplates	17 F
C ₅	C _{top}	Frame top	12 F
C ₆	C _{side}	Frame sides	12 F
C ₇	C _{manifold}	Manifolds	10 F
C ₈	C _{bottom}	Frame bottom	18 F
C ₉	C _{baseplate}	Baseplate	19 F
C ₁₀	C _{shield}	Underbody shielding	4.7 F
C ₁₁	C _{ag}	Total air gap	0.2 F
C ₁₂	C _{cover}	Cover	27 F
C ₁₃	C _{BMS}	BMS and plastic	9 F
C ₁₄	C _{bulkhead}	Bulkhead	10 F
T ₀	T _{core}	Cell core temp	10-45 V
T ₁	T _{fluid}	Inlet fluid temp	10-45 V
T ₂	T _{cp}	Cooling plate	10-45 V
T ₃	T _{cell}	Cell surface	10-45 V
T ₄	T _{endplate}	Endplates	10-45 V
T ₅	T _{top}	Frame top	10-45 V
T ₆	T _{side}	Frame sides	10-45 V
T ₇	T _{manifold}	Manifolds	10-45 V
T ₈	T _{bottom}	Frame bottom	10-45 V
T ₉	T _{baseplate}	Baseplate	10-45 V
T ₁₀	T _{shield}	Underbody shield	10-45 V
T ₁₁	T _{inside cover}	Inside cover	10-45 V
T ₁₂	T _{outside cover}	Outside cover	10-45 V
T ₁₃	T _{BMS}	BMS	10-45 V
T ₁₄	T _{bulkhead}	Bulkhead	10-45 V

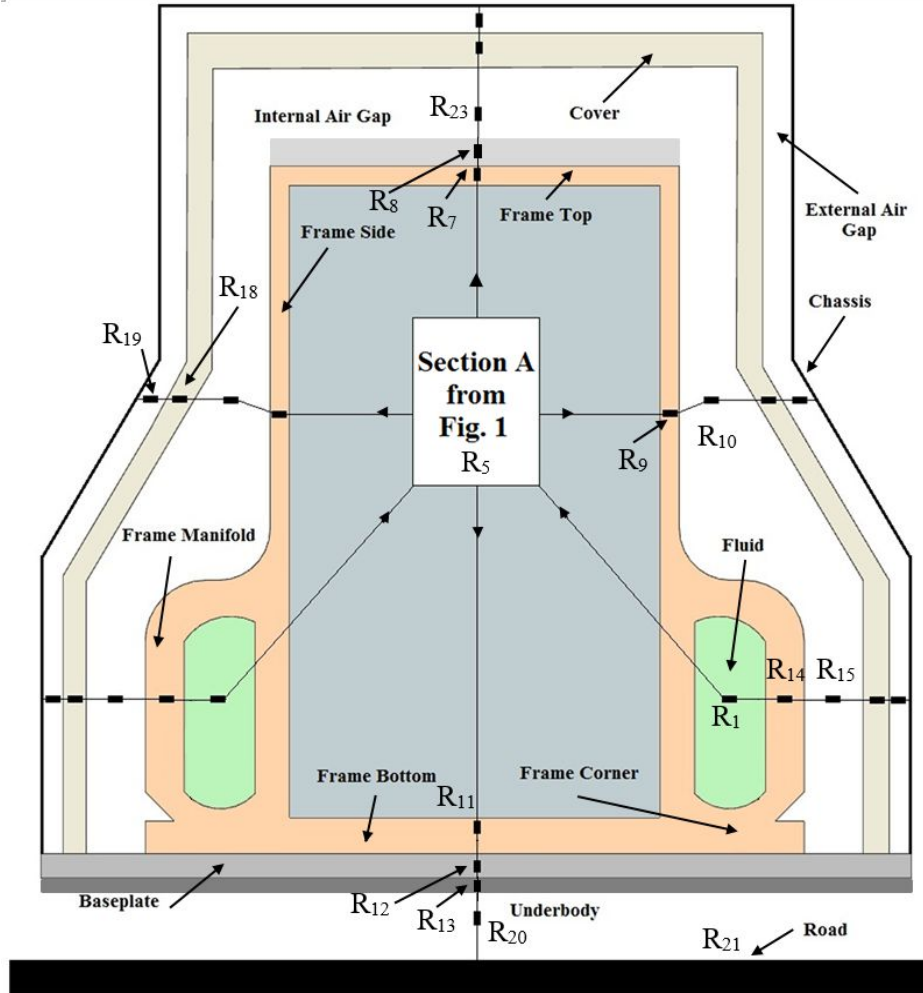


Figure 5.17 – Cross-section of cell packaging showing placement of equivalent resistances in sections A, B and C. R5 from Section A is surface area partitioned to respective branches

From this image, it should be noted that surface area partitioned equivalent resistances are assigned to some elements. For example R5 represents lateral heat transfer from the cell interior outwards. Figure 5.17 depicts these parallel paths as arrows, each accounting for a portion of the cell frame surface area. Such heat flow paths are computed on a geometric and physical basis (mean path length & thermal conductivity) and applied in order to scale down the complexity of the model to be solved. For instance, the inlet and outlet sides of the pack are combined into one equivalent parallel path due to symmetry; R_{side} is the result of adding the resistance of the inlet and outlet sides together in parallel as shown in

Equation 5.6. An extensive spreadsheet was developed to combine the many individual component and path values into equivalent circuit quantities by a similar methodology.

$$R_{side} = \left(\frac{1}{R_{inlet\ side}} + \frac{1}{R_{outlet\ side}} \right)^{-1} \quad 5.6$$

For drive cycle simulations, the values of the external resistors (R_{17} , R_{19} , R_{20} , R_{21}) and sources vary dynamically to reflect the change in ambient climatic conditions coincident with the vehicle's velocity and/or operation of the IC power plant. This is seen in Figure 5.16 by the variable resistors shown with a unique symbol set in PSPICE. The programming of these resistors are found in the thesis of a member on the research team [91]. The element used was a voltage controlled current source linked to a look-up table that makes it act as a "resistor" element.

5.3.1 Simplified Thermal Equivalent Circuit and Experiments

In order to validate the thermal equivalent circuit model, and primarily to assess accurate values for the key thermal resistances at play, the circuit model is simplified to represent the lab test conditions rather than the full situation seen on the vehicle. This reduced circuit is shown in Figure 5.18 where section A is replaced by resistors R_1 , R_4 and capacitors to ground C_1 and C_3 . The C_1 value represents the fluid loop conditioning cart's lumped dynamic characteristics combined with that of the cooling plate; the conditioning cart replaces the vehicle's thermal management loop in the lab environment.

Since the cell temperature nodes T_0 - T_3 are inaccessible without disassembling the entire battery pack, the detailed examination of heat transfer in this portion (Section A) was deferred; rather the emphasis was placed on how the balance of the cell packaging arrangement is affecting heat transfer to the environment. To this end the Section A components together with the fluid loop conditioning cart were lumped as R_1 and C_1 , with T_3 . The initial transient behavior of this system response to step input was curve fit to experimental data in order to assign appropriate values for the components in the model. The inlet fluid temperature T_1 (which is also equal to T_3) of the reduced model in Figure

5.18 is taken to be a near equivalent to the cell surface temperature due to the very low resistances associated with the cooling plate.

Although lumping Section A of the circuit obfuscates the precise heat flow pattern internal to the cell frames, it does not hold back the overall analysis. Circuit component values initially estimated were experimentally refined by instrumenting the surfaces of the cell retention frames with heat flux sensors and thermocouples. They are considered accurate for this reduced model, as will be seen in the validation section. The exact values of R_2 , R_3 , and R_5 are being determined by a separate set of experiments via another Masters student involving disassembled cells / retention plates.

The initial resistances were refined experimentally for the simplified circuit, and are detailed in Table 5.8. This model was created by the research team member charged with analyzing the thermal characteristics of the full battery assembly [91] and refined during the validation process and further adjusted for diurnal simulations by the author.

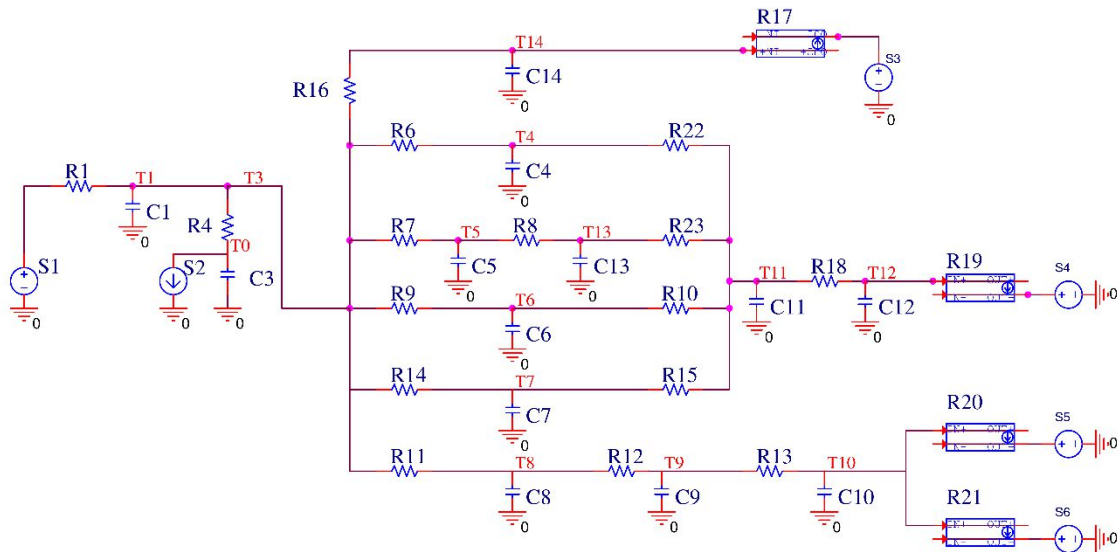


Figure 5.18 – Simplified thermal equivalent circuit used for validation experiments and predictive modeling

Table 5.8 – Modified Components (balance of values as per Table 5.7)

Symbol	Label	Value or Range
R ₆	R _{endplate}	57 Ω
R ₇	R _{top}	30 Ω
R ₈	R _{BMS}	89 Ω
R ₉	R _{side}	32.5 Ω
R ₁₀	R _{agside}	100 Ω
R ₁₁	R _{bottom}	57 Ω
R ₁₂	R _{baseplate}	40 Ω
R ₁₃	R _{shield}	56.6 Ω
R ₁₄	R _{manifold}	42.5 Ω
R ₁₅	R _{agmanifold}	135 Ω
R ₁₆	R _{bulkhead}	1313 Ω
R ₁₈	R _{cover}	2.2 Ω
R ₂₃	R _{agtop}	69 Ω
C ₁	C _{lumped}	32 F

Thermocouples (Omega K-type with IPETRONIK M-THERMO modules for data acquisition) and thermopile-type heat flux sensors (Omega HFS-4 with IPETRONIK M-SENS modules for data acquisition) were used to record the temperature and heat flux measurements at nodes T₃-T₁₄ of the simplified circuit. Figure 5.19 depicts an overview of the battery pack assembly (with the cover removed) and experimental setup. Heat flux sensors attached to the bulkhead and part of the baseplate are shown along with thermocouples placed at other nodes of the circuit.

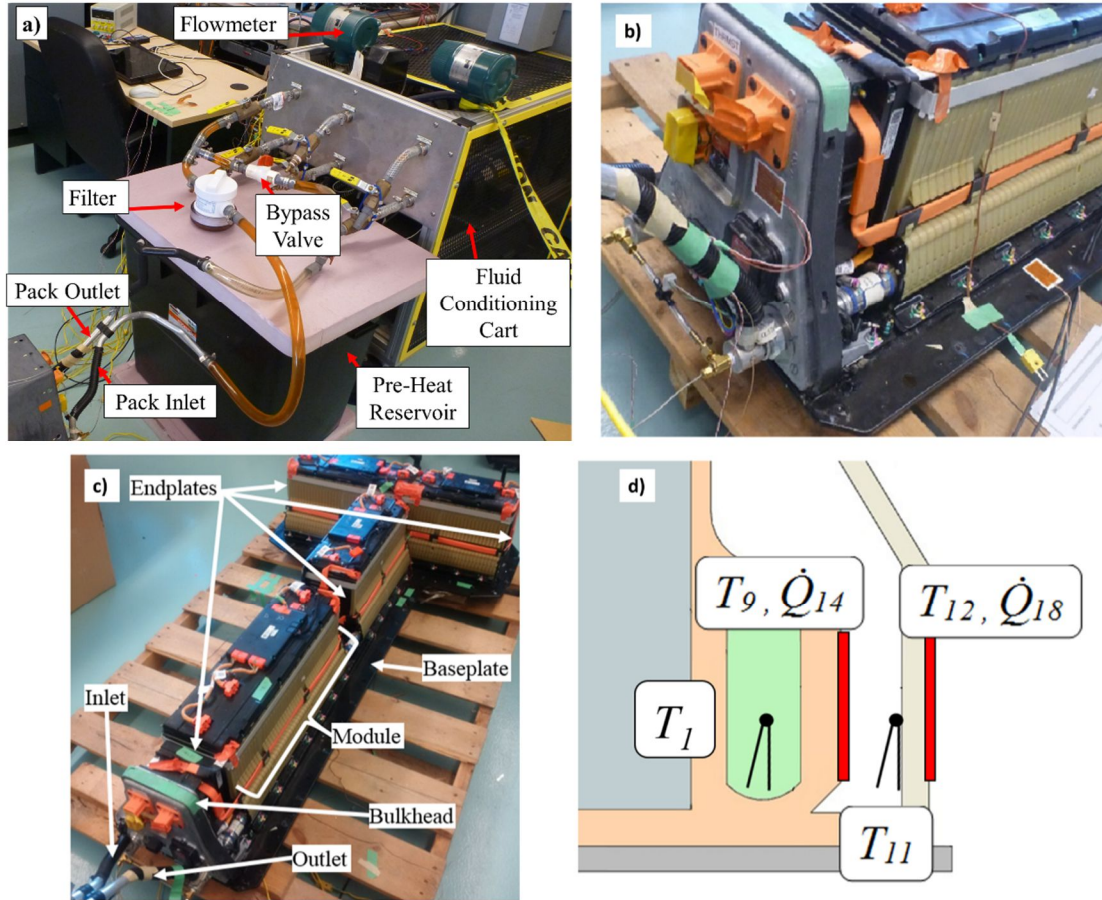


Figure 5.19 – Fluid conditioning cart and pre-heating reservoir setup (a), front bulkhead with heat flux sensors (b), pack with regions identified (c), manifold path sensor placement (d)

The experimental procedure [91] begins by heating up the battery pack through circulating fluid continuously. Once steady-state is reached (about 3 hours), the thermal resistance is calculated by simultaneously measuring the heat rate and temperature difference across each resistor in the circuit and applying Ohm's law to these measurements. After holding at steady-state for at least one hour, the fluid flow is stopped and the pack is allowed to cool down to room temperature. Figure 5.19d schematically demonstrates an example of sensor placement used to measure the resistances through the manifold path. The temperatures and heat rates are labeled according to the nodes in Figure 5.18. In this example, the heat flux sensors are placed on the frame and cover surfaces, where they measure both heat flux and surface temperature (HFS-4 has a built-in K-type

thermocouple). The heat flux reading is converted to heat rate by multiplying it by the surface area of the face being measured. For each resistor in the network, a heat rate through the resistor as well as the temperature drop across the resistor must be measured. Using Figure 5.19d as a guide, the procedure for calculating the manifold path resistances is explained below.

The fluid to manifold resistance (R_{14}) is determined by:

$$R_{14} = \frac{T_{fluid} - T_{manifold}}{\dot{Q}_{manifold}} = \frac{T_1 - T_9}{\dot{Q}_{14}} \quad 5.7$$

Similarly, the airgap resistance (R_{15}) and cover resistance (R_{18}) are calculated as follows:

$$R_{15} = \frac{T_{manifold} - T_{inside\ cover}}{\dot{Q}_{manifold}} = \frac{T_9 - T_{11}}{\dot{Q}_{14}} \quad 5.8$$

$$R_{18} = \frac{T_{inside\ cover} - T_{outside\ cover}}{\dot{Q}_{cover}} = \frac{T_{11} - T_{12}}{\dot{Q}_{18}} \quad 5.9$$

The same experimental verification method applies for the resistors across the remaining thermal paths. These improved values over the ones initially inferred on the basis of geometry and materials are reflected in Table 5.8 and are incorporated in the validation and simulation results described subsequently.

5.4 Thermal Equivalent Circuit Validation

The thermal equivalent circuit model was validated against the full scale production battery seen in Figure 5.19 by the author of Reference [91]. Ambient air in the lab was $\sim 23^\circ\text{C}$ and the inlet fluid temperature and flowrate were 45°C and 6 L/min respectively. For the lab setup, the simplified circuit environmental sources (chassis, engine, and underbody) were replaced by the lab's ambient temperature. The values of the convective/radiative resistances ahead of these sources (R_{17} , R_{19} , R_{20} , R_{21}) are also adapted to the laboratory ambient conditions of 23°C . Internal heat generation from the cells (S_2) is held dormant in

these calibration experiments since it would not be possible to reach and maintain a representative thermal steady-state through discharge before the pack is depleted. Instead, the sudden circulation of heated fluid (S_1) is used as the known step input source to drive the system dynamics. The following points are used for validation:

- Frame top, side, manifold temperatures;
- Baseplate temperature;
- Frame side and manifold heat rates;
- Baseplate heat rate.

Fluid at constant temperature was circulated through the pack until it reached steady state and the data acquired from the test was compared to the thermal equivalent circuit with the inlet temperature used as the voltage source (S_1) input. Figure 5.20 shows a time-based comparison between the experimental and simulation results at select test nodes.

For the baseplate, the simulation results were comparable to the experimental results with a slight deviation due to an uncontrollable change in HVAC related ambient lab conditions. However, the deviation between the data set is only 0.7°C and indicates the calculated thermal capacitance value for the baseplate is accurate.

The frame top portion also has a slight deviation in the transient section showing the calculated thermal capacitance (C_5 , C_{top}) is likely somewhat too large, which causes the simulation to lag behind the experiment; the largest deviation in the transient section being 1°C . In the steady state period, the simulation is 0.1°C higher than the experiment and this is attributed to a slightly higher resistance value for R_{23} (R_{agtop}).

The frame side data sets show comparable results with very little deviation in the transient region. The largest difference in the transient section is a 1°C lag, and 0.2°C offset towards the experiment's end. Much like the deviation in the frame top, this is caused by a higher calculated thermal capacitance, in this case C_6 (C_{side}).

The last set of data in Figure 5.20 is the manifold, which displays the same trend as the other frame components. The deviation in the transient section of 1°C is attributed to the higher calculated thermal capacitance of C_7 (C_{manifold}).

Variations of 0.5°C or slightly greater are considered to be within the guaranteed measurement error band of the thermocouple wire as supplied by the manufacturer, and for practical purposes, the achievable accuracy of the measurement system employed.

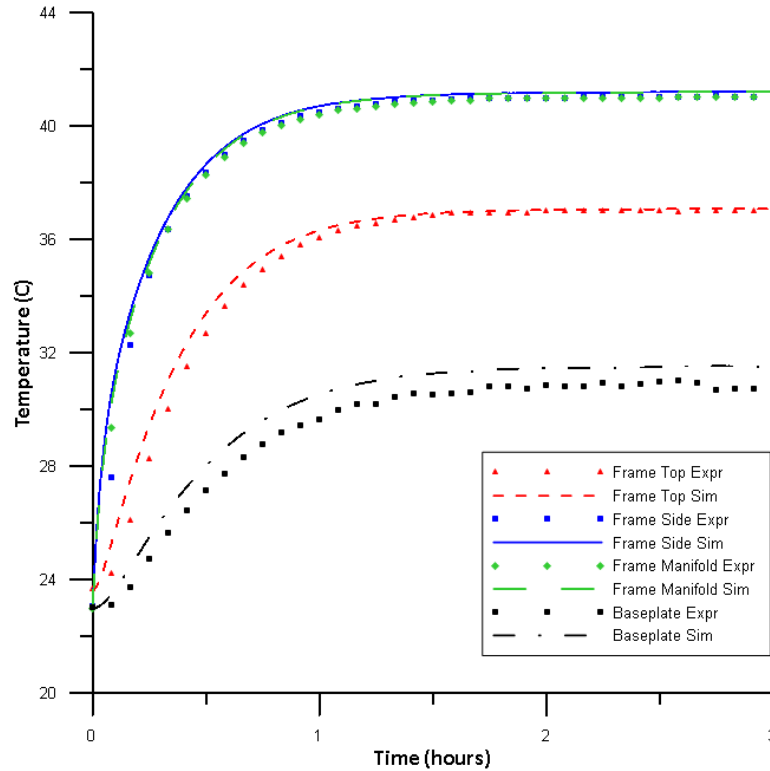


Figure 5.20 – Simulation and experimental frame and baseplate temperatures (circuit Section B and D)

In Figure 5.21 the heat rate is plotted on a per cell basis, and comparisons are made for the same components given in Figure 5.20. It should be noted that the experimental baseplate heat rate is more scattered compared to the other components due to sensor noise pickup from small local air currents, but the overlap with the computed value is accurate and averages to 0.12 W/cell difference only.

The frame top exhibits a difference of 0.005 W/cell between the experimental and computed data sets and, when scaled to the whole pack, amounts to a 1.44 W difference (insignificant). The frame side exhibits a difference of 0.01 W/cell in the steady state region while the manifold simulations show a smaller deviation to their respective experimental data. The manifold also has the greatest transient deviation of 0.015W/cell which amounts

to 4.32 W difference when scaled to the whole pack. This is an acceptable variation given the size of the battery pack and duration of the tests. For reference, about 110 W were being dissipated to the environment in steady state with an initial 8000 W heat absorption peak occurring during the first minute, and ~3400 W averaged over the first 10 minutes at the pack level.

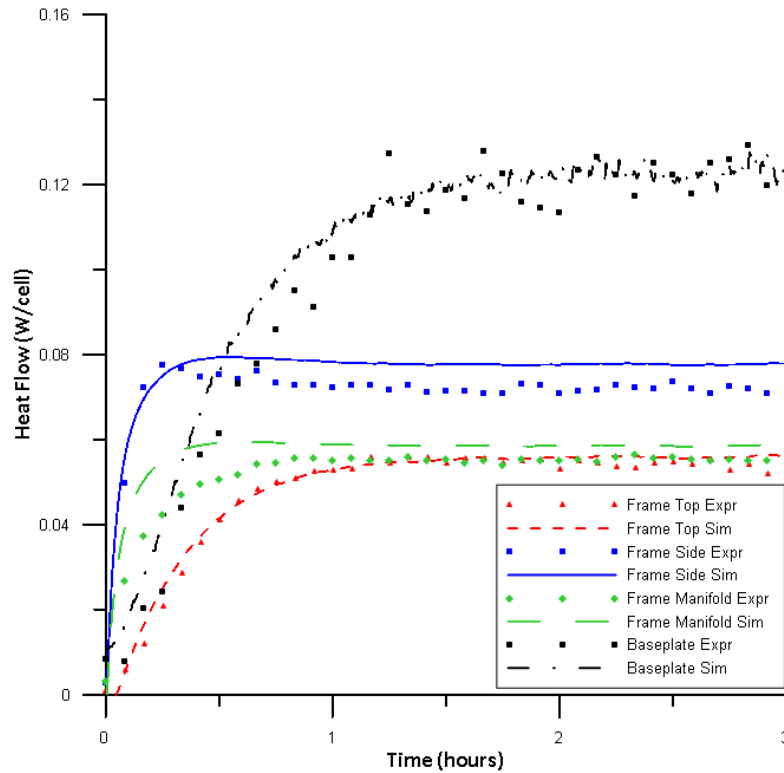


Figure 5.21 – Simulation and experimental frame and baseplate heat flows (circuit Section B and D)

Some of the error analysis for the experiments to refine the resistor values in the simplified circuit and the validation results are shown in Appendix C. Sample calculations for the equations in Appendix C can be found in the referenced material.

5.5 Cooling System Logic Controls

The data acquired from the road and vehicle thermal chamber testing uncovered aspects of the thermal management system operation. The fluid inlet temperature was recorded through the vehicle's CANbus while the system was active. Throughout the various vehicle experimental tests the cooling system was shown to become active when the cell temperature reached 32°C and shut off around 24°C. The operational time to draw down the temperature was also consistent taking approximately 600 seconds for each cooling cycle. The system appears to operate as a simple thermostatic control. This data was used in the development of the cooling flow rate for the S_{fluid} source.

Using the inlet fluid temperature profile, the cooling rate per cell was back calculated from the thermal circuit model in Ref [91]. The data revealed the cooling system initially removes a maximum of 3200 W of heat. However, this settles to approximately 1800 W of heat in the later stages of operation. Figure 5.22 depicts the compressor power profile during a cooling cycle. A peak power consumption of 1700 W is first observed which decreases over the length of the cycle to the 680-720 W range. If a cooling event is longer than 600 seconds, a value of 700 W is held until the system deactivates. The compressor has an average power and COP value of 1057 W and 1.5 respectively. This equates to approximately a 3.7 W/cell cooling rate. It appears the compressor speed is constant when 'on'. The motor torque required to run is proportional to the volume of refrigerant gas to be compressed. This is a function of ΔT at the condenser for the evaporator/chiller loop. The system is constrained by how much heat the chiller absorbs and brings to the compressor.

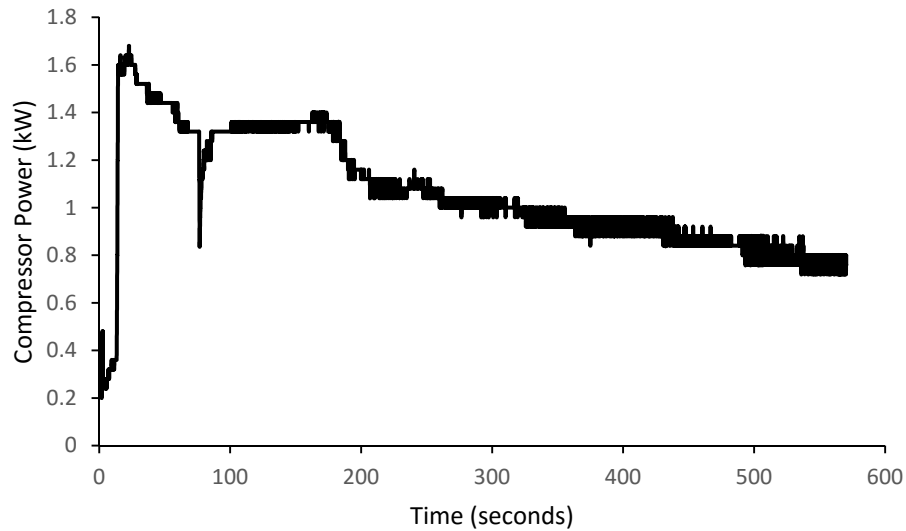


Figure 5.22 – Compressor power during cooling cycle collected from vehicle testing

With the operating parameters of the cooling system identified from vehicle testing, a cooling strategy in Simulink was created. Figure 5.23 shows the Simulink cooling control strategy, with cell surface temperature as the input, which is an output of the thermal equivalent circuit model. A switch determines if the cooling system is active or not. When this “On/Off” constant block is set to 1, the cooling system activates as the threshold temperature of 32 °C is triggered. The cell temperature, once it passes through the switch, becomes the input to the Stateflow logic block. An “Enable” trigger is included in the Stateflow logic which applies the cooling rate to the cooling source. This profile is programmed in the “Cooling Power Value” block in Figure 5.23A which is then fed into the thermal equivalent circuit.

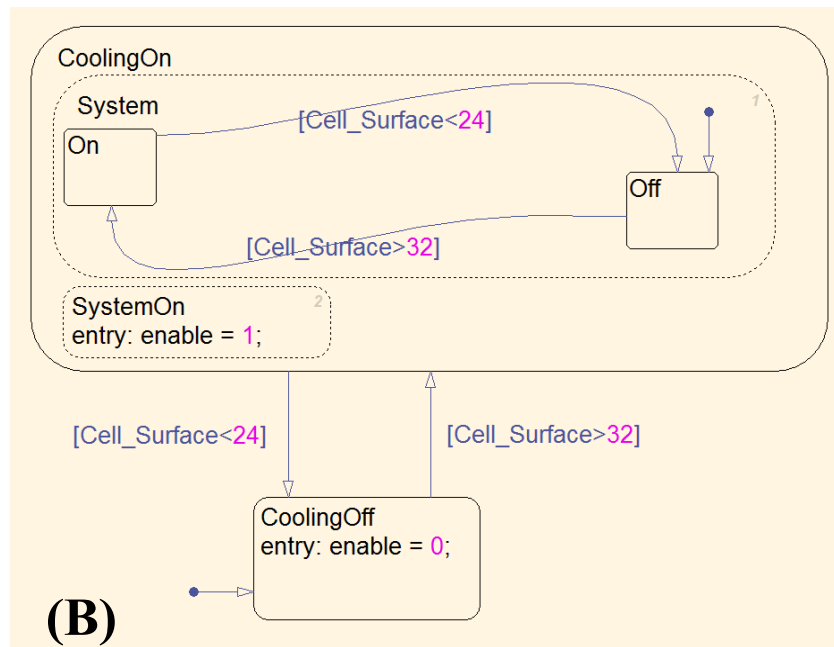
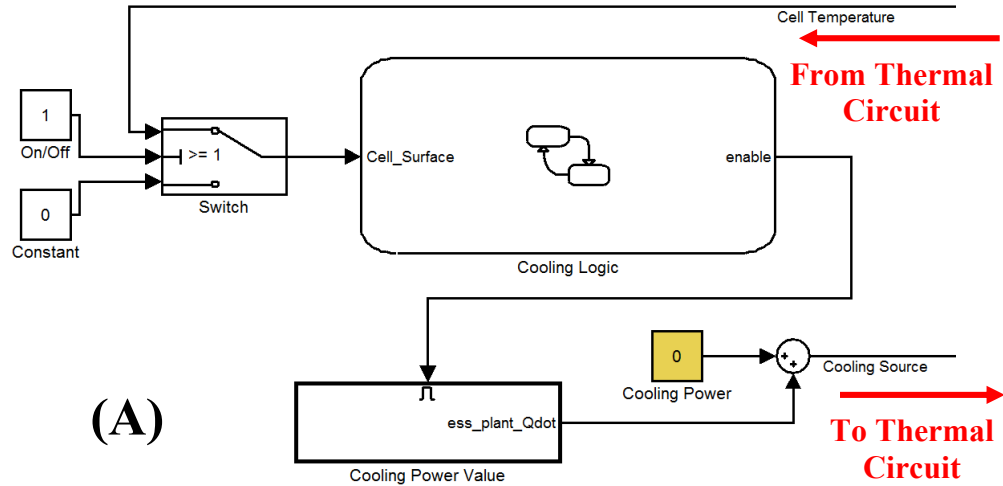


Figure 5.23 – Simulink cooling control strategy (A) and expanded Stateflow cooling logic (B)

5.6 Liquid Cooling Control Validation

To validate the liquid cooling system, data recorded from the vehicle is compared to the Simulink model with the Stateflow control logic developed. For the Stateflow logic to be considered valid, it must provide the same rate of cooling as seen in the vehicle over the same time period. A snapshot of the cooling system in operation during the road test was analyzed to determine the amount of cooling being applied to the system on a per cell

basis, referenced to the compressor power [91]. The cooling rate is used as the input to the current source (S_1). Measuring the voltage at the current source yields the inlet fluid temperature into the battery pack for the simulation model. Figure 5.24 shows the comparison between the vehicle and simulation inlet pack temperatures.

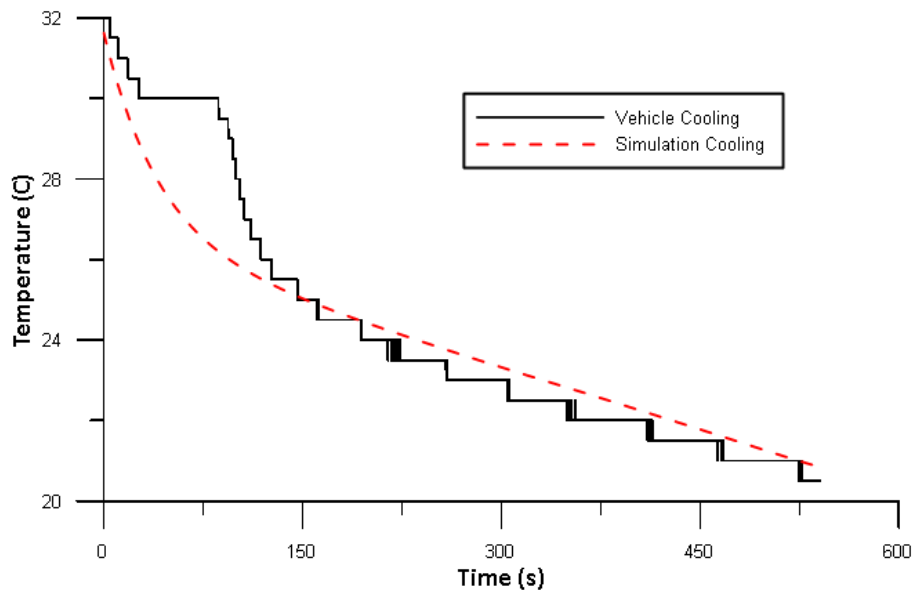


Figure 5.24 – Cooling control comparison of inlet fluid temperature

The cooling system becomes operational at 32°C and turns off when the cell temperature is approximately 24°C . The cell temperature never reaches the inlet fluid temperature, therefore the inlet temperature is around 20°C at the end of the cooling cycle. Initially, the compressor operates at around 1800 W which creates a 7°C drop in 150 seconds. As the compressor power decreases, the inlet temperature decreases almost linearly and settles to a cooling rate of $0.6^{\circ}\text{C}/\text{min}$. The vehicle cooling trace appears as a step function because the data output from the CANbus are in increments of 0.5°C whereas the simulation has a greater resolution to create a smoother curve. The simulation and experimental data are in agreement with the exception around 100 seconds. This is attributed to the operation of compressor and the vehicle cooling controller which are based on the internal vehicle sensors, valves and fluid pumps. Recreating the controller action from the production vehicle is difficult as the system does not operate exactly the same way every time the cooling system becomes active based on data acquired from the vehicle. It is evident that a transitory period exists between 0 to 120 seconds as the compressor powers up and

sufficient cold refrigerant becomes available at the thermostatic expansion valve for the evaporator and chiller loop to see heat absorption. This is coupled with the impact of a slug of hot fluid emptying from the battery pack which saturates the system at first. The system however does operate within a given window for a period of time with an inlet fluid temperature profile that is captured in the Stateflow logic. Therefore, the simulation's interpretation of the cooling system is considered adequate as it operates within the cooling temperature setpoints and takes approximately 600 seconds to cool the battery pack inlet fluid temperature from 32°C to 20°C.

5.7 Summary of Thermal Equivalent Circuit Development

To accurately analyze the BTMS, a thermal equivalent circuit was developed in PSPICE for real time simulations. Components in the battery pack were arranged into heat flow paths and grouped into different sections in the thermal circuit. Each resistor and capacitor within the circuit represents the temperature and heat flux on a per cell basis. The PSICE simulations are integrated in MATLAB/Simulink to combine the cooling system logic capturing the complete BTMS operation. The model developed was validated with laboratory experiments that showed minimal difference between the circuit model and experiments. The thermal equivalent circuit captures the combined dynamic effects of environmental factors such as engine heat wash, road radiation and ambient temperature which has not been previously investigated. The inputs in the PSPICE model for ambient and road temperatures are based on regional conditions which are outlined in the next chapter.

CHAPTER 6 - DEVELOPMENT OF ENVIRONMENTAL CONDITIONS

Incorporating environmental condition into the models developed requires environmental data to run simulation test cases. It allows the EREV to be simulated under real world conditions which may reveal unique heat flow characteristics of the battery pack.

6.1 Road Temperature Modeling

In the previous section, the thermal equivalent circuit development was explained. One of the sources in the circuit, the road temperature defined as S_5 , needs to be calculated given the ambient temperature. The construction industry utilize specific pavement software that computes the road surface temperature based on the ambient temperature, solar zenith angle and cloud coverage [92]. The equation used to calculate the surface temperature is shown below in Equation 6.1.

$$T_s = T_{air} + 24.5(\cos(Zn))^2 \cdot C \quad 6.1$$

Where:

T_s = Maximum predicted asphalt surface temperature in °C

T_{air} = Maximum air temperature in °C

Zn = Solar zenith angle of the sun

C = Cloud cover index

For the cloud cover index, the values are based on the air temperature where:

$C = 1.1$ if $T_{air} > 30^\circ\text{C}$

$C = 1.0$ if monthly mean air temperature $< T_{air}(\text{max}) < 30^\circ\text{C}$

$C = 0.25$ if $T_{air} < \text{monthly mean air temperature}$

The solar zenith angle of the sun can be calculated, however, solar data is available from astrological monitoring stations. The National Oceanic & Atmospheric Administration

(NOAA) is a division of the US Department of Commerce [93]. The NOAA has produced a solar position calculator which identifies a location by the longitude and latitude coordinates. The specific month, day, year and time are defined inputs. Based on the selected location and time, the cosine of the solar zenith angle is automatically calculated which corresponds to the value used for $\cos(Z_n)$ in Equation 6.1. Daily temperature profiles can be created which are useful for simulations longer than the proposed drive cycles. This allows the thermal equivalent circuit developed to simulate daily, weekly, or monthly travel data and provide a more robust analysis of the battery and thermal system outside of standardized testing.

6.2 Environmental and Initial Conditions

The Autonomie and thermal equivalent circuit models developed in the previous sections have outlined the full EREV simulation with the BTMS. These models allow for real time simulations and analysis of various driving and environmental conditions combined. However, these models are only as strong as the inputs selected. Previous analysis which have experimentally tested battery submodules, or simulations using CFD, select arbitrary initial conditions which may not be representative of what a vehicle actually experiences. Vehicles sold across the world are subject to various climates, driving, and parking conditions. Investigating the EREV design and the effectiveness of the BTMS, various regions in North America were selected based on environmental characteristics and the anticipated effects of the selected drive cycles to follow. Before the drive cycles can be simulated, the correct initial temperature conditions for all components (C_1 - C_{14}) in the battery pack need to be identified. A parked vehicle (outdoors) in the test region is simulated for a week to identify the day and time during which the battery is at the most critical point based on internal temperatures.

6.2.1 Environmental Test Regions

There are many locations in North America that could be selected as test regions. However, when considering the BTMS in it was decided to commence the analysis for locations reaching approximately 45°C, 35°C, and 20°C during the hottest recorded week

annually. This criteria covers a temperature range that is on the high, medium and normal end of suggested Li-Ion cell operation. The absolute maximum temperature isn't the sole criteria when selecting test regions, the change in temperature from day time highs to nightly lows can have a significant effect on internal pack temperatures. For this analysis, weather data from 2015 was selected with a 7:00 AM start and finish time for the selected week of highest recorded temperatures. Below, details of the selected test regions and key parameters with reference to where the data was procured from are given.

- Mesa, Arizona (AZMET [94])
 - August 12th – 19th, hottest recorded week
 - Peak temperature 45.2°C
 - Average weekly temperature of 37°C
 - 12°C daily change in temperature
- Toronto, Ontario (Environment Canada [95])
 - July 26th – August 2nd, hottest recorded week
 - Peak temperature 32.5°C
 - Average weekly temperature of 25.6°C
 - 8-12°C daily change in temperature
- San Francisco, California (NOAA [93])
 - August 12th – 19th, hottest recorded week
 - Peak temperature 21.3°C
 - Average weekly temperature of 16.8°C
 - 7.5°C daily change in temperature

The test week ambient data for Mesa, Arizona is presented in Figure 6.1. From the figure, the daily peak temperature can be seen increasing a few days before the peak and falling afterwards. The 12°C daily change in temperature indicates a significant temperature fluctuation which helps curb internal battery pack temperatures from reaching critical levels. With an average weekly temperature of 37°C, this region prompts the vehicle to be consistently at elevated temperatures which suits the analysis for a BTMS in a hot/desert environment.

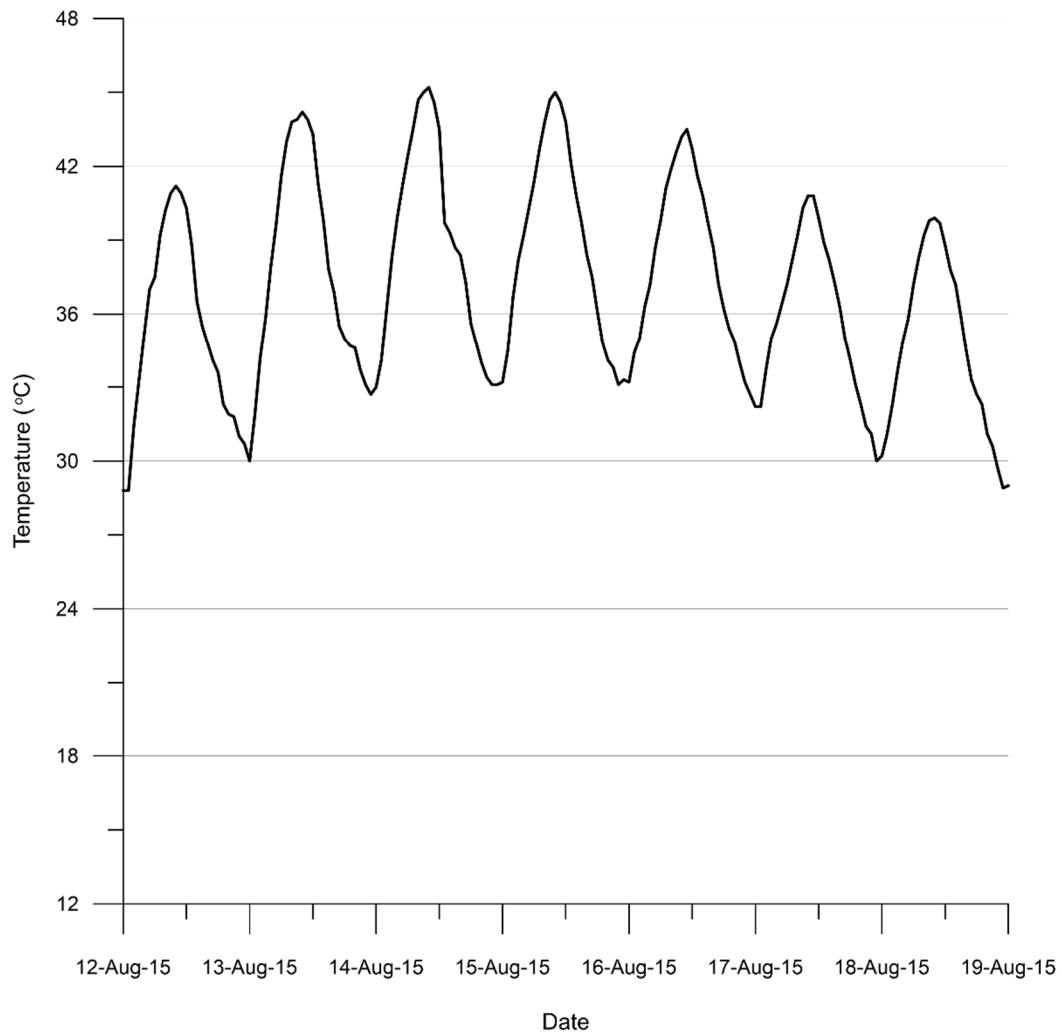


Figure 6.1 – Mesa, Arizona test week ambient data

Ambient data for Toronto, Ontario is shown in Figure 6.2. The overall temperature profile for the week has more fluctuations compared to the Mesa data. The daily peak temperatures vary leading up to the maximum temperature of 32.5°C. The change in daily temperature is not constant either when compared to Mesa. The average weekly temperature of 25.6°C indicates the battery might be at an average temperature range for Li-Ion cells. However, the varying weather data shows the unpredictability of daily events which a vehicle encounters. For the BTMS, the lower environmental temperature combined with the drive cycles to be simulated represent a vehicle driven during the summer months in the Great Lakes region.

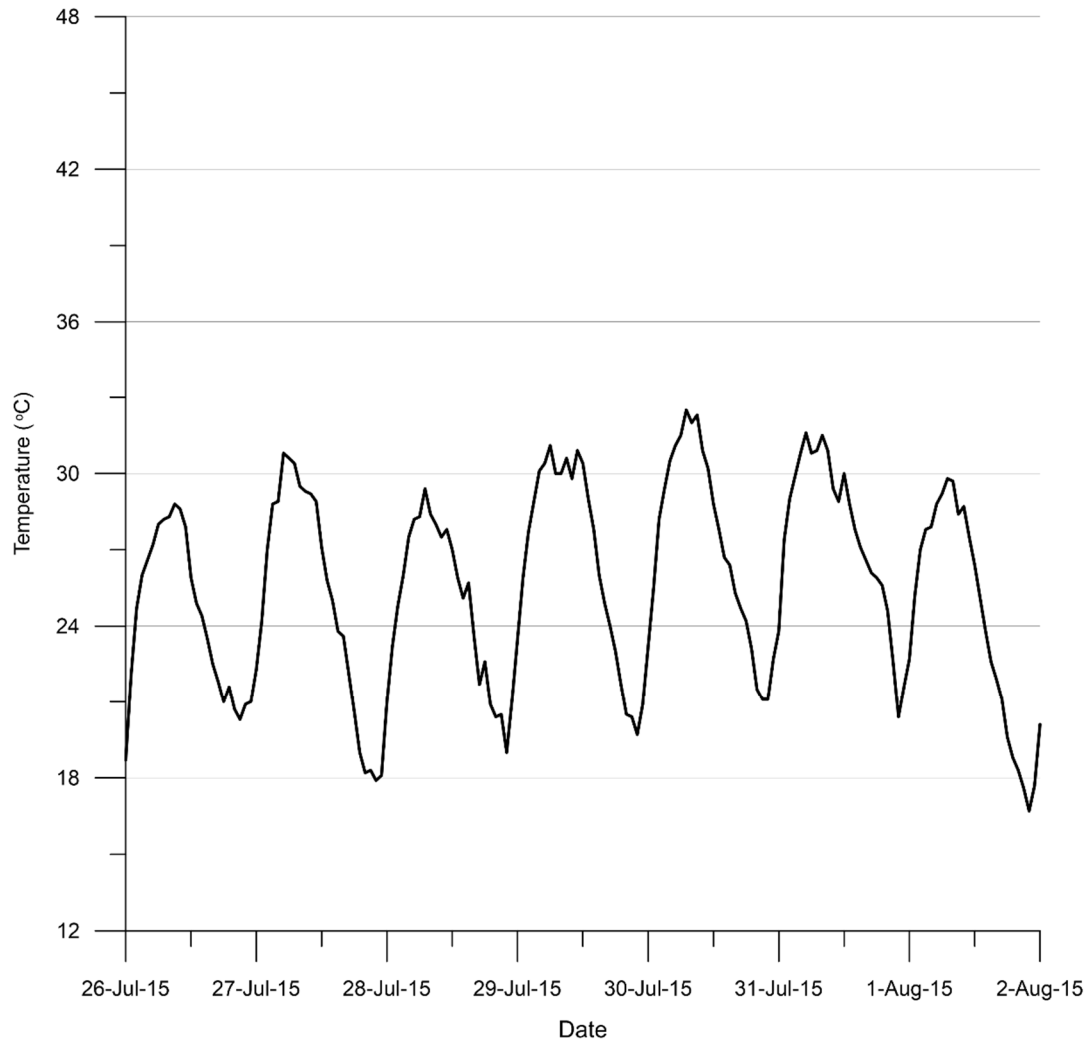


Figure 6.2 – Toronto, Ontario test week ambient data

Figure 6.3 depicts the test week weather data for San Francisco, California. From the figure one can see the seven day weather pattern is more uniform compared to the Mesa and Toronto regions. The daily peak temperatures and temperature swings are consistent at 21.3°C and 7.5°C respectively. The average weekly temperature of 16.8°C is substantially lower than the other regions but also the uniform daily temperatures have an impact on the battery pack and BTMS performance. San Francisco, as part of the San Francisco Bay Area region experiences this type of weather pattern due to the cool marine air. The annual weather data shows consistently small daily temperature fluctuation with the summer months peaking around 22°C. These represent ideal conditions for a HEV or EVs with large

battery packs as the mild weather implies the battery pack would not experience large fluctuations in temperature, especially if the vehicle was parked for long periods of time. Such conditions help increase the operational life of the battery.

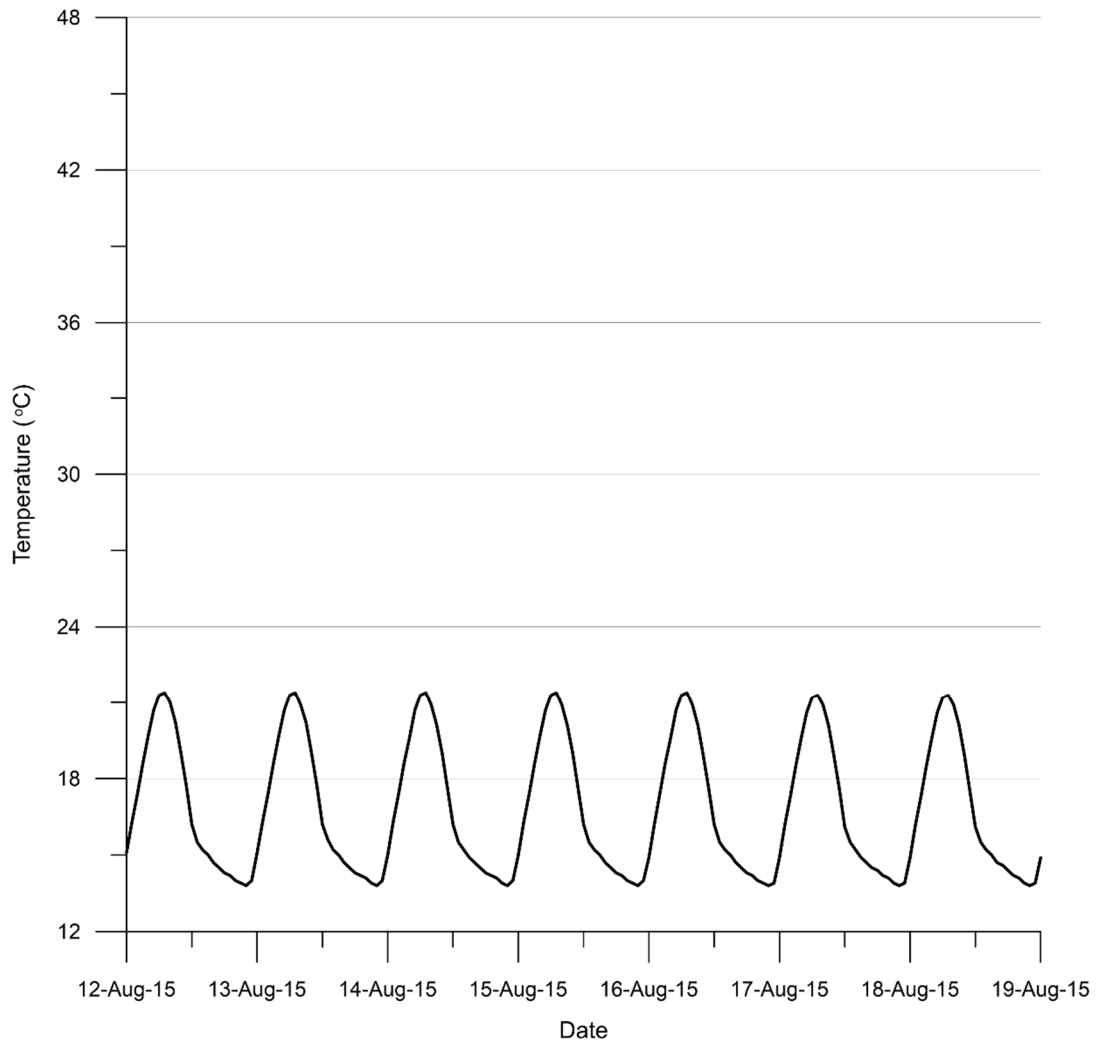


Figure 6.3 – San Francisco, California test week ambient data

In summary, the three regions selected and detailed above aim to analyze the EREV performance in hot, moderate, and mild regional temperature conditions in high population urban areas where HEVs and EVs provide the most benefit. The test week weather data presented in this section is utilized in the following section where simulation initial conditions are determined.

6.2.2 Determination of Initial Conditions

Selecting initial conditions in simulations is crucial to producing quality results. Initial conditions become magnified when trying to simulate a real world system which has multiple distributed components where there is no temperature uniformity. The thermal mass of each component as well as the proximity to heat sources determines the change in temperature. The EREV battery pack contains a collection of internal hardware components used to secure the cells in place as well as integrating the liquid cooling system. A single starting temperature for all components within the system cannot be used when simulating the selected drive cycles. An investigation is warranted using the ambient data presented in the previous section to help determine how temperature propagates through the pack components from diurnal cycles alone. From this basis, the temperature behaviour on the selected test day for driving in the three geographical regions can be identified, thus revealing the appropriate initial conditions for drive cycle simulations.

6.2.2.1 Simulation Initial Conditions

It is a multistep process to identify the initial conditions which starts with picking the identified test week in each of the selected regions. The EREV is taken to be parked outside for one week. Since no other systems are operational, the ambient temperature data is used as inputs for all voltage sources in the simplified circuit model in PSPICE (Figure 5.18). There is also no road radiation simulated as the shadow underneath the vehicle when parked creates ambient conditions. The average wind speed is taken into account from the collected weather data. However, only the ambient conditions are known and the battery components need a starting temperature before beginning the simulation. To select the appropriate starting component temperatures, two weeks of static simulation were used as identified below:

- Test Week – The week where the highest annual recorded temperature occurs (outlined in Section 6.2.1)
- Week Prior – The week prior to the selected test week in Section 6.2.1

For the week prior to the test week simulations, the ambient data is compiled and the starting conditions for all components begin as the average ambient. This lead time provides the system a sufficient period to balance its dynamic internal temperature distribution. At the end of the week prior to simulation, the temperatures of the individual components are used as the initial conditions for the start of the test week. This ensures the week long simulation starts with the correct values. The process is illustrated by the example in Figure 6.4 where the cell temperature is compared using different starting initial conditions for the Toronto region during the test week. The three cases shown in Figure 6.4 use (1) the week prior data as the initial condition, (2) averaging the cell temperature over the week prior simulations to start at 23.4°C, (3) arbitrarily selecting 25°C as an initial condition.

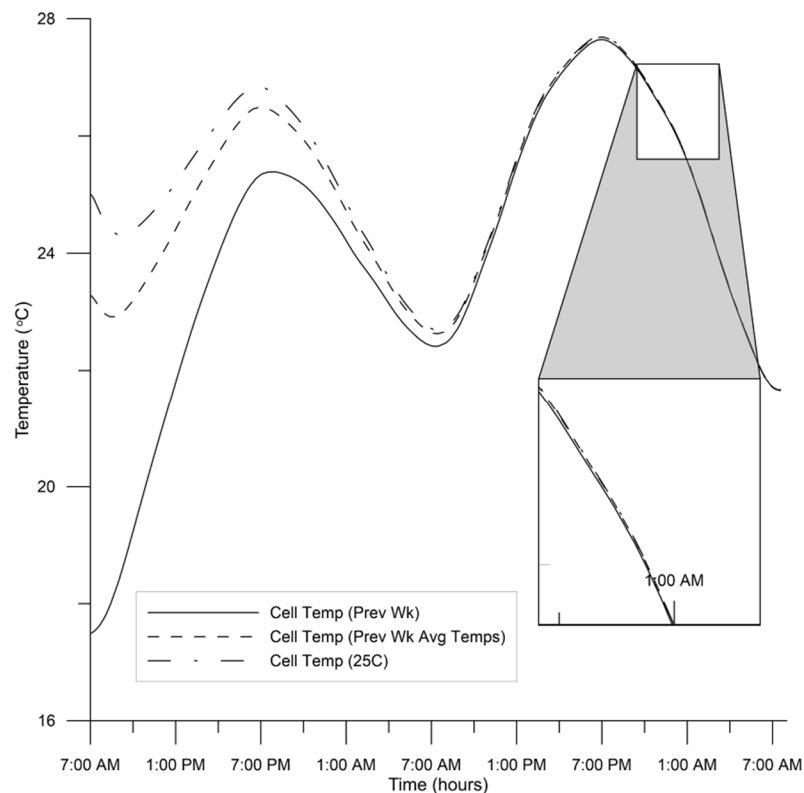


Figure 6.4 – Cell initial condition test cases for Toronto test week

The convergence time is about 30 hours. Using the week prior initial condition ensures the test week simulations start with balanced battery component temperatures. The time scale in Figure 6.4 is in hours, but drive cycle simulations are shorter and on the scale of minutes.

This highlights the importance of understanding key elements, especially initial conditions, when creating a simulation for a real world system.

With the process outlined for setting the initial temperature conditions for each component within the battery during the test week, a seven day static test can be conducted for all regions to examine the temperature distribution experienced for the battery components. Figure 6.5 to Figure 6.7 depict the full component analysis of Mesa, Toronto and San Francisco respectively. There are eleven components shown on these busy graphs, which will be magnified and sorted in the next section. Observing the figures, it becomes apparent there is a distinct time delay between the daily peak ambient temperature and the internal battery component temperatures. This delay phenomena outlines the importance of including all internal battery hardware when attempting to design or analyze a BTMS. The component's thermal mass are modeled as capacitors in the PSPICE model which build up charge (ie: change in temperature) at different rates based on the values of the capacitors and their location within the circuit. For the static case, the bulkhead, shield, baseplate and cover are the components closest to the ambient sources. Therefore, these components will react to the changes in temperature quicker than more interior components. The cells have the most thermal mass within the pack, reflected by the largest capacitor value in the thermal equivalent circuit. The figures show that the cells reach maximum temperature many hours after the peak ambient temperature. This behaviour has not been previously discussed or published in regards to BTMS design as it is a critical observational point. The model developed is analyzing a battery pack placed under a vehicle. However, a similar type of analysis might reveal different phenomena for HEVs and EVs with battery packs under the hood, in the cabin, or in the trunk area of the vehicle. This constitutes the benefit of real time full vehicle modeling.

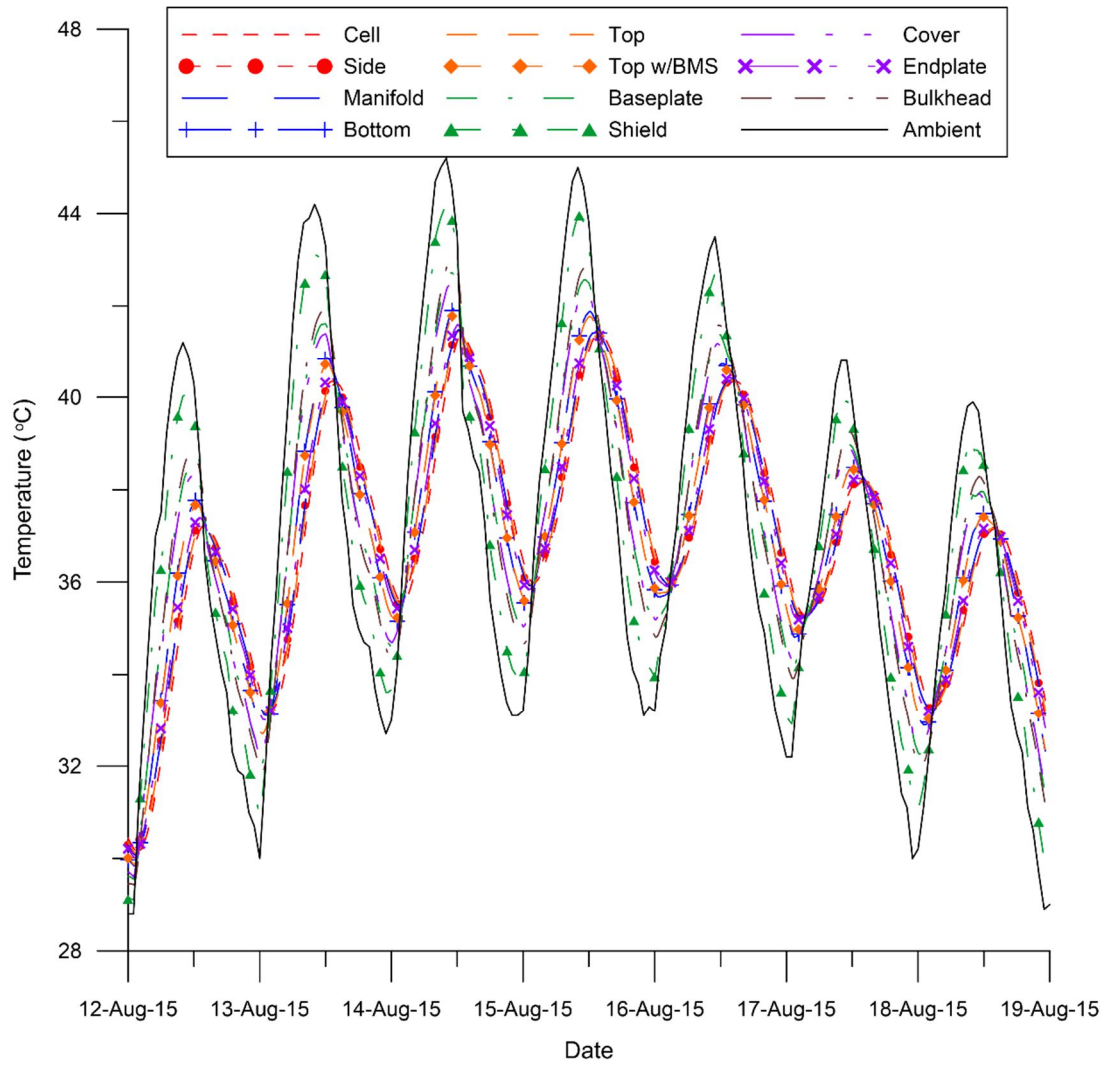


Figure 6.5 – Mesa test week component analysis

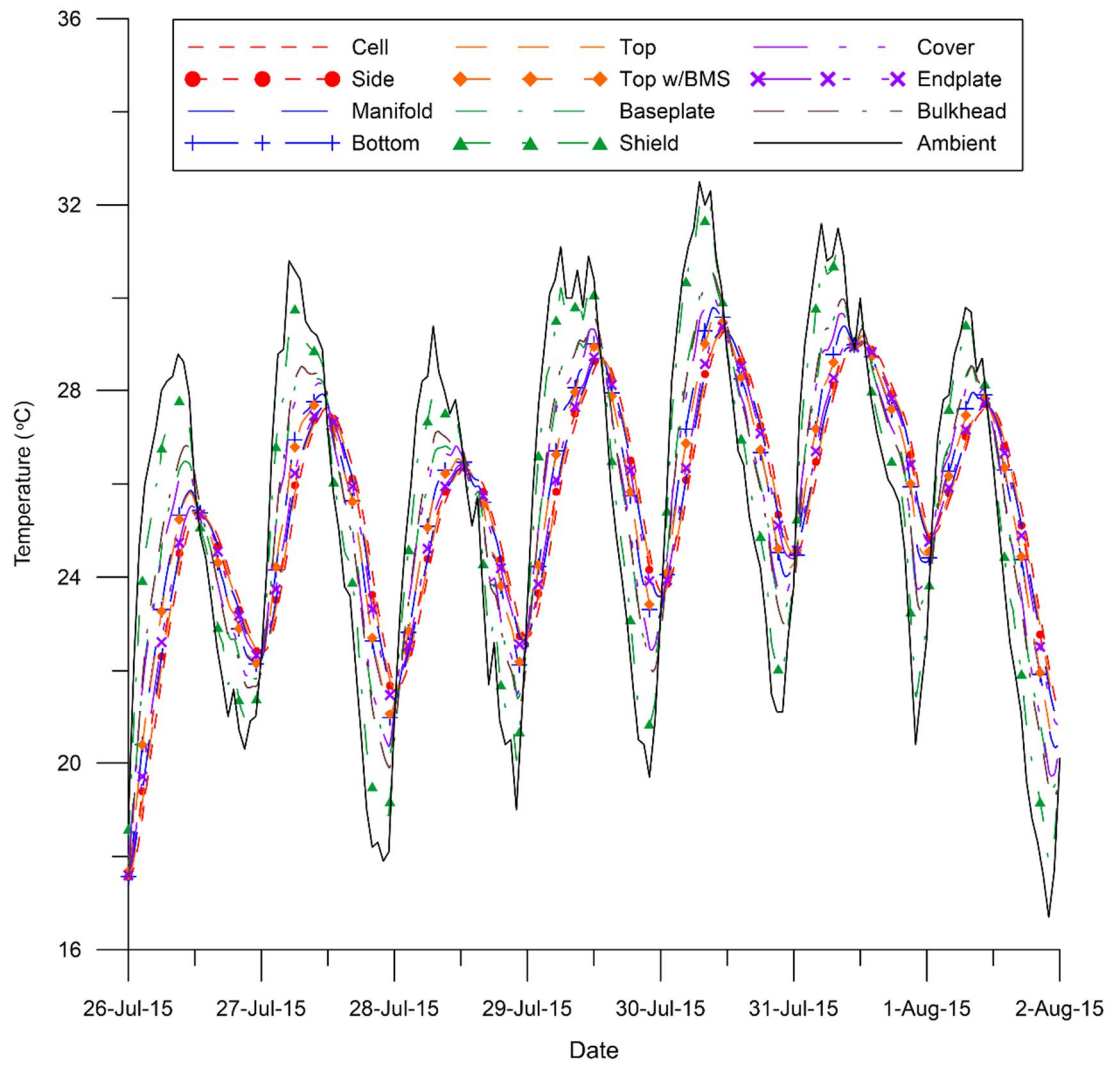


Figure 6.6 – Toronto test week component analysis

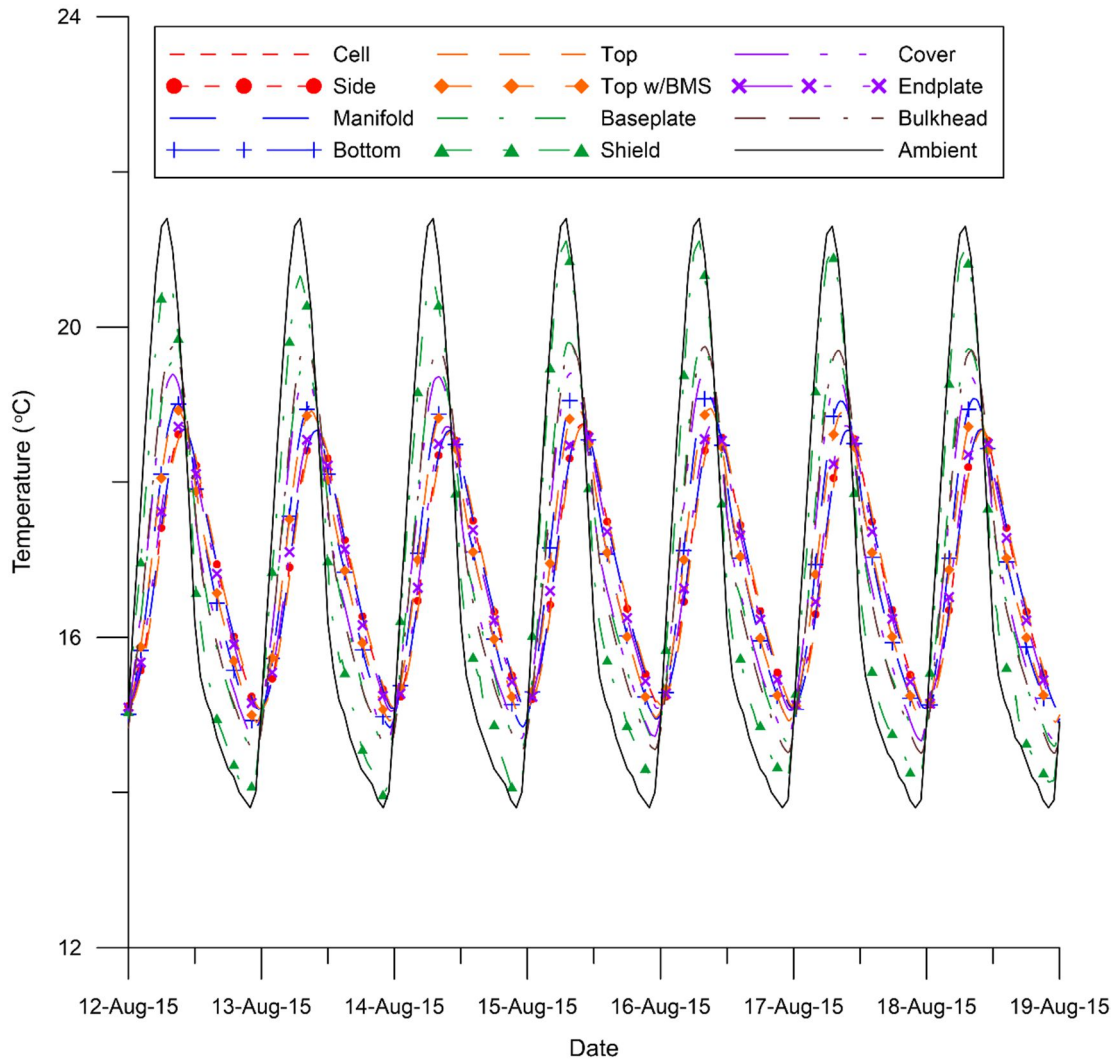


Figure 6.7 – San Francisco test week component analysis

6.2.3 Identifying Initial Conditions for Drive Cycle Simulations

In the previous section, the process for selecting initial conditions for the test week was outlined. This ensures the system model and respective components are outputting the correct data from the PSPICE simulations. To simulate drive cycles, the hottest day in the test week will be selected for each region. However, a specific time of day needs to be selected which will set the initial condition for all components. Figure 6.8 shows the test day for Mesa, Arizona which is August 14th 2015. From Figure 6.8 the temperature profile for each component can be seen more clearly as well as the time delay associated with each component reaching its maximum temperature. The cell temperature, having the highest

thermal mass, increases the slowest. This delays their maximum temperature to hours after the day time peak ambient temperature, better shown in the magnification.

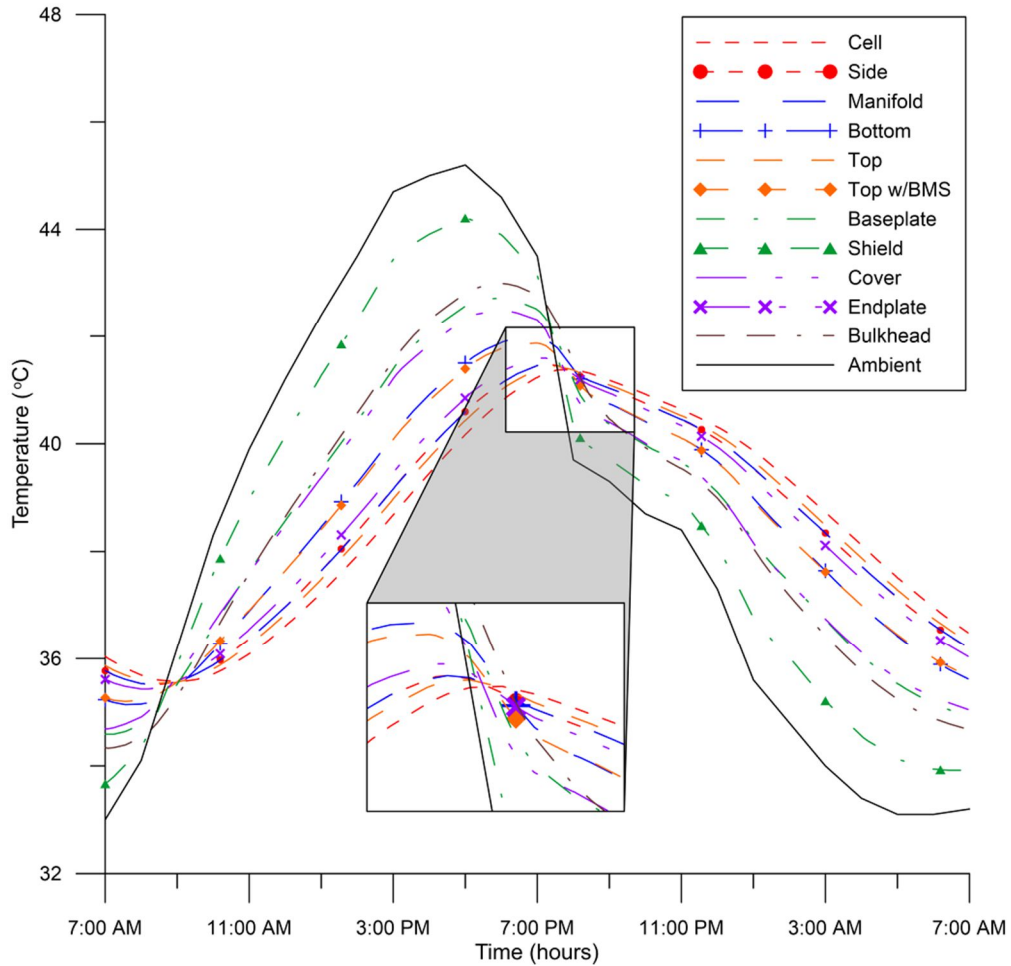


Figure 6.8 – Mesa test day component analysis

There are three notable points on the graph where by the components are experiencing unique conditions. The first is at approximately 9:00 AM, where the majority of components are approximately the same (low) temperature. This is also the time when the ambient temperature, and by extension the road temperature, is increasing. This time of day could represent someone leaving for work. The second point is at peak ambient temperature. The road temperature will also be the hottest which would create the most heat flow into the pack through the lower shield and baseplate when driving. This also corresponds to the largest temperature difference between components. The third point is

around 7:00 PM when the cell temperature is at its maximum and the majority of components are again at the same temperature (seen in the magnification). Here the ambient temperature is falling, and by extension, the road temperature as well. This time of day could represent someone going out for the evening or starting a night shift for work. The Toronto and San Francisco regions on their respective test days exhibit the same trends seen in the Mesa test day data with a slight variance in the time when these key events occur. Figure 6.9 shows the Toronto test day which is July 30th 2015 from Figure 6.6. Figure 6.10 shows the San Francisco test day data which is August 15th, 2015 from Figure 6.7.

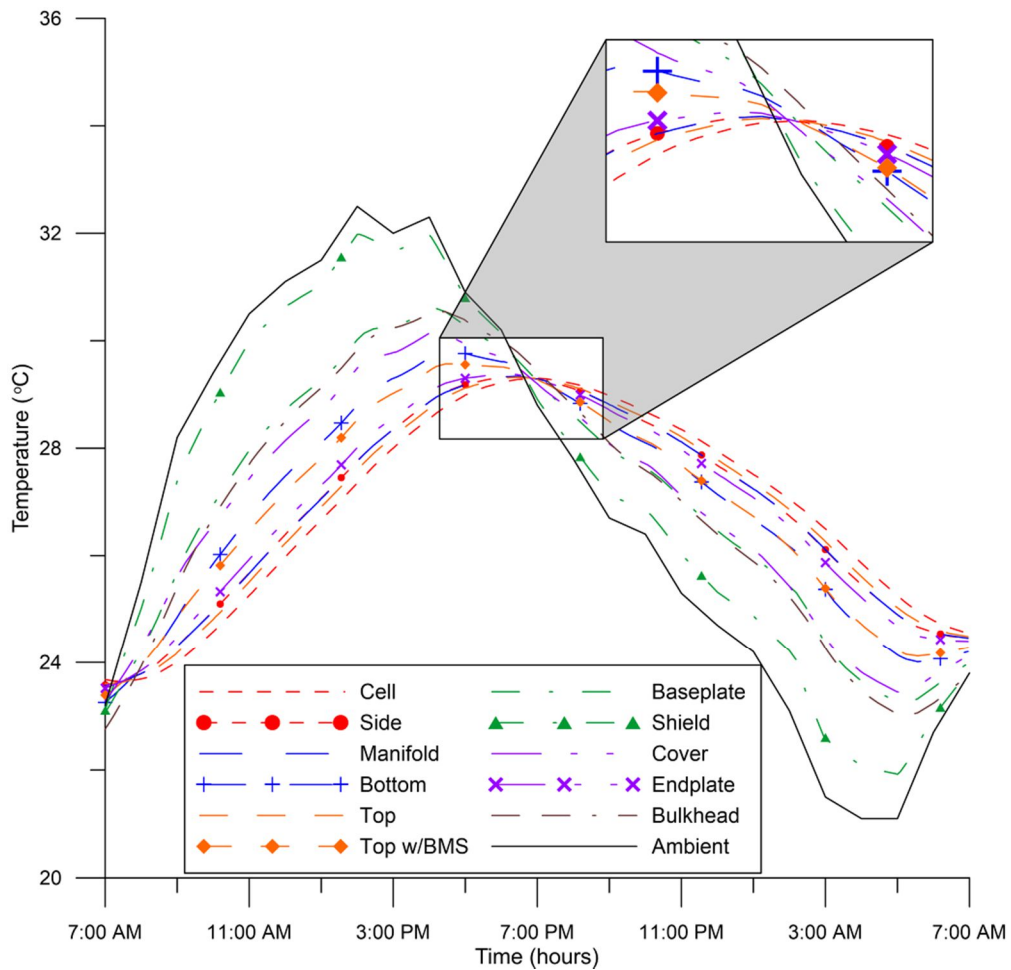


Figure 6.9 – Toronto test day component analysis

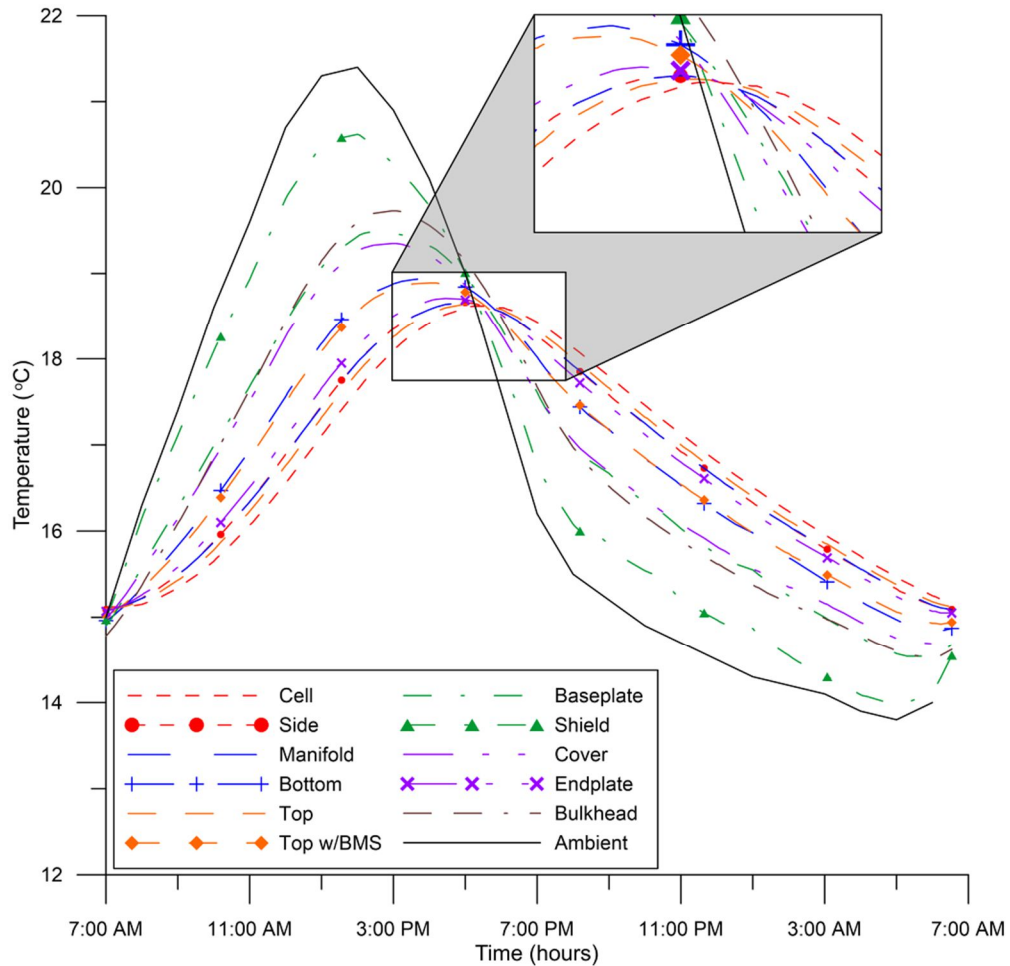


Figure 6.10 – San Francisco test day component analysis

To set which time of day that represents the worst case scenario for the cell, drive cycles are simulated at the identified times for the key events. The PSPICE model utilizes the component temperatures at such selected times as the initial conditions for the system. The cooling system will be set as not active in these simulations so the overall cell temperature rise throughout the drive cycle can be analyzed. Figure 6.11 shows four consecutive US06 cycle simulations on the Toronto test day at different run times. The appropriate road temperature was also calculated for different times of day in each simulations. The output datasets are parallel to each other with the cell temperature reaching a maximum of 44°C at the end of the 6:50 PM simulation. When examining the UDDS and LA92 cycles, the same trend is present, where the datasets run parallel and the 6:50 PM simulation produces the maximum cell temperature. When the drive cycle

simulations are expanded to the Mesa and San Francisco regions, similarly the evening time produces the worst case scenario for the battery pack.

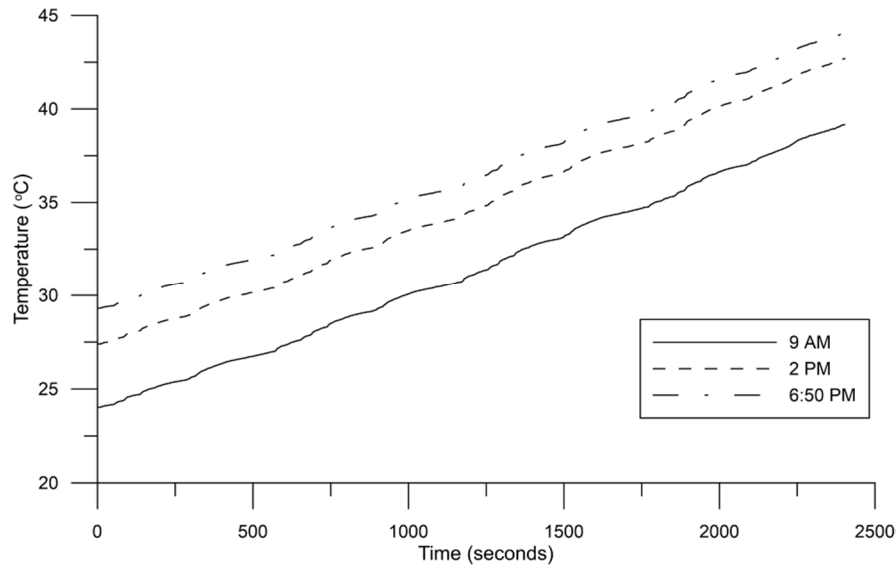


Figure 6.11 – Toronto test day US06 cell temperature comparisons

This indicates the drive cycle simulations in the regions should be conducted in the evening corresponding to when the cell temperatures are at their maximum. It also reveals the peak ambient condition coupled with the hottest road temperature does not constitute the worst case for temperatures during the drive cycles. The thermal mass of the cells and the resistance network causes the maximum temperature to be reached later during the day and this needs to be accounted for when analyzing a BTMS. Therefore, the drive cycle simulations and analysis presented in Chapter 6 will employ the initial conditions at the evening time, when the cell temperature is at its maximum in the Mesa, Toronto, and San Francisco regions.

6.2.4 Ambient and Road Surface Temperatures

The following figures show the difference in ambient temperature to the road surface temperature for the selected test day in each region. The worst case scenario of the test days was selected based on when the cells were at their highest temperature. However, it is important to note other critical times of day and the effect on the battery pack. Figure

6.12 shows the ambient and road surface temperatures for the Mesa test day. Due to the thermal lag, 8:00 PM was the selected time and the figure shows the road temperature is the same as the ambient. Conversely, the day time peak road surface temperature is 65°C, a delta of 22°C between the ambient and road surface. Figure 6.13 and Figure 6.14 depicts the ambient and road surface temperatures for the Toronto and San Francisco test days respectively.

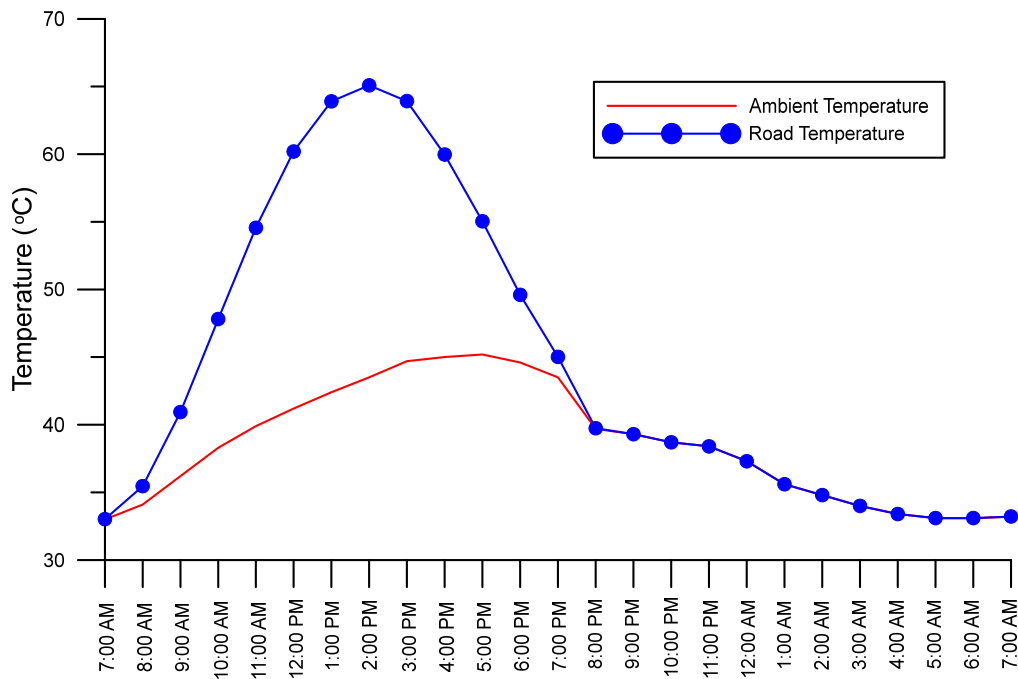


Figure 6.12 – Mesa test day ambient and road temperatures

Both Mesa and San Francisco are at lower latitudes than Toronto which attributes to the road temperature equaling the ambient at 8:00 PM. The solar zenith angle is registered as 0° as the sun has started to or already set in those two regions. Since Toronto is further north, the road surface temperature is a bit higher than ambient at 8:00 PM as a solar zenith angle was recorded but the sun is beginning to set. All the figures show at peak solar angle, a large delta exists between the ambient and road surface temperatures. While the battery pack is not at its worst when parked in these conditions, driving at the peak solar angle can affect the heat flowing into the battery pack from hot asphalt.

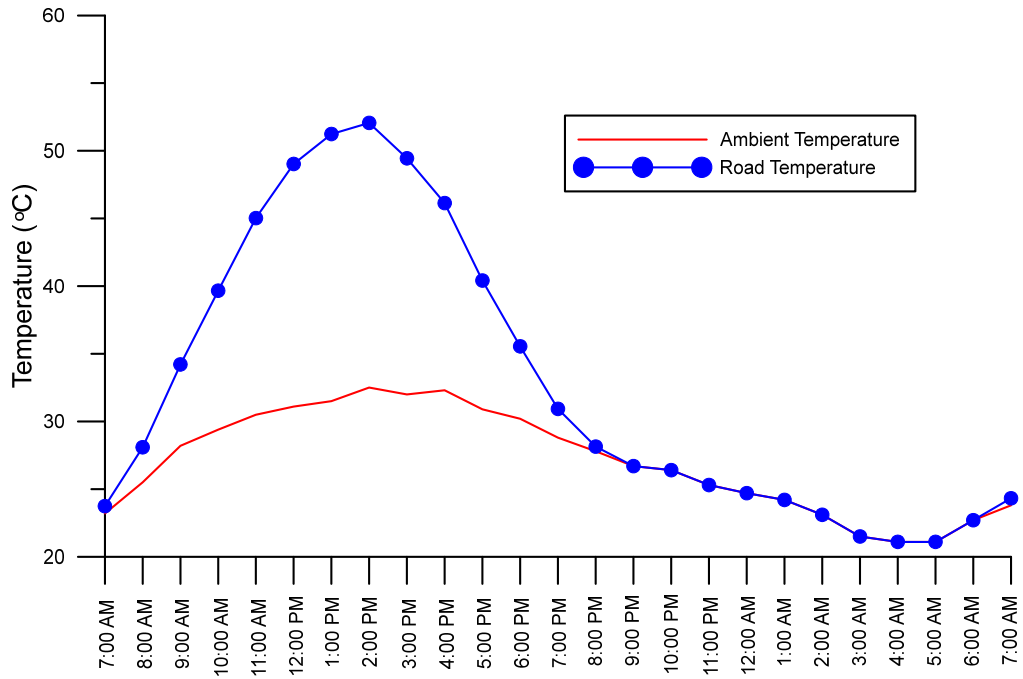


Figure 6.13 – Toronto test day ambient and road temperatures

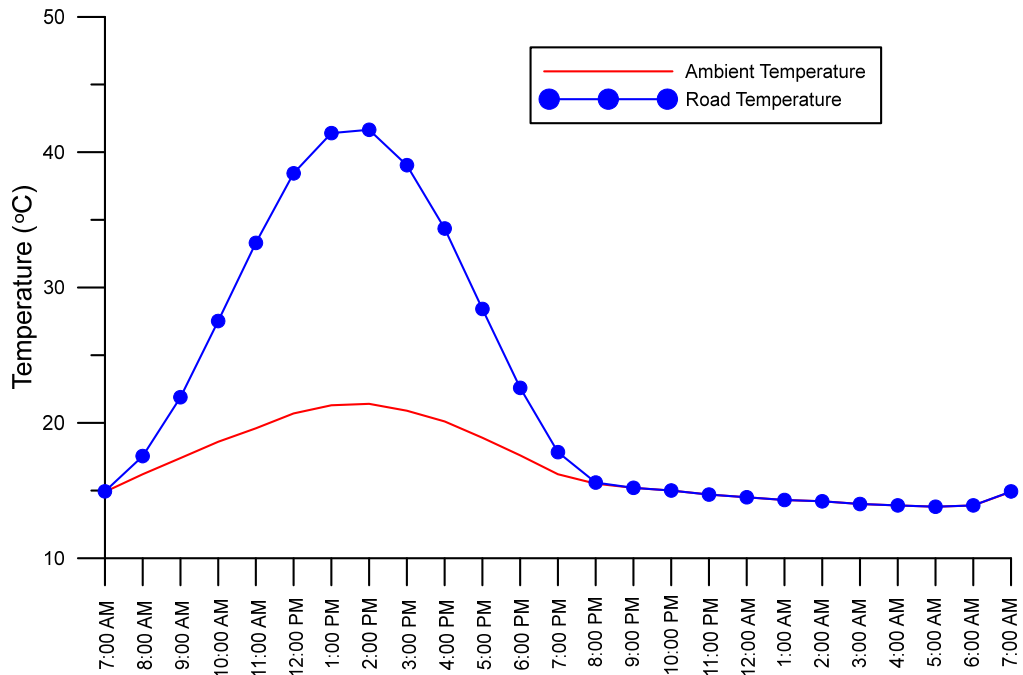


Figure 6.14 – San Francisco test day ambient and road temperatures

6.3 Summary of Environmental Conditions

A parked vehicle is simulated for a week in each region using the appropriate initial conditions for each component of the battery pack assembly. The simulations revealed incorrect initial conditions took 30 hours to converge towards the actual temperature distribution. From the test week explored, the proposed test day was selected in which the drive cycle would be simulated. The target was the day with the peak ambient temperatures during the test week. The simulations revealed the temperature distribution between the battery pack components and highlighted the importance of including all internal hardware and environmental conditions when analyzing a BTMS. On the test day, three points of interest were observed. The component temperatures were well grouped together in the morning and evening as a result of the heat flux reversal that occurs, with the evening showing the cell temperatures at their daily maximum. There was also a great difference in component temperatures while the ambient temperature was at its peak. The component temperatures at these three specific times of day were used as initial conditions to simulate drive cycle initiations. Those simulations helped identify that the battery would be at its worst exposure if simulations were conducted in the evening just as the cell temperature was reaching its maximum. The peak solar angle and temperature delta between the ambient and road surface also show the importance of capturing the effects of higher road surface radiation on the battery pack.

With the completed vehicle model running in Autonomie, a cooling system model in Simulink, and the thermal equivalent circuit in PSPICE, the production EREV was simulated as a whole. The next chapter analyzes the BTMS operation throughout various drive cycles and environmental regional exposures.

CHAPTER 7 - FULL VEHICLE SIMULATION RESULTS

The Autonomie model and thermal equivalent circuit was developed in the previous chapter. This section will investigate the effects of the US06, UDDS, and LA92 on the battery pack in three different test regions. The heat flow through the various components will also be examined to help understand how the heat propagates into and out of the pack. Under the different test conditions, the efficiency of the cooling system can be evaluated to identify if the system is under, over, or adequately designed. The effects of the ICE turning on during CS mode will be discussed due to the placement of the engine in front the battery pack. A workday and weeklong simulation in Mesa is explored to determine the benefit of a low power quiescent cooling strategy. Battery aging is discussed in relation to prolonged high temperature exposure. The model developed allows for system modifications which aid in the investigation of various scenarios and possible cost effective improvements to the pack design. Based on the results generated, the addition of extra insulation under the baseplate and around the top cover is investigated to determine if there are evident benefits for the pack. Finally, the vehicle is simulated in colder weather to examine these effects on the cell and related battery components.

7.1 Model Validations

The Autonomie model was validated against data from INL in the previous chapters. Recorded vehicle test data was used to further verify the Autonomie model as well as the cooling control logic developed in Simulink. The thermal equivalent circuit was also validated with laboratory experimental data.

7.1.1 Autonomie Validation Using Vehicle Test Data

To verify the compiled Autonomie model, vehicle data recorded from the vehicle's CANbus was compared to model generated results. The vehicle's pack voltage, current, SOC and speed were recorded while being driven in the Greater Toronto Area in Ontario, Canada with a mix of city, highway and rural driving. For each regional drive cycle, the appropriate grade profile was created using online resources which map the grade of the

Google Map trace. This is an important part of validation as the change in grade strongly affects the outputs from Autonomie. Without the grade profile, the voltage, SOC and current would have a high percentage of error when compared to the experimental results. Air conditioning usage was also recorded which represents the electrical accessory load in Autonomie. The first test involved rural secondary roads with some city driving towards the end of the cycle, with the vehicle in charge depleting mode for the entire cycle. Figure 7.1 shows the pack voltage for Test 1. The Autonomie model follows the experimental data well. There is a maximum of 8 V difference. Figure 7.2 gives a SOC comparison between the simulation and experimental results indicating a 1% SOC difference. In comparing the current levels between the simulation and vehicle recordings, the average current difference over the entire cycle was calculated to be only 0.05 A.

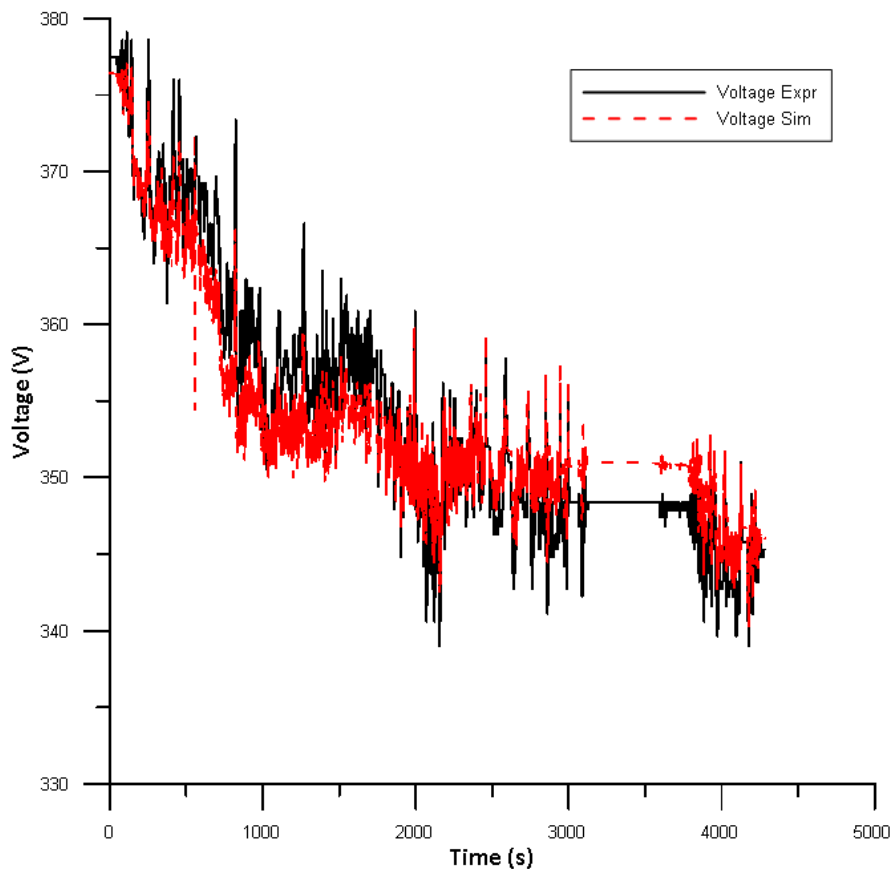


Figure 7.1 – Test 1 pack voltage

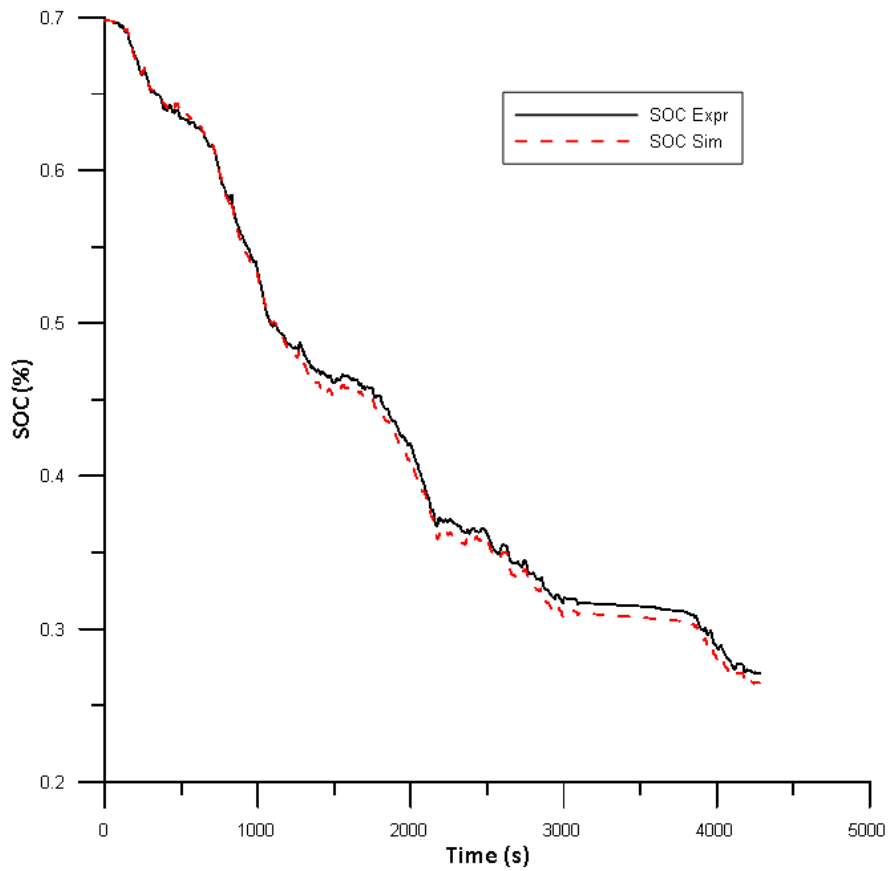


Figure 7.2 – Test 1 SOC

The second test was approximately 20 minutes long, consisting of aggressive city driving with the vehicle started in charge sustaining mode. Figure 7.3 shows the pack voltage comparison for Test 2, again about 8 V difference maximum. Figure 7.4 shows the SOC for Test 2 had a maximum of 5.5% error around the 600 second mark. It should be noted the SOC controller model block in the vehicle is complex and cannot be completely replicated in Autonomie in its current incarnation. However, the controller present in Autonomie is still capable of producing realistic results. The average percent error during the rest of the cycle is approximately 2.5%. The average current difference was calculated to be 0.18 A.

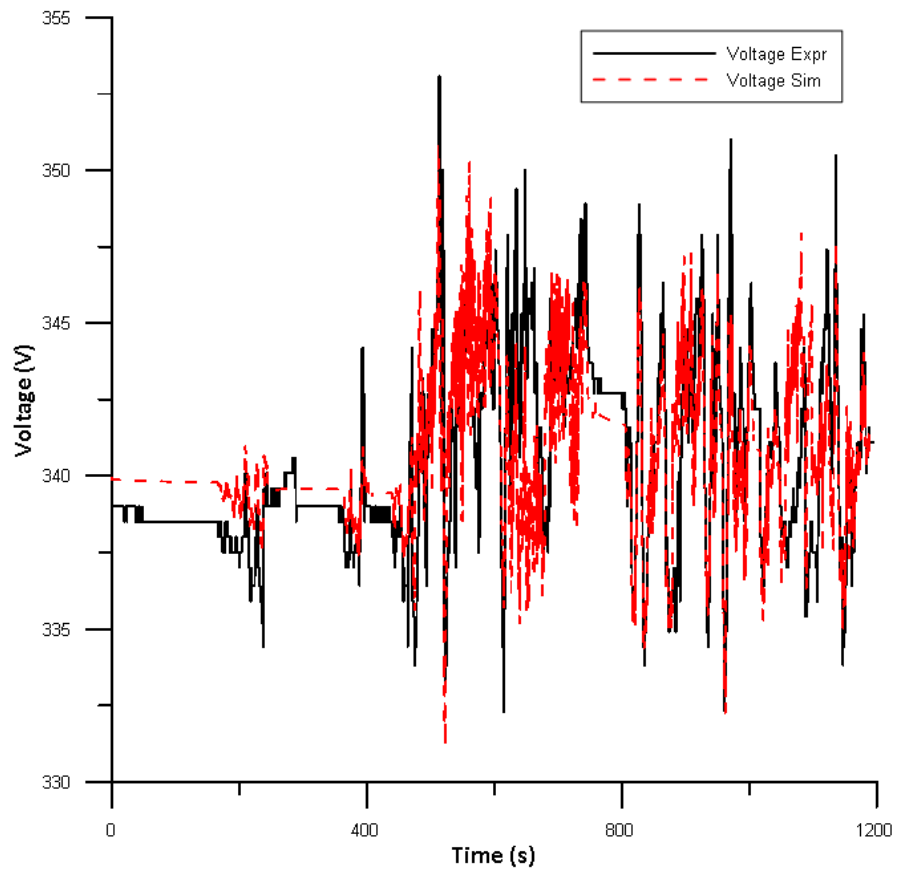


Figure 7.3 – Test 2 pack voltage

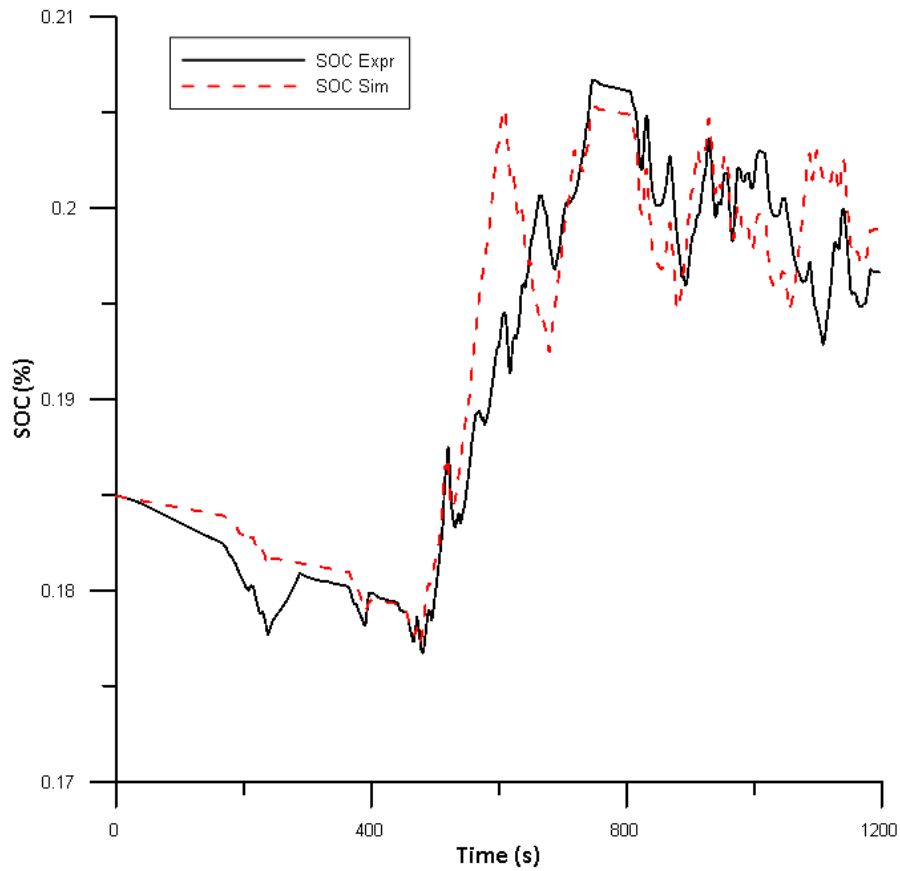


Figure 7.4 – Test 2 SOC

The 3rd test was approximately 75 minutes driving within the city in charge depleting mode, mainly in subdivisions which had frequent start and stops. Figure 7.5 and Figure 7.6 shows the pack voltage and SOC comparisons. Both the voltage and SOC simulations appear to deviate from the experimental results about half way through the cycle. This is possibly due to a slight error in the vehicle data log for mapping out the travel route which was done manually. However, the results are still with reason showing a 2.5% and 4% error on the pack voltage and SOC respectively. For the SOC, the 4% error is equal to approximately a 2% SOC difference in absolute terms between the simulation and experiment. The average current difference here was calculated to be approximately 0.56 A.

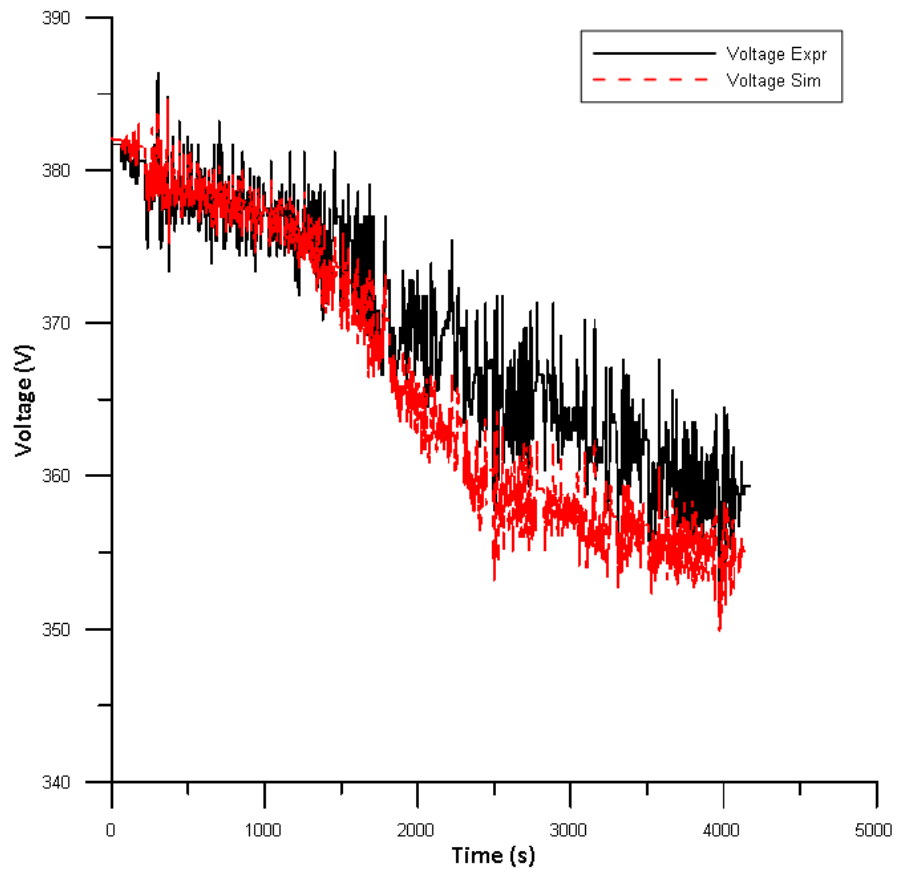


Figure 7.5 – Test 3 pack voltage

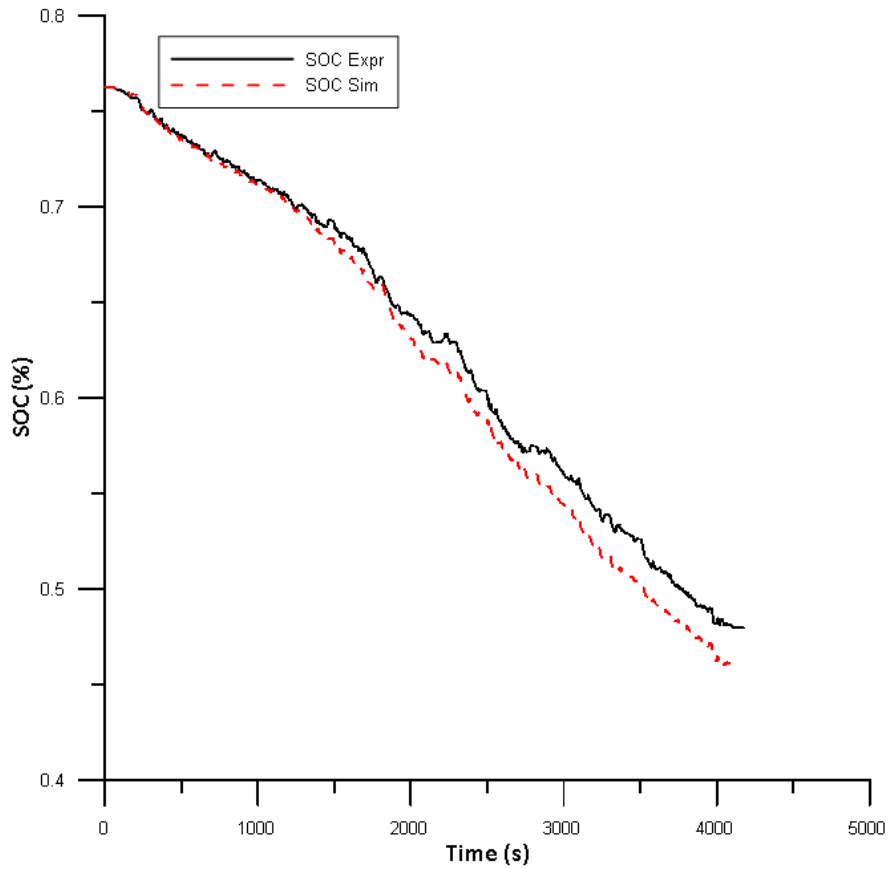


Figure 7.6 – Test 3 SOC

For the standardized EPA drive cycles examined, Table 7.1 summarizes the trace errors. As outlined by the EPA, a vehicle should not miss the drive cycle trace by 2 mph for more than 2% of the time [82]. There are deviation allowances outlined by the EPA, so if a simulation shows 0% missed trace, it does not necessarily mean that the simulation followed the drive cycle perfectly, rather it confirms the simulation followed the trace within the acceptable error window. It should be noted the EPA cycles have no road gradient component.

Table 7.1 – Trace Errors for EPA Standardized Drive Cycles

Cycle	# of cycles	% Time Trace Missed by 2mph
US06 (HC)	4	0.2
US06 (FC)	4	0.2
UDDS (HC)	4	0
UDDS (FC)	4	0
LA92 (HC)	4	0.52
LA92 (FC)	4	0.52
FTP (FC)	2	0
FTP (FC)	2	0
HWFET (HC)	4	0
HWFET (FC)	4	0
SC03-AC (HC)	1	0
SC03-AC (FC)	1	0

The Autonomie model clearly shows the capability of the propulsion controller to reproduce results matching reasonably with the experimental drive cycles. The voltage and SOC percent errors are low and the current differences are under 1 A for all tests. The model is equally capable of simulating EPA standardized drive cycles within the defined error allowances. These results indicate the output data from the battery pack in the Autonomie model can be used as appropriate inputs into the thermal circuit for simulation of the battery pack.

7.2 Drive Cycle Effects on Cell Temperature

The effects of the drive cycles on the cell temperature in the three test regions are investigated in this section. Two vehicle battery states are examined, half charged (HC) and fully charged (FC). As detailed previously, the EREV takes 80% SOC of the cells as FC and 20% SOC activates CS mode. Given the 60% SOC variation window, HC simulations start at 50% cell SOC. The environmental conditions in each region are identical for HC and FC simulations. Therefore, any difference in the cell temperatures are due to the differences in internal heat generation between the two simulated vehicle states. For all test regions and cycles, the HC simulations reached the 32°C threshold temperatures faster than the FC simulations, which indicates more net internal heat generation when the cycle starts at half charged.

7.2.1 US06 Drive Cycles

Figure 7.7 shows the cell temperature profiles in the different test regions while driving through 4 consecutive US06 cycles. The transition from CD to CS mode is also indicated for the two vehicle cases. In Toronto, two cooling events are observed at around 500 and 2250 seconds. The first cooling event lasts approximately 1000 seconds (15 mins). The HC simulation reaches the 32°C threshold 216 seconds prior to the full charge start condition. Both the HC and FC simulations have a pull down rate of 2°C/min within the first 150 seconds of cooling (same time comparison as Figure 5.24).

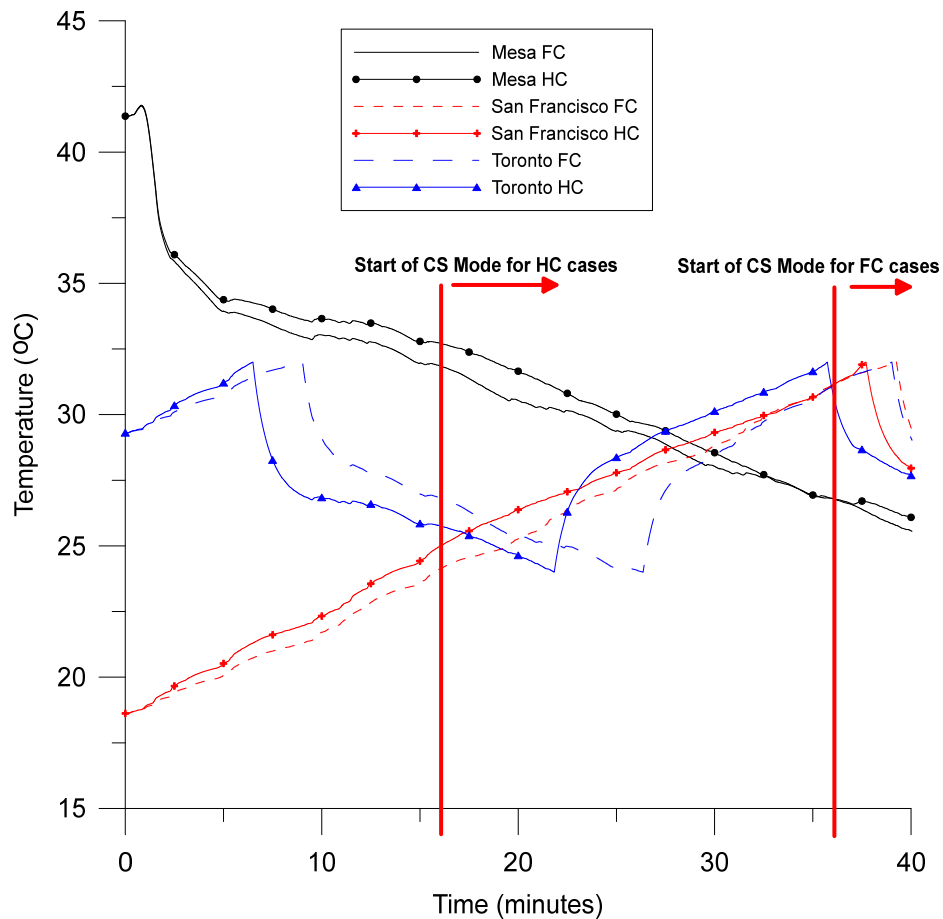


Figure 7.7 – US06 cell temperatures

Mesa simulations have a starting temperature of 41.4°C, well above the cooling system's 32°C threshold. Therefore, the drive cycle sequence begins with the cooling

system activated. The combination of the simulation starting above 40°C and the highest heat generation per cell of the all standardized drive cycles leads to the cooling system being active for the entire cycle. This type of cooling behaviour was also observed in the thermal chamber testing where the heat soaked vehicle saw the cells start at a maximum of 38°C and the duration of driving was slightly longer than the four cycle US06 simulations. At a constant vehicle road load of 10 kW the cell temperatures reached a minimum of 32°C with the cooling system operational throughout the cycle. For San Francisco cooling begins towards the end of the HC and FC simulations. The starting temperature of 18.6°C and low ambient conditions contributes to the 32°C threshold occurring towards the end of the cycle. It took 2200 seconds (37 mins) for the cells to increase 13.4°C in a near linear fashion.

The pack internal resistance for the HC and FC states being generated from the Autonomie simulations is shown in Figure 7.8 for 4 consecutive US06 cycles.

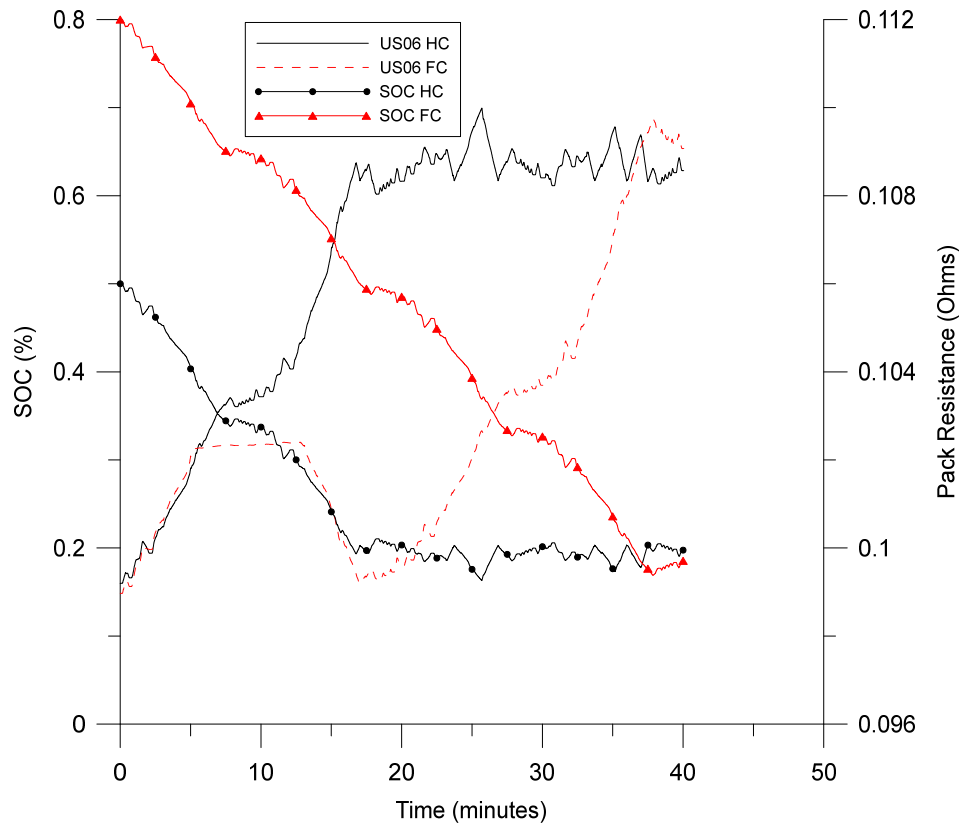


Figure 7.8 – Consecutive US06 cycle pack resistance and SOC

7.2.2 UDDS Drive Cycles

Cell temperatures for the UDDS simulations are shown in Figure 7.9. Only the half charge cases enter CS mode at 4334 seconds (72 mins) which is indicated on the figure. Since the heat generation rate is much lower, the cooling cycle onset is delayed for the Toronto case, and pull-down occurs within 10 minutes once triggered. The HC battery condition triggers the cooling event approximately 13 minutes sooner. Similar to the US06 cycle, the cooling pull down rate is $2^{\circ}\text{C}/\text{min}$ within the first 150 seconds

Mesa simulations show the cooling system is still capable of drawing down the cell temperature to 24°C which wasn't seen in the US06 simulations. However, it takes 1258 seconds (21 mins) to draw the temperature down to 24°C which is twice as long as a normal cooling event. The HC and FC states both trigger another cooling event towards the end of the cycle with approximately 543 seconds (9 mins) offset in the thresholds.

San Francisco saw no cooling events occur as the overall battery temperature rise was only 5.1°C for the HC state and 3.4°C for FC. The final temperature difference between the end states is 1.6°C . Figure 7.10 shows the resistance and SOC generated by Autonomie for the consecutive UDDS cycles.

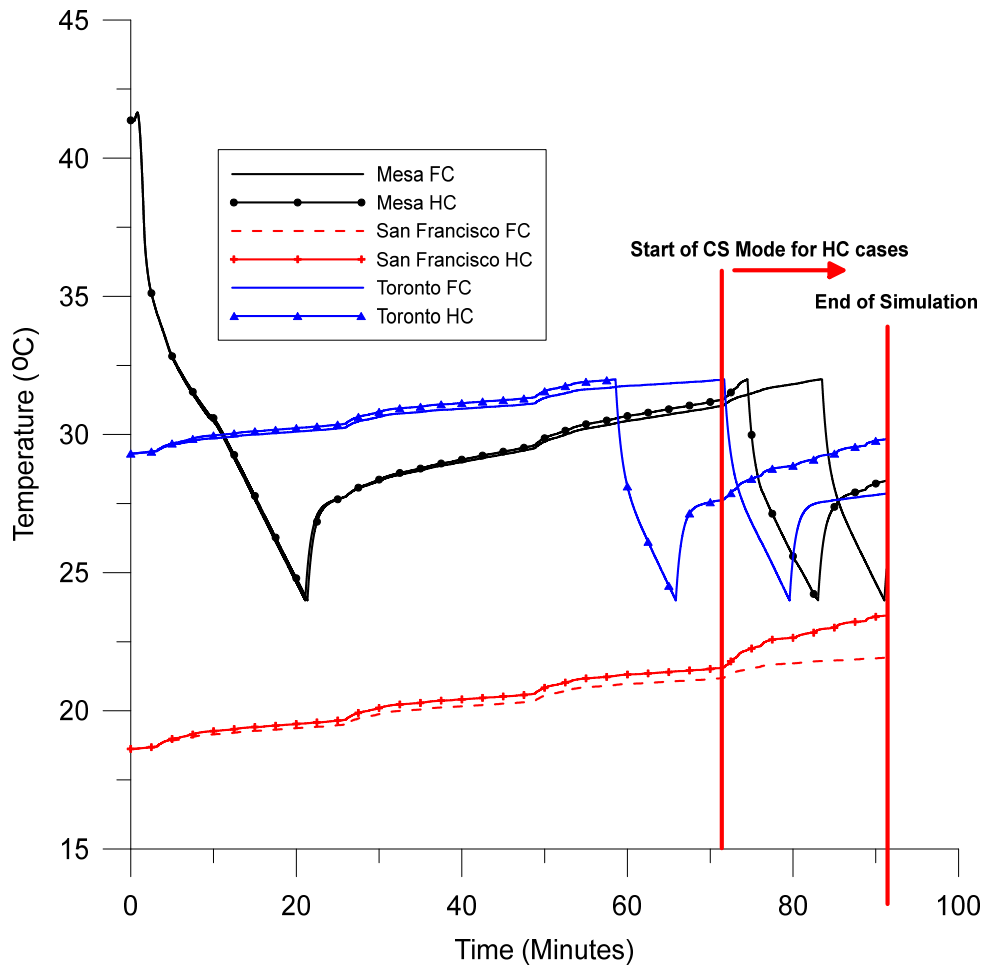


Figure 7.9 – UDDS cell temperatures

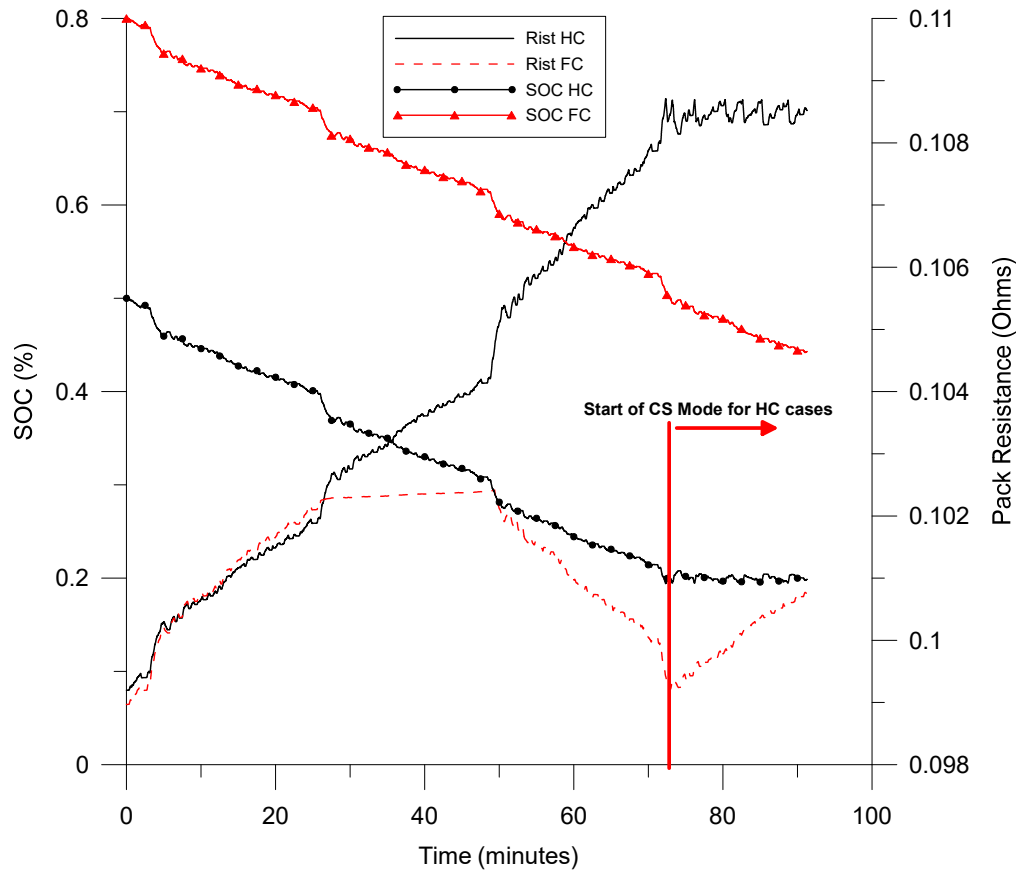


Figure 7.10 – Consecutive UDDS cycle pack resistance and SOC

7.2.3 LA92 Cycle

The LA92 cycle has higher heat generation than the UDDS cycle but not as much as the US06. The trends observed for these simulations are similar to those seen in the previous drive cycles. Figure 7.11 shows the cell temperatures for the LA92 simulations. The vehicle enters CS mode around 2800 seconds (47 mins) for the HC cases which is indicated on the figure.

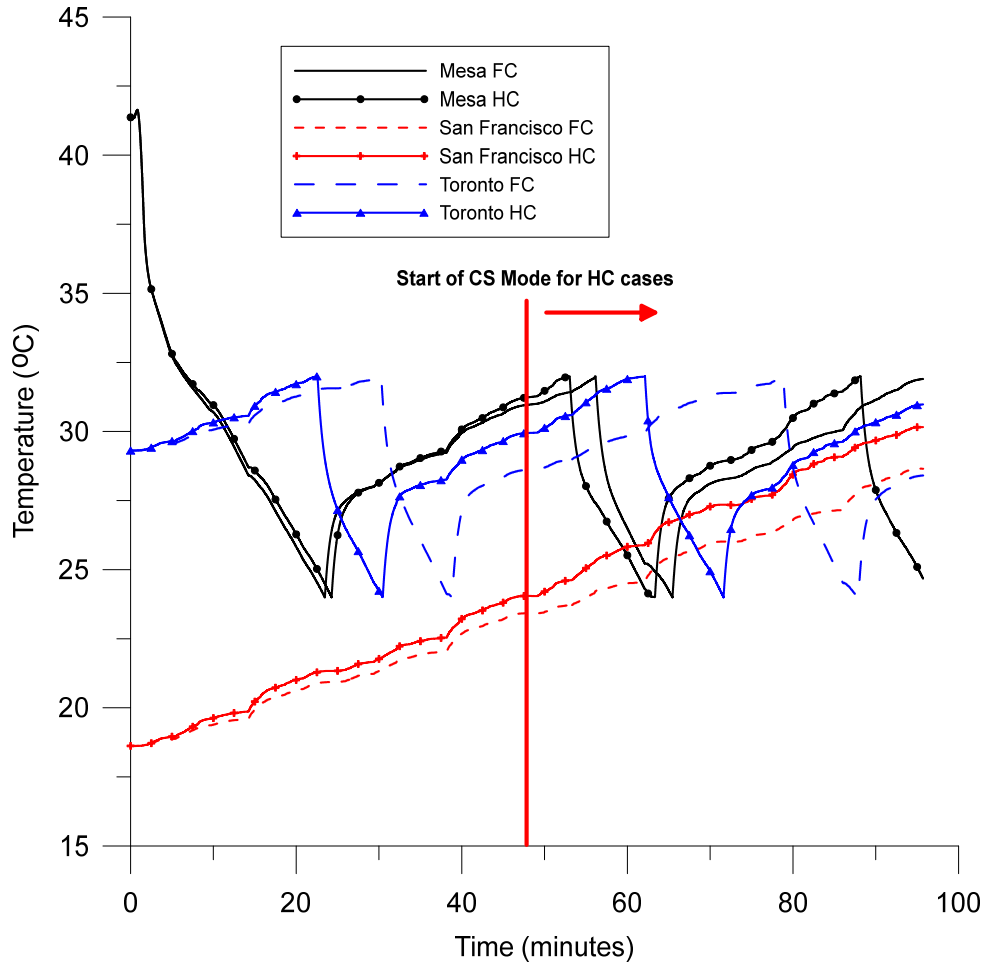


Figure 7.11 – LA92 cell temperatures

Both the Mesa and Toronto drive simulations with this drive cycle experience multiple cooling events, each lasting under 600 seconds (10 mins) with a consistent cooling pull down rate of $2^{\circ}\text{C}/\text{min}$ within the first 150 seconds. No cooling events occurred for the San Francisco simulations, the HC and FC battery initiation had final temperatures of 31.3°C and 28.6°C respectively. Compared to the UDDS simulations, the length of four consecutive cycles is approximately the same but the higher internal heat generation of the LA92 cycle leads to higher final temperatures. Figure 7.12 shows the pack resistance alongside the SOC for the LA92 simulations generated by Autonomie. The vehicle is in the highest resistance range of the battery pack, between $0.108 - 0.11$ Ohms for more than half the length of the cycle, this is the same battery resistance range seen in the US06 simulations. Additionally the HC simulations have 20.9% higher average heat generation

compared to when the vehicle starts the cycle fully charged. Higher demand of the LA92 cycle verses the UDDS cycle accounts for the smaller time gap between the triggers for the cooling events.

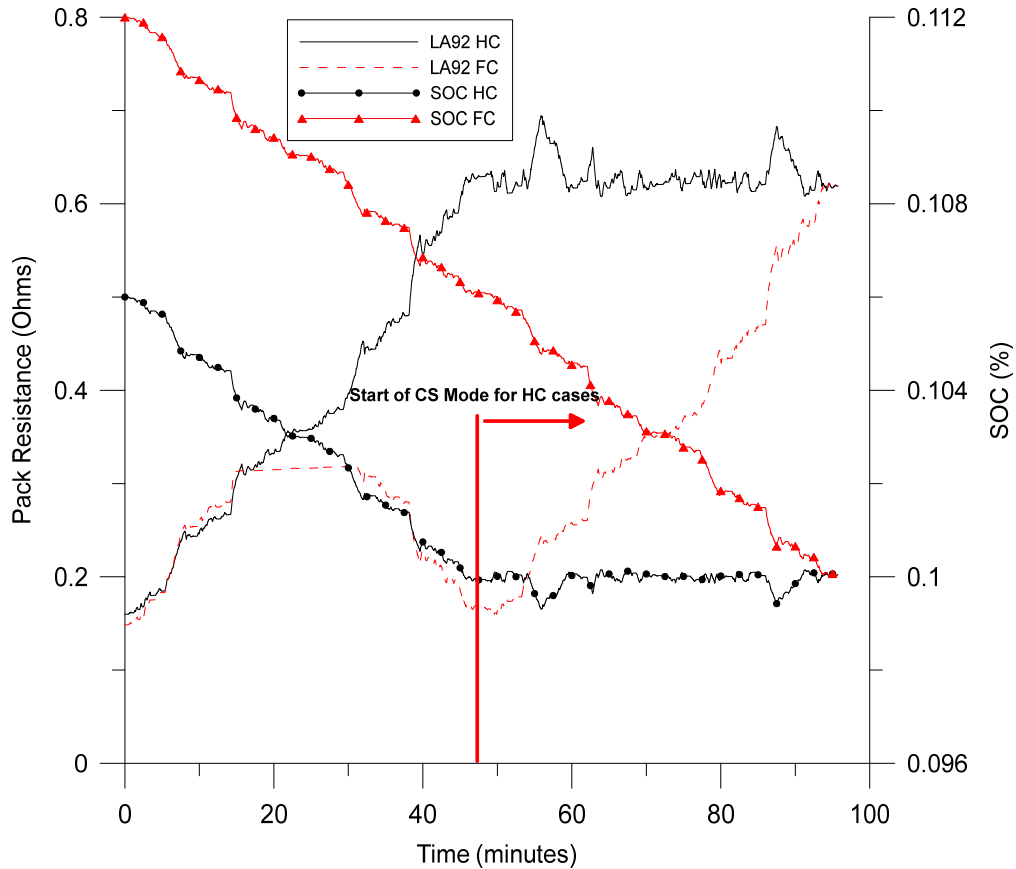


Figure 7.12 – Consecutive LA92 cycle pack resistance and SOC

7.2.4 Davis Dam Cycle

Referencing Figure 4.15, the Davis Dam has the highest heat generation among drive cycles selected for simulations. This cycle was simulated using Mesa climate data. However, unlike the previous simulations where the vehicle was examined in HC and FC states, the Davis Dam utilizes the CD and CS modes. In the vehicle, the driver can select “mountain mode” which aids the vehicle in situations where there are large grade and elevation changes by cycling the engine on and off more frequently and changing charge/discharge set points of the ESS for transitioning at approximately 45% SOC into

CD mode. However, the current vehicle controller modelled does not have this higher power mode programmed; errors in simulations result when the vehicle transitions from CD to CS modes. In CD mode the vehicle starts with a full charge (80% SOC). CS mode begins the simulation using 20% SOC (as if the vehicle were NOT put into mountain mode). Figure 7.13 shows the cell temperatures for the Davis Dam cycle overlaid on the speed and elevation traces. It is apparent the vehicle held in CD mode develops more cell heat than the CS mode as the battery current draw uniquely propels the vehicle. While in CS mode, the ICE via its generator supply primary energy that ends up flowing to the wheels, much through the mechanical path of the driveline allowing the battery to cool. This lowers the average current draw.

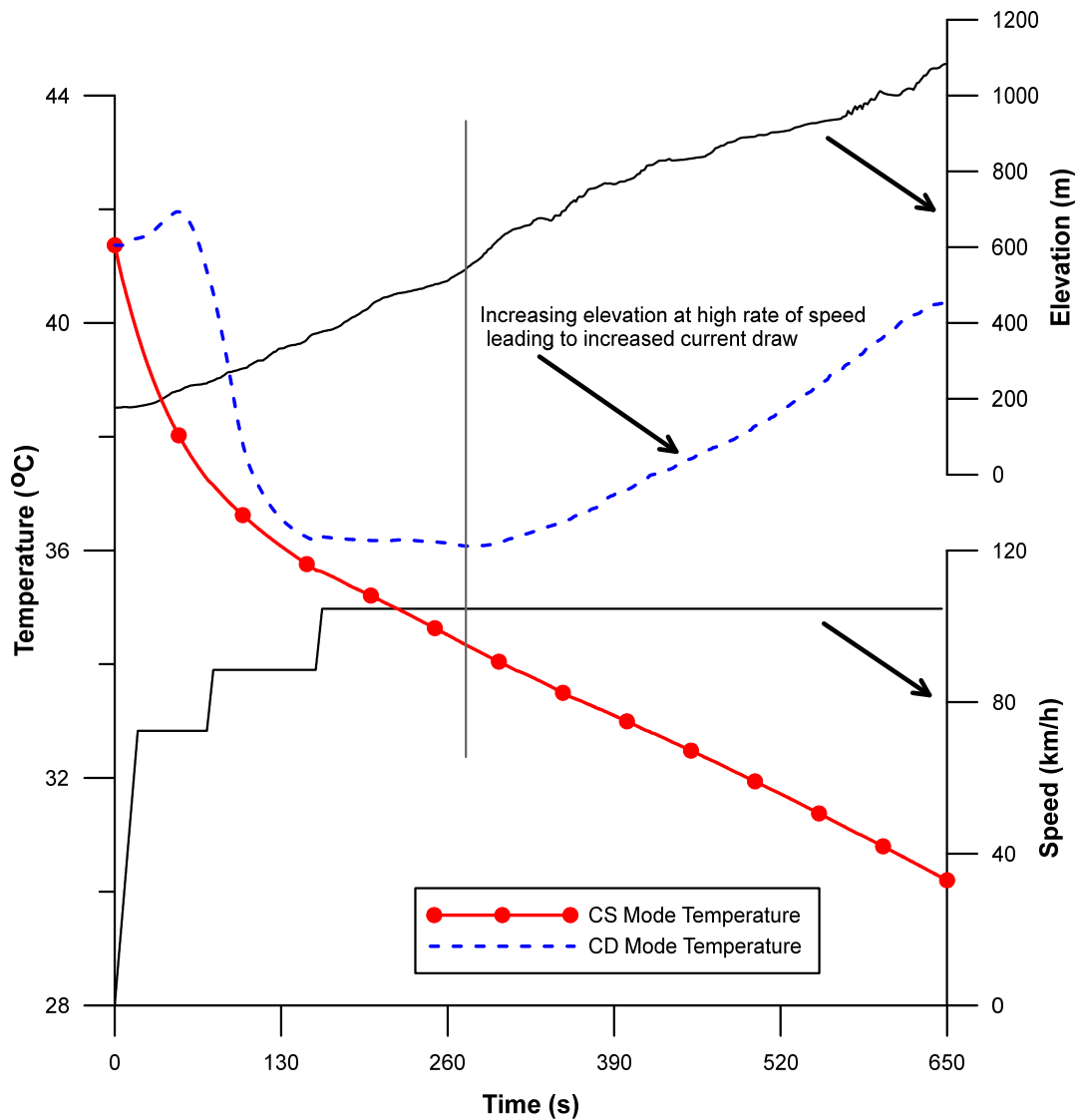


Figure 7.13 – Davis Dam cell temperatures

The reversal in cell temperature while in CD mode is due to the cooling system's inability to effectively remove enough heat due to the Davis Dam cycle generating 7.5 W/cell of heat (Figure 4.15). The compressor delivers a higher amount of cooling at the beginning of the cycle (seen up to 130 seconds) which draws down the cell temperature. However, the effectiveness reduces as cell temperatures go lower. Additionally the speed is increasing as is the grade which is indicated in the figure around 260 seconds. Further investigation reveals this is due to the programmed compressor power profile for the cooling system (Figure 5.22). The vehicle testing which produced the power profile didn't have as high a heat generation. When the compressor profile settles to the lower value, the Davis Dam heat generation becomes much greater than the cooling provided hence the reversal in cell temperature. Extended thermal chamber testing or vehicle testing at the Davis Dam might reveal how the control strategy changes when there is increasing heat generation. Conversely, while in CS mode, the heat generation of only 0.73 W/cell allows a temperature pull-down.

With "mountain mode" engaged, it is reasonable to expect the cell temperature will not see such a drastic condition as the engine would assist more. The simulation describes a worst case scenario where only battery power is available (as a case where the engine runs out of fuel).

7.3 Heat Flow through the Battery Pack

In order to examine the influence of battery pack design elements and packaging configuration in a more systematic way, the rate of heat flowing into and out of the pack through the various components was tabulated and plotted.

7.3.1 US06 Heat Flows

Average heat flow values are calculated in Table 7.2 per cell for the individual component for each of the test regions. Such average values quantify the amount of heat flowing through each component but does not show the direction of heat flow, this is depicted in later figures. The internal heat flow crosses the frame components, BMS unit and endplates. External components are the shield, cover, baseplate and bulkhead. In the

half charge simulation cases, the total heat flow values trend higher compared to the fully charged battery due to the bulkhead components heating once the engine turns on as the vehicle transitions to CS mode. Figure 7.14 plots a graphical representation of Table 7.2 and the percentage of heat flow through each component in the test regions. The top graph of Figure 7.14 shows there is very little separation between the HC and FC simulations for all regions.

Table 7.2 – US06 Average Heat Flow (mW/cell)

Pack Section	Component	TO	TO	SF	SF	Mesa	Mesa
		HC	FC	HC	FC	HC	FC
Interior	Frame Side	10.90	11.61	36.12	34.64	38.92	41.03
	Manifold	7.77	8.28	26.44	25.31	28.43	29.99
	Frame Bottom	12.56	13.41	45.96	43.49	49.89	52.94
	Frame Top	13.03	13.83	35.90	34.81	40.11	42.04
	Top BMS	2.52	2.73	11.84	10.83	11.57	12.56
	Endplate	8.07	8.61	27.91	26.71	29.78	31.44
Exterior	Bulkhead	18.37	0.38	25.15	1.53	31.07	1.21
	Baseplate	9.77	10.35	50.25	45.81	48.49	52.92
	Shield	6.33	6.11	22.20	20.18	22.21	24.04
	Cover	20.51	20.91	40.70	39.04	23.79	25.60

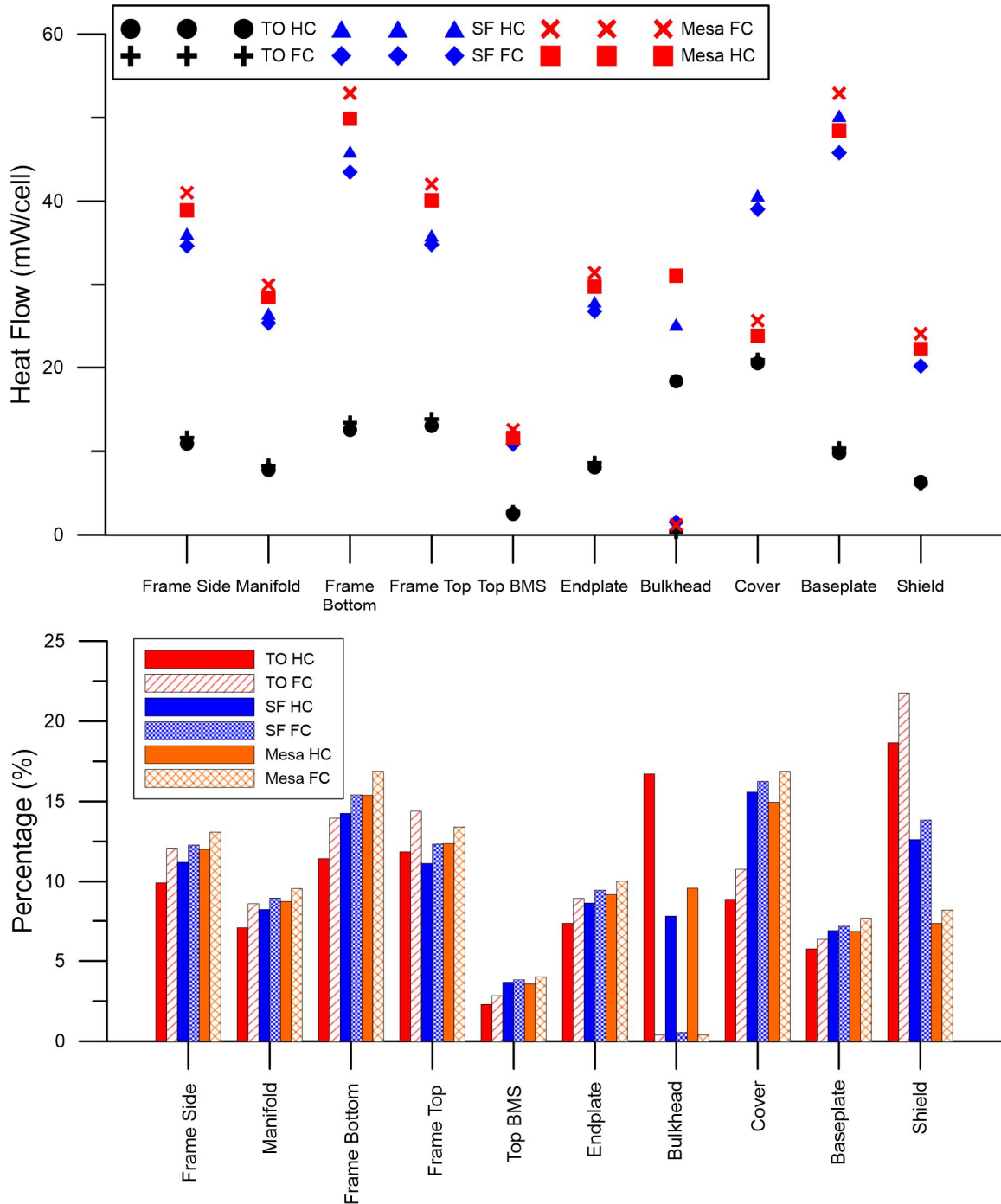


Figure 7.14 – US06 component heat flow values (top) and percentage (bottom)

The average values for the individual components between HC and FC conditions are similar in each region. The bulkhead value contributes to the increase in inward heat flow when the engine is active for the HC cases. The heat flow will follow the path of least resistance. This is reflected in the average values of Table 7.2. The frame bottom admits

the highest amount of heat flow due to the high temperature differential laying between node T₃ and ambient. The manifold and endplate share similar values as their resistances (R₆ and R₁₄) and capacitance are also similar in the circuit; their branches being in parallel. The large resistance value of R₈, constitutes the BMS and plastic covers, so less heat flows through the top.

The shield component, underneath the vehicle, shows the highest heat flows among all components. Convection and radiation resistors are connected in parallel to the shield component, Figure 7.15 illustrates the percentage contribution of convection and radiation heat flows respectfully as well as the absolute values.

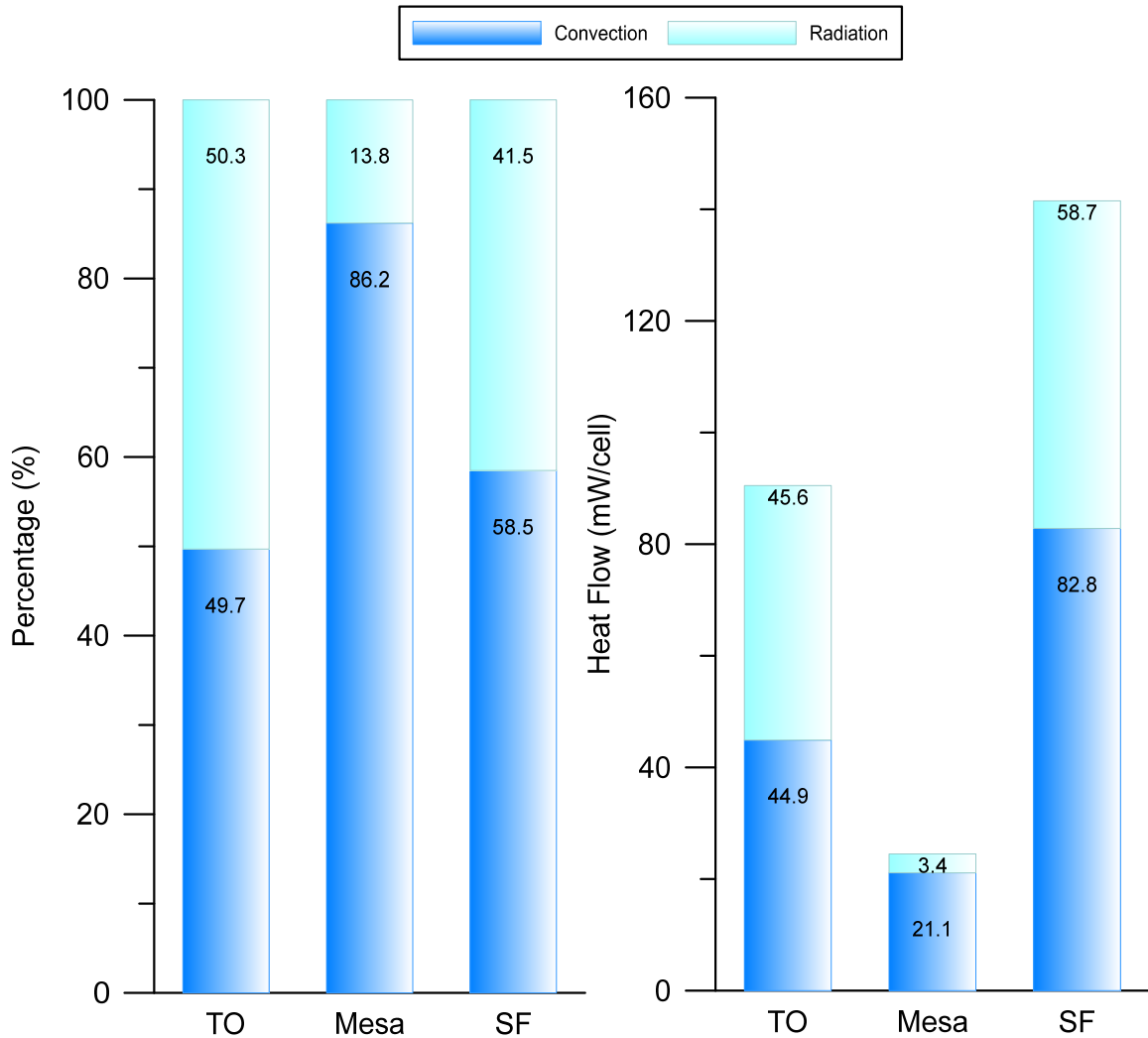


Figure 7.15 – HC US06 shield heat flow percentage (left) and heat flow value (right)

In Toronto, the combination of outside temperature (29°C) and road surface temperature of 32°C creates a near equal contribution between radiant heat transfer and conduction. The temperature difference is 3.3°C between the road and environment. In San Francisco, a balance of convection and radiation is also seen with a similar temperature difference. For Mesa, the ambient temperature is at 39.7°C and the road at 39.74°C . The near equal temperatures is due to the data acquired from NOAA for the Zenith angle to calculate the road surface temperature. As explained in the previous chapter, the sun was setting or already set at 8:00 PM for the Mesa simulations. The heat flow values show when there is little to no solar radiation, convection is the more dominant influence under the vehicle. By contrast when examining the regions at peak solar position, the change in heat flow percentage is noticeable and the heat flow values for convection and radiation are significantly higher as outlined in Figure 7.16. This indicated the importance of road radiation in full vehicle simulations when investigating battery thermal systems.

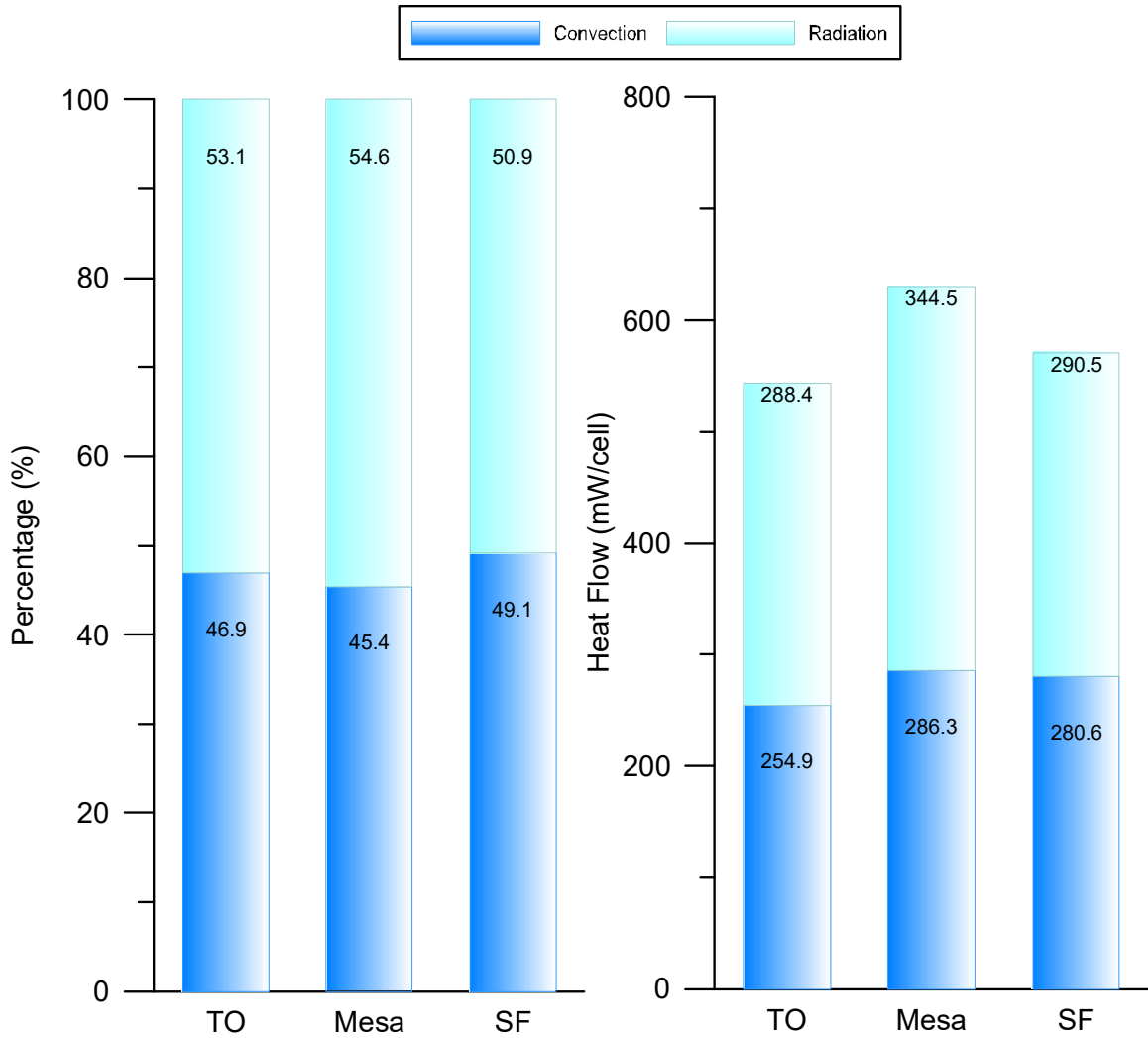


Figure 7.16 – HC US06 shield heat flow percentage (left) and heat flow value (right) at peak solar position

At peak solar position for each region, the radiation component is higher than the convection. Looking at the Mesa region, the radiation component is 341.1 mW/cell higher in relation to Figure 7.15. The analysis in Section 6.2.3 shows the battery temperature was at its worst in the evening due to the thermal lag of the cell mass, and this time of day experiences reduced impact of solar effects. For comparison, Figure 7.17 shows the difference in heat flow through the frame bottom, baseplate and shield components which see the most influence from underbody effect. At peak solar the overall heat flow values are much higher and this trend extends to all peak solar simulations across every region and charge levels. The results in Figure 7.16 indicate how significant of a difference the

position of the sun makes on the convection and radiation components. Although this heat influx occurs earlier in the day, the heat remains trapped and permeating towards the cells so it will affect them eventually regardless of drive cycle commencement times.

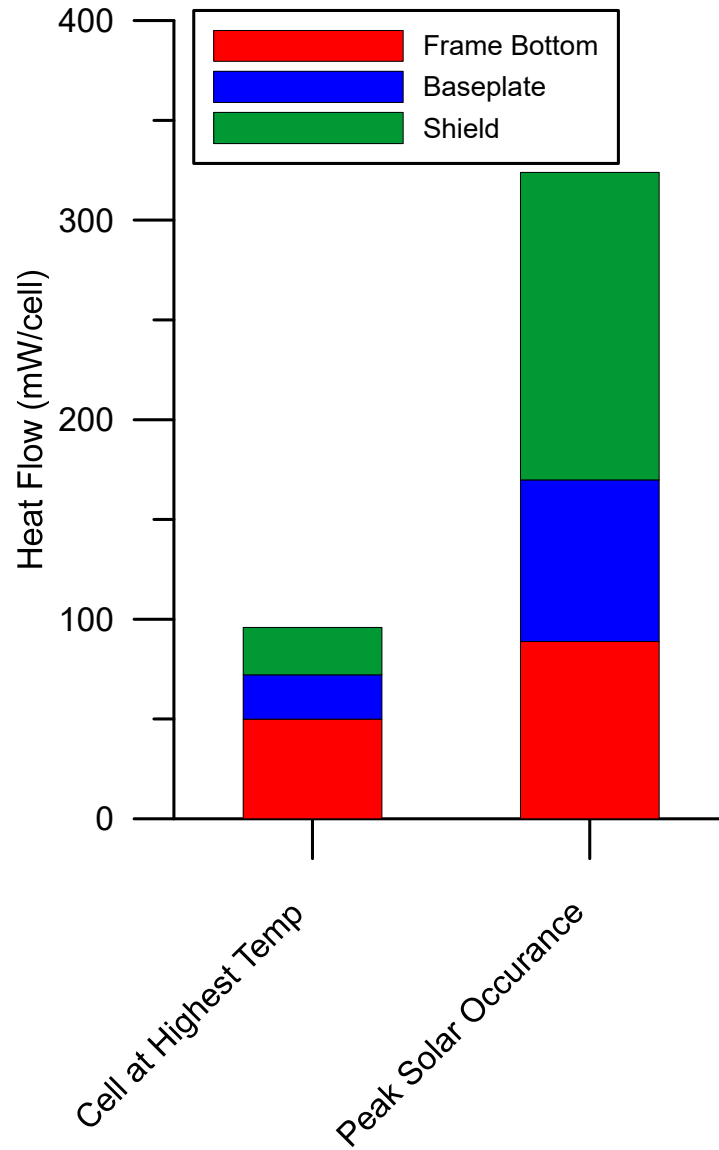


Figure 7.17 – Mesa HC component comparison, different times of day

The direction of heat flow needs to be examined in the individual test regions as the average values do not take direction into consideration rather only identifies conductive areas. Each of the frame components exhibited similar heat flow profiles, therefore, only a cell frame side component will be discussed as exemplar. Since the frame element is closest to the cell, the frame side temperature is compared to the cell temperature. Cell temperature is graphed on a secondary y-axis in Figure 7.18.

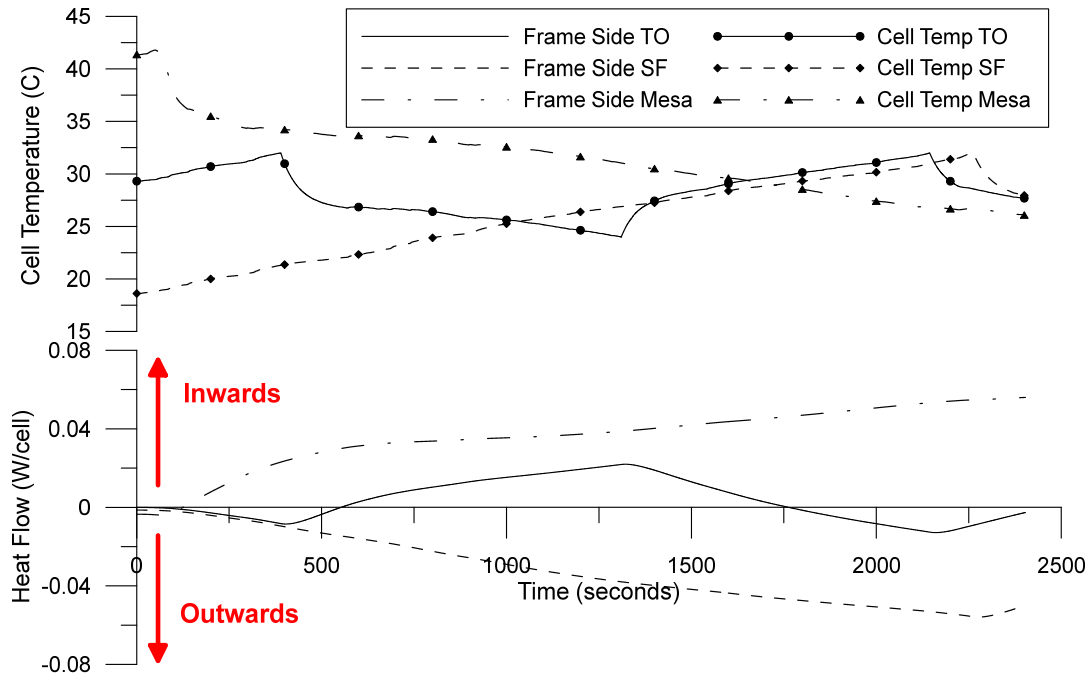


Figure 7.18 – US06 cycle frame side heat flow comparison for HC battery simulation

The cells are viewed as the core of the battery pack. Heat flow outward is considered negative as heat is flowing from the cells to the surroundings, and positive if heat is flowing towards the cells. The cell temperature profiles show when the cooling events occur; these soon promote inward heat flow. Node T₃ in the simplified circuit (cell surface temperature) is linked to the frame branches as well as the cooling system source. An active cooling system absorbs heat both from the cells and their immediate surroundings shortly thereafter.

The external components show more variance in heat flow across the test regions compared to the internal components. These can be examined over the entire drive cycle. Figure 7.19 records the heat flow through the shield component.

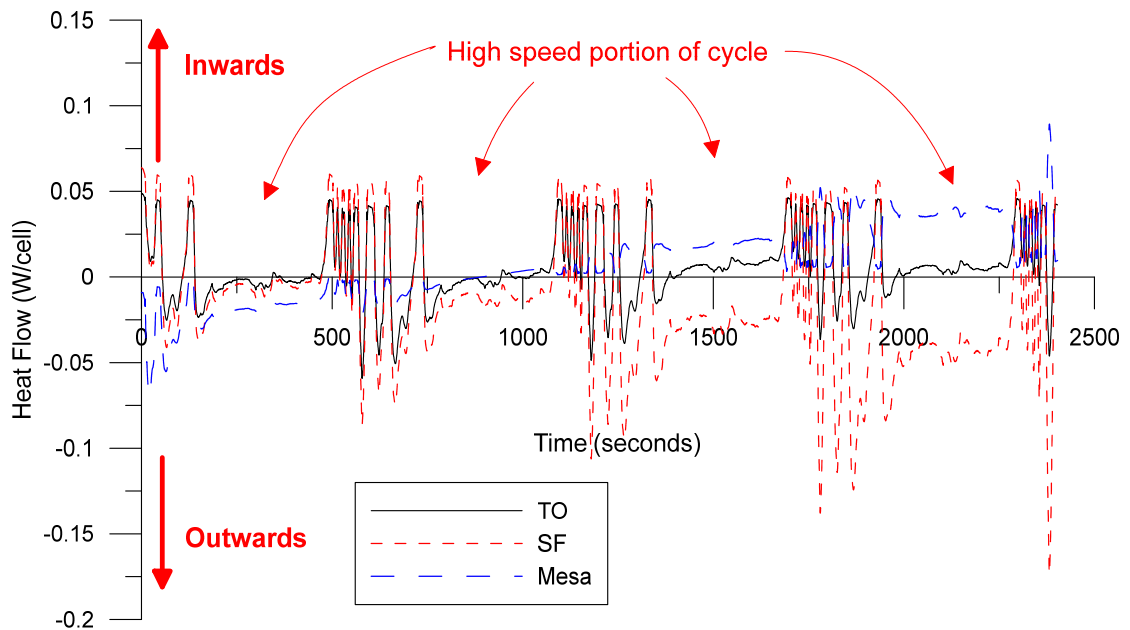


Figure 7.19 – US06 shield heat flows

The oscillations seen are due to forced convection. The speed of the air under the vehicle is programmed into the underbody resistor R_{20} . When the vehicle is at high velocity, the heat flow through the shield increases since resistance drops with speed. The road radiation resistance, R_{21} , has a more predominant influence relative to convection when the vehicle is stationary. The interesting part to note is the longer duration trend for heat flow either inward or outward depending on how ambient conditions relate to where the average internal cell temperature sits as determined by the cooling system setpoint. For Mesa it is an influx of heat, San Francisco demonstrates an outward flux and for Toronto it is almost balanced but with a slight inward trend. The Mesa simulation ends the cycle with more heat flow into the pack than the Toronto simulation. Unlike Toronto and San Francisco, here the difference between the shield's initial starting temperature and the ambient temperature is less than 1°C . This is attributed to the time of day when the Mesa simulations were selected; the sun has already set and the road temperature is close to ambient. However, the ambient temperature was 39.7°C and the cell temperature plot (Figure 7.7) showed the cooling system was active for the entire cycle. As the internal pack temperature decreased, this caused an influx of heat to the system.

Examining the other external components (baseplate, cover, bulkhead) for directions of heat flow, Figure 7.20 plots these results. The frame side component is also shown in addition to explain the heat flow direction in relation to the BTMS operation.

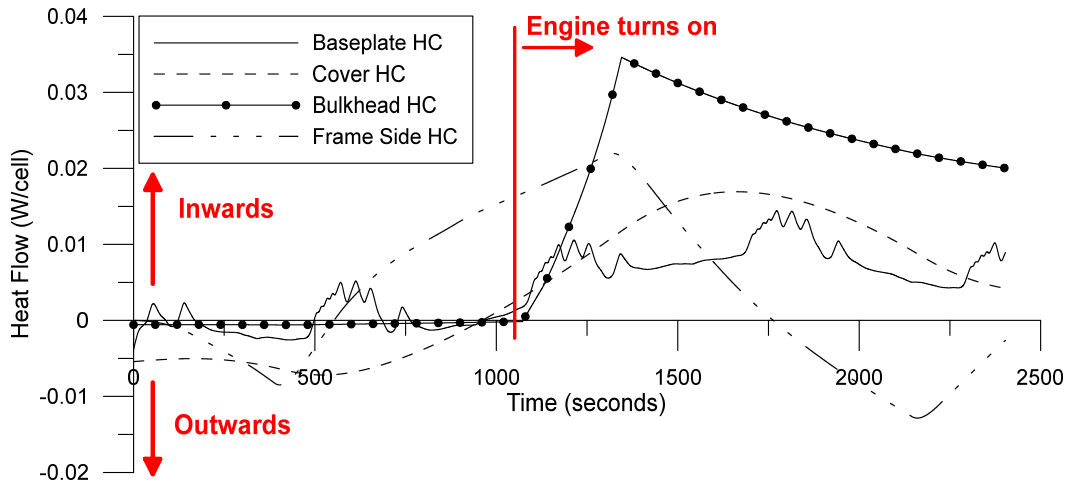


Figure 7.20 – Toronto US06 external component heat flow

The shielding covers the baseplate and the heat flow through the baseplate is similar to that of the shield. There aren't any large oscillations as seen in the shield but the heat flow does resemble the inverse of vehicle speed. The oscillations are smaller due to the resistance and capacitance of the baseplate (R_{12} and C_9). As the heat flows into or out of the pack, the thermal mass of the baseplate creates a thermal lag for heat propagation through the material. The resistance limits the amount of heat flow from the frame bottom and/or shield as these components are in the same branch. The bulkhead heat flow remains close to zero until the engine turns on at approximately 1100 seconds. There is a subsequent influx of heat into the system through the bulkhead which peaks at 1340 seconds then slowly decreases. The peak corresponds to when the cooling system shuts off as the cells reached the low temperature setpoint. Thereafter, the temperature differential to the cell core (which is the driving force for heat flow) diminishes and both the cover and bulkhead response of lower heat flux results. The cover and baseplate are both experiencing the effects of the cooling system being active but those effects are not as pronounced or immediate as for the frame components. The simplified circuit of Figure 5.18 shows the frame sides, manifold, top, BMS units, endplates and associated air gaps are connected to the cover component. The capacitance of the cover (C_{12}) is the second largest capacitance in the circuit at 27 F,

with the cells being the largest at 338 F. The capacitance of the cover causes the thermal lag resulting in a 390 seconds delay in peak values compared to the frame side component.

7.3.2 UDDS Heat Flows

While the US06 cycle has the highest heat generation of the standardized cycles, the UDDS cycle is at the opposite end of the spectrum. Table 7.3 shows the component average heat flow values.

Table 7.3 – UDDS Average Heat Flow (W/cell)

Pack Section	Component	TO HC	TO FC	SF HC	SF FC	Mesa HC	Mesa FC
Interior	Frame Side	8.06	8.91	11.54	9.64	42.77	40.81
	Manifold	5.82	6.46	8.55	7.16	31.67	30.23
	Frame Bottom	8.81	9.37	12.68	10.03	62.39	59.89
	Frame Top	9.06	9.79	10.14	8.28	39.23	37.51
	Top BMS	2.82	3.38	5.64	4.97	21.82	21.30
	Endplate	6.08	6.76	9.18	7.7	33.81	32.27
Exterior	Bulkhead	11.39	0.6	16.28	0.86	21.35	2.67
	Baseplate	12.24	14.87	25.03	22.17	98.28	96.14
	Shield	4.88	5.47	8.58	7.42	45.85	45.20
	Cover	26.63	27.63	38.99	38.22	50.43	49.92

Figure 7.21 shows the value and percentage of heat flow through each component using the values found in Table 7.3. The notable difference compared to the US06 results is that the lower internal generation rate promotes a higher fraction of heat transmittance via the higher resistance paths (ie. Top BMS) resulting in a more uniform contribution among the interior components.

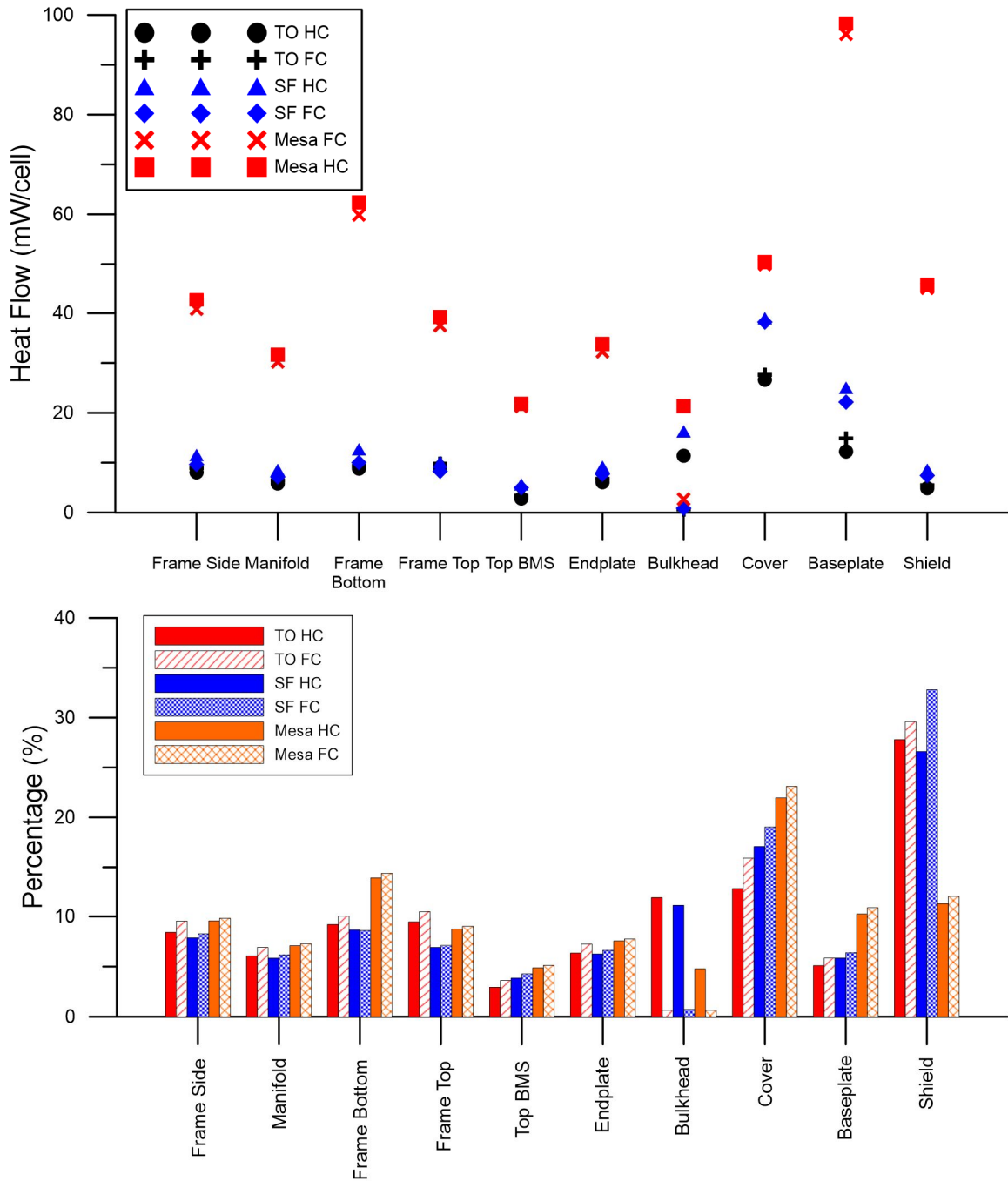


Figure 7.21 – UDDS component heat flow values (top) and percentage (bottom)

For the heat flow direction, the trends observed are identical to those seen in the US06 simulations. When the cooling system is active, heat flows through the frame towards the cell making it positive. When the system is off, heat flows outwards towards the environment. The peak heat flow value of 0.07 W/cell for the Mesa simulations is higher

than the 0.04 W/cell seen in the US06 simulations. This is due to cooling system lowering the cell temperature to 24°C and the low internal heat generation. Whereas the US06 simulations saw the cooling system active the entire cycle because of the high internal heat generation, which created two competing heat flows. The peak value of 0.02 W/cell in the Toronto simulations is the same as the US06 cycle whereas the San Francisco simulation experiences half the heat flow. This is again attributed to lower internal heat generation of the UDDS Cycle.

The behaviour of the shield component, is also analogous to that of the US06 simulations. However, here there are more oscillations due to the stop and go nature of the UDDS drive profile. Toronto and San Francisco experience the same trends as the heat flow represents the reciprocal of the speed profile. The Mesa simulation sees the opposite trend which was also observed in the US06 simulations.

7.3.3 Summary of Heat Flow Results

The results presented in this section illustrated the heat flow through the battery pack components. The half charged battery simulations were discussed for the US06 and UDDS drive cycles. The general trends are the same for all drive cycles and charge states. The results not shown in this section (LA92, Davis Dam, and all full battery charge simulations) can be found in Appendix D.

The heat flow analysis on the US06, UDDS, and LA92 drive cycles in the three test regions were conducted. The Davis Dam heat flow was also analyzed using the Mesa climate data. The percentage of heat flow contribution for each component in the drive cycle were calculated. Results showed a higher heat flow though the path of least resistance when there was high internal heat generation. Lower internal heat generation also resulted in an increased heat flux into the battery pack from the environment due to the cells being held cooler on average.

Results for the shield component show the effects of convection are equal or slightly greater than that of the road radiation for the test day simulations. This is due to the convection resistor (R_{20}) utilizing the vehicle speed in its calculations. When there is more variation in the speed profile, like for the UDDS, this slightly augments the effects of radiation verses convection as the vehicle slows down and/or stops. However, the radiation

effects do not greatly exceed that of convection, and this is attributed to the time of day chosen for the simulations where there is a small temperature difference between the ambient and road temperature. When the radiation and convection are examined at peak solar times, the values are significantly higher. However, the overall effects on the cell are not yet apparent with the highest solar radiation as the thermal lag affects the criteria for drive cycle start time when examining worst case scenarios. The larger difference in ambient and road temperatures did not finally lead to higher cell temperatures (Figure 6.11) at the end. The elevated temperature of the Mesa region showed the warm air moving under the vehicle due to motion caused heat flow into the shield whereas the other regions saw the heat flow stay neutral or to flow out of the pack.

When the cooling system became active, it promoted heat flow into the pack towards the cells. This was seen by examining the heat flow through the frames which are closest to the cells. This trend was also observed in the external components (cover and baseplate), however, the thermal lag due to the capacitance of the components lead to the peak heat flows occurring after the cooling system had turned off. The bulkhead also contributed to a greater amount of heat flowing into the system in HC cases, because the vehicle entered CS mode which turns on the engine source.

7.4 Cooling Performance

When analyzing a heating or cooling system, the Coefficient of Performance (COP) is calculated. The COP is a ratio of the useful heating or cooling over the required work needed. A high value of COP is desired as it results in lower operating costs and the value is dependent on operating conditions. This type of analysis is useful for heat pumps, refrigeration and air conditioning systems. For the EREV thermal system, this type of analysis does not yet aid in understanding how much cooling is directed to the cells, lost to the internal hardware and the effect of environmental heat flux into the pack. Understanding the percentage of cooling directed to the cells helps quantify how effective the thermal system really is. This can also aid in the design of thermal system components to potentially reduce system losses within the battery pack.

This section details the percentage of cooling that is applied to the cells and lost to the internal and external components. A fully charged vehicle in the Toronto region is

simulated on the US06, UDDS and LA92 cycles. The Mesa region on the US06 and Davis Dam drive cycles is also investigated as the cooling system was active for the entire length of the cycles.

7.4.1 Drive Cycle Cooling Events

The total amount of cooling is shown in Figure 7.22 along with the cooling to the cell and battery components. In the thermal circuit, the total amount of cooling is found by measuring the current at R₁ which represents the fluid entering the pack. When the cooling system becomes active, measuring the current at R₄ reveals the amount of cooling directed to the cell surface. For the amount of cooling in the internal components, the current of the frame elements and endplates (R₆ through R₁₁) are summed together. The external components are the cover, baseplate, shield and bulkhead (R₁₂, R₁₃, R₁₆, R₁₈). When the cooling process begins, the effects of the external components are very minimal and almost zero when compared to the internal components. This trend is also seen in all the simulations which indicates when the thermal system is active, the total amount of cooling is distributed between the cells and internal hardware. To determine the percentage of cooling which is distributed to the cell and packaging, the cell and internal components are divided by the total amount of cooling with the results shown in Figure 7.23.

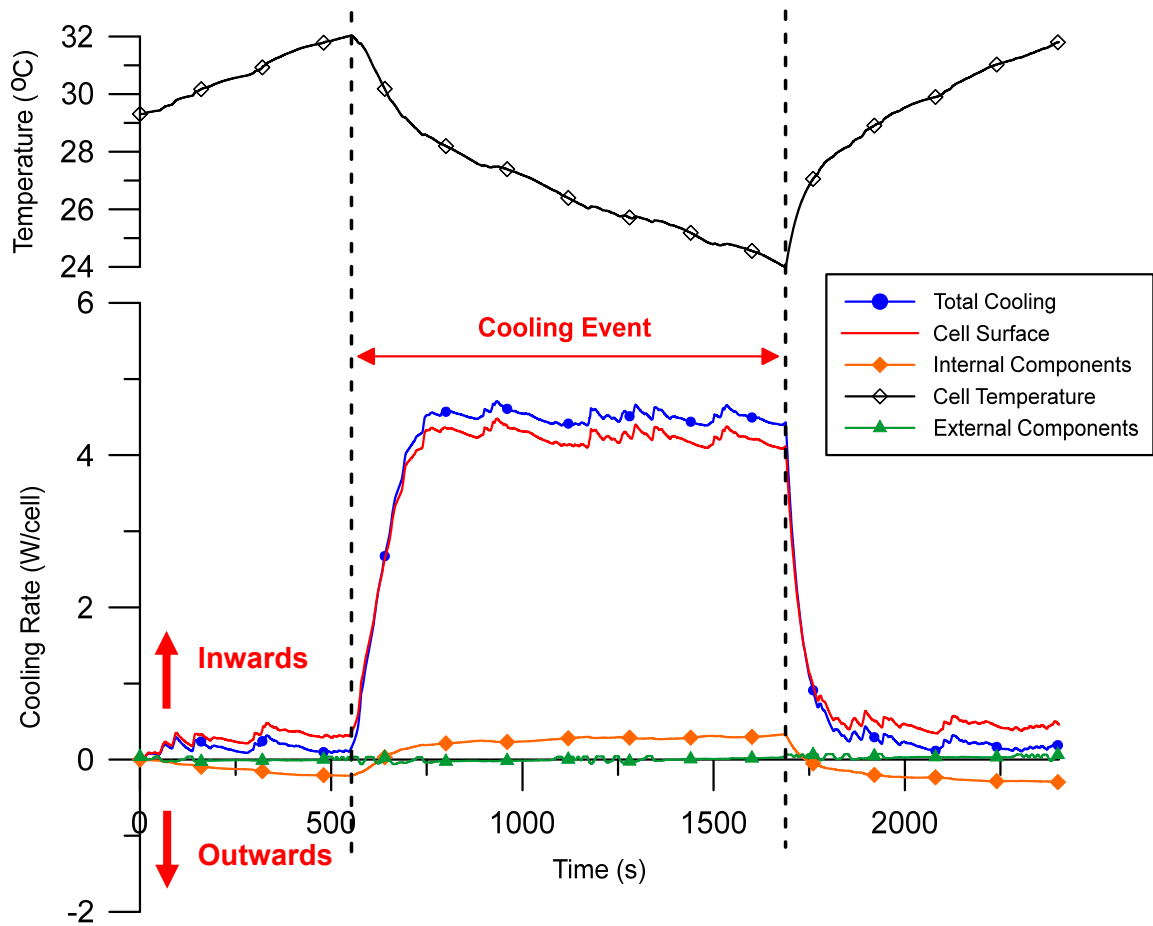


Figure 7.22 – US06 Toronto FC cooling effects

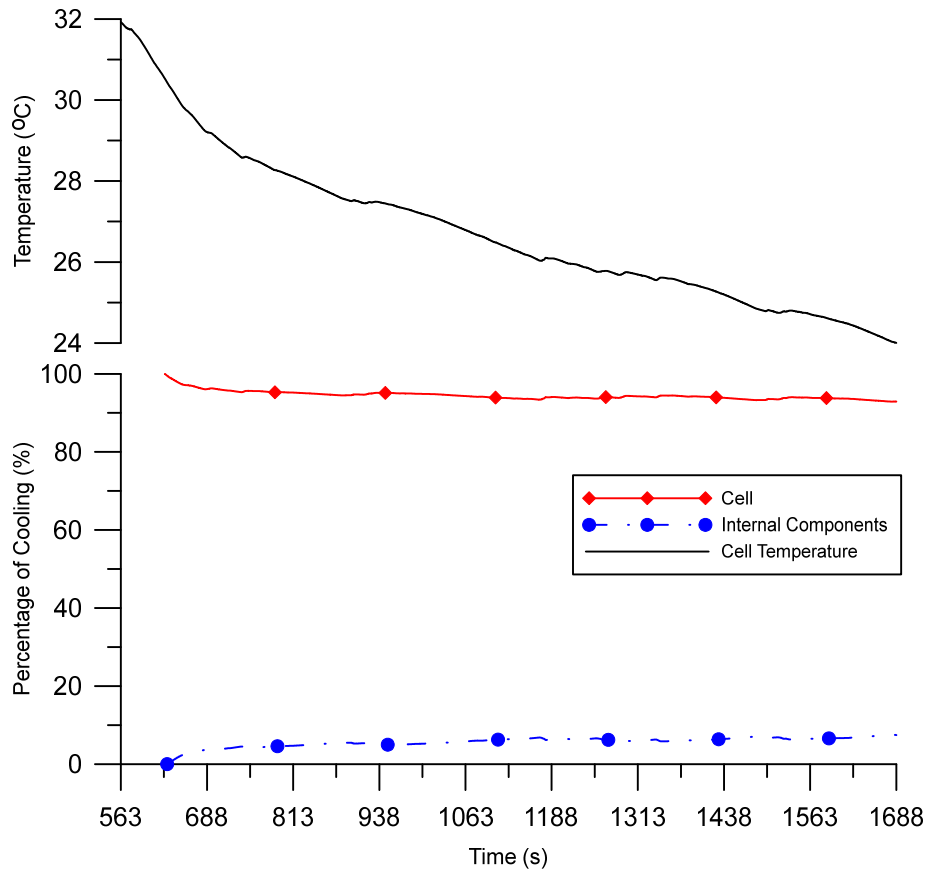


Figure 7.23 – US06 Toronto FC cooling percentages

The x-axis (time) reflects the period of time when the thermal system was active. At the beginning of the cooling cycle, the percentages of the cell and internal components are calculated to lie outside the 0-100% range. This stems from initialization of the cooling system and the thermal lag. The total amount of cooling is the current through R_1 in the circuit and the cell, internal, and external components are divided by the total. Before the compressor becomes active, it causes the percentage to be outside the 0-100% range because the R_1 current is small compared to the internal/external elements. After approximately one minute, the percentages stabilize and the results indicate approximately 92% of cooling is directed towards the cells and 8% to the internal components.

The US06 Mesa, UDDS Toronto, and LA92 Toronto simulations using the same process previously described all show 90% of the cooling is applied to the cells and 10% to the internal components. The graphs for these simulation can be found in the Appendix E.

The Davis Dam cycle, with the highest internal heat generation, saw the cell temperature to rise throughout the cycle indicating the thermal system could not effectively remove all the heat. Figure 7.24 and Figure 7.25 shows the cooling power and percentages respectively.

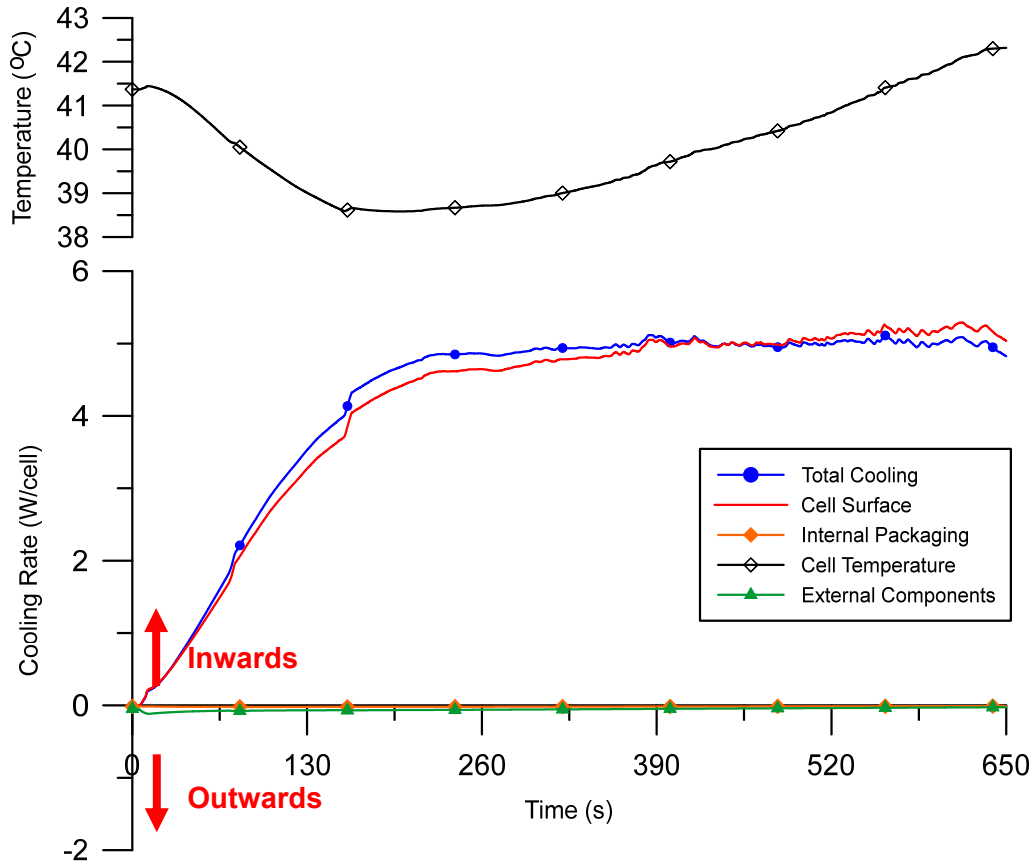


Figure 7.24 – Davis Dam FC cooling

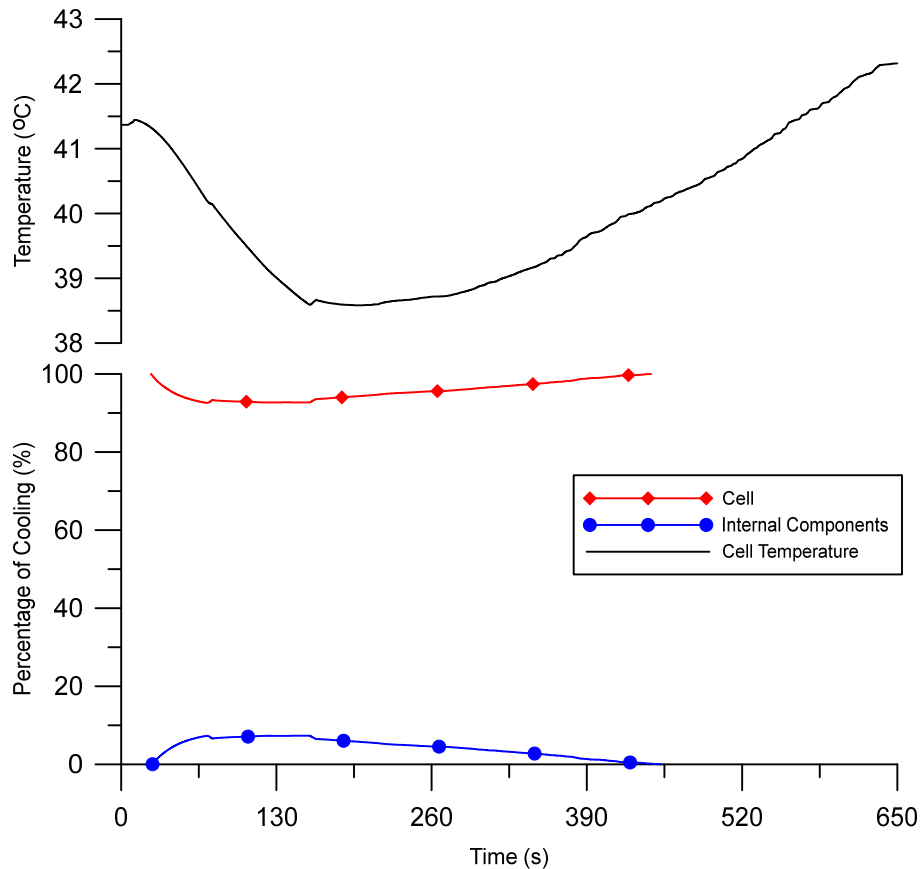


Figure 7.25 – Davis Dam FC cooling percentages

From Figure 7.24, the cell temperature begins to change direction around 200 seconds. At 400 seconds the cell surface cooling is equal to the total amount of cooling and then begins to increase. This indicates the internal heat generation is overpowering the amount of cooling available. The cell and internal components percentages in Figure 7.25 shows the cells and internal components receive 90% and 10% of the cooling respectively followed by a reversal in the trends due to increasing internal heat generation.

7.4.2 Summary of Cooling Performance

This section detailed the process for determining distribution of the available cooling power. The drive cycles usually show 90% of cooling is directed towards the cell and 10% towards the internal components. 90% of cooling directed to the cell is a substantial amount of the total available cooling power and indicates the current design achieves approximately a 10:1 ratio. More however would always be better. The Davis Dam cycle

showed the limitations of the cooling system when the internal heat generation overpowers. In this scenario, the cell temperature at the completion of the cycle was 42°C. However it is a short exposure time and not consequential in the bigger scheme. The Davis Dam simulation is a one off cycle, not normal driving behaviour. The thermal system is capable of safely and effectively cooling the cells when needed. The results presented evaluate the production system with possible improvements to be examined in later sections.

7.5 Effects of the ICE on Cell Temperature

To examine the effects of engine heat on the cell temperature, the UDDS and LA92 HC simulations in San Francisco are ideal as there are no cooling events. The San Francisco region in addition has the battery pack hotter than the ambient conditions resulting in heat flowing out of the pack to the environment. Therefore, the effects of the engine are not masked or magnified by other factors. In Figure 7.9 and Figure 7.11, a deviation in the cell temperatures between the HC and FC simulations in San Francisco were seen. Final differences were 1.6°C and 2.7°C for the UDDS and LA92 cycles respectively. Comparing the heat flow between the cell surface and at the bulkhead shows the direct impact rather than comparing temperatures. The cell surface temperature is determined by the internal heat generation which is node T₃ on the simplified circuit. Any additional heat flow from the bulkhead will affect the cell temperature because the bulkhead branch is also connected to node T₃. The cell surface and bulkhead heat flow was found by monitoring the current at resistor R₄ and R₁₆ respectively. Current at R₁₆ represents heat flow into the pack whereas the current at R₁₇ represents the heat flow into the bulkhead component. Figure 7.26 shows the difference in the heat flow between the HC and FC simulations on the UDDS cycle in San Francisco.

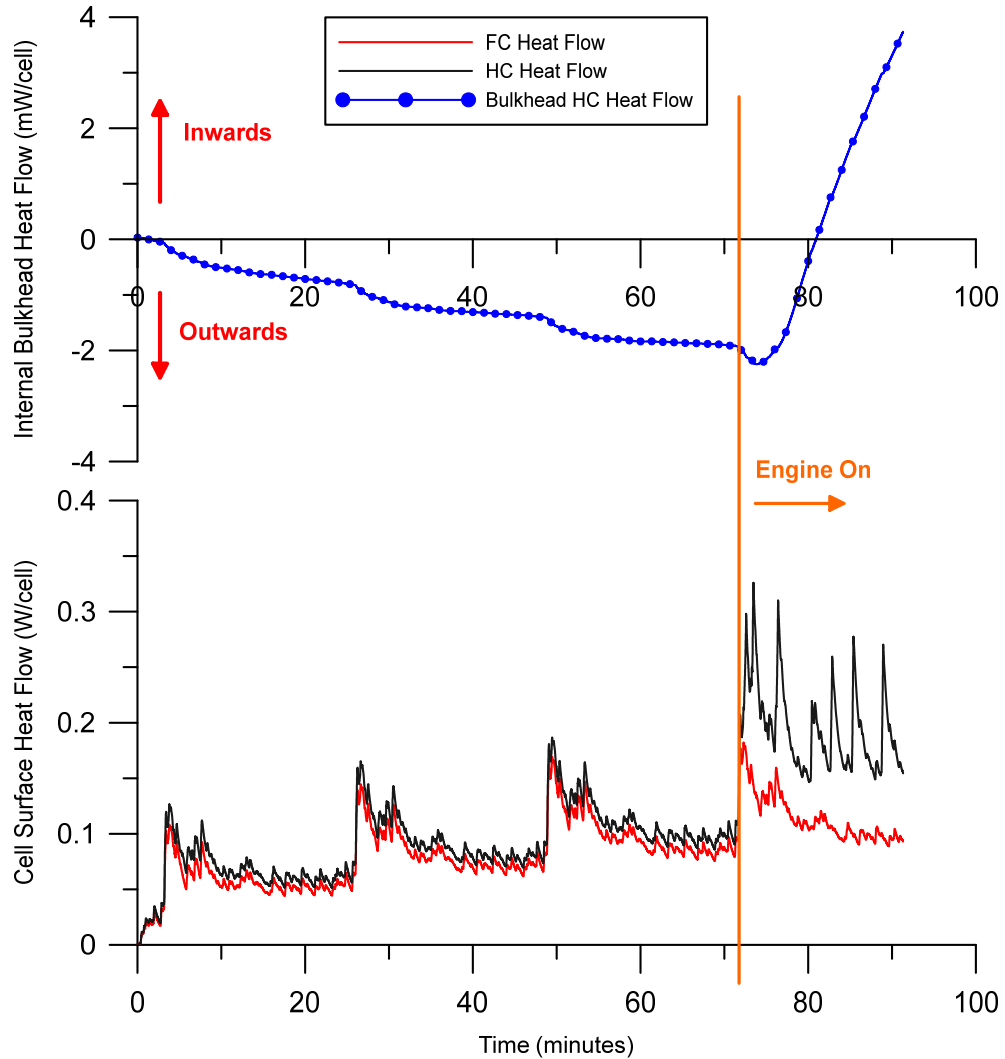


Figure 7.26 – UDDS San Francisco cell surface and bulkhead heat flows

At 4319 seconds (72 mins), the bulkhead heat flow increases sharply indicating the vehicle entered CS mode and the heat from the engine is now flowing inwards through the bulkhead. The FC simulation did not enter CS mode and can be referenced as the baseline. The outward cell heat flow peaks around 0.175 W/cell at 4300 seconds (72 mins). In comparison, the HC simulation experiences a sharp increase in heat flow similar to the bulkhead. It has a peak heat flow of approximately 0.3 W/cell at 4300 seconds. For the remainder of the simulation, it outputs higher heat flow values compared to the FC simulation. The average heat flow values for the cell under FC and HC conditions from 4300 seconds to the end of the cycle are 0.11 W/cell and 0.20 W/cell respectively and the bulkhead contributes 0.002 W/cell. This illustrates the bulkhead heat flow has a very

minimal effect on the heat influx into the battery pack. The bulkhead resistance (R_{16}) at 1313Ω is the highest resistance value in the simplified circuit which accounts for the low average heat flow. Figure 7.27 shows the difference in the heat flow between the HC and FC simulations on the LA92 cycle in San Francisco.

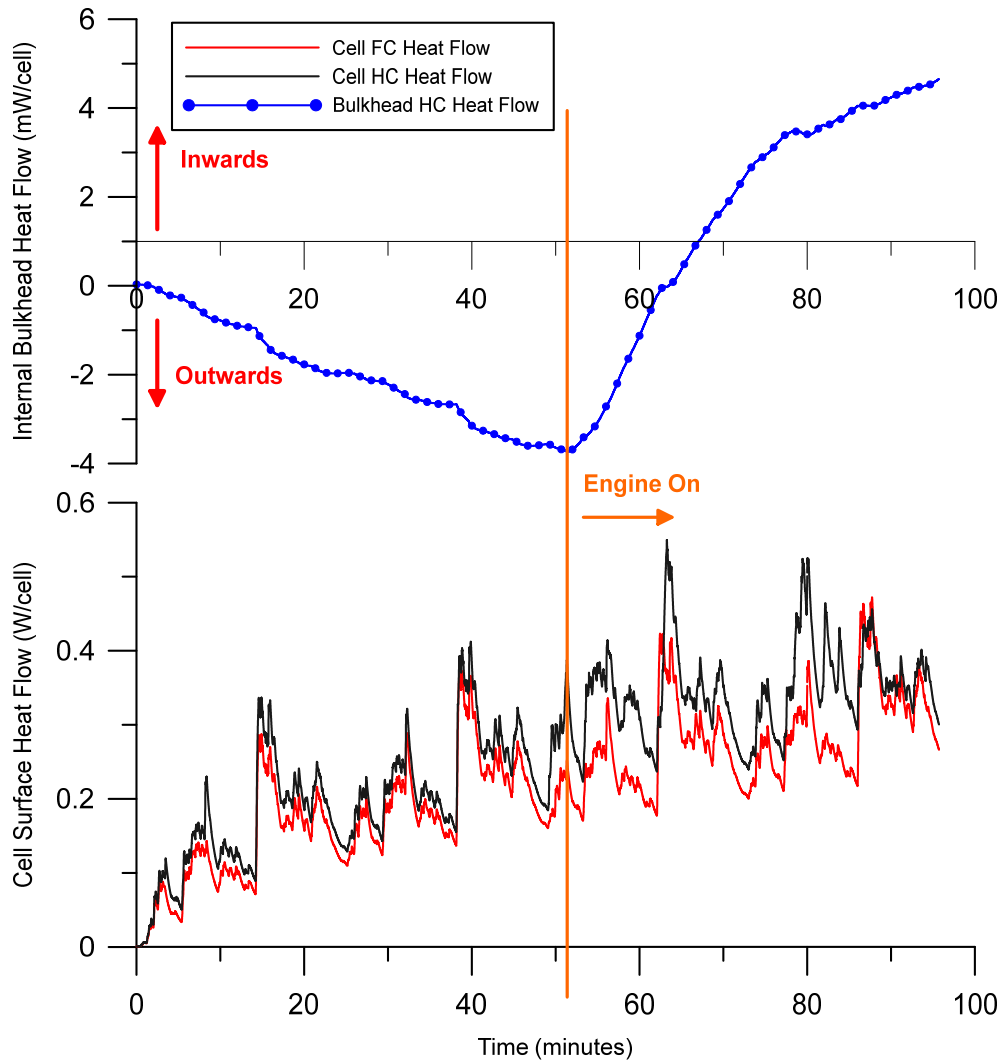


Figure 7.27 – LA92 San Francisco cell surface and bulkhead heat flows

The bulkhead does see an influx of heat at 3120 seconds (52 minutes) until the end of the cycle. Unlike the UDDS cycle, the difference in cell surface heat flow between the HC and FC is not as visually apparent. Examining the average heat flow from 3120 seconds to the end of the cycle, the cell's heat flow under FC and HC starting conditions are 0.29 W/cell and 0.35 W/cell respectively. By contrast the bulkhead contribution is 0.003 W/cell.

While the bulkhead contributes only a small amount of heat into the battery pack, it is not enough evidence to conclude the engine effects are small. This highlights a path that needs to be added to the circuit design. A direct path from the engine source to the underbody (shield) of the vehicle can capture the heat flowing under the vehicle. In order to quantify the effects of the engine wash under the vehicle, more experimentation is needed to properly incorporate this new path into the thermal equivalent circuit and identify a variable resistor “look up” table to model it. Much like the peak solar road radiation, the effects of added heat under the vehicle should be considered as it has the ability to permeate into the pack through the shield and baseplate. The bulkhead path alone presented in these results does not have the same impact.

7.6 Battery Aging

Increases in resistance over time are a concern in HEVs and EVs. The increased resistance affects the available capacity and augments the internal heat generation. As explained in the literature review, the augmentation in resistance over the number of cycles can be taken as a linear relationship up to a certain point. The simulations in this section investigate two resistance cases compared to the original simulations. The original drive cycle simulations utilize the resistance data from INL for a vehicle with 10,000 km which represents a (new) broken in vehicle. INL also detailed the resistance of the same vehicle at the end of their testing (EOT) with 208,000 km. Their testing period was over three years and that resistance data is used in simulations labeled as “INL EOT” to model a real vehicle with substantial mileage and age. The original resistance values are then doubled, labeled as “2x”, to investigate the sensitivity of the pack and thermal system to large increases of the internal resistance after 10 years of projected usage. The pack capacity is also reduced by 30% for the “2x” simulations. Figure 7.28 shows the resistance values as a function of SOC used for the simulations in this section.

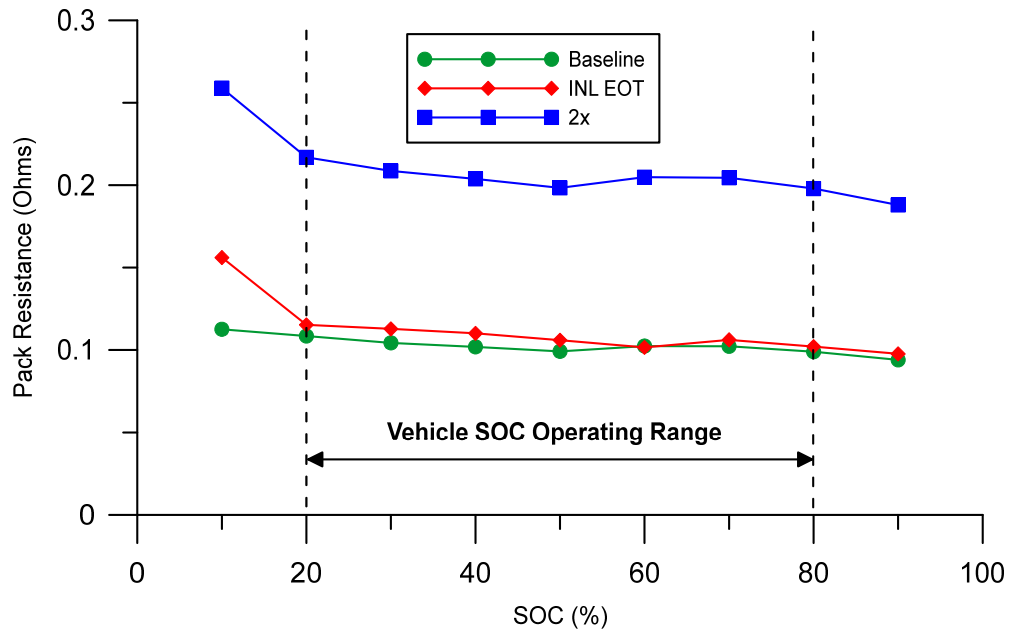


Figure 7.28 – Resistance values for aging simulations

The results shown are for the cell temperature in the Toronto region on the US06 drive cycle. Plots for the US06 simulations in San Francisco and Mesa can be found in the Appendix F along with the UDDS and LA92 drive cycles. All simulations are for a fully charged vehicle. Figure 7.29 depicts the resistance simulations on the US06 cycle. The “INL EOT” simulation increases the cell temperature to the 32°C threshold 57 seconds (at both cooling events) faster than then baseline simulation. Examining the average heat flow shows the “INL EOT” simulation generates 2.8 W/cell whereas the baseline generates 2.4 W/cell. This 0.4 W/cell increase accounts for cell temperature reaching the cooling threshold 57 seconds sooner. The “2x” simulation has a much greater effect on the cell temperature, most notably there is one cooling event that lasts the entire cycle. This simulation reached the threshold temperature 305 seconds (5 minutes) faster than the baseline. The average heat flow shows the “2x” generates 4 W/cell, almost twice that of the baseline. When the cooling system activates, the higher initial cooling power by the compressor allows the cell temperature to decrease to 27°C and slowly draws the temperature down throughout the cycle.

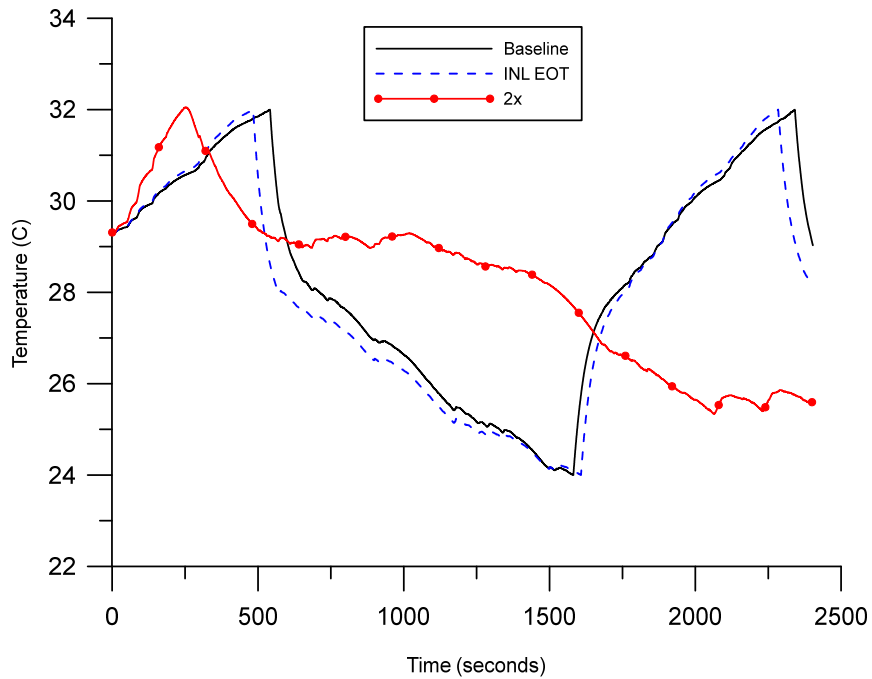


Figure 7.29 – US06 Toronto resistance simulations

All the simulations exhibit the same trend which is the “2x” triggers the cooling event sooner than the baseline or “INL EOT” scenarios. The important feature to note is that aggressive highway driving coupled to ageing/high mileage cells will lengthen the cooling cycle duration measurably and in time may present situations that severely tax the cooling system capabilities, similar to Davis Dam.

7.7 Workday and Weeklong Analysis

The drive cycles provided analysis on the cell temperature under different driving and environmental conditions using Autonomie and the thermal equivalent circuit model developed. Further capabilities of the thermal equivalent circuit allow for analysis of conditions a battery pack may experience when parked. Such scenarios are investigated along with a typical workday operation of the vehicle. The 24 hour and 7 day climate data for the hottest day of the year (mid-August 2015) in Mesa, Arizona is simulated with various quiescent cooling rates. Climate data and initial conditions for the battery components are the same as used for the test week initial condition simulations. The road radiation source temperature is identical to the ambient conditions due to under vehicle shading. The average ambient wind speed is used for the air flow under the vehicle.

Background cooling rates of 0 W (“No cooling”), 20 W, 50 W and 100 W are invoked whenever the vehicle is parked to suppress the heat flux from the environment. This concept can be envisioned as a solar powered or self-energized thermoelectric heat pump system. A “No cooling” case serves as a baseline for comparison of the cooling and isolation efficacies. The quiescent cooling scenario implicitly assumes that the vehicle is not plugged in and thus self-reliant, not impacting battery energy reserves. One might consider a solar panel trickle charging the battery pack during the day with a background cooling system in continuous operation (24/7) or as needed.

Figure 7.30 shows a static vehicle outdoors in the Meza, Arizona area for 24 hours beginning at 7 AM on August 12th 2015 where the cells have a starting temperature of 35.4°C. The various cooling scenarios show the time delayed response the battery pack experiences, attributed to the thermal mass of the system. When no cooling is applied, the cell temperature approaches a maximum of 40°C three hours after peak ambient conditions. With 20 W of cooling applied, the peak temperature recorded is 37.5°C. 32°C is the programmed setpoint the vehicle utilizes for active cooling. 50 W of cooling reduces the peak temperature to 33.1°C, which appears acceptable given that over the 24 hour period the cells actually decreased in temperature. A constant cooling rate of 100 W would be excessive as this brings the cell temperature below 20°C. Interpolating the results indicates a cooling rate of 75 W would be more than sufficient to maintain cell temperature within the setpoint range of 24-32°C.

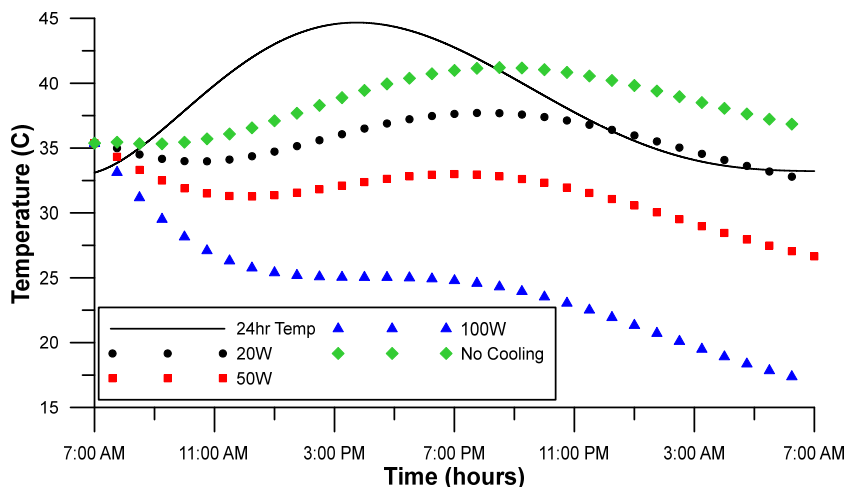


Figure 7.30 – 24 hour soak period with various cooling rates

The work day scenario (Figure 7.31) with cell heat generation occurring is also simulated under Mesa ambient conditions. On a simulated work day, it is assumed that the individual leaves for work at 7:30 AM and arrives home at 6:00 PM with a travel time of 30 minutes in each direction. The vehicle remains parked outside in the interim. To model the heat generation of the cell during the travel time, three consecutive US06 cycles are simulated. Active cooling keeps the battery within an optimal temperature range of 24°C to 32°C during the drive portions. S_{fluid} remains at constant low quiescent levels (same rates as previous case) between 8:00 AM to 5:30 PM and 6:00 PM onwards. The no cooling case reaches a temperature of 38.5°C before the drive home. The second driving event brings the cell temperature to 24°C but it continues to rebound to 36.6°C once stationary. The results for 20 W of cooling marginally improves the situation however, the temperatures when stationary are still above the optimal temperature range. The cells maintained with 50 W of cooling stay nicely within the setpoint range. One may also note that the instantaneous cell heat generation rate through the drive cycle spikes to approximately 35 W/cell. Fortunately their thermal mass mitigates this and the average current level throughout the drive cycle of 80 Amps is low enough to set the average heat generation to approximately 600 W which is easily overcome by the active cooling system.

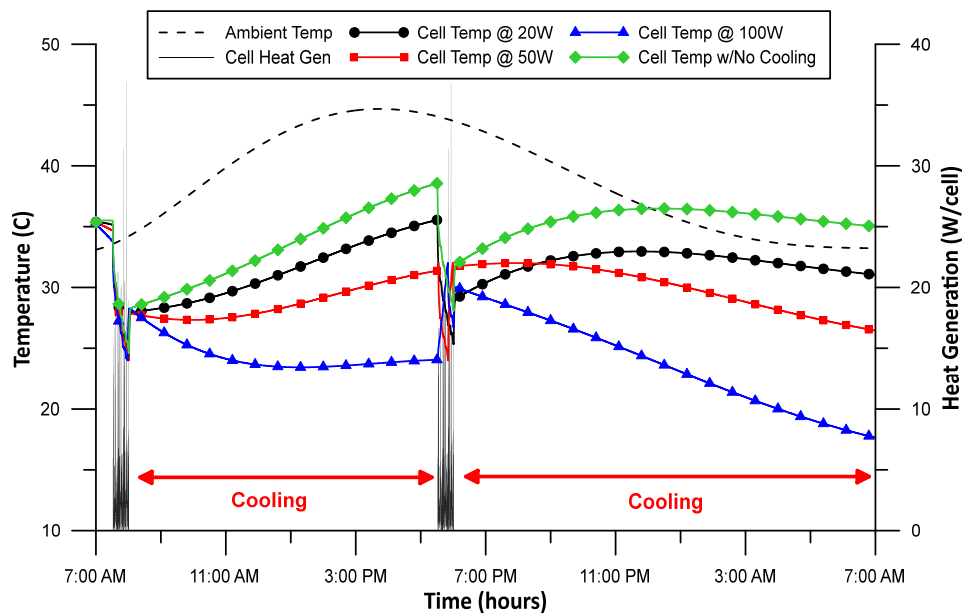


Figure 7.31 – Simulated workday with cell heat generation and quiescent cooling

A 7 day static condition during the test week in Mesa, Arizona is simulated in Figure 7.32 under the same background cooling conditions with the mean temperature shown in the legend. When no cooling is applied the cell temperature does not reach the peak ambient, however, the mean cell temperature is the same as the ambient mean. As observed one can take note of the time shift between ambient and cell temperature peaks of about 4 hours. A mean temperature of 27°C with 50 W of cooling cycles the cells within their optimal range, so one might consider that as a target value for quiescent background cooling.

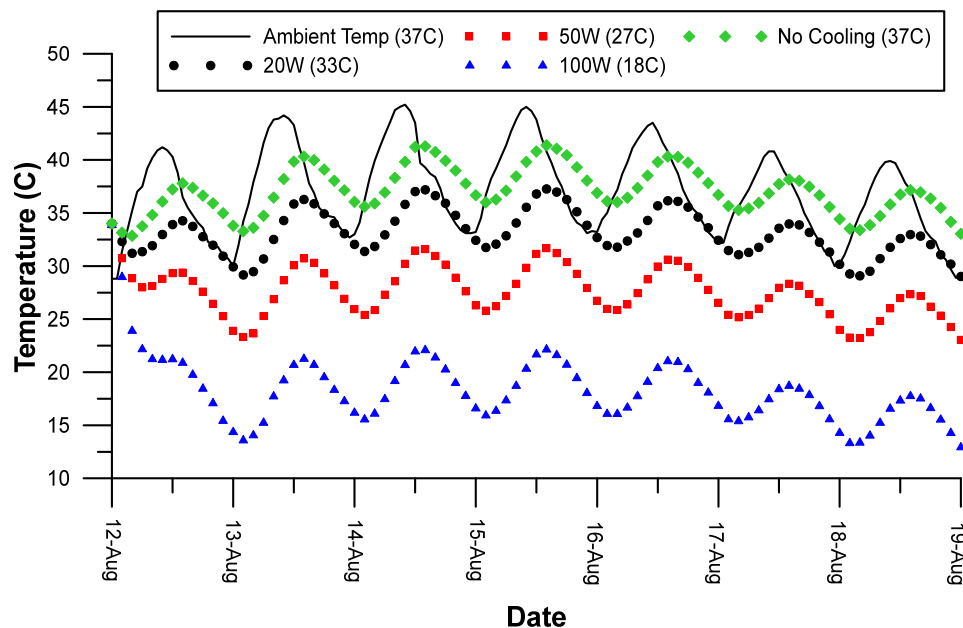


Figure 7.32 – 7 day static simulation with various cooling rates

7.8 System Improvements

The previous sections detailed the design and operation of the production EREV in various simulated scenarios which provided a baseline operation of the thermal management system. The flexibility of the cooling logic and thermal equivalent circuit allow for improvements to the baseline system to be investigated. Two proposed improvement will be investigated which are changes to the thermal setpoints and the implementation of additional insulation.

7.8.1 Thermal Set Point Simulations

The EREV initiates the thermal system when the cells reach 32°C and turns off when the cell reach 24°C. To determine if this temperature range is the most efficient, the baseline will be compared with two other setpoints as explained below.

- **35°C to 25°C** – At 35°C the cells are still in a safe operating range. This simulation will examine the performance of the system with a slightly higher threshold temperature and greater temperature delta. These setpoints should allow for more driving time before the system activates.
- **30°C to 20°C** – These setpoints are lower than the baseline system and targets to keep the cells under 30°C. Over the life of the battery pack, the lower operating temperatures could lead to extended battery life.
- **25°C to 20°C** – Unlike the previous setpoints which have a 10°C change in temperature, these points are mean to keep the cells in a tighter temperature range near room temperature. It is expected the thermal system will be more active and the performance will be examined to determine if it benefits the system or is wasted energy.

Two drive cycle examples are simulated, the US06 and LA92 FC cases in the Toronto region. Simulations in the Mesa regions begin the simulations above 40°C and in the case of the US06 drive cycle, it ends with the cell temperature at 27°C. The elevated starting temperature does not allow for a comprehensive comparison for the proposed setpoints. Furthermore, the San Francisco region did not have many cooling events in any of the drive cycles given the 18°C starting temperatures. Therefore, the US06 and LA92 in the Toronto region are the best scenarios to simulate given starting temperature of 29°C and the multiple cooling events observed. Figure 7.33 shows the setpoint simulations for the US06 drive cycle.

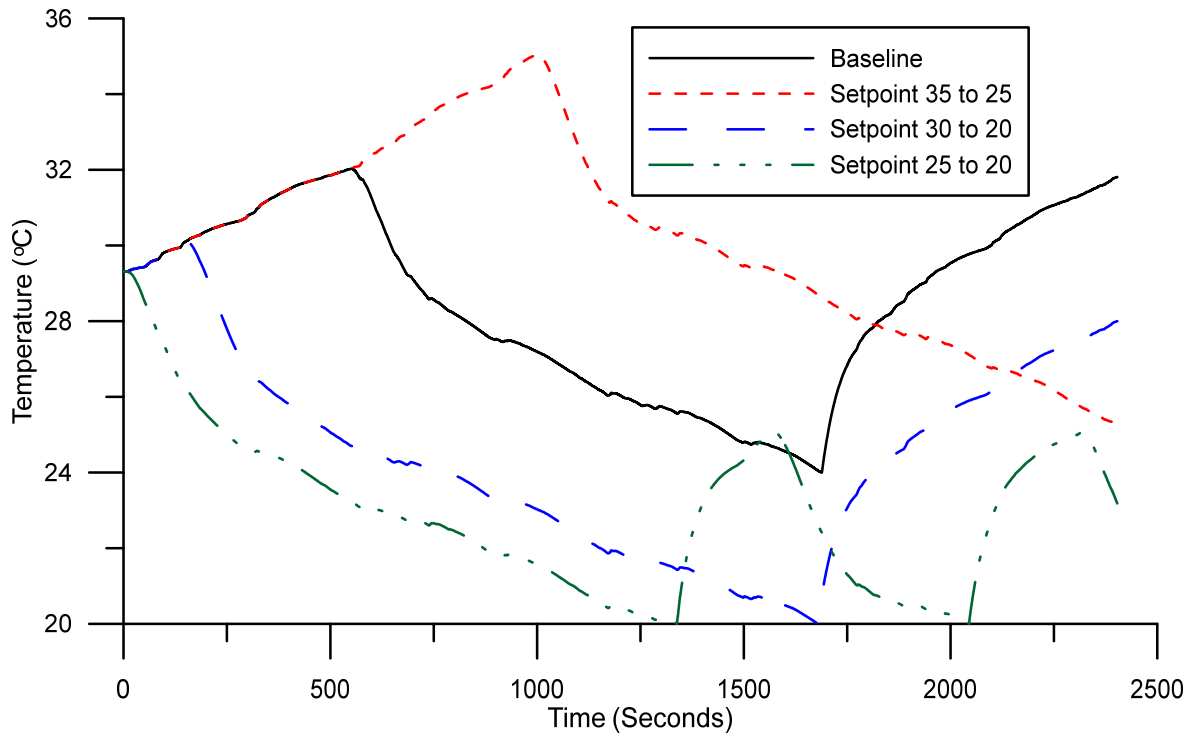


Figure 7.33 – Cell temperatures for the Toronto US06 thermal setpoint simulations

The baseline thermal cycle initiated at 564 seconds and lasted 1084 seconds. Comparing the baseline to the other simulations, the setpoint at 35°C was triggered at 1015 seconds, 451 seconds longer than the baseline trigger and the length of the cooling cycle was 5.5 minutes longer. By contrast, the 30°C setpoint was triggered sooner than the baseline with a shorter cooling cycle length. The 25°C setpoint has multiple cooling events separated by 250 seconds. Figure 7.34 shows the setpoint simulations on the LA92 drive cycle where the pattern is similar.

The two drive cycles presented indicate that lowering the setpoint range stretches the duration of the operating cycle. For the setpoint with a 5°C delta, the compressor power and cooling load is not fully captured as 250 seconds is not enough time for the high and low side refrigerant pressures to stabilize. This would result in maximum compressor power more often. The unknowns for the actual compressor profile with different setpoints means it is not clear if average COP is affected, but the higher percentage of transient operation is likely detrimental to the efficiency.

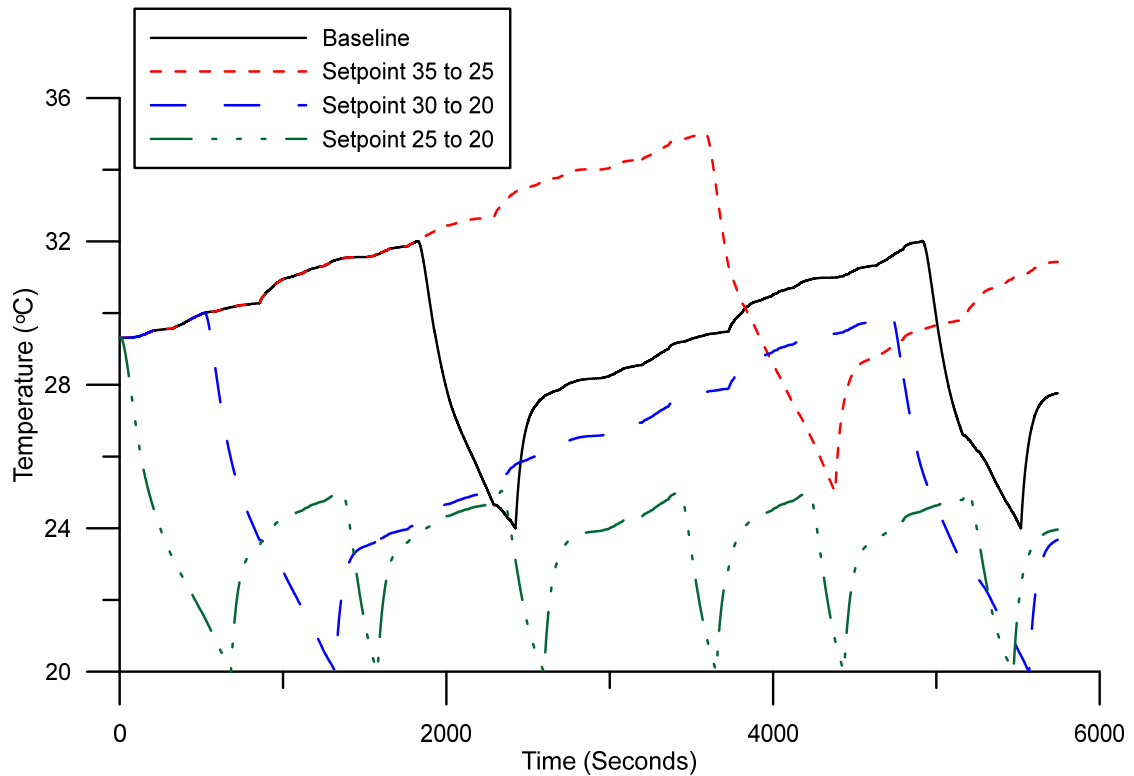


Figure 7.34 – Cell temperatures for the Toronto LA92 thermal setpoint simulations

7.8.2 Addition of Insulation for the Battery Pack

From Section 7.3, the heat analysis during the drive cycles revealed the shield and cover components had the highest percentage of heat flow. While the internal components are not easily modified, the cover and underside of the vehicle allow for insulation to be added without altering the geometry/shape of the battery pack. There are four locations where insulation can be implemented; the first is between the attached shield to the outside of the baseplate. The other locations are the inside and outside of the cover and isolating the cell pouch edge from touching the frame. Insulation in these areas should diminish heat propagation into the battery pack. To analyze the potential benefits, the thermal equivalent circuit is modified. The insulation simulated under the vehicle and around the cover is Aspen Aerogel's Cryogel Z [96]. There are two available thickness, 5 mm and 10 mm blankets. For the space available on the stock battery pack, the 5 mm thickness was selected. For the insulation to isolate the cell edge from the frame, polyurethane closed-cell foam was selected which has a conductivity between 0.02-0.024 W/mK. For these simulations, 0.02 W/mK was selected.

For insulation placed between the road shield and baseplate, the shield resistance and capacitance needs modification. The resistance originally calculated for the shield incorporates a 13 mm airgap between the baseplate and shield. Inserting 5 mm of insulation in this air gap alters the shield resistance. Figure 7.35 shows the addition of the underbody insulation components in the thermal equivalent circuit, with insulation resistance and capacitance of 100Ω and 4.47 F respectively and shield resistance of 43.9Ω .

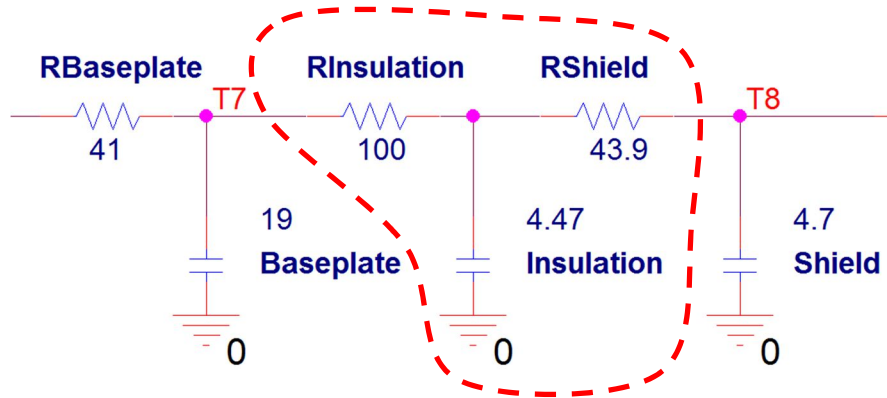


Figure 7.35 – Underbody insulation in the thermal circuit

For an exterior cover, the corresponding resistance and capacitance are calculated to be 45.3Ω and 9.88 F respectively. These are placed between the cover and variable resistor as seen in Figure 7.36. This represents insulation in the air gap between the outside cover and vehicle sheet metal of the underbody (tunnel area).

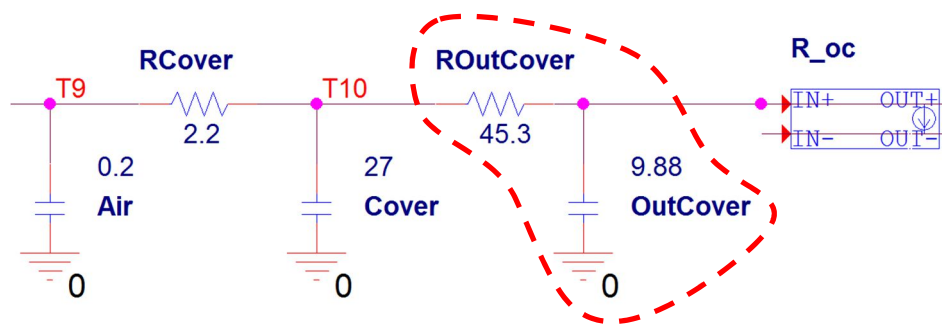


Figure 7.36 – Outside cover insulation implementation

To simulate insulation on the inside of the cover, this requires a re-calculation of the inside air resistances since the 5 mm insulation replaces some of the internal airgap between the frame and cover. The value of the internal air resistances are taken to vary linearly with the

airgap length. The inside cover insulation resistance and capacitance are identical as the outside cover value given the surface areas are approximately the same. Figure 7.37 shows the inside cover insulation circuit with the modified internal air gap resistances and Figure 7.38 is for insulation on both the inside and outside of the cover.

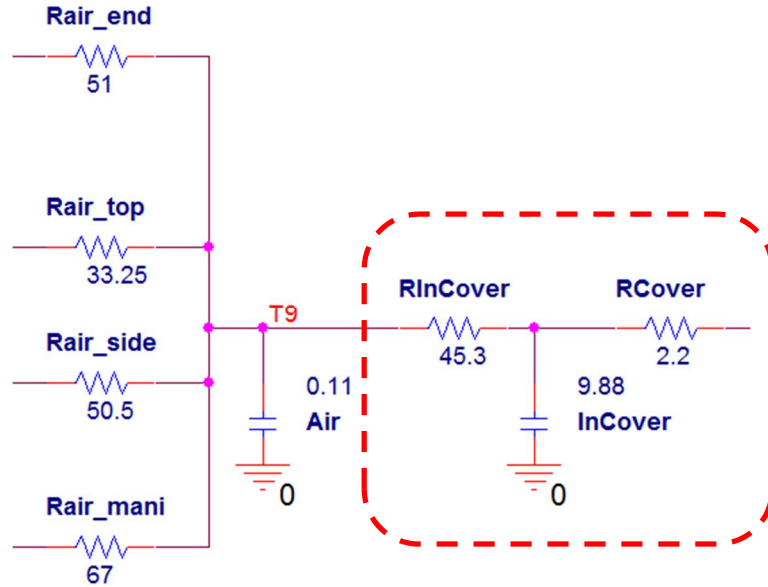


Figure 7.37 – Inside cover insulation implementation

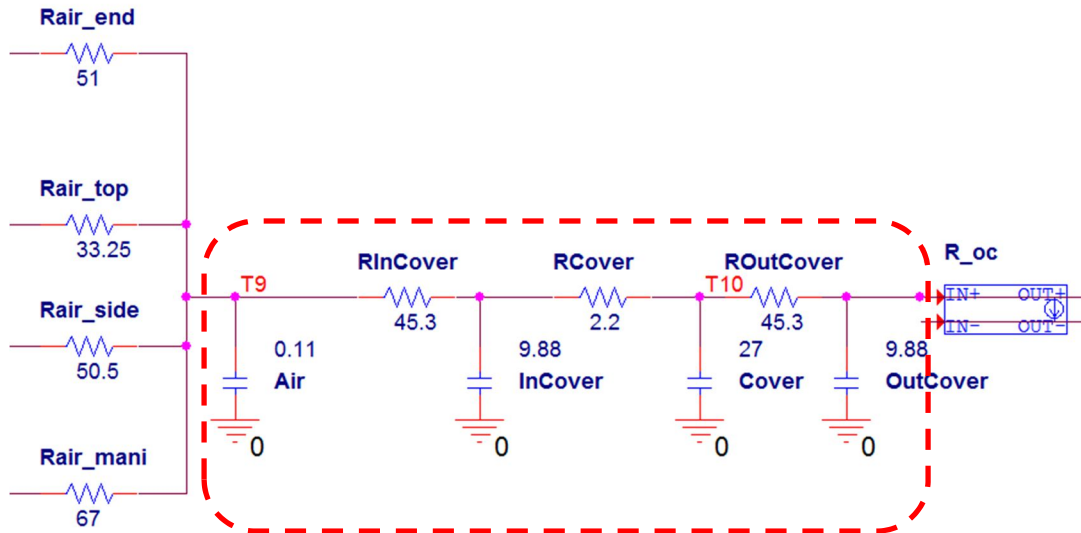


Figure 7.38 – Inside and outside cover insulation

Such fast and easy modifications to the circuit illustrate the exploratory nature of the design and modeling approach. Thermal bridging between the cell and frame is investigated to see how isolating the cell and frame reduces heat influx to the cell and improves cooling capabilities. The placement of the insulation around the cell edge was previously investigated by a Master's student on the research team which is showed good improvements over the base design [97]. A cross-section for the cell and frame configuration is illustrated in Figure 7.39. The sequence of parts is visible which was also shown in Figure 4.20. For the two cells within a single frame, one cell edge is in contact with the frame and another cell edge is held in place with the frame compression tab via the adjoining frame. Figure 7.40 and Figure 7.41 depicts the frame compression tabs on the face of the frame. To incorporate insulation between the cell and frame, it is assumed the cell tabs have been removed from the frame, all other geometry remains the same. Given the size of the compression tabs, removing them has negligible impact on the resistance and capacitance values in the thermal circuit.

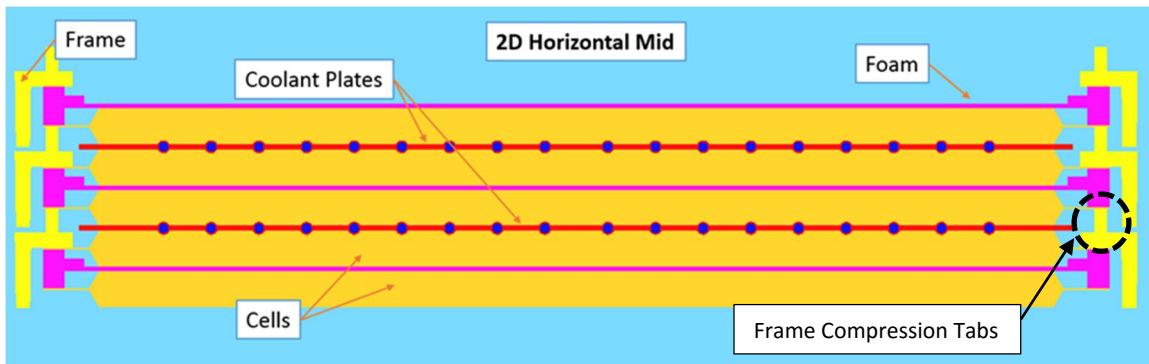


Figure 7.39 – Cell and frame cross-section [97]

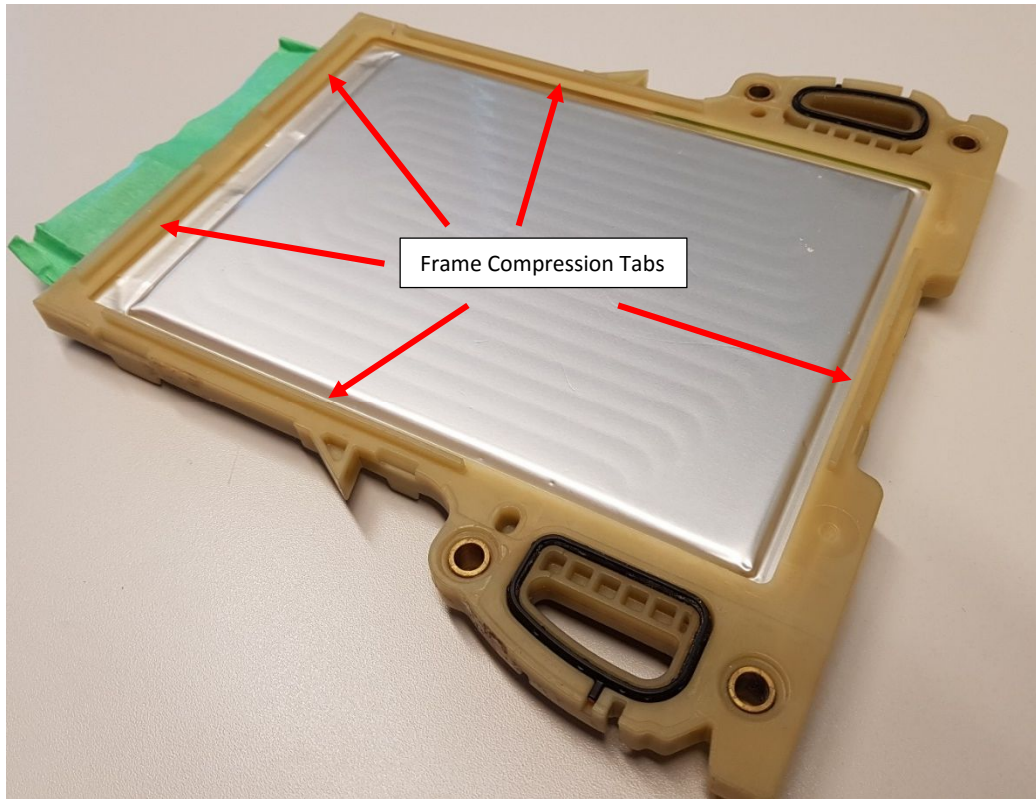


Figure 7.40 – Frame compression tabs

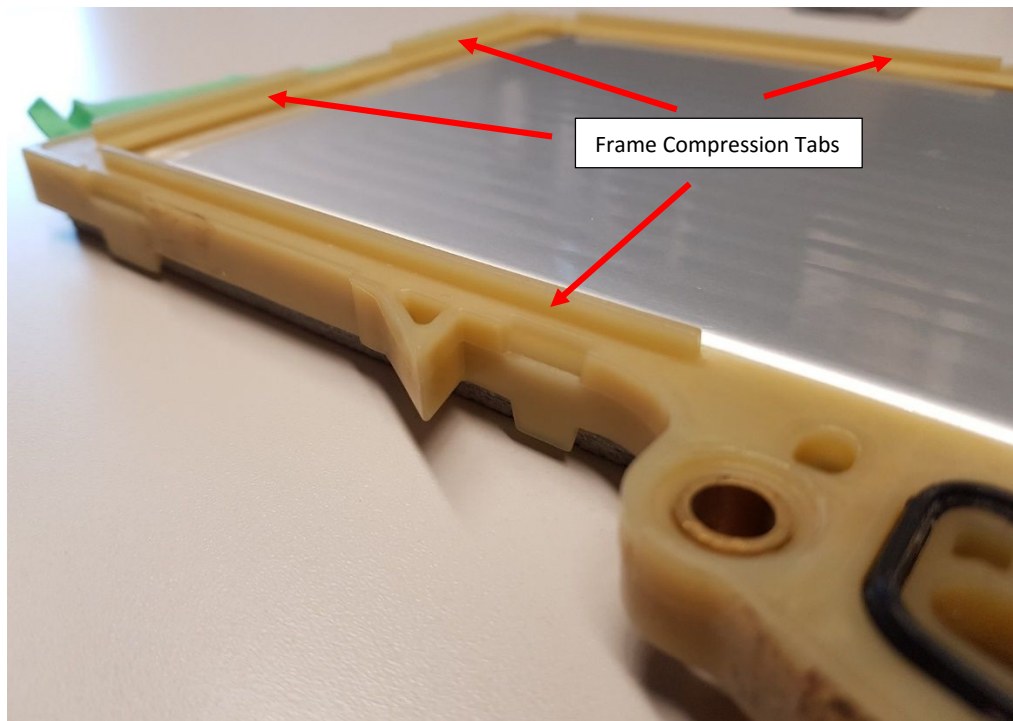


Figure 7.41 – Frame compression tab profile

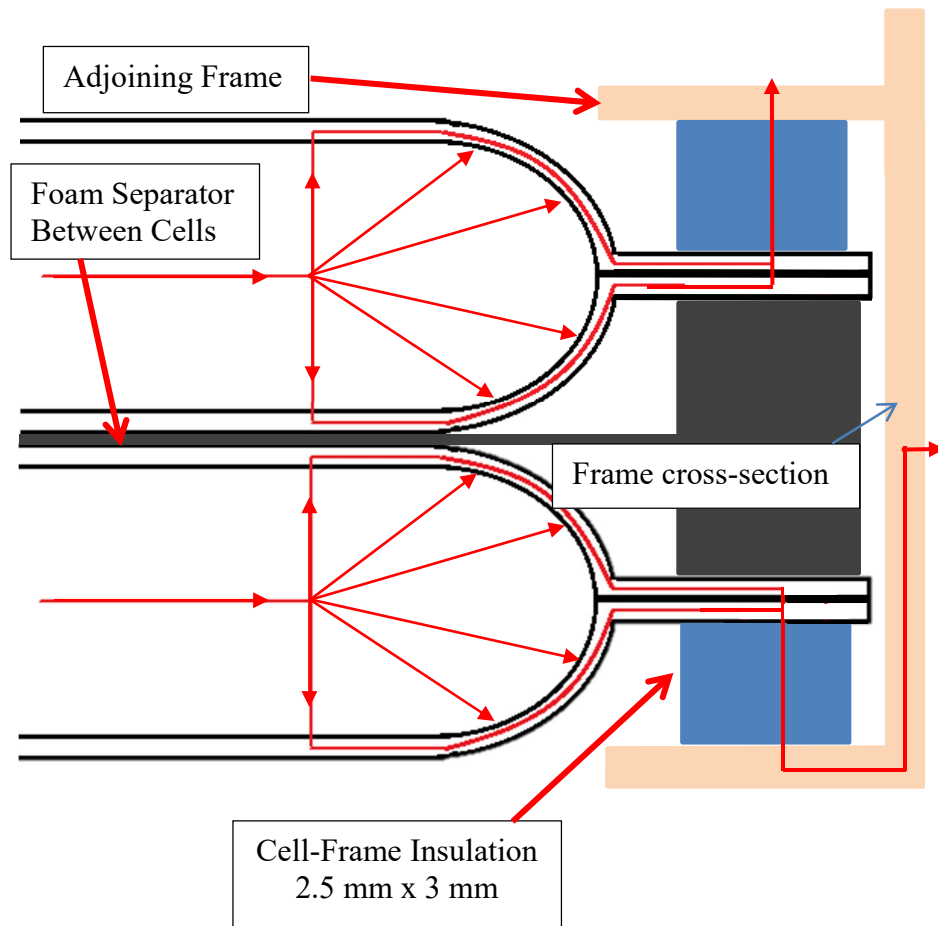


Figure 7.42 – Modified frame section with added insulation

Figure 7.42 illustrates a modified frame with insulation added between the cell and frame. This configuration replaces the compression tab assembly so that the face of the adjoining frame adds compression to the insulation and secures the entire arrangement. The periphery of the cell edge is 5 mm with the top edge near the cell tabs being 10 mm. Therefore, there is a 2.5 mm x 3 mm strip of insulation around the sides and bottom and a 2.5 mm x 5 mm strip at the top. Figure 7.43 is an example of foam placement around the cell edges. The addition of the foam isolation to the thermal equivalent circuit is shown in Figure 7.44 with the calculations outlined in Appendix B.

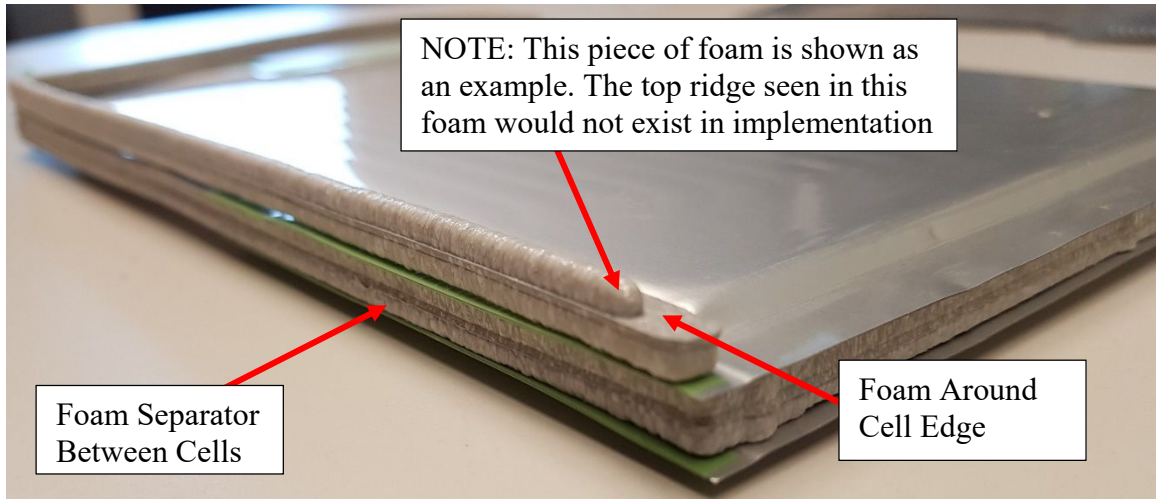


Figure 7.43 – Example of foam around the cell edge

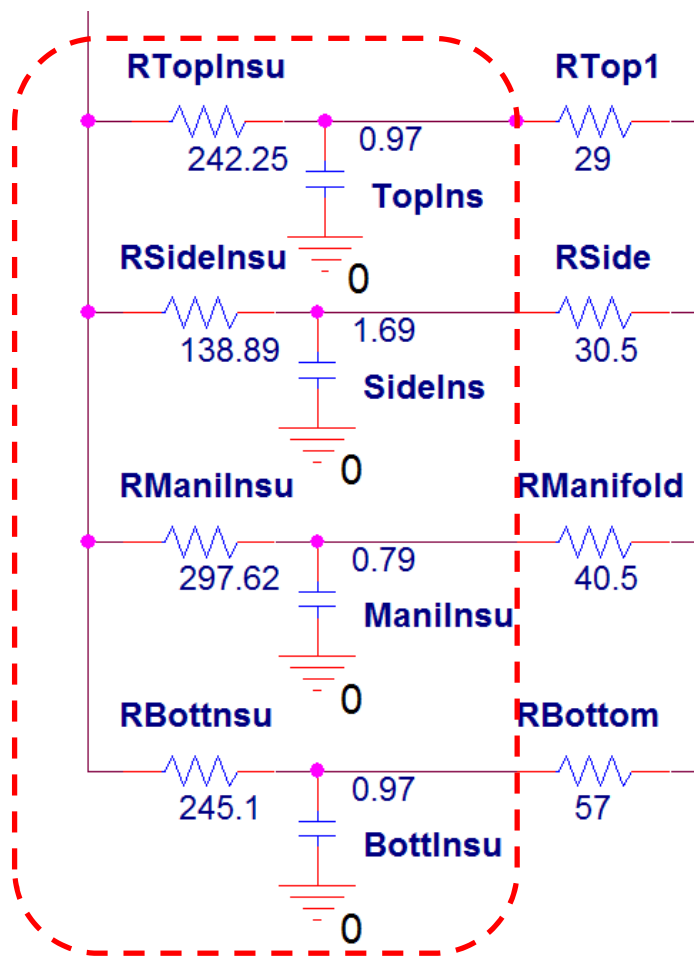


Figure 7.44 – Cell to frame isolation resistance and capacitance added to thermal circuit

To determine which insulation implementation or combination is the most beneficial, the weeklong simulation in the three test regions were run again. On the selected test day, the insulation effects on the cell temperature were examined as before and the thermal circuit with the added insulation was also run on the drive cycles to see potential improvements. The procedure for determining the weeklong regional data with the proposed insulation remained the same. Figure 7.45 shows the added insulation performance against the baseline simulation in Mesa, AZ. The abbreviations used in the plot are as follows:

- Baseplate Insulation – BP
- Outside Cover Insulation – OC
- Inside Cover Insulation – IC
- Cell to Frame Insulation – CF

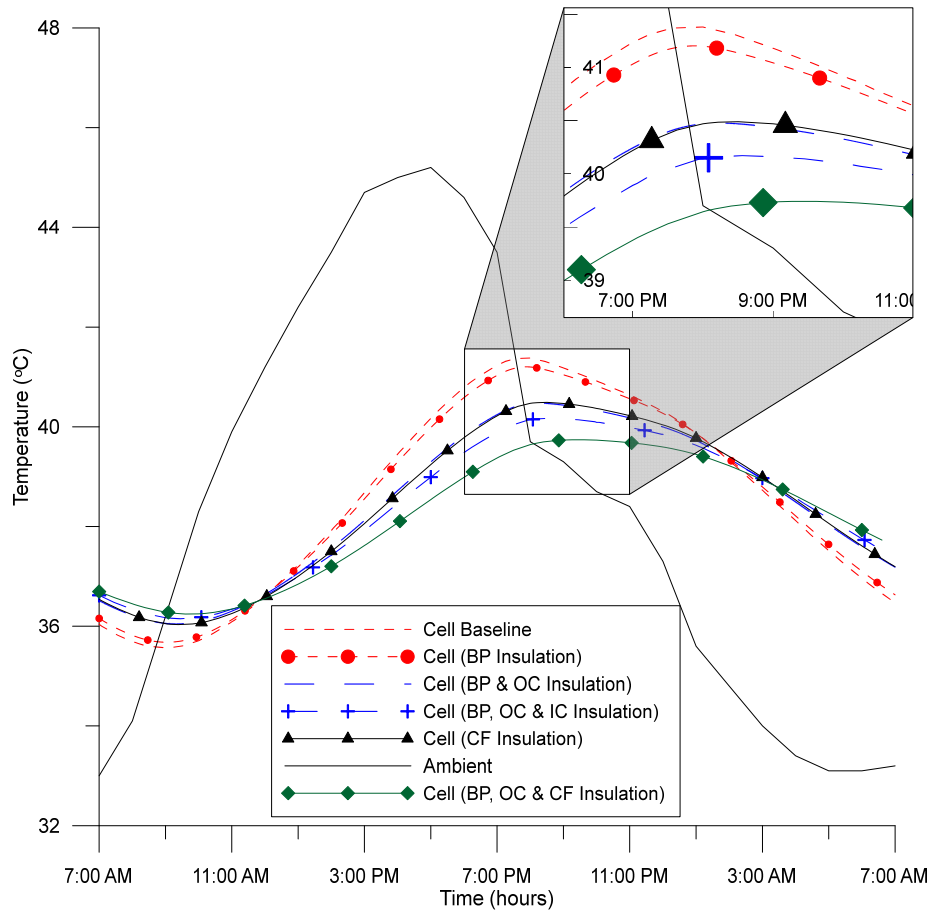


Figure 7.45 – Mesa, AZ test day cell temperatures with added pack insulation

The baseline simulation had a peak cell temperature of 41.4°C whereas the simulation with added baseplate insulation peaked at 41.2°C, a negligible improvement. When baseplate and outside cover insulation is simulated, the peak cell temperature becomes 40.5°C, 0.9°C drop, and when insulation is added to the inside cover, the peak temperature goes down to 40.2°C. This shows the gradual additive effects. However the single most significant addition is the cell to frame insulation which is equivalent to the baseplate and outside cover insulation combined. The maximum effect achieved with all three insulations present was a 1.6°C drop. These results are extended to the San Francisco and Toronto test days which can be found in the Appendix G. Based on these results, three combinations of insulation were simulated on the drive cycles (BP & OC, CF, BP-OC-CF). Figure 7.46 shows the regional results for the US06 drive simulations with the insulation implementations as compared to the baseline. The results discussed for the US06

simulations are extended to the UDDS and LA92 simulations (shown in Appendix G) as they display the same trends.

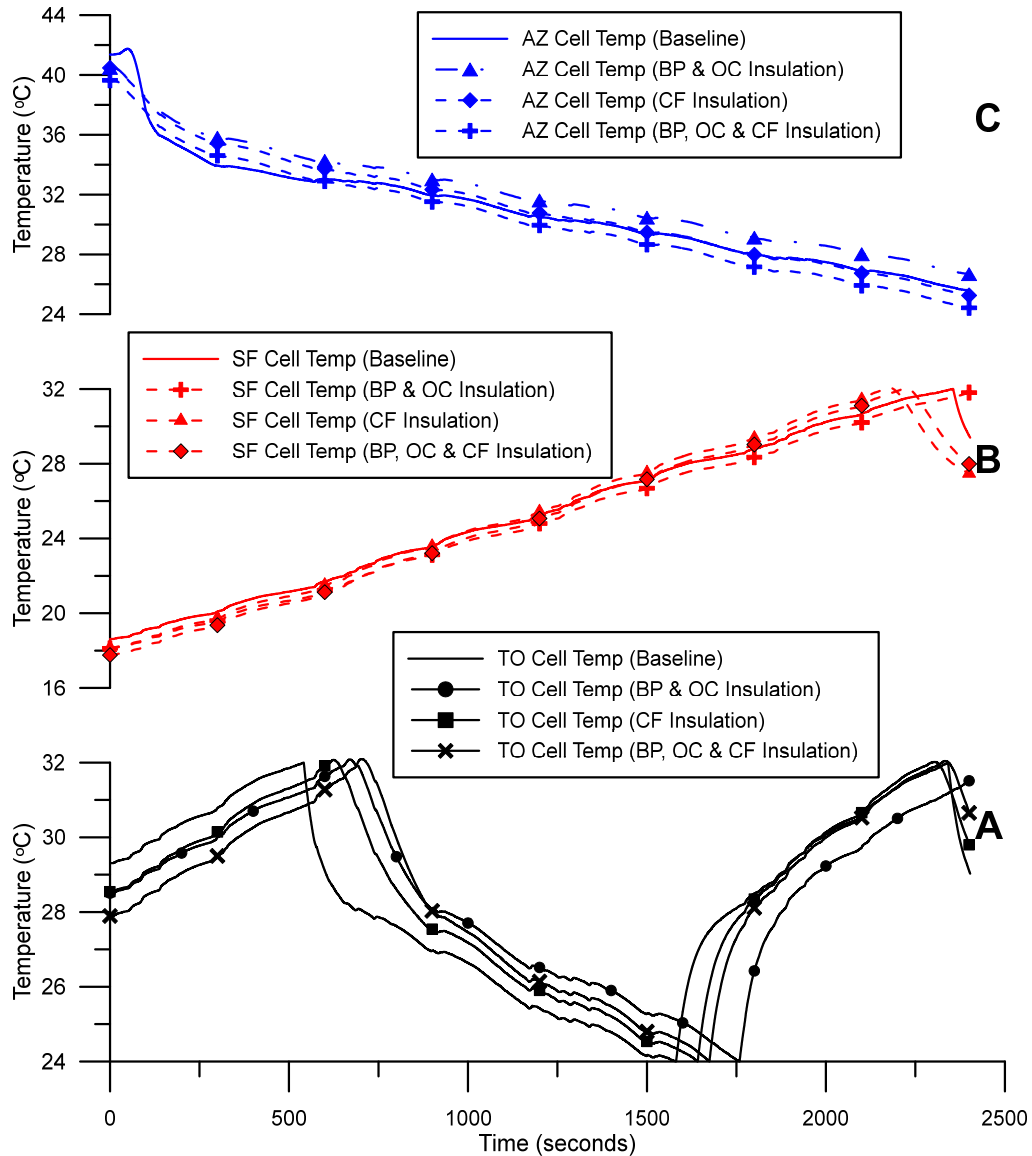


Figure 7.46 – US06 regional simulations with insulation implementation, A: Toronto, B: San Francisco, C: Mesa

For the Toronto simulations (Figure 7.46A), all the cases with added insulation begin the cycle 1-1.5°C lower than the baseline. This leads to the insulated cases triggering the cooling system operation approximately 125 seconds later. Towards the end of the cycle, the second cooling event isn't even triggered in the BP-OC case, this is not observed for the other cases as insulation situated around the cell edges lowers their effective thermal

mass, so they heat a little faster prior to the cooling system turning on. The cooling rate pull down within the first 150 seconds decreased to 1.6°C/min (a 0.4°C/min drop). However, the total cooling event was 20 seconds faster than the baseline. This trend was also observed with the UDDS and LA92 Toronto simulations where there were improvements between 32-114 seconds resulting in a shorter cooling cycle. The San Francisco simulations (Figure 7.46B) show a negligible change in cell temperature between the simulations. The BP-OC simulation was the only one to complete the drive cycle without having the cooling becoming active. The other cases which include the CF insulation triggered the cooling event approximately 162 seconds earlier than the baseline. The Mesa simulations (Figure 7.46C), increased the cell temperature 0.4°C or remained unchanged. The BP-OC-CF case in Mesa performed better than other simulations by reducing the cell temperature at the end of the cycle by 1.2°C over the baseline. For this case, because the cooling system is always operating the insulation directed more cooling to the cells without losing it to the surrounding packaging. Comparing such results to the UDDS and LA92 drive cycles, the Toronto and San Francisco regions exhibit the same type of differences between the insulation cases and baseline simulations. The overall lesson is that although the decoupling of the cell's thermal mass with that of the cell retention frames lowers the thermal mass of the core region, it also cools more quickly and effectively once the cooling system operates.

The heat flow through the components was analyzed to quantify noticeable effects on the thermal system's distribution of cooling towards the cell and internal components with insulation added. The average environmental heat flow through the cover and baseplate components were significantly reduced for the BP-OC case. The frame components also saw a decrease in heat flow when there was only CF insulation, while other components saw increasing heat directed to paths in the circuit. When there is insulation placed everywhere (BP-OC-CF) the frame components see further decrease over the baseline. Table 7.4 shows the US06 Mesa average heat flow percentage comparison for the insulated and baseline simulations.

The addition of insulation on the baseplate and outside cover did not affect the distribution of cooling power towards the cell and frame components it only holds back the environmental ingress. Here the results for the cooling power were near identical for the

insulation and baseline cases and showed approximately 90% of the cooling directed to the cells and 10% to the internal packaging. However, for the cases where insulation was placed around the cell edges it did significantly increase the amount of cooling directed to the cells. Examining the US06 case, the simulations in Toronto saw near 100% cooling directed to the cells and Mesa simulations saw approximately 95% directed towards the cells. This is a notable improvement over the 90% observed for the baseline simulations. Figure 7.47 and Figure 7.48 graph these findings.

Table 7.4 – US06 Mesa Average Heat Flow Comparison

Component	Baseline %	BP & OC Insulation %	CF Insulation %	BP, OC & CF Insulation %
Frame Side	13.08	18.33	13.17	9.29
Manifold	9.56	14.39	3.99	1.40
Frame Bottom	16.87	20.16	10.10	12.48
Frame Top	13.40	17.71	8.52	6.61
Top BMS	4.00	7.65	5.80	10.38
Baseplate	7.66	2.05	14.16	8.27
Shield	8.16	2.38	18.56	11.48
Cover	16.87	4.41	21.74	11.78
Endplate	10.02	12.70	41.77	37.99
Bulkhead	0.39	0.22	1.15	1.27

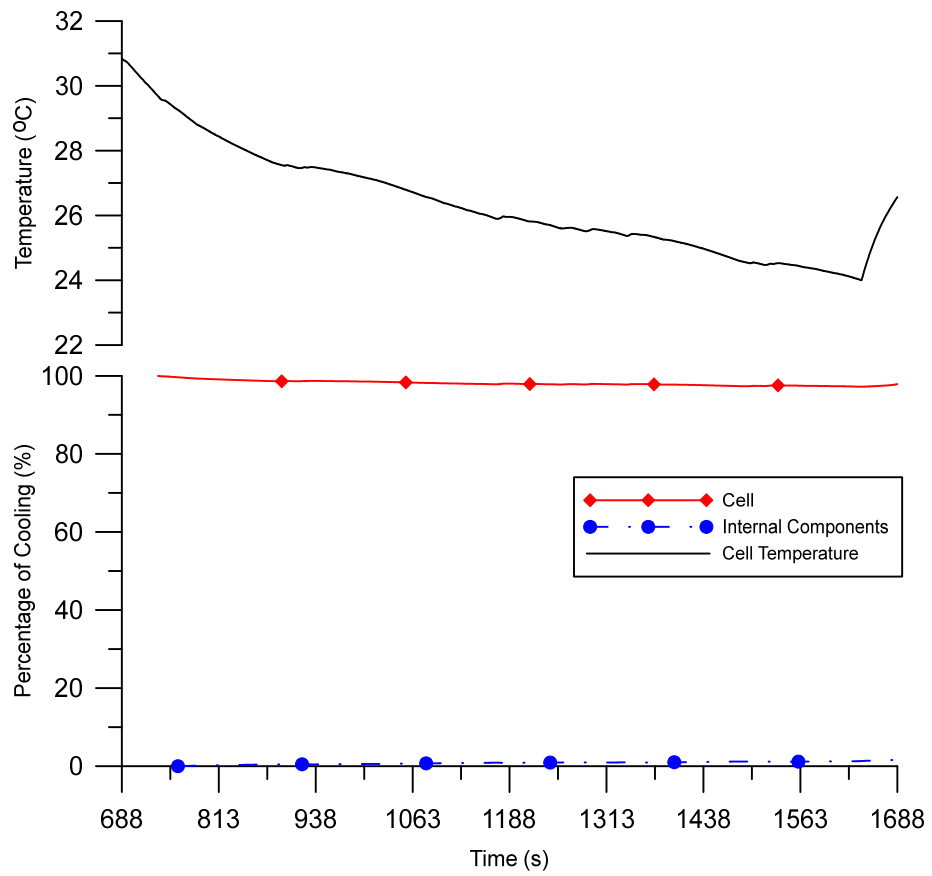


Figure 7.47 – US06 TO simulation with CF insulation

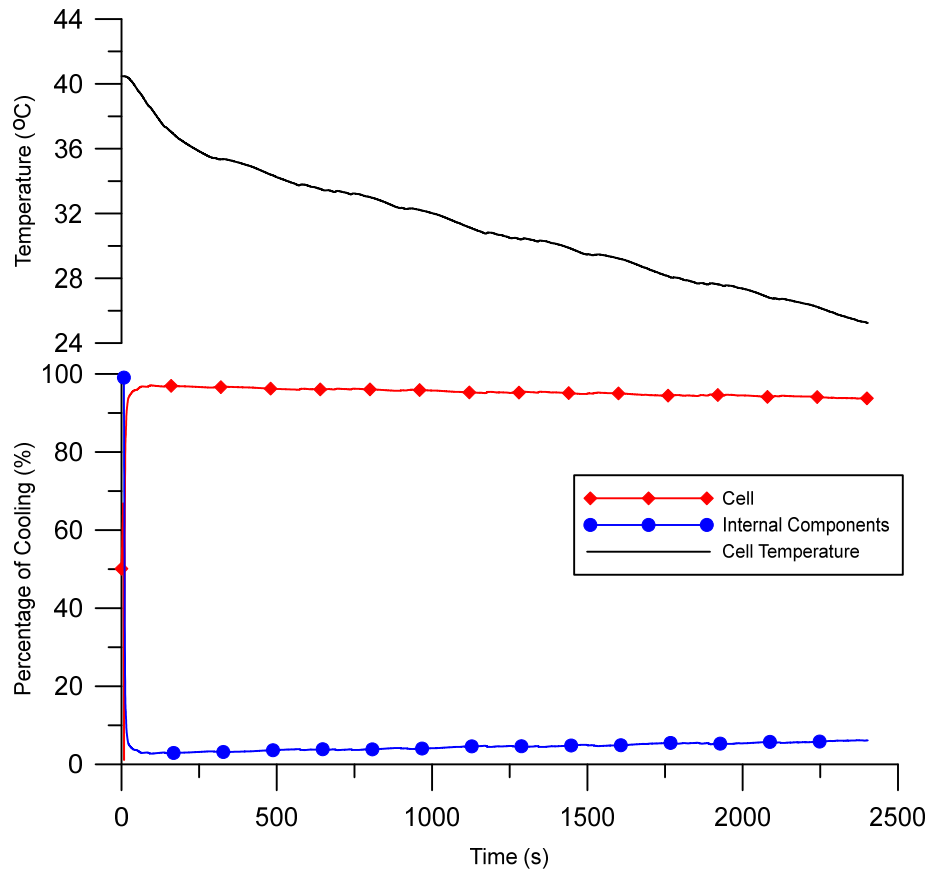


Figure 7.48 – US06 Mesa simulation with CF insulation

Examining the cell and frame insulation on the 24 hour workday with different quiescent cooling rates, improvements are also observed. Figure 7.49 shows the results with the change in temperature at key points. During the first quiescent cooling portion of the simulation, all the temperatures were lower towards the beginning of the second driving event. At the end of the second cooling event, the quiescent cooling again lowered the cell temperatures. These results indicate the CF insulation can improve the quiescent cooling abilities due to a greater fraction of the cooling capacity directed towards the cells. As the cooling power decreases this effects is ever more important. The baseline results (Figure 7.31) concluded 50 W would be sufficient to maintain the cell temperatures around 25°C, these new results show 20-50 W of quiescent cooling would now be more than sufficient which is up to a 60% decrease in power requirement and renders the idea even more feasible.

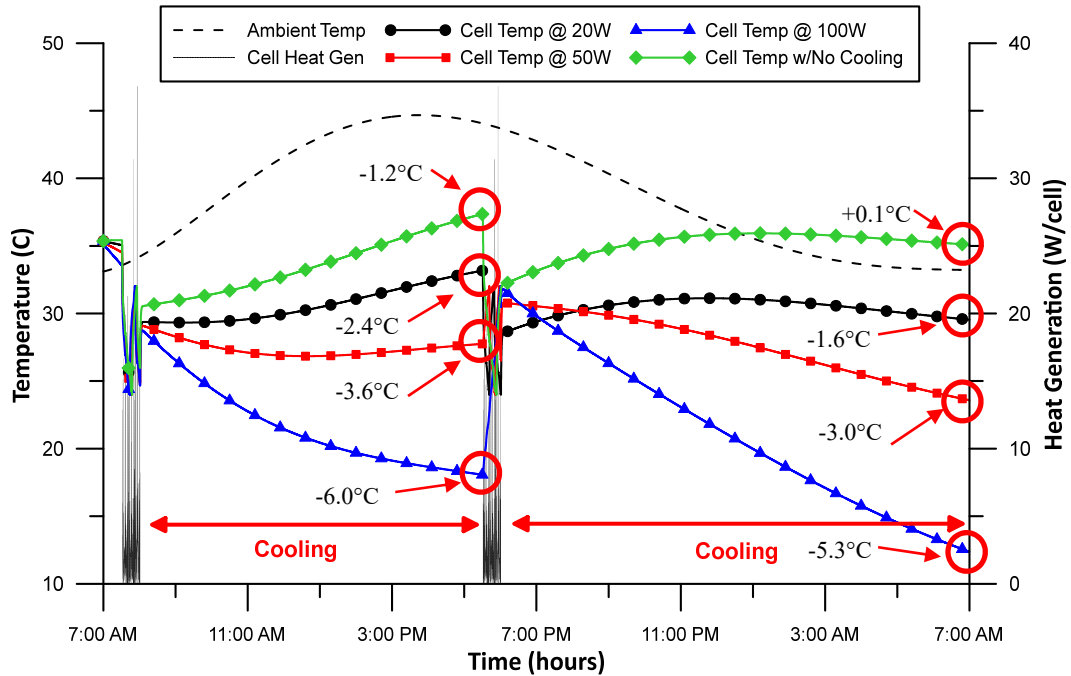


Figure 7.49 – 24hr workday simulation with CF insulation and quiescent cooling

7.8.3 Cold Weather Simulations

This section briefly examines how colder weather affects the cell temperatures and heat flow in the battery pack. The results presented are simulated in Toronto on the US06, UDDS and LA92 drive cycles. The test day has been identified as December 12th 2015 at 7:00 AM to simulate a morning commute. The time of day and initial conditions were identified using the 7 day static simulations presented in Chapter 5. On the test day, the ambient temperature was 2.1°C and at 7:00 AM the sun had not risen. A colder day was not selected due to the findings of INL [54] where it was shown the Chevrolet Volt engine cycled on at outside air temperatures below -3°C. The controller in the Autonomie model does not have a specific function programmed, and the exact trigger conditions are unknown therefore, simulations at the lowest outside temperature before the engine cycled were utilized. All simulations begin with the vehicle fully charged. Table 7.5 summarizes the change in cell temperature over the drive cycles. These changes are in line with the amount of heat generation through the respective drive cycles. Figure 7.50 depicts the heat flow across the external battery pack components with the cell retention frame as the reference point for all heat flow emanating to or from the cells.

Table 7.5 – Cell Temperatures on Simulated Cold Drive Cycles

Drive Cycle	Starting Temp	End Temp	ΔT
US06	4.93°C	18.33°C	+13.4°C
UDDS	4.93°C	7.72°C	+2.79°C
LA92	4.93°C	13.91°C	+9.0°C

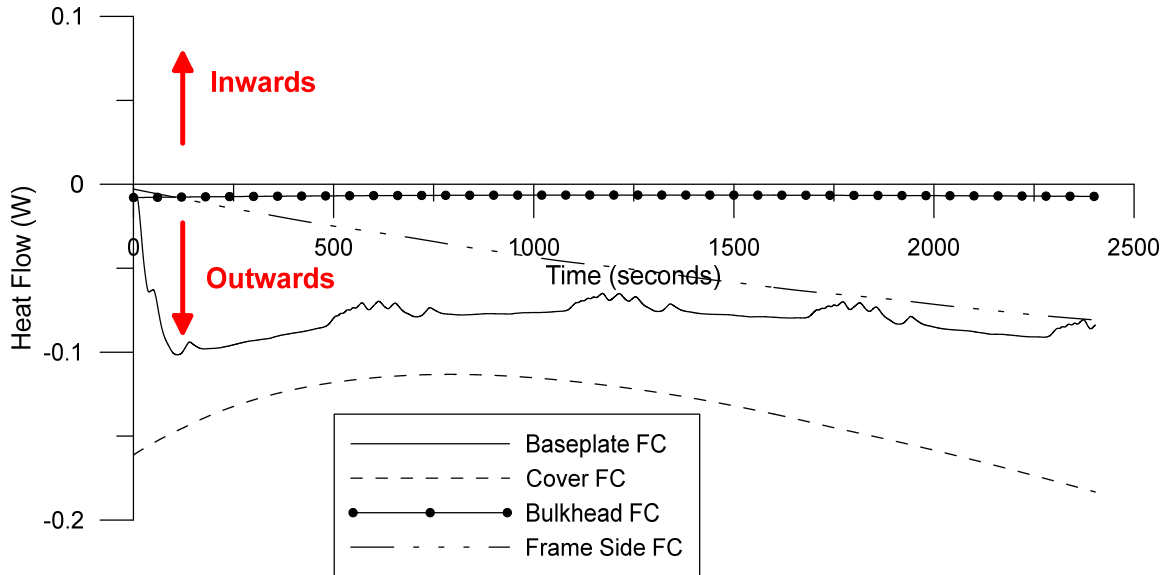


Figure 7.50 – Toronto US06 external component heat flow for fully charged (FC) cold simulation

The figure shows there is really only outward heat flow, which is to be expected. The simulations on the UDDS and LA92 drive cycles exhibit the same trends in Appendix H. Cell ambient temperature was approximately 3.8°C above ambient as a result of timelag with the diurnal fluctuations. Table 7.6 and Table 7.7 recounts the results of the cell temperatures with CF and BP-OC-CF insulation added.

Table 7.6 - Cell Temperatures on Simulated Cold Drive Cycles with CF insulation

Drive Cycle	Starting Temp	End Temp	ΔT
US06	5.81°C	20.64°C	+14.83°C
UDDS	5.81°C	9.07°C	+3.26°C
LA92	5.81°C	15.98°C	+10.17°C

Table 7.7 – Cell Temperatures on Simulated Cold Cycles with BP-OC-CF insulation

Drive Cycle	Starting Temp	End Temp	ΔT
US06	6.55°C	21.46°C	+14.91°C
UDDS	6.55°C	9.88°C	+3.33°C
LA92	6.55°C	16.78°C	+10.23°C

Firstly, addition of any insulation results in an increase in the starting cell temperature. Insulation around the cell edge (CF) increased the starting cell temperature by 0.9°C whereas also adding insulation inside and outside the pack (BP-OC-CF) increased the starting cell temperature by 1.6°C. Net heating of the cell by the end of the drive cycle is virtually unaffected by the exterior insulation (BP-OC).

7.9 Summary of System Improvements

This section outlined potential improvements to the baseline configuration of the EREV thermal system and battery pack. Raising the upper setpoint to 35°C changed when then thermal system became active, to reduce the number of cooling events over the drive cycle.

Insulation was added to the circuit model between the baseplate and shield as well as around the outside cover. The results demonstrated the ability to lower the initial cell starting temperatures in the Toronto and San Francisco regions. This lead to the thermal system activating at a later time. However, in the Mesa region, the cell temperature increased or stayed at the same point for the beginning of the drive cycle. There were no notable gains. Only with insulation added to the cell edges was the cooling system able to direct a greater percentage of its output towards the cells. The distribution of cooling towards the cell and internal components remained a 90%/10% split respectively with only external insulation.

Once insulation was added between the cell edges and frame the simulations showed the ability to lower the initial cell starting temperatures in all regions. However, this lead to the thermal system activating earlier than the baseline simulations, an unexpected consequence of isolating the thermal mas of the cells. Even though the thermal system was

triggered sooner, it improved the distribution of cooling towards the cell, increasing it from 90% to near 100% in the US06 Toronto simulations. In Mesa simulations, the cooling distribution improved to 95% from 90%. When insulation around the cell edges was combined with insulation on the baseplate and outside cover, the starting cell temperatures were further lowered but did not substantially affect the cooling directed towards the cells. The analysis showed this configuration was the most beneficial overall as it brought the cell temperature closer to the diurnal average while lowering the cell starting temperatures and improved the cooling directed to the cells. However it is the most expensive proposition.

Cold weather simulations showed the heat was flowing out of the system. When outside insulation was added to the cold weather cases, it increased the starting cell temperature, a benefit. With the cell edge insulation present; baseplate and outside cover insulation addition provided the best results compared to the baseline.

These results can be summarized: The addition of insulation overall helped reduce the initial cell temperature for the simulations and significantly improved the cooling efficiency. More specifically if the goal is to get close to the diurnal average, adding insulation around the outside of the pack is effective. Introducing insulation at the core (cell to frame) aids in directing more cooling/heating power directly at the cells and isolates their thermal mass from everything else. This causes earlier cooling system operation in a drive cycle and may increase the number of operating cycles, so a wider setpoint gap may be needed to compensate. Changing the thermal system setpoints proved to have a tangible effect on the performance of the vehicle and is an easy implementation through software. It may be remarked that the early transient portion of the cooling system is considered inefficient as a large slug of fluid in the lines that has absorbed heat must first be cooled before anything can be directed at the battery pack, so suppressing the number of transient events is desirable.

CHAPTER 8 - SUMMARY AND CONCLUSIONS

8.1 Summary

As the number of HEVs, EVs and vehicles that bridge across these architectures increase globally, a well-designed BTMS is required to keep the battery system in an optimal temperature range. This thesis investigated the development of a full vehicle simulation integrated with a BTMS design that included all relevant battery components and environmental conditions to understand how battery packing affects the thermal system. The absence of a full vehicle simulation with a detailed BTMS in previous studies is the motivation for the research presented in this thesis. In Chapter 4, a production EREV model developed in Autonomie was validated against published and experimental data. Chapter 5 showed the BTMS represented as a thermal equivalent circuit model in PSPICE which was validated against laboratory experimental results. The flexibility of the thermal equivalent circuit analysis then allowed for drive cycles in different global regions to be simulated including the effects of wind, solar, road gradient and dynamic ambient conditions; most of which have been neglected in previous studies. The heat flow and cooling capabilities of the battery pack were presented in Chapter 7 as well as proposed system improvements.

8.2 Conclusions

1. The Autonomie model described in Chapter 4 gave the ability to simulate drive cycles with little error and outputs necessary results. The degree of accuracy attained is based on the validity of the components being modeled. Without independent data to compare against and/or one's own experimental data, it is difficult to verify the applicability and accuracy of the outputs the vehicle simulations are producing. While the vehicle simulated in this thesis was a Chevrolet Volt, any vehicle and architecture can be simulated utilizing the approach outlined here since the EREV design represents the most complex arrangement possible. Vehicle testing proved to be a crucial element to gathering data that would not have been otherwise available. For vehicle testing to be effective, a test plan needs to be created to solve for unknown

variables. Furthermore, being able to access many signals through the vehicle CANbus with the appropriate database to decode strengthened the results generated. Given the published INL dynamometer and battery pack data and experimental results collected firsthand to compare against, the model developed was deemed capable of completing the selected drive cycles well below the acceptable practice 2% trace error.

- a. The largest error generated was a 0.53% trace miss on the LA92 cycle.
 - b. The model created was capable of mimicking custom road tests run by the research group that included road gradients and solar load. This is a step beyond ordinary drive cycle schedules.
 - c. The voltage, SOC and current outputs from the model generated less than 5% error under multiple complex validations.
2. Calculations concluded the battery pack cannot be considered as a lumped model when the associated hardware to retain the cells are included. This analysis highlighted the deficiencies in many studies which are focused on simulating cells through CFD or cell tests set in thermal chambers; and then extending the findings to a vehicle in operation. Lumped system analysis on a complex battery pack oversimplifies the physics of the assembly leading to a very fuzzy understanding of the system dynamics under real operating conditions. This was the original motivation for the development of the thermal equivalent circuit.
- a. The Biot number calculated was 0.23 which is a very borderline lumped system analysis, and essentially not accurate enough to illicit any detailed understanding.
3. The thermal equivalent circuit described in Chapter 5 demonstrated the ability to generate results with very little computational effort and a high degree of accuracy in a small amount of time. The thermal circuit doesn't replace the need for other types of analysis (like CAE and CFD) instead it enhances the understanding of the component's design and function in the bigger scheme.
- a. PSPICE simulation time generated results in under 30 seconds.

- b. Static simulations showed improper initial conditions takes 30 hours to converge to the same answer. This highlights the importance of beginning the simulation with the right conditions or results can be skewed.
 - c. Static simulations showed the cell temperature reached its highest value 3 hours after peak solar due to the thermal lag of the battery pack.
 - d. Road radiation effects are three times (3x) higher at peak solar conditions when compared to the time of day when the cells are at their highest temperature (coincides with the sun setting, therefore lower pavement temperature).
 - i. 100 mW at peak cell temperature versus 300 mW at peak ambient (per cell).
 - e. Convection underneath the vehicle impacts the heat flow into the baseplate depending on the speed.
 - i. Slowing down results in heat influx to the battery due to road radiation whereas a vehicle at speed reduces that relative influence.
 - f. Using the thermal circuit as a proof of concept can help narrow down innovative ideas to feasible and cost effective solutions. This leads to a reduction in development time resulting in cost savings to manufacturers. For customers, a well-designed system will lead to more satisfaction due to increased reliability of the system.
4. The cooling system was analyzed to determine the percentage of the cooling power directed towards the cells, via internal packaging and environment influences.
- a. The baseline system directed 90% of the cooling towards the cells with the remaining 10% to the packing (specifically the cell retention frame).
 - b. The Davis Dam simulations showed the heat generation overpowered the cooling system. However this highlights the following:
 - i. Overpowering of the cooling system is linked to a controls issue in the simulation. The actual system is able to trigger a higher compressor speed under extreme demand.

- ii. The compressor profile was neither triggered nor recorded in the thermal test chamber because vehicle power demand was set too low.
 - iii. A detailed understanding of compressor operation and controls is needed to catch corner case simulations.
- 5. A simulated work day and weeklong static cooling with quiescent background cooling active showed that in a hot climate with an aggressive drive event and the vehicle parked outside results in cell temperatures approaching 40°C if there is no cooling.
 - a. A quiescent cooling rate of 50 W would be sufficient to reduce the cell temperatures to an ideal temperature range below 30°C.
 - b. Such a small amount of power might be supplied by a solar panel instead of drawing upon the high voltage battery.
- 6. Insulation implemented in key areas of the pack indicated improvements over the baseline design.
 - a. Placing insulation between the cell and retention frame resulted in the single most significant improvement.
 - b. Cooling power directed to the cells increased to approximately 100% from the initial 90% baseline.
 - c. The cooling pulldown rate in the first 150 seconds of operation decreases by 0.4°C/min, but this still results in an overall faster cooling cycle event (20-114 seconds faster depending on the drive cycle).
 - d. Insulation between cell and retention frame reduced the background quiescent cooling requirement closer to 20 W from the initial 50 W.
 - i. This indicates a solar panel could well be used to provide the power which is more feasible than previously imagined.
- 7. Cold weather operation was briefly explored but selecting the appropriate region within the constraints of the Autonomie vehicle controller were limiting. The actual

vehicle controller forces an IC engine turn-on cycle when the pack temperature approaches 0°C in order to heat it.

- a. Added insulation shifts cell temperatures towards the diurnal average and prevents the cells from getting too cold.
 - i. The insulation increased the starting cell temperature for the drive cycles by 1.6°C.

8. From the simulations, the battery pack was capable of cooling the cells regardless of the conditions put forth. To reach temperatures upwards of 50°C there needs to be an aggressive drive cycle in an extremely hot environment. A fully working cooling system should limit cell temperatures from reaching the point of SEI layer decomposition which can result in an internal short circuit (ISC) or thermal runaway. As the battery ages, this guarantee of performance lessens, lengthening the cooling cycles until the cool-down rate is no longer adequate at the extremes. Cold temperatures require more attention because the heating system is much smaller compared to the AC system (about half the maximum power level), therefore heating would take much more time. The propensity to irreversibility damage cells in the cold is a greater reality. In the case of the Volt, engine power is used to advantage to reduce the stress on the battery and regen functions are disabled until the battery is ready to accept charge.

CHAPTER 9 - CONTRIBUTIONS AND FUTURE WORK

9.1 Contributions

The overarching contribution was developing and validating a sophisticated simulation model of the production vehicle hardware, then integrating these results into a bespoke BTMS circuit model with very low computational time that includes the environmental elements most often neglected. To date, there has not been a comprehensive study that utilizes very detailed assembly models to generate battery thermal data under real world dynamic scenarios. The methodology presented in this thesis can be deployed by OEMs that build and design battery packs for HEVs and EVs, or any architecture variant in between, to help design engineers achieve a better cooling/heating solution and work towards more innovative and efficient approaches. The Autonomie and PSPICE models simulated various regions and temperature profiles spanning days with a resolution in minutes and an execution time of a few seconds. The same type of simulations in CFD would have taken many orders of magnitude longer given the complexity of the battery pack. While only one vehicle was simulated in this thesis, the methodology is applicable to any, along with a test region and terrain of interest. Furthermore, all models developed were created in readily accessible software so they can be reproduced by others.

Five key discoveries elicited and quantified in this particular pack design were:

1. The simulations must be run with approximately 30 hours' worth of prior ambient environmental and drive cycle history to set initial component temperatures; before evaluating the effects of any new drive cycle on the battery system due to the deep propagating wave of heat stored within. Lacking this, simulations will give erroneous results.
 - a. This highlights the diurnally caused temperature distribution that exists in the internal hardware. The entire battery pack cannot be assumed to exist at a uniform temperature like it has been in previous studies.

2. A typical thermal lag time for the external environment to first hit the cells is 3 hours, and this would lengthen with the addition of further insulation. In practice such finding translates into the worst case for the cells existing around sunset, particularly for initiating a drive cycle, given the car was parked outdoors.
 - a. This highlights the cell temperatures cannot be assumed to be at the ambient conditions like implied in previous studies or when testing/simulating in thermal chambers.
3. Insulation added at the cell to retention frame interface shows by far the highest improvements for both efficient uses of the cooling/heating power percentage directed at the cells, and mitigating the ingress of environmental influence per unit volume of added material. It's also the most cost and space effective implementation of insulation. All insulation added, even if placed elsewhere, remains effective and beneficial at keeping the cells closer to the diurnal average.
 - a. This highlights why internal packing hardware should not be neglected like it has been in previous studies. There are efficiencies to be gained when there is an understanding of the BTMS in relation to internal hardware.
4. The heat leakage rate into this battery pack averages 50 to 75 watts over the course of daytime exposure through the worst ambient/solar loads known in North America. A self-powered background cooling strategy that leverages on the thermal mass of the system to offset the impact of a heat wave entering, especially in combination with extra insulation, would mitigate against premature ageing due to extreme prolonged thermal soaks. The effectiveness of such a low power quiescent rate was not anticipated.
 - a. This can help create new avenues and ideas for low powered cooling devices to gain efficiencies by not powering a high voltage compressor.
5. A tightening of the thermal setpoints for battery cooling initiation, particularly in hot environments, is counterproductive from the point of view forcing more

frequent transient high power compressor operating profiles. Widening the thermal setpoints shows the ability to reduce the frequency of the BTMS operation by allowing a slightly higher upper threshold while keeping the overall cell temperature within the suggested thermal operating range. The selection of setpoints also needs to account for the physical limitations of the compressor, especially with small deltas between setpoints and frequent high power cycling. The cooling power provided by the compressor will vary based on the in-car thermostatic controls due to heat generated within the battery pack as well as HVAC requests. These factors affect the rate of decrease in cell temperature and heat flow through the battery pack components.

- a. This highlights the pull down rates are limited by how the compressor is commanded to operate which needs to be considered when simulating a cooling system. Assumptions of cooling rates suggested in previous studies may not be physically possible in practice, nor is the efficient dynamic operating range of a compressor considered, the prime reason why the system needs to cycle in the first place.

Below, a detailed summary of contributions and findings brought forth by this research follows by category.

Autonomie Vehicle Model

- Identified, developed and implemented the improved motor/generator efficiency maps to resemble the production vehicle.
- Identified battery operating characteristics (current, voltage, SOC) through vehicle testing which were integrated into the battery model file.
- Identified the charge sustaining mode controller thresholds and SOC operating window from vehicle testing and implemented the changes into the Autonomie vehicle level controller model.
- Quantified the production vehicle electrical accessory losses while using A/C and RESS cooling then implemented these into the Power Accessory model

- Validated the model developed against vehicle test data and independent published INL dynamometer data.
- Quantified the impact standard drive cycles have on cell heat generation under charge depleting and charge sustaining modes.
- Developed the Davis Dam drive cycle profile which incorporates the climate data and precise road gradients, and quantified its extreme effect on the BTMS requirements.
- Identified drive cycles with similar heat generation rates which reduced the number of drive cycles needed to cover the spectrum of interest, and classified environmental test regions to run them in that represent extreme, average and mild cases of lifetime exposure.

Thermal Equivalent Circuit

- Developed the thermal equivalent circuit for the battery pack in the EREV capturing all necessary detail of internal hardware that have been generally neglected in other studies.
- Integrated the simulation results generated from Autonomie into the thermal equivalent circuit for a completely unified vehicle and BTMS simulation.
- Validated the thermal equivalent circuit against the production vehicle battery pack using laboratory experimental data.
- Designed vehicle testing experiments to generate key vehicle data sets to be used in the thermal equivalent circuit which includes:
 - Compressor current, voltage, and power response to request for battery cooling.
 - Coolant temperature profile into the battery pack.
 - Vehicle demand on cooling performance.
 - Quantify the effects of road radiation and underbody air flow.
- Developed the cooling controls strategy to active the BTMS based on the dynamic response of the thermal equivalent circuit outputs on various drive cycles.

- Quantified the cooling power on a per cell basis considering the transient compressor power profile derived from vehicle tests.
- The results from the thermal circuit analysis quantified how the retaining hardware plays a pivotal role in the amount of heat retained and dissipated through the battery pack.

Environmental and Initial Conditions

- Developed a method to utilize available solar data to create the road temperature profile in combination with the ambient diurnal profile.
- Developed a procedure to identify the correct initial temperature conditions for all the components in the thermal equivalent circuit.
- Quantified that incorrect initial conditions take approximately 30 hours running time to converge from a false premise, hence incorrect initial conditions impact the results generated from the majority of previous simulations seen in the literature.
- Identified it takes at least 2 days of ambient data to generate the correct initial conditions, and for full accuracy a week of prior data was employed in some instances.
- Quantified the thermal lag that exists between the battery components which shows the cell temperatures reach their maximum ~3 hours after the daytime peak ambient temperature for this battery pack configuration.
- Determined the evening time around sunset to be the worst case scenario for the battery pack in terms of a start time for a drive cycle, as the road radiation at peak ambient is only then transgressing into the cells.
- Identified and quantified how battery system simulations cannot simply assume all internal and external components to be at a uniform temperature, but also identified two unique times during the course of the day when such an assumption almost holds true and how this occurs.

Cell Temperatures and Battery Cooling

- Quantified the effects of the various standard drive cycles on the cell temperature and BTMS operation which showed the level to which high heat generation cycles activated the thermal control system more frequently.
- Identified how the SOC of the battery pack at the beginning of the drive cycles impacted the cell temperature rise, resulting in an earlier activation of the BTMS.
- Identified that the BTMS is capable of cooling the battery pack throughout the drive cycle adequately and quantified how the cell heat generation affected the length of BTMS operation.

Heat Flow Analysis

- Quantified the amount of heat flow through the individual battery pack components and identified key paths of heat flow into and out of battery pack.
- Identified and quantified the following phenomena that impact design.
 - Aggressive drive cycles contribute to higher amount of heat flow through the cell retention frames compared to urban drive cycles.
 - The effects of solar radiation are most strongly felt via the heat flow through the lower shield and baseplate components, and not the chassis path via the greenhouse effect of the passenger compartment.
 - The effects of road radiation are seen in a more pronounced manner on low speed urban drive cycles where they are not masked by high internal heat generation of the cells.
 - The heat flow direction through the battery pack components is nominally outward towards the environment, and this reverses direction when the BTMS becomes active as the cooler internal pack temperature attracts heat from the environment.
 - Contributions of under vehicle convective air flow and road radiation can be near equal under the worst case cell temperature test scenario, but is highly dependent on the azimuth solar position.

- Heat flow from road radiation and underbody convection at peak solar is three times (3x) the amount seen later in the day when the cells finally experience their highest temperature. The time lag modeling of these factors is extremely important towards gaining accurate results.

Cooling Performance

- Developed a method to calculate efficiency of the BTMS using the thermal equivalent circuit model.
- Quantified the production BTMS directs ~90% of the available cooling towards the cell with the remaining 10% diverted to the cell retention frames and beyond, indicating the current system is capable cooling battery down without too significant losses.
- Implemented an aged battery model into Autonomie to represent the expected 10 year battery aging resistance increment, and established adequate cooling performance remaining under such scenario.
- Quantified the BTMS was still capable of cooling battery pack but with reduced effectiveness as the higher resistance from the aged battery contributes twice or more the internal heat generation, compared to the baseline system.
- Developed a quiescent cooling model and calculated 75W of background cooling is more than sufficient to mitigate cell temperature when the vehicle is stationary in the hottest North American climates, and surmised such cooling power could be provided through solar cells, if not the battery itself.

System Improvements

- Implemented changes to the BTMS control setpoints and quantified how increasing the temperature delta between the setpoints reduced the number of cooling events while still keeping the battery pack within an optimal temperature range.
- Designed and modeled insulation elements to be added to the thermal equivalent circuit which demonstrated improvements over the baseline system.

- Insulating the outside of the cover and baseplate helps prevent heat from propagating into the battery pack during hot ambient fluctuations and brings the cell temperatures closer to the diurnal average.
- Quantified how placing insulation between the cell and retention frame to reduce the thermal bridging between the components makes this approach as effective as exterior insulation at bringing the cell temperatures closer to the diurnal average, for a much lower cost.
- Showed that decoupling the cell thermally from its retention frame also lessens the effective thermal mass of the cell core, driving up the frequency of the BTMS operation (whilst shortening the cooling period), hence requires readjustment of the thermal setpoints to compensate.
- Calculated the reduction in thermal bridging between the cells and retention frames increasing the cooling efficiency from ~90% to the 95-99% range.
- Quantified that cell to frame insulation reduces the worst case quiescent cooling power from 75W to 50W, which makes the concept a stronger candidate for the requisite power to be supplied by solar cells – and indefinitely ward off the heat soak accelerated aging phenomena experienced in hot climates.
- Quantified the contributions of adding insulation on the exterior and interior of the battery pack and showed the cell temperature is bettered by 1.5°C at the beginning of cold (around freezing) drive cycles and mitigated heat lost to the environment.
- Definitively showed that added insulation has notable positive effects under all conditions simulated, either hot or cold, since it brings the cells temperatures closer to the diurnal average, which is almost universally a milder condition than the extremes seen at night or during the day.

9.2 Directions for Future Work

While the Autonomie model is accurate, there needs to be more development for some of its components. The ESS model neglected two capacitive electrical time constants which can be found through specific cell experiments. These will help better define the

instantaneous heat generation and its spread from the cell core to the cooling plates and improve resolution of core cell temperature profiles over shorter time scales as during transient operations. The ESS model can also be expanded to handle separately the charge and discharge resistances thus produce a more accurate voltage map. The electric machines simulation can also be refined through vehicle chassis dynamometer testing to extract accurate efficiency maps which reflect all driveline losses. The propulsion controller definitely needs improvements as the present iteration does not allow the simulation of drive cycles with large grades, since it lacks “mountain mode” where the charge sustaining setpoint is raised and a more pronounced power level of the IC engine is sought. Cold weather simulation is not properly captured in the vehicle controller; this requires specific logic for IC engine initiation to warm the battery in sub-zero environments. Learning how and when the controller cycles the engine and to program this relationship into the Autonomie controller is a substantive task.

The thermal circuit can be improved by adding a few features. Section A, which represents the cell and cooling plate interface connects to the rest of the circuit and needs to be expanded. Too little is yet known about the heat spread within the cell. A more detailed cell model will enhance the capabilities of the thermal circuit. Some of the external heat flow branches also need to be re-evaluated. In the results, it was revealed the effects of the engine really only showed themselves through the bulkhead component. There also needs to be a branch which connects the engine to the shield and baseplate – via a source that captures the hot engine and radiator wash under the car when the vehicle is stationary or traveling at lower speeds. The greenhouse effect of the passenger compartment still needs to be investigated further as the heat trapped is significant in hot ambient conditions. The time lag for the cabin air to permeate to the chassis sheet metal (a source in the thermal circuit) considering the carpeting and sound insulation needs to be better determined than over the relatively short time periods (a few hours) investigated during the experiments. The cooling source itself could also be divided into two sources representing the inlet and outlet fluid. This modification would require the thermal circuit to be expanded into a cell module to attain further detail. The use of other sources representing thermoelectric and phase change materials could be added to examine different cooling technologies and their combined operating strategies for energy savings. A cost-benefit analysis coupled with a

sensitivity analysis would enhance the quantification of the improvements from a manufacturing point of view. This approach can help determine the solutions that provide the best results for the lowest cost.

Finally, given that Autonomie is MATLAB and Simulink based, it would bode well for the cooling system model developed to be integrated into Autonomie as a standalone block. This would shorten the simulation times even further by having an all-in-one model. To achieve such seamless integration the cooling model would have to be added to Autonomie using the built in tool provided. This requires extensive de-bugging since the PSPICE Simulink integration required user prompts to run which are an issue for Autonomie since mid-simulation prompts are not supported. Having one integrated model could help create close looped simulations and aid in the development of predictive controls strategies. This enables updating the cell electro-thermal characteristics dynamically, as Autonomie already supports such tables, and would improve simulation accuracy further. Also the question of phase change material placement, and resulting system interactions could be thoroughly modeled and investigated for effectiveness.

Hopefully this work encourages others to delve further into leveraging the knowledge gained towards attaining more efficient battery thermal management systems.

REFERENCES

- [1] A. Pesaran, "Battery thermal management in evs and hev's: issues and solutions," *Proceedings of the Advances automotive battery conference Golden, Colorado: NREL*, 2001.
- [2] A. Pesaran, A. Vlahinos and T. Stuart, "Cooling and preheating of batteries in hybrid electric vehicles," *Proceedings of the The 6th asme-jsme thermal engineering joint conference Golden, Colorado: NREL*, no. TED-AJ03-633, 2003.
- [3] G. Kim and A. Persaran, "Battery thermal management system design modeling," *Proceedings of the 22nd international battery, hybrid and fuel cell electric vehicle conference and exhibition Yokohama, Japan*, no. NREL/CP-540-40446, 2006.
- [4] D. Bruni, L. Benini and B. Ricco, "System lifetime extension by battery management: an experimental work," *Grenoble: ACM*, vol. Proceedings of the Cases 2002, no. 1-58113-575-0, pp. 232-237, 2002.
- [5] R. Spotnitz, "Battery modeling," *The Electrochemical Society*, vol. 14, no. 4, pp. 39-42, 2005.
- [6] F. Thomas, M. Doyle and J. Newman, "Simulation and Optimization of the Dual Lithium Ion Insertion Cell," *Journal of the Electrochemical Society*, vol. 141, p. 1, 1994.
- [7] D. & W. R. Fan, "A mathematical model of a dealed nickel-cadmium battery," *Journal of Electrochemical Society*, vol. 138, no. 1, pp. 17-25, 1991.
- [8] C. Y. Mak, H. Y. Cheh, G. S. Kelsey and P. Chalilpoyil, "Modeling of Cylindrical Alkaline Cells. I. Quasi-Equilibrium Analysis," *Journal of the Electrochemical Society*, vol. 138, p. 1607, 1991.
- [9] C. Y. Wang, W. B. Gu and B. Y. Liaw, "Micro-Macroscopic Coupled Modeling of Batteries and Fuel Cells I. Model Development," *Journal of the Electrochemical Society*, no. 145, p. 3407, 1998.

- [10] N. Harb and R. M. LaFollette, "Mathematical Model of the Discharge Behavior of a Spirally Wound Lead-Acid Cell," *Journal of the Electrochemical Society*, vol. 146, no. 3, p. 809, 1999.
- [11] R. Rao, S. Vrudhula and D. Rakhmatov, "Battery modeling for energy-aware system design," *Computer*, vol. 36, no. 12, pp. 77-87, 2003.
- [12] T. D. Hatchard, D. MacNeil, D. A. Stevens, L. Christensen and J. R. Dahn, "Importance of Heat Transfer by Radiation in Li-Ion Batteries during Thermal Abuse," *Electrochemical Solid-State Letters*, vol. 3, no. 7, pp. 305-308, 2000.
- [13] C. Pals and J. Newman, "Thermal model of the lithium/polymer battery - 1. discharge behavior of a single cell," *The Electrochemical Society*, vol. 142, no. 10, pp. 3274-3281, 1995.
- [14] R. Spotnitz, "Scale-up of lithium-ion cells and batteries," 2002.
- [15] R. Spotnitz, "Advanced ev and hev batteries," *Vehicle Power and Propulsion, 2005 IEEE Conference*, pp. 445-448, 2005.
- [16] T. Bandhauer, S. Garimella and T. Fuller, "A Critical Review of Thermal Issues in Lithium-Ion Batteries," *Journal of the Electrochemical Society*, vol. 158, no. 3, pp. 1-25, 2011.
- [17] D. Bernardi, E. Pawlikowski and J. Newman, "A general energy balance for battery systems," *Journal of Electrochemical Society*, vol. 132, no. 1, pp. 5-12, 1985.
- [18] D. Fan and R. White, "Mathematical modeling of a nickel-cadmium battery: effects of intercalation and oxygen reactions," *Journal of Electrochemical Society*, vol. 138, no. 10, pp. 2952-2960, 1991.
- [19] Y. Chen and J. Evans, "Three-dimensional thermal modeling of lithium-polymer batteries under galvanostatic discharge and dynamic power profile," *The Electrochemical Society*, vol. 141, no. 11, pp. 2947-2955, 1994.
- [20] J. Newman and W. Tiedemann, "Temperature rise in a battery module with constant heat generation," *Journal of Electrochemical Society*, vol. 142, no. 4, pp. 1054-1057, 1995.

- [21] C. Pals and J. Newman, "Thermal model of the lithium/polymer battery - 2. temperature profile in a cell stack," *The Electrochemical Society*, vol. 142, no. 10, pp. 3282-3288, 1995.
- [22] A. Pesaran, A. Vlahinos and S. Burch, "Thermal performance of ev and hev battery modules and packs," *Center for Transportation Technologies and Systems*.
- [23] D. Bharathan, A. Pesaran, A. Vlahinos and G.-H. Kim, "Electro-Thermal Modeling to Improve Battery Design," in *IEEE Vehicle Power and Propulsion*, Chicago, 2005.
- [24] A. Pesaran, A. Vlahinos and D. Bharathan, *Electrothermal Analysis of Lithium Ion Batteries*, Fort Lauerdale, Florida: NREL, 2006.
- [25] A. Pesaran, G. Kim and K. Smith, "Accelerating design of batteries using computer-aided engineering tools," in *Proceedings of the 25th electric vehicle symposium Shenzhen: NREL. NREL/PR-5400-50354*, 2010.
- [26] G. Kim, K. Smith, K. Lee, S. Santhanagopalan and A. Pesaran, "Integrated lithium-ion battery model encompassing multi-physics in varied scales: an integrated computer simulation tool for design and development of edv batteries," in *The 11th International Advanced Automotive Battery Conference*, Pasadena, 2011.
- [27] G. Kim, K. Smith, K. Lee, S. Santhanagopalan and A. Pesaran, "Multi-Domain Modeling of Lithium-Ion Batteries Encompassing Multi-Physics in Varied Length Scales," *Journal of The Electrochemical Society*, vol. 158, no. 8, pp. 955-969, 2011.
- [28] G. Kim, K. Lee, L. Chaney, K. Smith, E. Darcy and A. Pesaran, "Prediction of multi-physics behaviors of large lithium-ion batteries during internal and external short circuit," in *Battery Safety 2010 in Conjunction with 6th Lithium Mobile Power*, Boston, 2010.
- [29] A. Pesaran, G. Kim and K. Smith, "Accelerating design of batteries using computer-aided engineering tools," *Proceedings of the 25th electric vehicle symposium Shenzhen: NREL*, no. NREL/PR-5400-50354, 2010.

- [30] Y. Ma and H. Teng, "Comparative study of thermal characteristics of lithium-ion batteries for vehicle applications," *SAE International*, no. 2011-01-0668, 2011.
- [31] S. Jayaraman, G. Anderson, S. Kaushik and P. Klaus, "Modeling of battery pack thermal system for a plug-in hybrid electric vehicle," *SAE International*, no. 2011-01-0666, 2011.
- [32] H. Sun, B. Tossan and D. Brouns, " Thermal behavior study on hev air-cooled battery pack," *SAE International*, no. 2011-01-1368, 2011.
- [33] S. C. Getty, G. L. Neal and D. C. Haworth, " Development, verification, and validation of penn state extended range electric vehicle. International Scientific Conference on hybrid and electric vehicles," *RHEVE 2011 6-7 December 2011*, 2011.
- [34] C. Gokce, O. Ustun, M. Yilmaz and R. N. Tuncay, "Modeling and simulation of a serial – parallel hybrid electric vehicle. Unpublished manuscript," *Faculty of Electrical & Electronics Engineering, Department of Electrical Engineering, Istanbul Technical University, Maslak, Istanbul, Turkey.*, 2006.
- [35] V. Damodaran, S. Murugan, V. Shigarkanthi, S. Nagtilak and K. Sampath, "Thermal management of lead acid battery (pb-a) in electric vehicle," *SAE International*, no. 2011-01-0653, 2011.
- [36] S. Panchal, M. Mathew, I. Dincer, M. Agelin-Chaab, R. Fraser and M. Fowler, "Thermal and electrical performance assessments of lithium-ion battery modules for an electric vehicle under actual drive cycles," *Electric Power Systems Research*, vol. 163, no. A, pp. 18-27, 2018.
- [37] S. Karagol and M. Bikdash, "Generation of Equivalent-Circuit Models From Simulation Data of a Thermal System," *IEEE Transactions on Power Electronics*, vol. 25, no. 4, pp. 820-828, 2010.
- [38] S. Karagol and M. Bikdash, "Steady-state thermal response using equivalent-circuit models from simulation data of a 2D thermal system with radiation," in *2011 IEEE 43rd Southeastern Symposium on System Theory*, Auburn, 2011.

- [39] A. Jain, R. Jones, R. Chatterjee and S. Pozder, "Analytical and Numerical Modeling of the Thermal Performance of Three-Dimensional Integrated Circuits," *IEEE Transactions on Component and Packaging Technologies*, vol. 33, no. 1, pp. 56-63, 2010.
- [40] X. Hu, L. Shaohua, S. Stanton and L. Wenyu, "A Foster Network Thermal Model for HEV/EV Battery Modeling," *IEEE Transactions on Industry Applications*, vol. 47, no. 4, pp. 1692-1699, 2011.
- [41] X. Lin, H. Perez, S. Mohan, J. Siegel, A. Stefanopoulou, Y. Ding and M. Castanier, "A lumped-parameter electro-thermal model for cylindrical batteries," *Journal of Power Sources*, vol. 257, no. 1, pp. 1-11, 2014.
- [42] L. Saw, Y. Ye and A. Tay, "Electro-thermal characterization of Lithium Iron Phosphate cell with equivalent circuit modeling," *Energy Conversion and Management*, vol. 87, pp. 367-377, 2014.
- [43] L. Saw, A. Tay and W. Zhang, "Thermal Management of Lithium-ion Battery Pack with Liquid Cooling," in *2015 31st Thermal Measurement, Modeling & Management Symposium (SEMI-THERM)*, San Jose, 2015.
- [44] A. Greco, D. Cao, X. Jiang and H. Yang, "A theoretical and computational study of lithium-ion battery thermal management for electric vehicles using heat pipes," *Journal of Power Sources*, vol. 257, pp. 344-355, 2014.
- [45] I. Baghdadi, O. Briat, A. Eddahech and J. Vinassa, "Electro-thermal model of lithium-ion batteries for electrified vehicles applications," in *2015 IEEE 24th International Symposium on Industrial Electronics (ISIE)*, Buzios, 2015.
- [46] N. Damay, C. Forgez, M.-P. Bichat and G. Friedrich, "Thermal modeling of large prismatic graphite battery. Coupled thermal and heat generation models for characterization and simulation," *Journal of Power Sources*, vol. 283, pp. 37-45, 2015.
- [47] C. Zhang, K. Li and J. Deng, "Real-time estimation of battery internal temperature based on a simplified thermoelectric model," *Journal of Power Sources*, vol. 302, pp. 146-154, 2016.

- [48] D. Zhang, B. Haran, A. Durairajan, R. White, Y. Podrazhansky and B. Popov, "Studies on capacity fade of lithium-ion batteries," *Journal of Power Sources*, vol. 91, pp. 122-129, 2000.
- [49] L. Lam and P. Bauer, "Practical Capacity Fading Model for Li-Ion Battery Cells in Electric Vehicles," *IEEE Transactions on Power Electronics*, vol. 28, no. 12, pp. 5910-5918, 2013.
- [50] K. W. Steffke, S. Inguva, D. Van Cleve and J. Knockeart, "Accelerated Life Test Methodology for Li-Ion Batteries in Automotive Applications," *SAE International*, no. 2013-04-08, 2013.
- [51] M. Daigle and C. Kulkarni, "End-of-Discharge and End-of-Life Prediction in Lithium-Ion Batteries with Electrochemistry-Based Aging Models," in *AIAA SciTech 2016*, San Diego, 2016.
- [52] M. Daigle and C. Kulkarni, "Electrochemistry-based Battery Modeling for Prognostics," in *Annual Conference of the Prognostics and Health Management Society 2013*, New Orleans, 2013.
- [53] J. Yi, U. S. K. Kim, C. B. S. Shin, T. Han and P. S. , "Modeling the temperature dependence of the discharge behavior of a lithium-ion battery in low environmental temperature," *Journal of Power Sources*, vol. 244, pp. 143-148, 2013.
- [54] J. Smart, "Advanced Vehicle Testing Activity – Cold Weather On-road Testing of a 2012 Chevrolet Volt," *Idaho National Laboratory*, Vols. INLÉEXT-14-34030, 2014.
- [55] J. Jaguemont, L. Boulon, P. Venet, Y. Dube and A. Sari, "Low temperature aging tests for lithium-ion batteries," in *2015 IEEE 24th International Symposium on Industrial Electronics (ISIE)*, Buzios, 2015.
- [56] J. Jaguemont, L. Boulon, Y. Dube and F. Martel, "Thermal Management of a Hybrid Electric Vehicle in Cold Weather," *IEEE Transactions on Engery Conversion*, vol. 31, no. 3, pp. 1110-1120, 2016.

- [57] G. Technologies, "GT-SUITE Overview," Gamma Technologies, [Online]. Available: <https://www.gtisoft.com/gt-suite/gt-suite-overview/>. [Accessed December 2018].
- [58] G. M. Ehrlich, in *Handbook of Batteries*, 3rd ed., New York, McGraw-Hill, 2002, p. p. 35.
- [59] K. Amine, L. Jun and I. Belharouak, "High-temperature storage and cycling of C-LiFePO₄/graphite Li-ion cells," *Electrochemistry Communications*, vol. 7, no. 7, pp. 669-673, 2005.
- [60] P. Liu, J. Wang, J. Hicks-Garner, E. Sherman, S. Soukiazian, M. Verbrugge, H. Tatara, J. Musser and P. Finamore, "Aging Mechanisms of LiFePO₄ Batteries Deduced by Electrochemical and Structural Analyses," *Journal of The Electrochemical Society*, vol. 157, no. 4, pp. A499-A507, 2010.
- [61] J. Fan and S. Tan, "Studies on Charging Lithium-Ion Cells at Low Temperatures," *Journal of The Electrochemical Society*, vol. 153, no. 6, pp. A1081-A1092, 2006.
- [62] S. Zhang, K. Xu and T. Jow, "Low-temperature performance of Li-ion cells with a LiBF₄-based electrolyte," *Journal of Solid State Electrochemistry*, vol. 7, no. 3, pp. 147-151, 2003.
- [63] G. Sikha, B. Popav and R. White, "Effect of Porosity on the Capacity Fade of a Lithium-Ion Battery," *Journal of The Electrochemical Society*, vol. 151, no. 7, pp. A1104-A1114, 2004.
- [64] S. Shi, P. Lu, Z. Liu, Y. H. J. L. Qi, H. Li and S. Harris, "Direct Calculation of Li-Ion Transport in the Solid Electrolyte Interphase," *Journal of The American Chemical Society*, vol. 134, no. 37, pp. 15476-15487, 2012.
- [65] B. Smith, "Chevrolet volt battery incident overview report 1," U.S. Department of Transportation, National Highway Traffic Safety Administration, 2012.
- [66] NTSB, "Rep. No. PB2014-108867," National Transportation Safety Board, DC, 2014.

- [67] Y. Xia, T. Wierzbicki, E. Sahraei and X. Zhang, "Damage of cells and battery packs due to ground impact," *Journal of Power Sources*, vol. 267, no. 1, pp. 78-97, 2014.
- [68] Q. Wang, J. Sun, X. Yao and C. Chen, "Thermal stability of LiPF₆/EC + DEC electrolyte with charged electrodes for lithium ion batteries," *Thermochimica Acta*, vol. 437, no. 1-2, pp. 12-16, 2005.
- [69] C. von Luders, V. Zinth, S. Erhard, P. Osswald, M. Hofmann, R. Gilles and A. Jossen, "Lithium plating in lithium-ion batteries at sub-ambient temperatures investigated by in situ neutron diffraction," *Journal of Power Sources*, vol. 342, no. 28, pp. 17-23, 2017.
- [70] G. Motors, "Canadian Limited Warranty," [Online]. Available: https://www.chevrolet.ca/content/dam/Chevrolet/northamerica/ca/nscwebsite/en/home/warranty/2018MY_Canadian_CBG_WM_23168736A_2017JUL27.pdf. [Accessed December 2018].
- [71] N. Canada, "Warranty Information," [Online]. Available: <https://www.nissan.ca/content/dam/nissan/ca/owners/warranty/2825201-2018-nissan-leaf-english-wib.pdf>. [Accessed December 2018].
- [72] Tesla, "New Vehicle Limited Warranty," [Online]. Available: <https://www.tesla.com/sites/default/files/downloads/tesla-new-vehicle-limited-warranty-en-us.pdf>. [Accessed December 2018].
- [73] O. Gross and S. Clark, "Optimizing Electric Vehicle Battery Life through Battery Thermal Management," *SAE International Journal of Engines*, vol. 4, no. 1, pp. 1928-1943, 2011.
- [74] P. Groenveld and G. Bower, "Gen 2 Volt Transmission Operating Modes Explained," GM-Volt, 20 February 2015. [Online]. Available: <http://gm-volt.com/2015/02/20/gen-2-volt-transmission-operating-modes-explained/>.
- [75] A. Rousseau and S. Halbach, "Autonomie Large Scale Deployment," US Department of Energy, 2011.

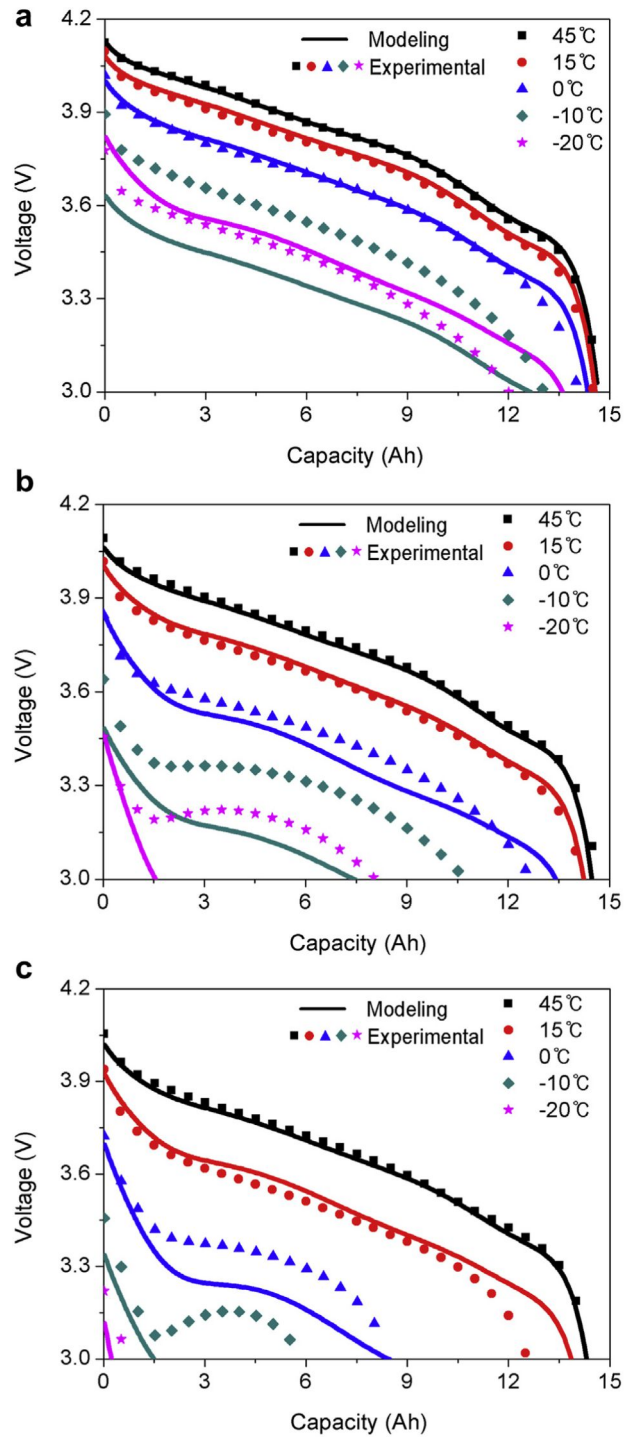
- [76] BorgWarner, "HVH Series Electric Motor," 2016. [Online]. Available: <https://www.borgwarner.com/technologies/electric-drive-motors/hvh-series-electric-motor>.
- [77] H. He, R. Xiong and J. Fan, "Evaluation of Lithium-Ion Battery Equivalent Circuit Models for State of Charge Estimation by an Experimental Approach," *Energies*, vol. 4, pp. 582-598, 2011.
- [78] A. Nikolian, J. de Hoog, K. Fleurbay, J.-M. Timmermans, O. Noshin, P. Van de Bossche and J. Van Mierlo, "Classification of Electric modelling and Characterization methods of Lithium-ion Batteries for Vehicle Applications," in *European Electric Vehicle Congress*, Brussels, 2014.
- [79] T. Gray, J. Wishart and M. Shirk, "2011 Chevrolet Volt VIN 0815 Plug-In Hybrid Electric Vehicle Battery Test Results," Idaho National Laboratory (INL/EXT-12-29678), Idaho, 2013.
- [80] X. Gong, Modeling of Lithium-Ion Battery Considering Temperature and Aging Uncertainties, Dearborn: University of Michigan, 2016.
- [81] U. EPA, "Dynamometer Drive Schedules," United States Environmental Protection Agency, [Online]. Available: <https://www.epa.gov/vehicle-and-fuel-emissions-testing/dynamometer-drive-schedules#vehicleDDS>.
- [82] Office of the Federal Register National Archives and Records Administration, The Code of the Federal Regulations of the United States of America, 40 ed., vol. 86, Washington: U.S. Government Printing Office, 2003, pp. 86.115-78.
- [83] ACEEE, "greencars.org," 2014. [Online]. Available: http://www.greencars.org/guide_epameas.htm.
- [84] SAE, "Performance Requirements for Determining Tow-Vehicle Gross Combination Weight Rating and Trailer Weight Rating J2807_201602," 4 February 2016. [Online]. Available: https://www.sae.org/standards/content/j2807_201602/.
- [85] C. Y.A., Heat and Mass Transfer: A Practical Approach, 3rd Edition, New York: McGraw Hill, 2007.

- [86] D. R. Heldman, D. B. Lund and C. Sabilov, Handbook of food engineering, second edition., Boca Raton: CRC Press, 2006, p. 412.
- [87] H. S. Ramaswamy and M. Marcotte, Food processing: principles and applications, 1st ed., Boca Raton, FL: CRC Press, p. 47.
- [88] A. Faghri, Y. Zhang and J. R. Howell, Advanced Heat and Mass Transfer, Columbia, MO: Global Digital Press, 2010.
- [89] Targray, "Aluminum Laminate Pouch," 17 May 2011. [Online]. Available: <http://www.targray.com/documents/pds-targray-aluminum-laminate-pouch.pdf>. [Accessed 2014].
- [90] G. Motors, "GM Announces Enhancements to Chevrolet Volt," 5 January 2012. [Online]. Available: http://media.gm.com/media/us/en/gm/news.detail.html/content/Pages/news/us/en/2012/Jan/0105_volt.html. [Accessed 2014].
- [91] R. Fillion, "Thermal network model development for an extended range electric vehicle battery pack with experimental verification through dynamic environmental exposure," University of Ontario Institute of Technology, Oshawa, 2017.
- [92] S. Arangi and R. Jain, "Review Paper on Pavement Temperature Prediction Model for Indian Climate Condition," *International Journal of Innovative Research in Advanced Engineering*, vol. 28, no. 8, 2015.
- [93] National Oceanic & Atmospheric Administration, "NOAA Earth System Research Laboratory," US Department of Commerce, 2017. [Online]. Available: <https://www.esrl.noaa.gov/index.html>. [Accessed February 2017].
- [94] AZMET, "The Arizona Meteorological Network," University of Arizona, 2017. [Online]. Available: <https://cals.arizona.edu/azmet/29.htm>. [Accessed August 2015].
- [95] "Historical Climate Data," Government of Canada, [Online]. Available: http://climate.weather.gc.ca/historical_data/search_historic_data_e.html. [Accessed July 2015].

- [96] A. Aerogel, *Cryogel Z Product Data Sheet*, Northborough, MA: Aspen Aerogel Inc, 2017.
- [97] J. Brennan, "Experimental and Numerical Quantification of EV and PHEV Battery Pack Thermal Isolation Strategies," University of Ontario Institute of Technology, Oshawa, 2015.
- [98] L. Fan, J. M. Khodadadi and A. A. Pesaran, "A parametric study on thermal management of an air-cooled lithium-ion battery module for plug-in hybrid electric vehicles," *Journal of Power Sources*, vol. 238, pp. 301-312, 2013.
- [99] Y. Chen and J. Evans, "Thermal analysis of lithium-ion batteries," *Journal of Electrochemical Society*, vol. 143, no. 3, pp. 2708-2712, 1996.
- [100] A. M. Aris and B. Shabani, "An experimental study of a lithium ion cell operation at low temperature conditions," in *1st International Conference on Energy and Power*, Melbourne, 2016.
- [101] J. Jaguemont, L. Boulon and Y. Dube, "A comprehensive review of lithium-ion batteries used in hybrid and electric vehicles at cold temperatures," *Applied Energy*, vol. 164, pp. 99-114, 2016.

APPENDIX

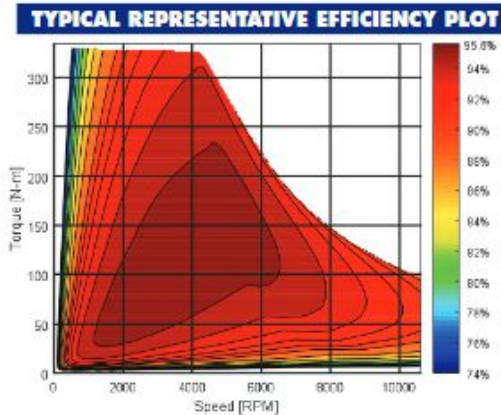
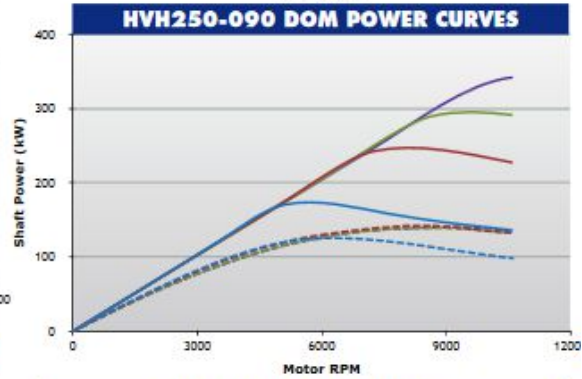
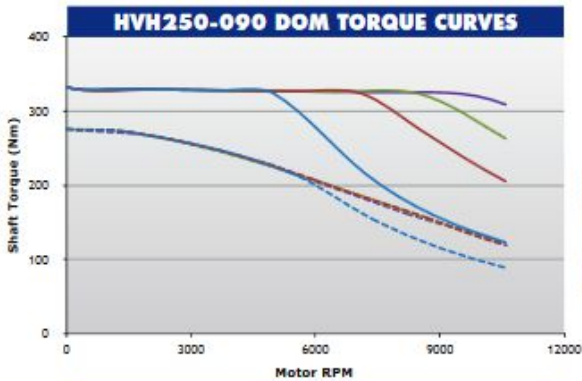
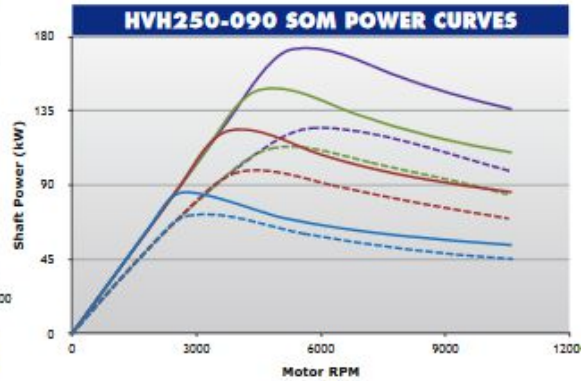
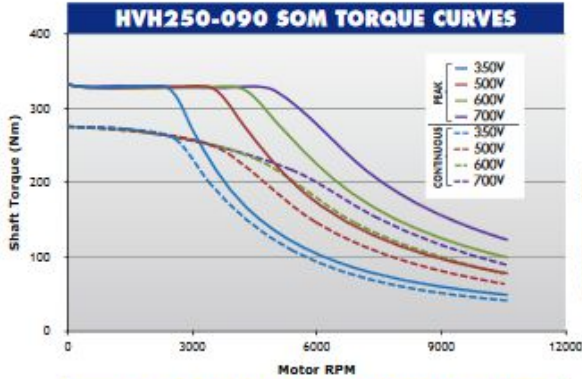
Appendix A – Data for Autonomie Model



A.1 – Experimental data for discharge rates ranging of (a) 1 C, (b) 3 C and (c) 5 C [53]

HVH250-090 Electric Motor

Product Details



OPERATING CONDITIONS	
Typical Coolant Inlet Temperature	up to 90 C
Typical Coolant Flow Rate	5 to 30 LPM
DC Bus Voltage	up to 700 V
Peak Current	300*/600** Arms
Rated Peak Operating Time	60 sec
Standard Cooling Medium	Dexron VI
MOTOR MASS DATA	
Motor Assembly	49 kg
Motor Rotational Inertia	0.067 kg-m ²

*Series wound stator **Dual path stator

Note: Graphs above are based on actual test data. The torque and power ratings are based on typical operating conditions as noted on the performance graphs. There are several variables that may change the motor performance, including coolant flow rate, operating temperature, inverter settings and parameters, etc. For actual performance, the motor must be evaluated in its final system and application. All specifications are subject to change.

BorgWarner Inc.
600 Corporation Drive
Purdieton, IN 46064 USA
© 2016 BorgWarner 3-16



A.2 – Motor specification from Remy (BorgWarner) [76]

Autonomie Component Model Equations

High Voltage Battery

$$P_{MaxDisch} = \min \left[\frac{V_{oc}^2}{4 \times R_{int}}, \frac{(V_{oc} - V_{min}) \times V_{min}}{R_{int}} \right]$$

$$P_{MaxCh} = \frac{(V_{max} - V_{oc}) \times V_{max}}{R_{int}}$$

Voltage Calculation

$$V_{out} = V_{oc} - (R_0 \times I_{load}) - (R_{p1} \times I_{p1}) - (R_{p2} \times I_{p2})$$

- I_{load} = current flowing into the load, that is, the input current from the voltage bus
- R_0 = series internal resistance of a cell
- $R_{p1,2}$ = first and second polar resistance of a cell
- $I_{p1,2}$ = first and second polar current in a cell

SOC Algorithm

$$SOC = SOC_{int} + \Delta SOC$$

$$\Delta SOC = - \int \frac{I_{in}}{Capacity_{max}}$$

- SOC_{int} = initial SOC (initial value of the integrator)
- I_{in} = input current into the battery from the bus
- $Capacity_{max}$ = maximum charge capacity

Matlab Initial Conditions Code

```
Ress_soc_init = 0.8;  
Ress_init_num_module = 6;  
Ress_init_num_cell_series = Ress_init_num_module*  
Ress_init_element_per_module;  
Ress_init_soc_min = 0.2;  
Ress_init_soc_max = 1;
```

```

Ress_init_volt_nom = 4.1;
Ress_init_cap = 45;
Ress_init_packaging_factor = 1.25;
Ress_init_soc_index = [0:0.1:1];
Ress_init_voc.idx1_soc = Ress_init_soc_index;
Ress_init_voc.map = [3.3 3.492 3.55 3.661 3.68 3.72 3.765 3.925 4.013
4.065 4.15];
Ress_init_rint.idx1_soc = Ress_init_soc_index;
Ress_init_rint_map = [0.003518281 0.003518281 0.003389594 0.003260719
0.003184594 0.003099903 0.0032005 0.003195188 0.003092769 0.002937269
0.002937269];

```

Motor/Generator

Saturation of the motor torque to the maximum torque allowed torque of the motor

$$T_{out} = \min(T_{in}, T_{peak})$$

Mechanical output power of the motor and output torque of the motor as a function of input speed and electrical power

$$P_{mech} = Spd_{in} \times T_{in}$$

$$T_{in} = f(Spd_{in}, P_{elec})$$

Maximum Torque

$$T_{max} = T_{cont} \times PWM_{heat_indx} + T_{peak} (1 - PWM_{heat_indx})$$

$$PWM_{heat_indx} = -0.3 + \int \frac{0.3}{\tau} \left(\frac{T_{out}}{T_{cont}} - 1 \right) dt$$

- T_{cont} = Continuous torque (from curve)
- PWM_{heat_indx} = Heat index

Matlab Initial Conditions Code

```

Mot_init_inertia = 0.0226; (kg-m^2)
Mot_init_time_response = 0.05;
Mot_init_coeff_regen = 1;

```

```

Mot_init_str_trq = 200;
Mot_init_cont_to_peak_ratio = 2;
Mot_init_motor_mass = 28.1; (kg)
Mot_init_controller_mass = 10; (kg)
Mot_init_cont_to_peak_ratio = Mot_init.cont_to_peak_ratio;
Mot_init_trq_cont.idx1_spd =
conversion_calc('rotational_speed', 'rpm', 'rad/s', [0:1000:12000]);
Mot_init_trq_cont_map = [118 118 118 113 84 62 51 42 31 28 22 20 17]

```

Mechanical Accessory Losses

Output torque of the mechanical accessories is the difference between the input torque and the torque consumed by the accessories

$$T_{out} = T_{in} - T_{loss}$$

When the engine is on at speeds just above idle, the accessories actively load the engine.

The accessory torque demand is calculated by:

$$T_{loss} = \frac{P_{loss}}{Spd_{in}}$$

Matlab Initial Conditions Code

```

Accmech_init_pwr = 500.0; (W)
Accmech_init_mass = 35; (kg)

```

Electrical Accessory Model

The current consumed by the accessory load is the constant power loss constant divided by the bus voltage

$$I_{in} = I_{out} + \frac{P_{loss}}{V_{in}}$$

Matlab Initial Conditions Code

```

Accelec_init_pwr = 200.0; (Watts)
Accelec_init_12v_mass = 18; (kg)
Accelec_init_mass = 20; (kg)

```


Final Drive

Speed Calculations

$$Spd_{FD_in} = Spd_{FD_out} \times K_{FD}$$

- Spd_{FD_in} = final drive speed in
- Spd_{FD_out} = final drive speed out
- K_{FD} = reduction gear ratio for the final drive

Torque Calculation

$$T_{out} = K_{FD} (T_{in} - T_{loss})$$

$$T_{loss} = f (Spd_{FD_in} - T_{in})$$

- T_{out} = final drive output torque speed
- Spd_{FD_in} = final drive input shaft speed
- T_{in} = final drive input shaft torque
- T_{loss} = final drive input torque loss
- K_{FD} = reduction gear ratio of the final drive

Inertia Calculations

$$J_{out} = J_{in} \times K_{FD}^2 + J_{FD}$$

- J_{in} = final drive input inertia from upstream components
- J_{out} = final drive output inertia fed forward to downstream components
- J_{FD} = inertia of the final drive
- K_{FD} = reduction gear ratio of the final drive

Matlab Initial Conditions Code

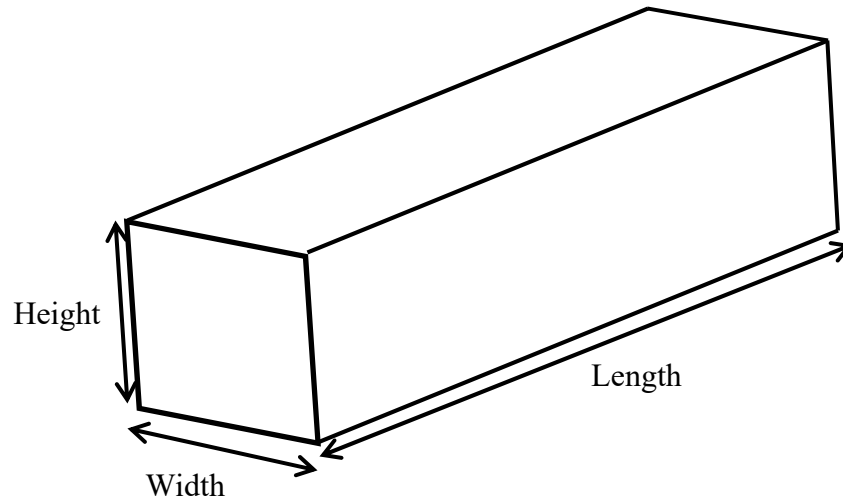
```
Fd_init_ratio = 4.438;  
Fd_init_inertia = 0;  
Fd_init_mass = 25;  
Fd_init_spd_thresh = 10;  
Fd_init_eff_trq.idx1_trq = [0 5000];  
Fd_init_eff_trq.idx2_spd = [0 1500];  
Fd_init_eff_trq.map =  
ones(size(Fd_init_eff_trq.idx1_trq,2),size(Fd_init_eff_trq.idx2_spd,2)).  
* 0.97;
```

```
Fd_init_trq_loss.idx1_trq = Fd_init_eff_trq.idx1_trq;  
Fd_init_trq_loss.idx2_spd = Fd_init_eff_trq.idx2_spd;  
Fd_init_trq_loss.map = zeros(length(Fd_init_trq_loss.idx1_trq),  
length(Fd_init_trq_loss.idx2_spd));
```

Appendix B – Sample Calculations

Lumped System Analysis

The battery pack in the production EREV is T-shaped. To calculate the Biot number, the cells are arranged in a straight line to simplify the calculations for overall surface area as shown in the figure below:



B.1 – Battery surface area

The battery is comprised of the following components:

B.2 – Components

Item	Value
# of cells	288
# of cooling plates	142
# of foam pieces	142
# of nylon holders	144

The measurements for the cells and components are outlined below:

B.3 – Components Dimensions

Parameter	Dimensions
Cell height	202 mm
Cell width	152 mm
Cell thickness	5.4 mm
Foam thickness	1 mm
Cooling plate thickness	0.889 mm
Nylon holder thickness	2.175 mm

The following properties for the total mass and individual mass for each component in the battery are listed below and used to calculate the effective thermal conductivity.

B.4 – Length and Resistance Values

Heat Path (edge)	Value	units	Heat Path (face)	Value	units
L1 (cell edge)	0.0216	<i>m</i>	L1 (cell face)	0.0054	<i>m</i>
L2 (nylon frame)	0.00218	<i>m</i>	L2 (cooling plate)	0.000889	<i>m</i>
			L3 (mylar sheet)	0.000085	<i>m</i>
k_{ce}	25	<i>W/mK</i>	k_{cf}	1	<i>W/mK</i>
k_{nh}	0.3	<i>W/mK</i>	k_{cp}	205	<i>W/mK</i>
			K_{ms}	0.15	<i>W/mK</i>

The resistance calculations for each flow direction are as follows:

Through cell edge

$$R_{ce} A_1 = \frac{L_1}{k_{ce}} = \frac{0.0216m}{25 \frac{W}{mK}} = 0.000864 \left[\frac{m^2 K}{W} \right]$$

$$R_{nh} A_2 = \frac{L_2}{k_{nh}} = \frac{0.002175m}{0.3 \frac{W}{mK}} = 0.00725 \left[\frac{m^2 K}{W} \right]$$

$$R_{contact} = (R_{nh} A_2) \cdot 10 = 0.00725 \frac{Km^2}{W} \cdot 10 = 0.0725 \left[\frac{m^2 K}{W} \right]$$

Through cell face

$$R_{cf} A_1 = \frac{L_1}{k_{cf}} = \frac{0.0027m}{1 \frac{W}{mK}} = 0.0027 \left[\frac{m^2 K}{W} \right]$$

$$R_{ms} A_2 = \frac{L_2}{k_{ms}} = \frac{0.000085m}{0.15 \frac{W}{mK}} = 0.000567 \left[\frac{m^2 K}{W} \right]$$

$$R_{cp} A_3 = \frac{L_3}{k_{cp}} = \frac{0.000889m}{205 \frac{W}{mK}} = 4.34 \times 10^{-6} \left[\frac{m^2 K}{W} \right]$$

The effective thermal conductivity for each heat flow direction are:

$$k_{eff,ce} = \frac{L_t}{R_{ce} A_{ce}} = \frac{L_1 + L_2}{\frac{L_1}{k_{ce}} + \frac{L_2}{k_{nh}} + R_{contact}} = \frac{0.0216m + 0.002175m}{0.004 \frac{m^2 K}{W} + 0.00725 \frac{m^2 K}{W} + 0.0725 \frac{m^2 K}{W}} = 0.29 \frac{W}{mK}$$

$$k_{eff,cf} = \frac{L_t}{R_{cf} A_{cf}} = \frac{L_1 + L_2 + L_3}{\frac{L_1}{k_{cf}} + \frac{L_2}{k_{ms}} + \frac{L_3}{k_{cp}}} = \frac{0.0054m + 0.000085m + 0.000889m}{0.0054 \frac{m^2 K}{K} + 0.000567 \frac{m^2 K}{K} + 4.34 \times 10^{-6} \frac{m^2 K}{W}} = 1.07 \frac{W}{mK}$$

The overall effective thermal conductivity of the system is calculated to be:

$$R_T A_T = \frac{(R_{ce} A_{ce})(R_{cf} A_{cf})}{R_{ce} A_{ce} + R_{cf} A_{cf}} = 0.005574 \left[\frac{m^2 K}{W} \right]$$

$$k_{eff} = \frac{L_{ce} L_{cf}}{R_T A_T (L_{ce} + L_{cf})} = \frac{(0.0216m + 0.002175m)(0.0054 + 0.000085m + 0.000889m)}{0.005574 \frac{m^2 K}{W} ((0.1m + 0.002175m) + (0.0054 + 0.000085m + 0.000889m))}$$

$$k_{eff} = 0.9 \frac{W}{mK}$$

The Biot number is calculated by:

$$Bi = \frac{hL_c}{k_{eff}}$$

$$L_c = \frac{V}{A_s}$$

The overall length of the battery is calculated to be 1863.2 mm. The various surface areas and volume are equal to:

$$A_{s,total} = 2 \cdot (152mm \cdot 202mm) + 2 \cdot (202mm \cdot 1863.2mm) + 2 \cdot (1863.2mm \cdot 152mm)$$

$$A_{s,total} = 1.38m^2$$

$$A_{s,edge} = 2 \cdot (202mm \cdot 1863.2mm) + 2 \cdot (1863.2mm \cdot 152mm)$$

$$A_{s,edge} = 1.32m^2$$

$$A_{s,face} = 2 \cdot (152mm \cdot 202mm)$$

$$A_{s,face} = 0.061m^2$$

$$V = L \cdot W \cdot H$$

$$V = 1863.2mm \cdot 152mm \cdot 202mm$$

$$V = 0.0572m^3 \rightarrow 57 \text{ liters of cell volume}$$

Therefore, the Biot number is equal to:

$$Bi_{total} = \frac{\left(5 \frac{W}{m^2K}\right) \left(\frac{0.0572m^3}{1.38m^2}\right)}{0.9 \frac{W}{mK}}$$

$$Bi_{total} = 0.23$$

$$Bi_{edge} = \frac{\left(5 \frac{W}{m^2 K}\right) \left(\frac{0.0572 m^3}{1.32 m^2}\right)}{0.29 \frac{W}{mK}}$$

$$Bi_{edge} = 0.74$$

$$Bi_{face} = \frac{\left(50 \frac{W}{m^2 K}\right) \left(\frac{0.0572 m^3}{0.061 m^2}\right)}{1.07 \frac{W}{mK}}$$

$$Bi_{total} = 44$$

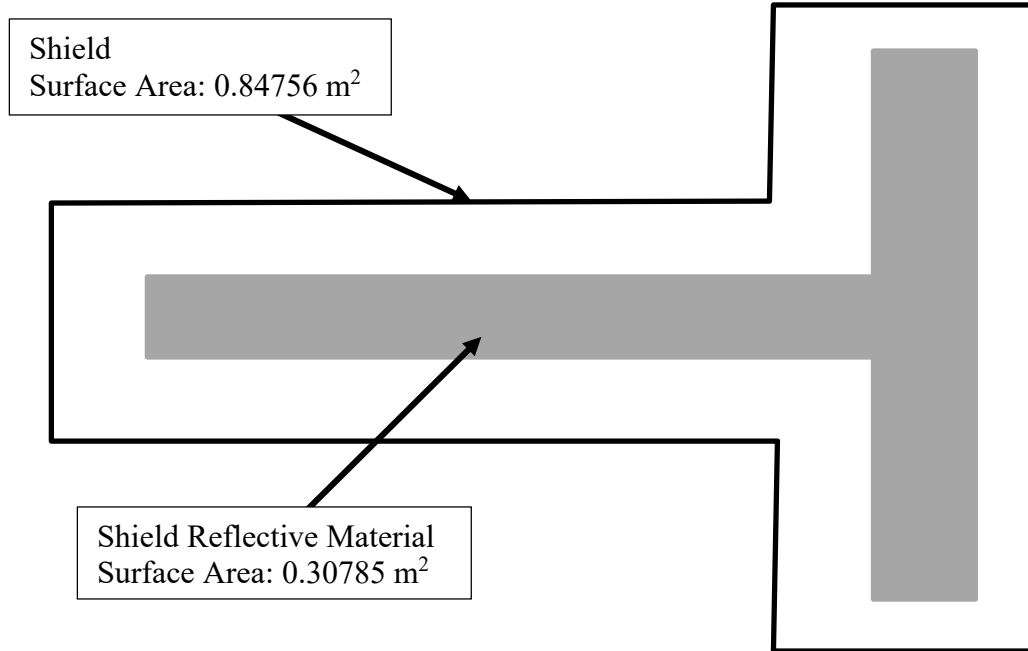
$$Bi_{total} = \frac{\left(200 \frac{W}{m^2 K}\right) \left(\frac{0.0572 m^3}{0.061 m^2}\right)}{1.07 \frac{W}{mK}}$$

$$Bi_{total} = 176$$

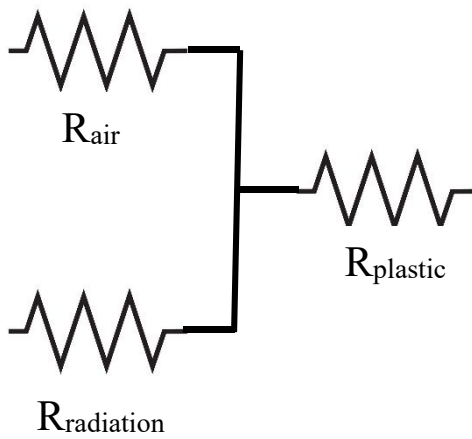
Thermal Circuit Properties and Sample Calculations

Material/Component	k (W/mK)	Cp (kJ/kgK)	Mass (kg)
Li-ion cell	0.8792 (Planar)/22.842 (Transverse)	0.85	0.384
Nylon Frame	0.3	1.59	0.12
Aluminum Cooling Plate	205	0.897	0.05
Steel Endplate	51.9	0.486	0.31
Fiberglass Cover	385	1.4	12
Steel Baseplate	51.9	0.49	19.8
Plastic Underbody Shield	0.3	1.5	0.9
Air	0.0265	1.01	-
Closed-Cell Foam	0.02	1.5	-
BMS Plastic	0.25	1.3	0.13
Bulkhead	167	0.96	3

Shield Component Resistance and Capacitance Calculations



Resistance Calculations



$$R_{air} = \frac{L}{kA} = \frac{0.013m}{\left(0.0265 \frac{W}{mK}\right)(0.84756m^2)} = 0.49 \frac{K}{W}$$

$$R_{plastic} = \frac{L}{kA} = \frac{0.00175m}{\left(0.3 \frac{W}{mK}\right)(0.84756m^2)} = 0.0069 \frac{K}{W}$$

$$R_{rad1} = \frac{1}{h_{rad}A}$$

$$h = \frac{(5.67e^{-8})(298^4 K - 293^4 K)}{\frac{1}{0.9} + \frac{1}{0.3} + 1} = 1.7 \frac{W}{m^2 K}$$

$$R_{rad1} = \frac{1}{h_{rad}A} = \frac{1}{\left(1.7 \frac{W}{m^2 K}\right)(0.30785m^2)} = 1.9 \frac{K}{W}$$

$$R_{rad2} = \frac{1}{h_{rad}A}$$

$$h = \frac{(5.67e^{-8})(298^4 K - 293^4 K)}{\frac{1}{0.9} + \frac{1}{0.9} + 1} = 4.8 \frac{W}{m^2 K}$$

$$R_{rad2} = \frac{1}{h_{rad}A} = \frac{1}{\left(4.8 \frac{W}{m^2 K}\right)(0.84756 - 0.30785m^2)} = 0.387 \frac{K}{W}$$

$$R_{parallel} = \left(\frac{1}{R_{air}} + \frac{1}{R_{rad1}} + \frac{1}{R_{rad2}}\right)^{-1} = \left(\frac{1}{0.49} + \frac{1}{1.9} + \frac{1}{0.387}\right)^{-1} = 0.19 \frac{K}{W}$$

$$R_{shield} = R_{parallel} + R_{plastic} = 0.19 + 0.0069 = 0.20 \frac{K}{W}$$

$$R_{shield} = 0.20 \frac{K}{W} * 288 = 57.8 \frac{K}{W} \text{ (per cell)}$$

Capacitance Calculations

$$m_{shield} = 1.1lbs = 900g = 0.9kg$$

$$C_{shield} = 1500 \frac{J}{kgK} \times 0.9kg = 1353.6 \frac{J}{K}$$

$$C_{shield} = \frac{1353.6}{288} = 4.7 \frac{J}{K} \text{ (per cell)}$$

Cell to Frame Resistance Calculations

TOP

$$\text{Length} = 170 \text{ mm}$$

$$\text{Insulation height} = 2.5 \text{ mm}$$

$$\text{Insulation width} = 5 \text{ mm}$$

$$A_{TOP} = 170mm \times 5mm = 516mm^2$$

$$A_{TOP} = 516mm^2 = 0.00052m^2$$

$$R_{TOP} = \frac{L}{kA} = \frac{0.0025m}{\left(0.02 \frac{W}{mK}\right)(0.00052m^2)} = 242.25 \frac{K}{W}$$

SIDE

$$\text{Length} = 150 \text{ mm}$$

$$\text{Insulation height} = 2.5 \text{ mm}$$

$$\text{Insulation width} = 3 \text{ mm}$$

$$A_{SIDE} = 150mm \times 3mm = 450mm^2$$

$$A_{SIDE} = 450mm^2 = 0.00045m^2$$

$$R_{SIDE} = \frac{L}{kA} = \frac{0.0025m}{\left(0.02 \frac{W}{mK}\right)(0.00045m^2)} = 277.78 \frac{K}{W}$$

There are two identical sides which are in parallel, therefore the total resistance for the side is:

$$R_{SIDE_Parallel} = \frac{R_{SIDE} R_{SIDE}}{R_{SIDE} + R_{SIDE}} = \frac{277.78 \times 277.78}{277.78 + 277.78} = 138.89 \frac{K}{W}$$

MANIFOLD

Length = 70 mm

Insulation height = 2.5 mm

Insulation width = 3 mm

$$A_{MANIFOLD} = 70mm \times 3mm = 210mm^2$$

$$A_{MANIFOLD} = 210mm^2 = 0.00021m^2$$

$$R_{MANIFOLD} = \frac{L}{kA} = \frac{0.0025m}{\left(0.02 \frac{W}{mK}\right)(0.00021m^2)} = 595.23 \frac{K}{W}$$

There are two identical manifolds which are in parallel, therefore the total resistance for the manifold is:

$$R_{MANIFOLD_Parallel} = \frac{R_{MANIFOLD} R_{MANIFOLD}}{R_{MANIFOLD} + R_{MANIFOLD}} = \frac{595.23 \times 595.23}{595.23 + 595.23} = 297.62 \frac{K}{W}$$

BOTTOM

Length = 170 mm

Insulation height = 2.5 mm

Insulation width = 3 mm

$$A_{BOTTOM} = 170mm \times 3mm = 510mm^2$$

$$A_{BOTTOM} = 510mm^2 = 0.00051m^2$$

$$R_{TOP} = \frac{L}{kA} = \frac{0.0025m}{\left(0.02 \frac{W}{mK}\right)(0.00051m^2)} = 245.1 \frac{K}{W}$$

Appendix C – Error Analysis

This appendix outlines the process for determining the error analysis for the experimental validation results. All sample calculations to the equations and methodology outline here can be found in the work developed by Filion [91].

Uncertainty Analysis

The uncertainty analysis for the thermal resistance is required since multiple direct measurements of the change in temperature and heat flow (ΔT and \dot{Q}) are used to make a compound measurement. The error in each measurement needs to be considered to determine the total amount of uncertainty. This will allow for the resulting uncertainty to define the tolerance range with each resistive element in the circuit. Below is a summary of the equations used to calculate the tolerance of the resistive elements with table C.1 showing the resulting values.

Result Uncertainty

$$U_R = \sqrt{B_R^2 + (tS_R)^2}$$

Where S_R = Precision Index and B_R = Bias Limit

$$B_R = \sqrt{\sum_{i=1}^n \left(\frac{\partial R_{M_i}}{\partial M_i} B_{M_i} \right)^2}$$
$$S_R = \sqrt{\sum_{i=1}^n \left(\frac{\partial R_{M_i}}{\partial M_i} S_{M_i} \right)^2}$$

As multiple measurements are taken for the resistive elements, the spread of uncertainty is equal to the error sum of two measurements when adding.

$$U_{sum} = \sqrt{U_{R1}^2 + U_{R2}^2}$$

The error in the product of two measurements is the fractional uncertainty in each measurement ($\pm\%$ of the nominal).

$$U_{sum} = \sqrt{\left(\frac{U_{R1}^2}{R1}\right)^2 + \left(\frac{U_{R2}^2}{R2}\right)^2}$$

Table C.1 is a sample of the uncertainty measurements with sample calculations found in the reference.

C.1 – Resistor Tolerance Values [91]

Resistor / Area (m ₂)	<i>R_i</i> (°C/W)	ΔT_i (°C)	$\partial R \partial \Delta T$	\dot{Q}_i (W)	$\partial R \partial \dot{Q}$	<i>BR</i>	<i>SR</i>	<i>UR</i> (°C/W)
<i>R_{bp}</i> (0.6590)	0.194	7.133	0.0307	37.55	0.0055	0.0113	0.0005	3.23
<i>R_{man inlet}</i> (0.1623)	0.314	2.733	0.1366	8.69	0.0409	0.0249	0.0004	7.18
<i>R_{man outlet}</i> (0.1623)	0.259	2.400	0.1299	8.99	0.0314	0.0209	0.0003	6.02
<i>R_{side inlet}</i> (0.2474)	0.196	2.500	0.1010	12.28	0.0178	0.0173	0.0003	4.98
<i>R_{side outlet}</i> (0.2474)	0.230	2.533	0.1090	10.92	0.0234	0.0211	0.0003	6.07
<i>R_{top1}</i> (0.2474)	0.134	1.633	0.1023	12.05	0.0128	0.0161	0.0002	4.64
<i>R_{top2}</i> (0.4168)	0.305	4.800	0.0759	15.93	0.0219	0.0287	0.0005	8.27
<i>R_{end}</i> (0.268)	0.207	3.667	0.0676	17.72	0.0135	0.0132	0.0002	3.79
<i>R_{bot}</i> (0.5116)	0.127	5.233	0.0286	40.09	0.0034	0.0061	0.0001	1.77
<i>R_{ag man outlet}</i> (0.1623)	0.853	7.167	0.1415	8.60	0.1172	0.0592	0.0010	17.05
<i>R_{ag man inlet}</i> (0.1623)	0.726	6.267	0.1383	8.84	0.0974	0.0498	0.0008	14.34
<i>R_{ag side outlet}</i> (0.2474)	0.496	6.100	0.0989	12.20	0.0462	0.0359	0.0006	10.36
<i>R_{ag side inlet}</i> (0.2474)	0.528	6.100	0.1012	12.04	0.0529	0.0408	0.0007	11.76
<i>R_{ag top}</i> (0.2474)	0.372	5.167	0.0779	15.04	0.0293	0.0375	0.0007	10.81
<i>R_{ag end}</i> (0.268)	0.473	7.733	0.0711	16.80	0.0330	0.0277	0.0005	7.97
<i>R_{bh1}</i> (0.0544)	1.087	6.567	0.1965	6.31	0.2169	0.0415	0.0007	11.95
<i>R_{c man}</i> (0.4354)	0.034	1.250	0.0269	37.12	0.0008	0.0031	0.0001	0.90

$R_{c\ side}$ (0.4538)	0.020	0.900	0.0226	44.18	0.0004	0.0025	0.0000	0.73
$R_{c\ top}$ (0.4122)	0.062	1.800	0.0344	29.07	0.0018	0.0044	0.0002	1.26
$R_{oc\ man}$ (0.4354)	0.390	14.000	0.0279	35.88	0.0093	0.0126	0.0010	3.66
$R_{oc\ side}$ (0.4538)	0.360	15.600	0.0231	43.30	0.0073	0.0102	0.0008	2.98
$R_{oc\ top}$ (0.4122)	0.569	11.500	0.0495	20.20	0.0221	0.0278	0.0022	8.11
R_{obp} (0.6590)	0.225	8.333	0.0307	37.55	0.0063	0.0129	0.0006	3.74
R_{obh} (0.0544)	2.368	14.133	0.1965	6.31	0.4640	0.0788	0.0034	22.78
R_{bh2} (0.0544)	4.295	6.681	0.7251	1.53	2.5051	0.4165	0.0198	120.53
R_{int}	0.003	0.483	0.0099	161.31	0.0000	0.0011	0.0000	0.31

Experimental and Simulation Error

The temperature and heat flow responses are compared and the resulting errors are presented. Differences in ambient temperature, starting temperatures, fluid bench behaviour, and air currents between testing days would introduce errors into the measurements. The validity of the experimental data compared to the PSpice simulation results is examined.

The temperature errors from Figure 5.20 are shown in table C.2 in the form of absolute maximum error, RMS error in °C, and RMS error as a percent of temperature rise. The maximum absolute error of 1.5°C, and RMS error of 0.5°C are targets, anything below these values is considered acceptable. The RMS value represent the average error in °C over the transient period of the temperature rise. The majority of the components are well below the maximum absolute limit of acceptance, with the manifold being the only outlier. The majority of RMS errors also lie within 0.5°C except for the manifold again. The percent error values are below 5% including the manifold.

C.2 – Experimental and Simulation Errors for Circuit Temperatures [91]

Component	Absolute Max Error (°C)	RMS Error (°C)	RMS Error (% ΔT)
Endplate	0.87	0.39	2.4
Top	0.36	0.14	1.0
Side	0.60	0.23	1.3
Manifold	2.30	0.60	4.2
Bottom	1.17	0.42	3.0
Baseplate	0.65	0.26	3.0
Bulkhead	0.87	0.18	1.3
Inside Cover	0.59	0.22	2.2
Outside Cover	0.39	0.12	1.3

The same procedures are followed to compare simulated heat flow to experimental data. The heat flux sensors have greater fluctuations than the thermocouples, especially on the outer surfaces which include the baseplate, cover, and bulkhead.

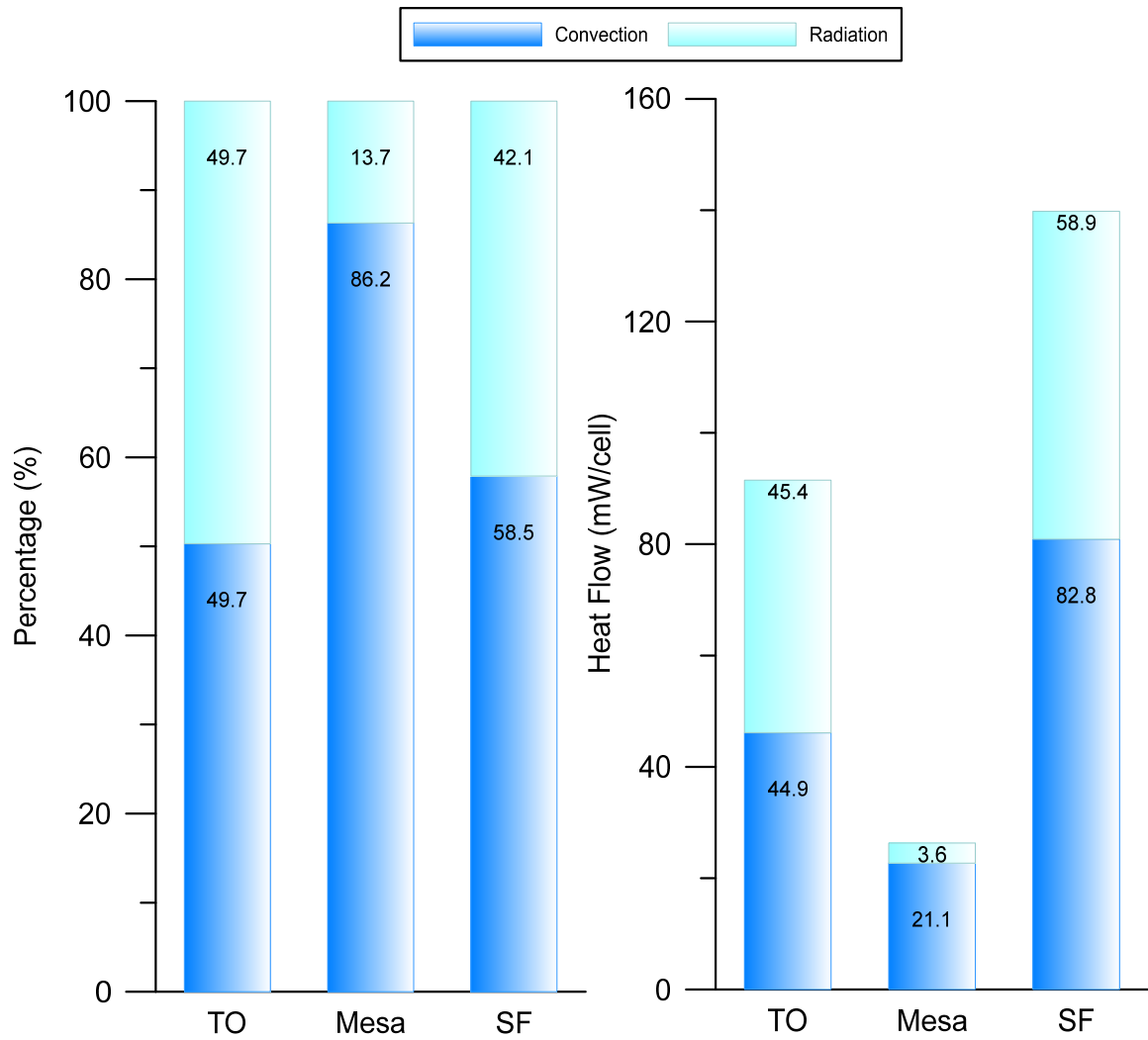
The heat flow errors in Figure 5.21 are shown in table C.3 as the absolute maximum and RMS errors. The level of measurement signal noise is included for comparison purposes. The error values are highly influenced by the level of sensor noise which gives a falsely high impression. It should be noted that no acceptable range of heat flow accuracy is present in available literature since temperature is usually the main focal point of studies. The level of measurement signal noise is included for comparison purposes.

The simulated heat rates represent the experimental measurements fairly accurately. Mild convection currents in the lab environment are environmental fluctuations which affect exposed surfaces. This can cause larger error calculations and is captured in the signal to noise ratio. While the values indicates a substantial amount of error, the RMS error values are close to the signal variation which indicates the error values are acceptable due to the environmental factors.

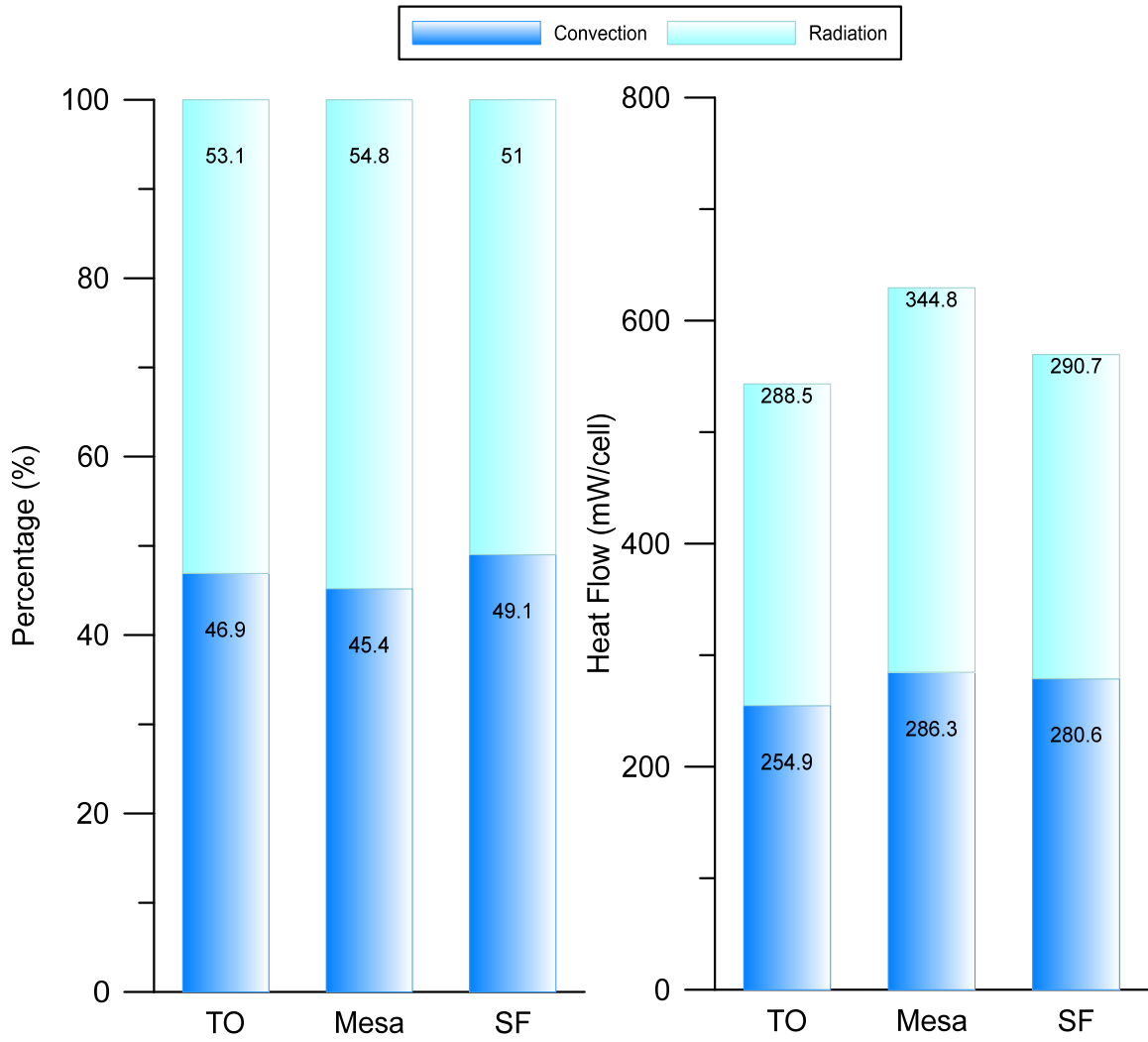
C.3 – Experimental and Simulation Errors for Circuit Temperatures [91]

Component	Max Absolute Error (mW)	RMS Error (mW)	Signal Noise (mW)
Endplate	8.61	2.47	1.15
Top	9.94	3.05	1.99
Side	15.69	5.43	1.96
Manifold	15.44	4.64	1.09
Baseplate	97.66	15.98	14.33
Bulkhead	13.44	2.65	2.32
Cover	88.68	16.88	18.24

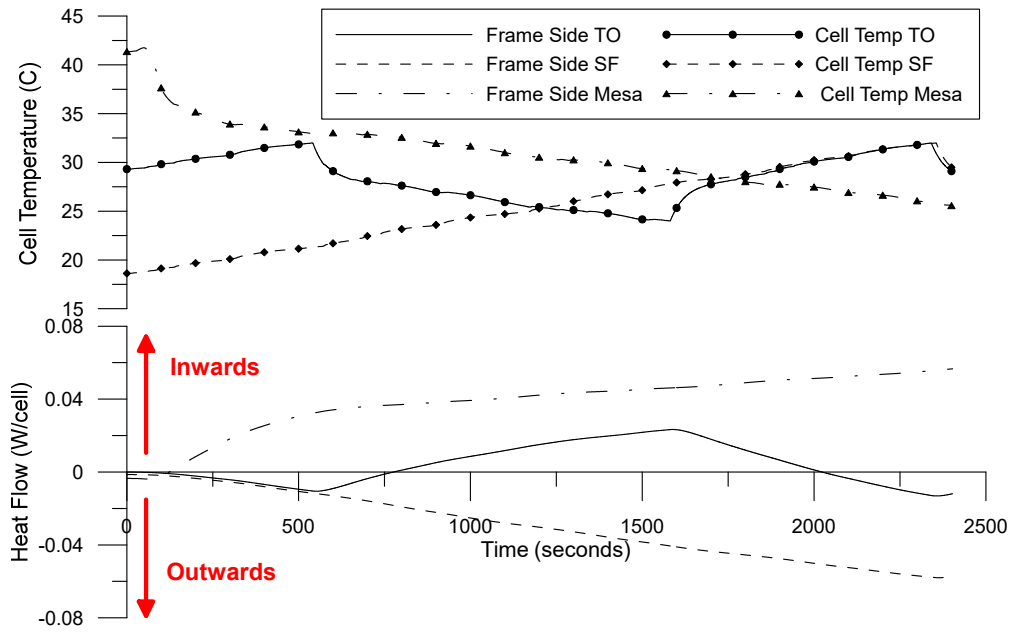
Appendix D – Drive Cycle Heat Flows



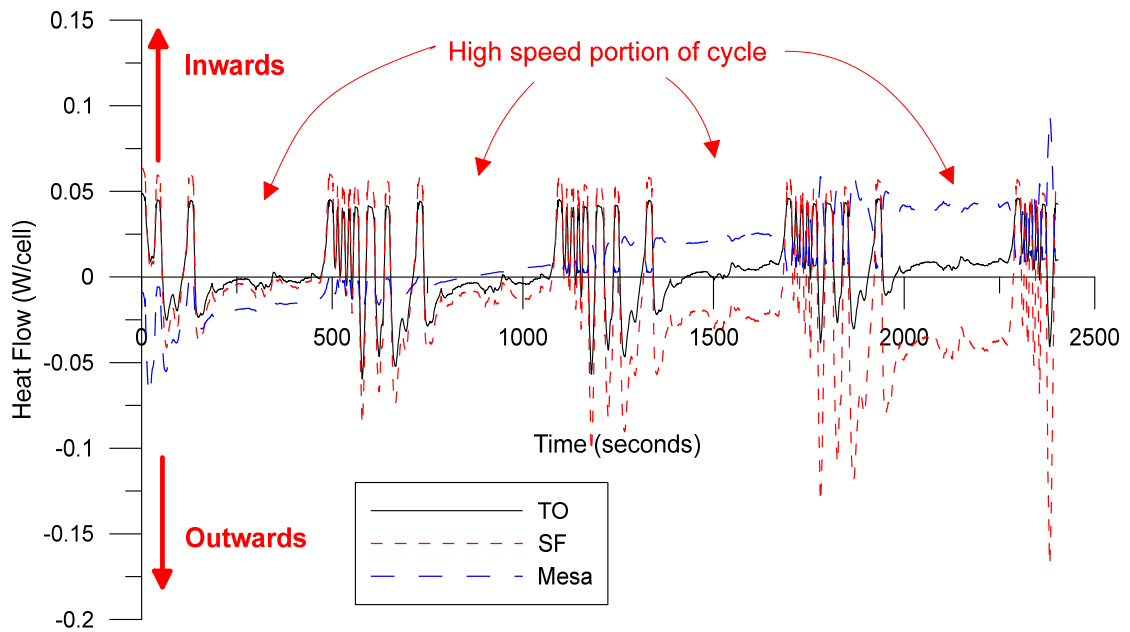
D.1 – FC US06 shield heat flow percentage (left) and heat flow value (right)



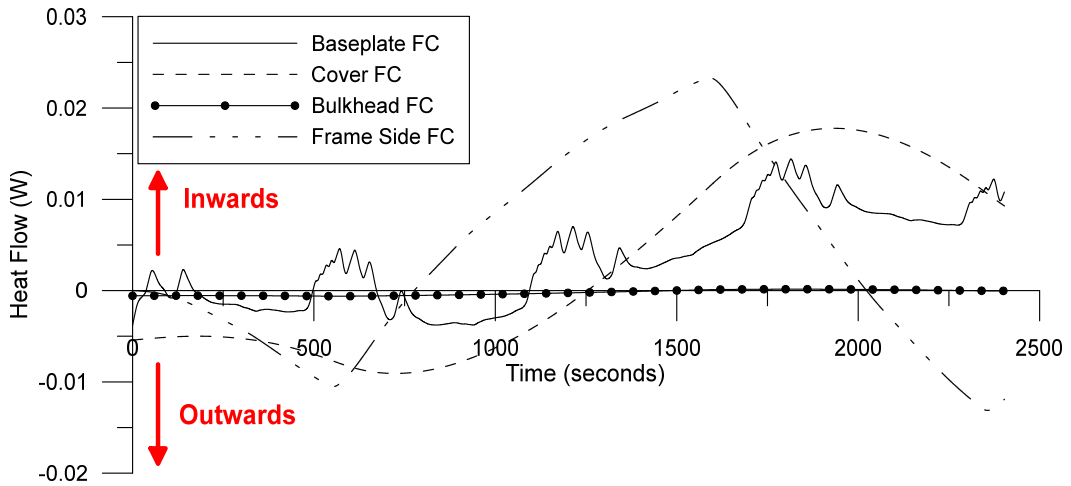
D.2 – FC US06 shield heat flow percentage (left) and heat flow value (right) at peak solar position



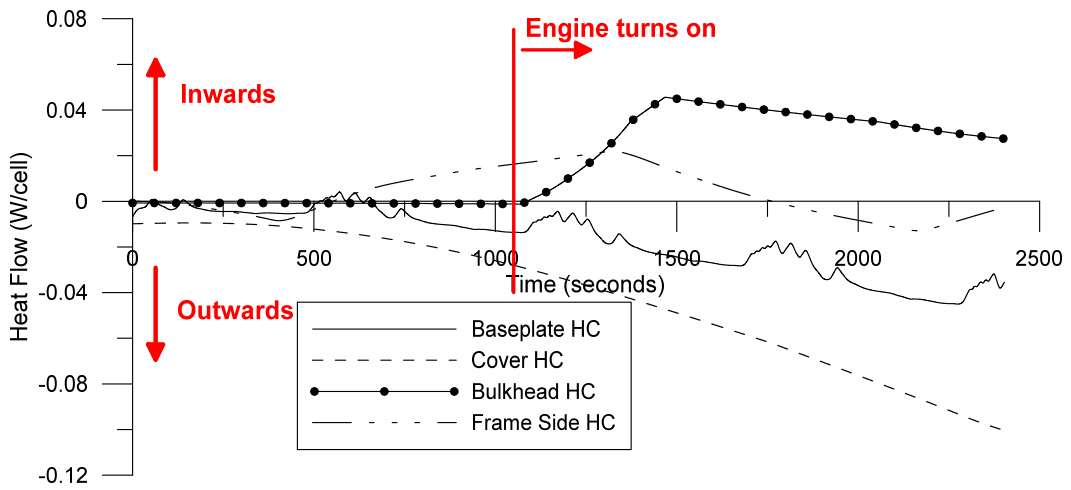
D.3 – US06 frame side heat flow comparison for FC simulation



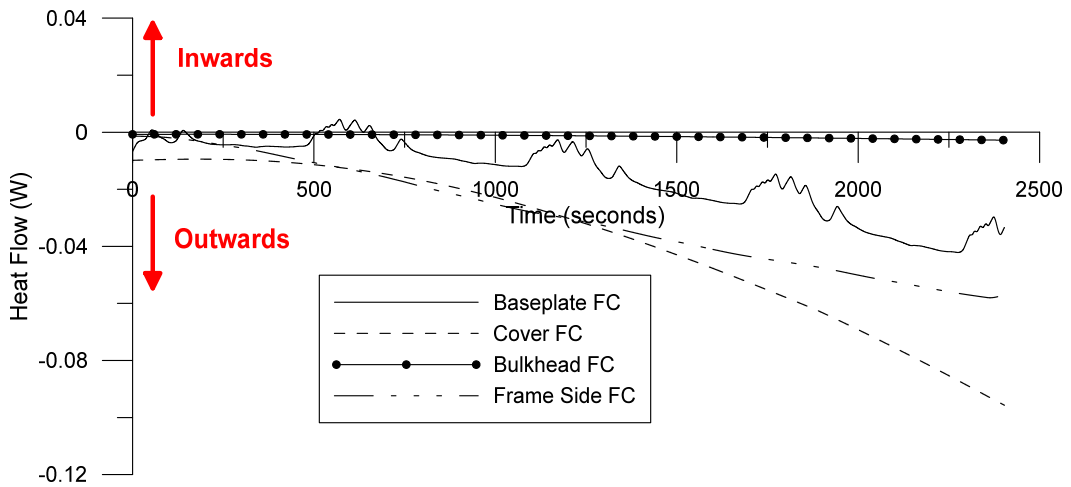
D.4 – US06 shield heat flows for FC simulation



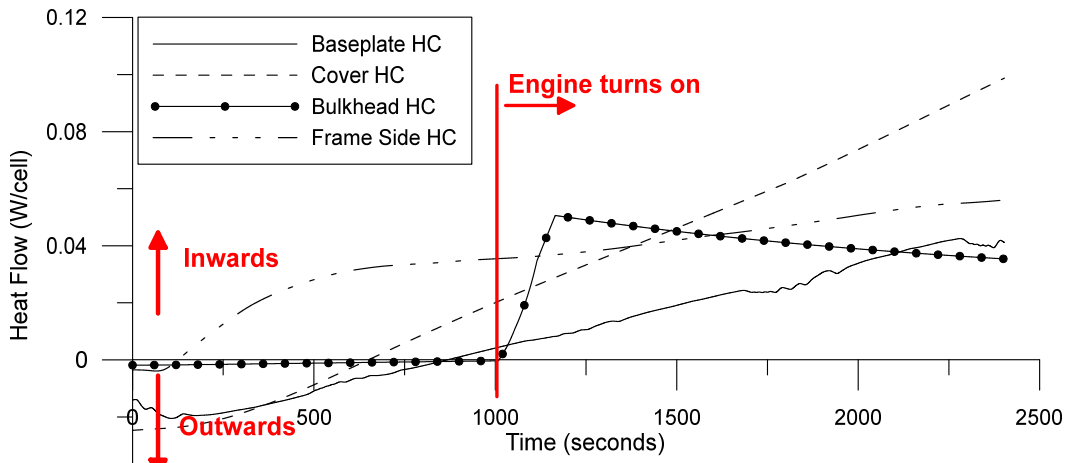
D.5 – Toronto US06 external component heat flow for FC simulations



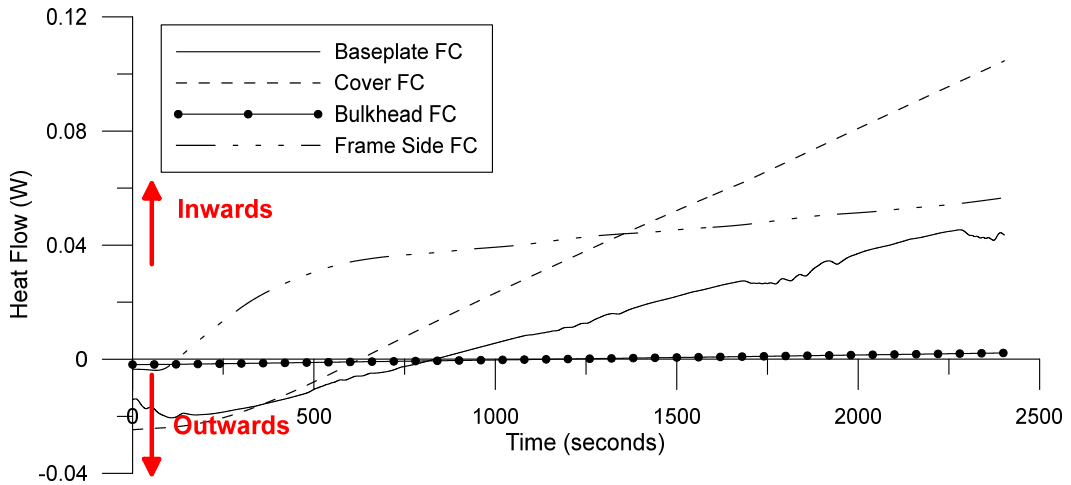
D.6 – San Francisco US06 external component heat flow for HC simulations



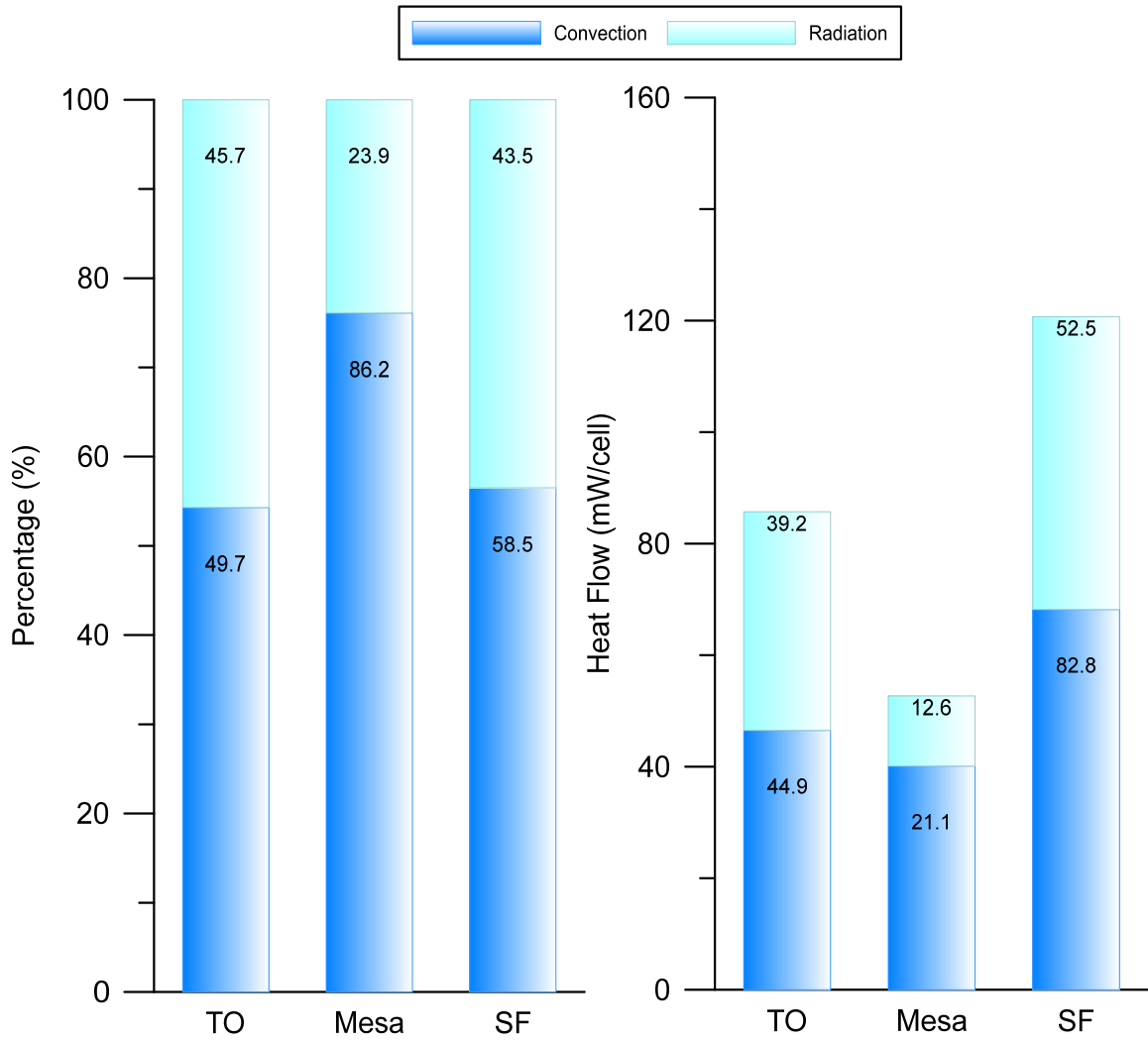
D.7 – San Francisco US06 external component heat flow for FC simulations



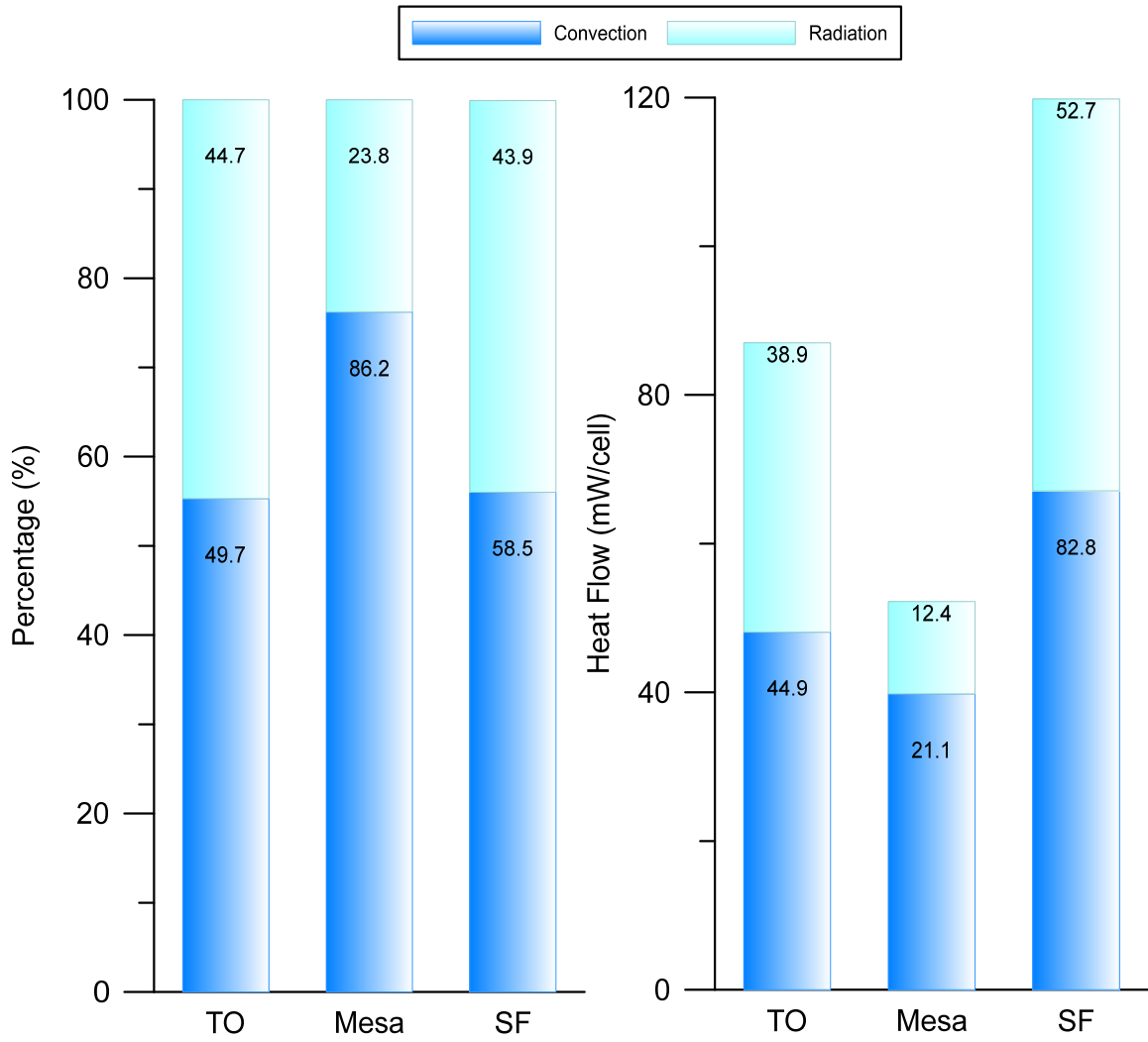
D.8 –Mesa external component heat flow for HC simulations



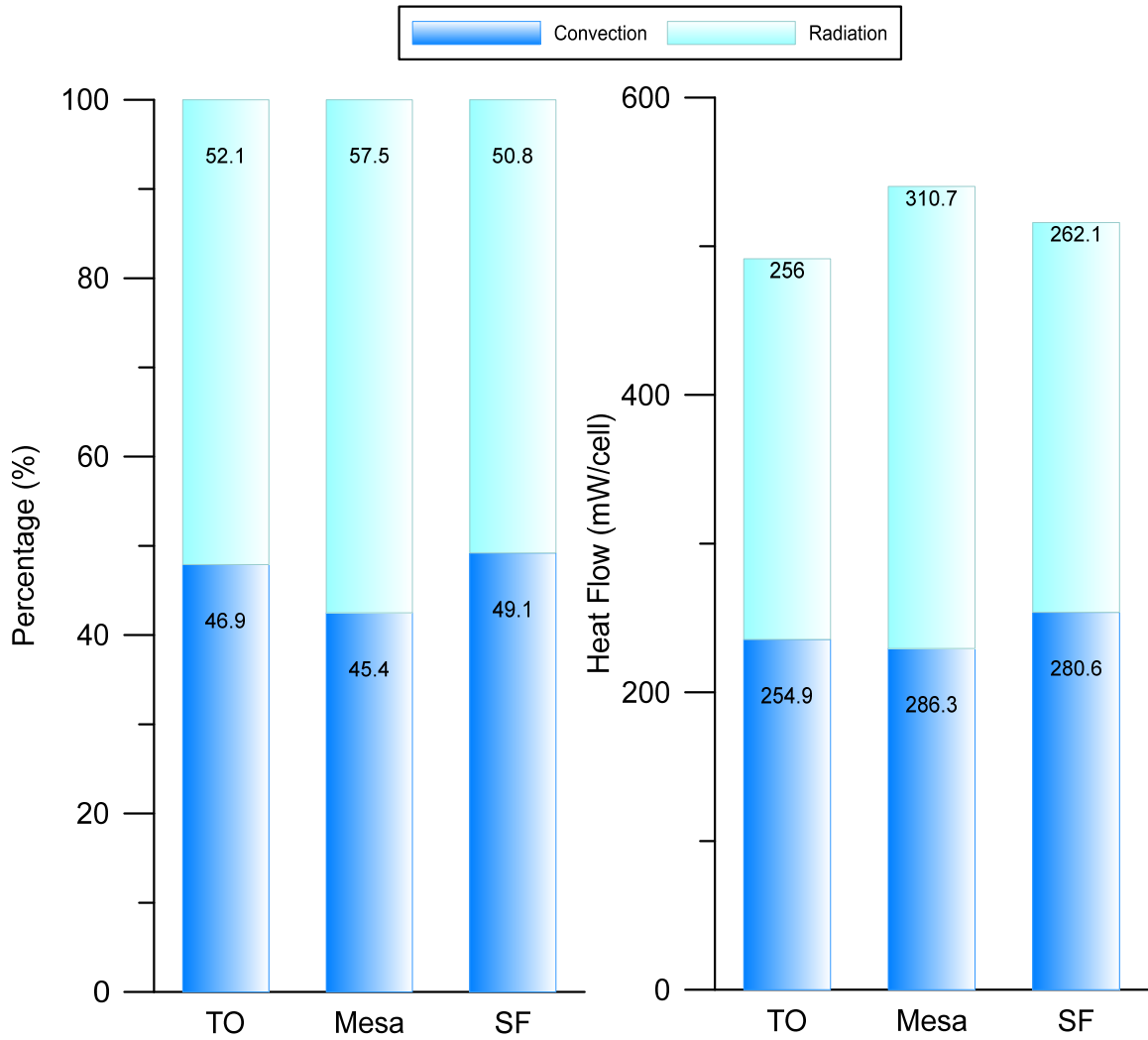
D.9 – Mesa US06 external component heat flow for FC simulations



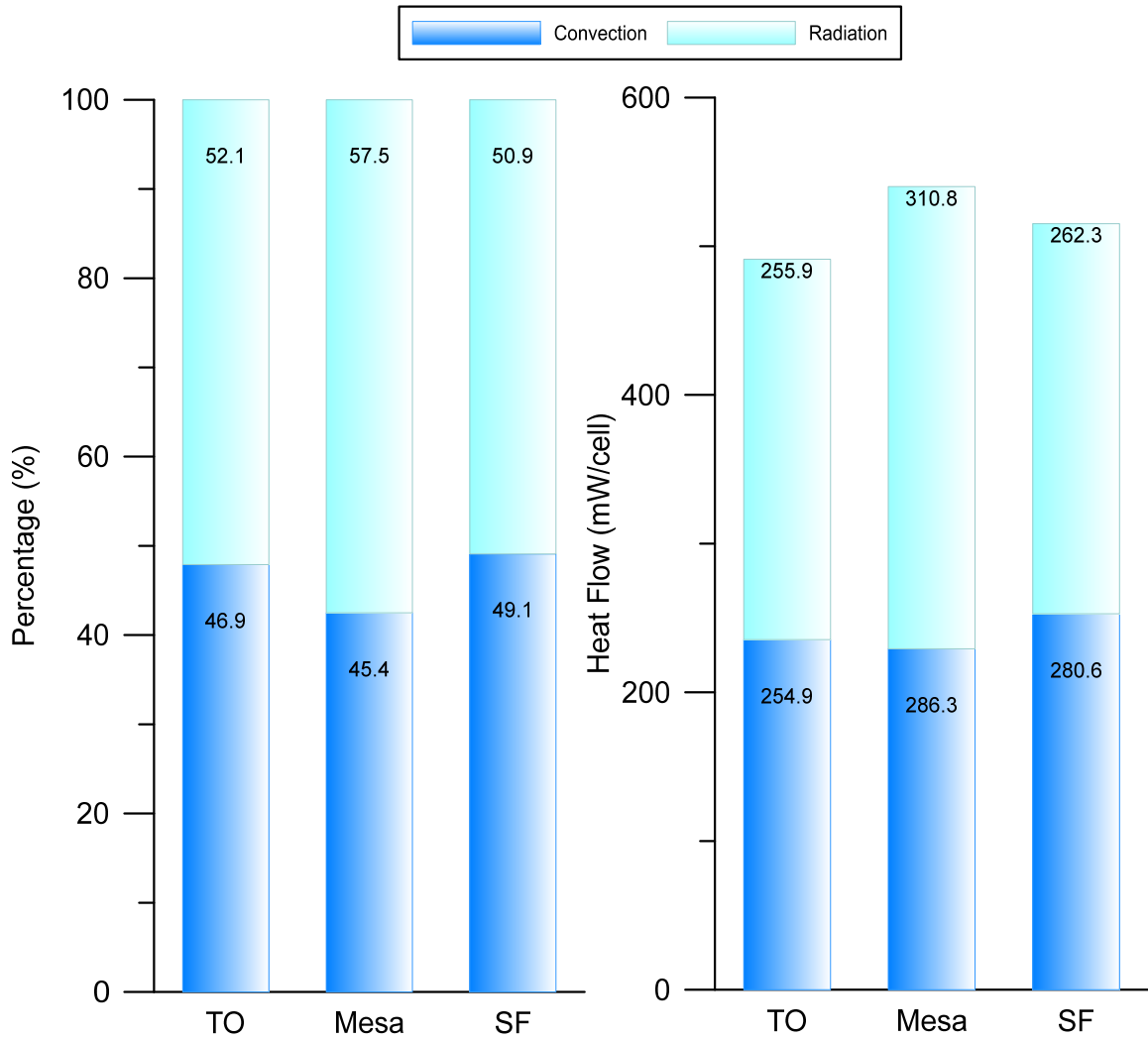
D.10 – HC UDDS shield heat flow percentage (left) and heat flow value (right)



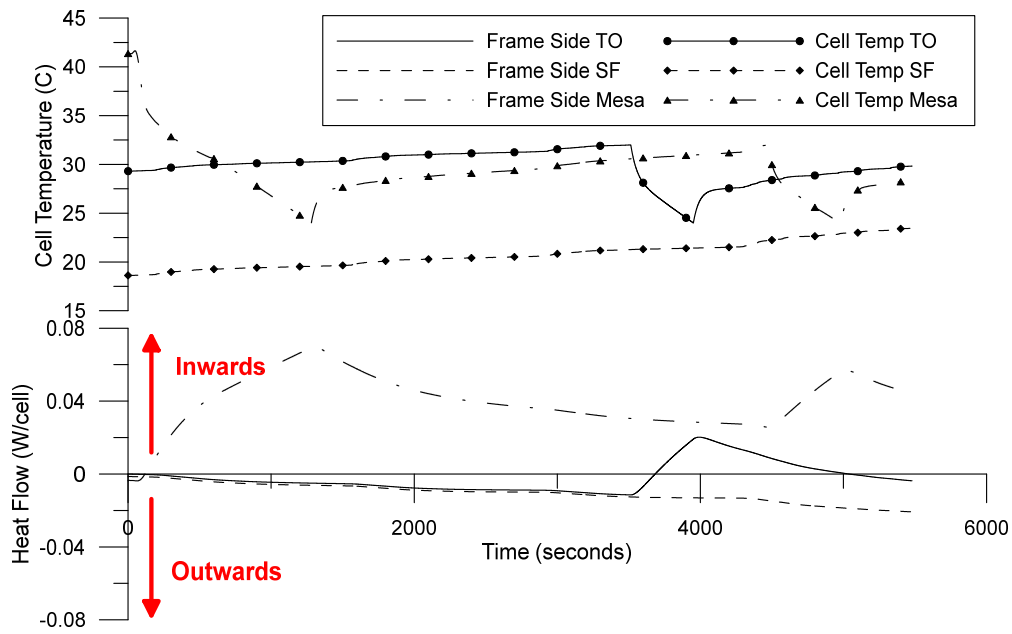
D.11 – FC UDDS shield heat flow percentage (left) and heat flow value (right)



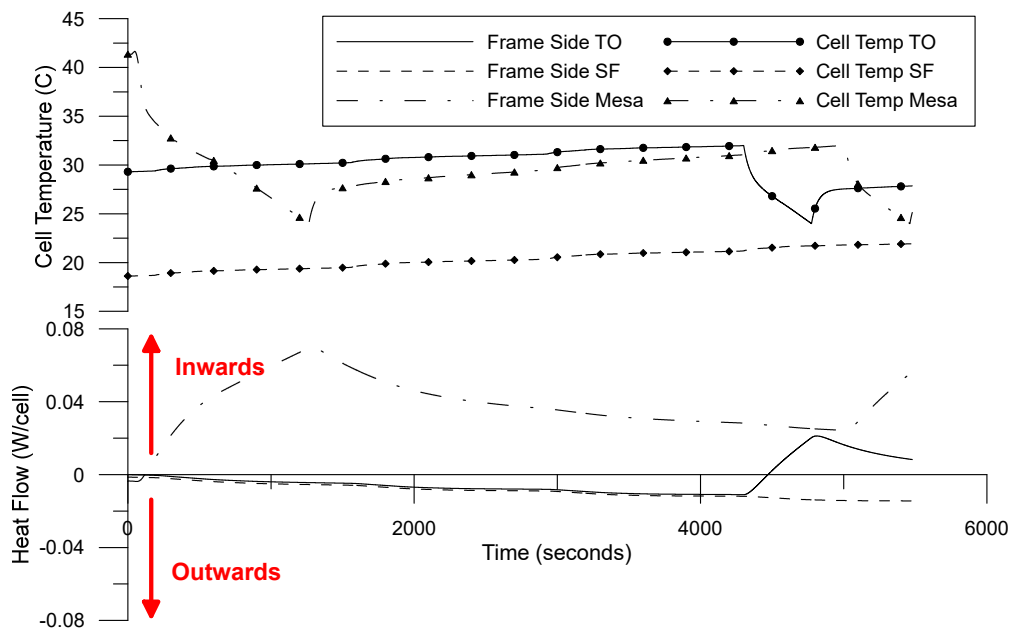
D.12 – HC UDDS shield heat flow percentage (left) and heat flow value (right) at peak solar position



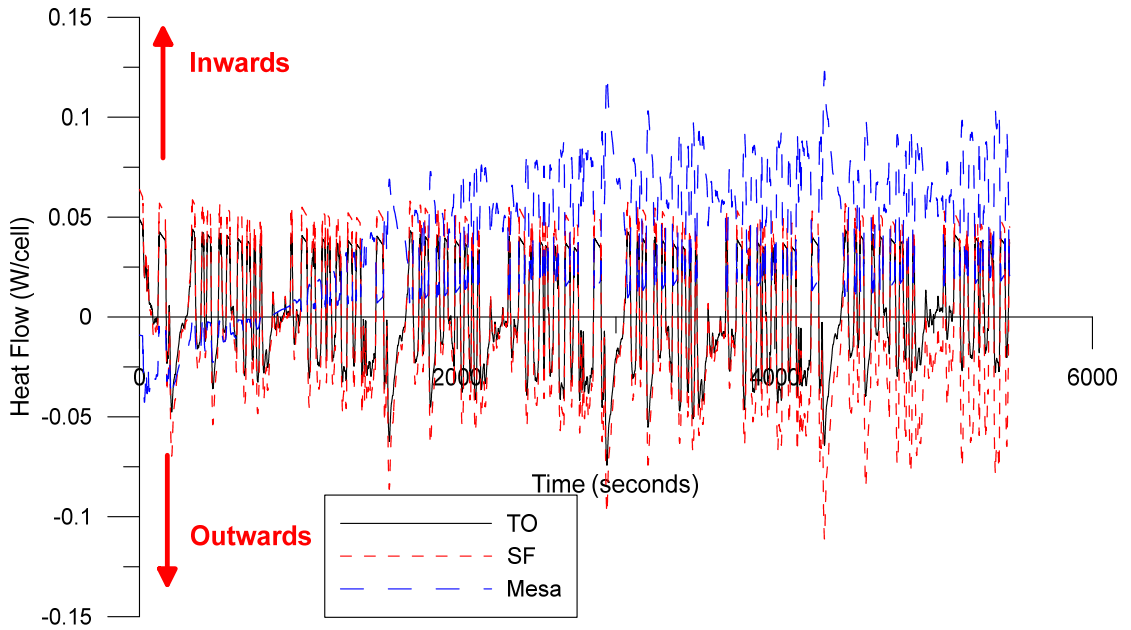
D.13 – FC UDDS shield heat flow percentage (left) and heat flow value (right) at peak solar position



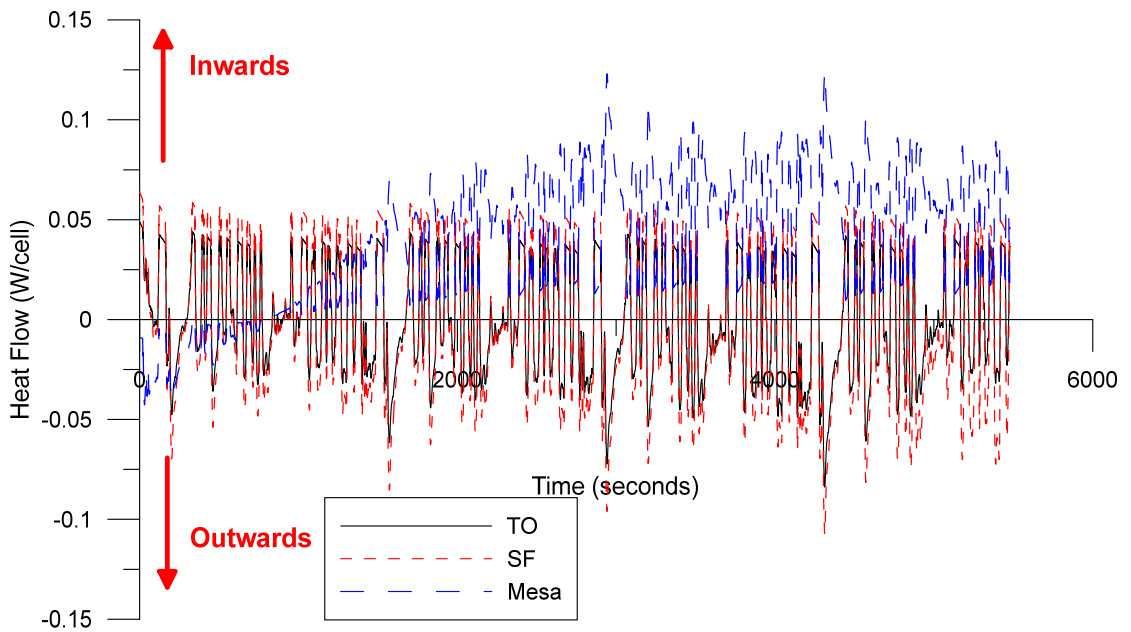
C.14 – UDDS frame side heat flow comparison for HC simulation



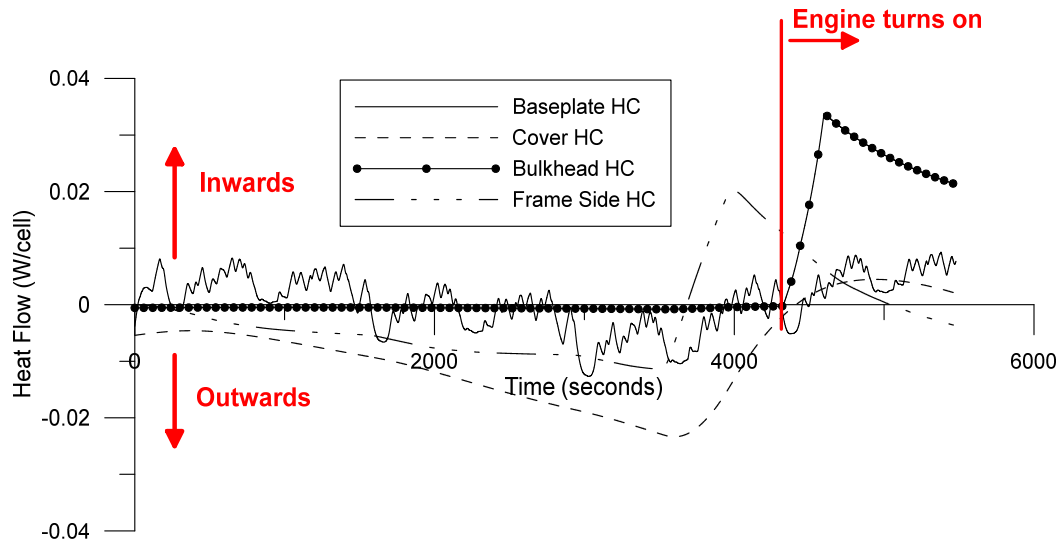
D.15 – UDDS frame side heat flow comparison for FC simulation



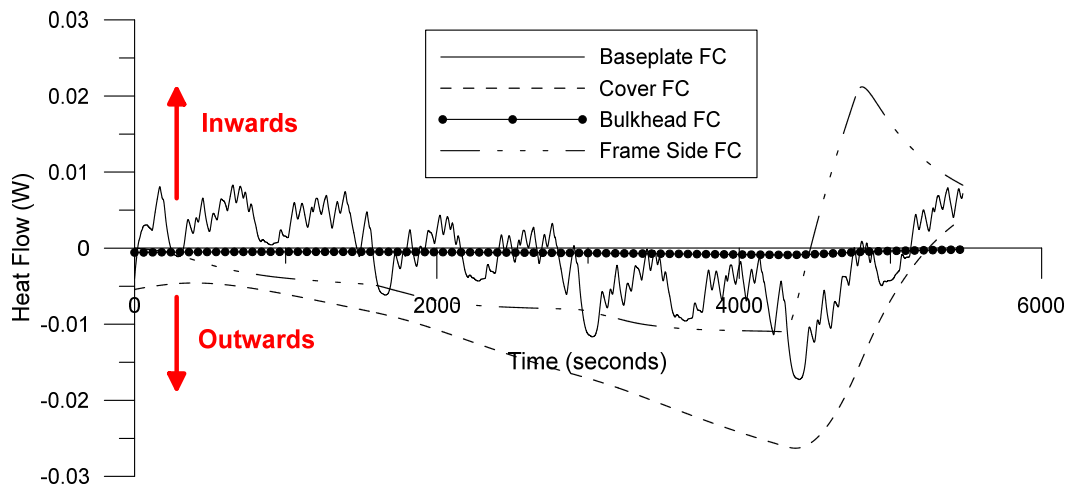
C.16 – UDDS shield heat flows for HC simulations



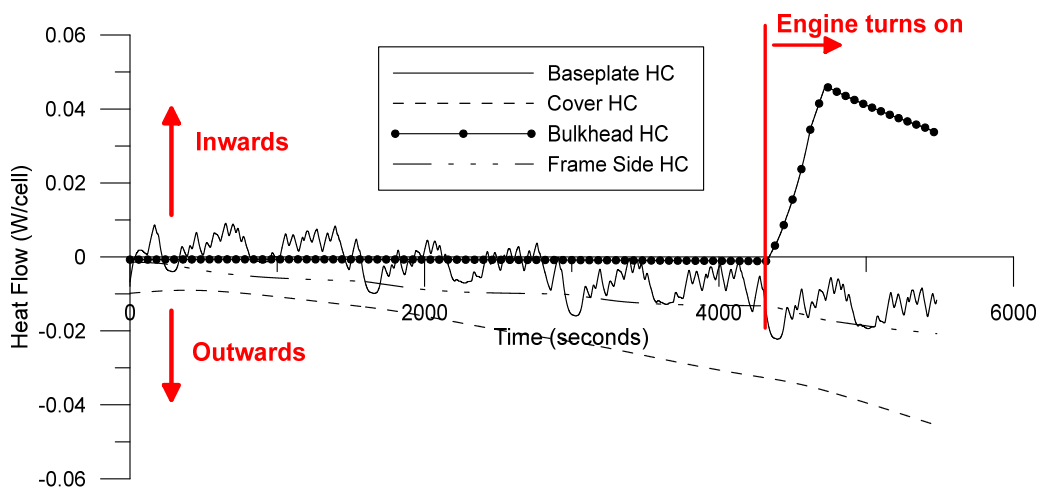
D.17 – UDDS shield heat flows for FC simulations



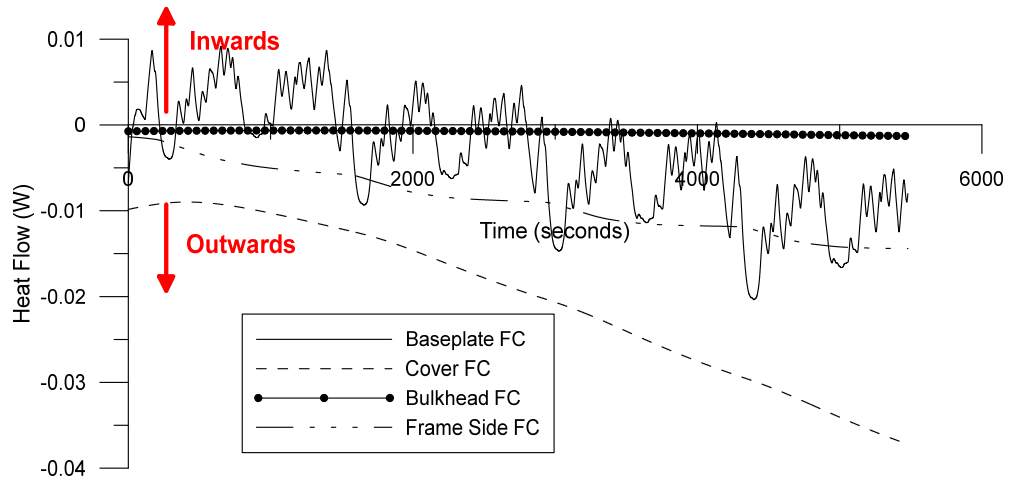
D.18 – Toronto UDDS external component heat flow for HC simulation



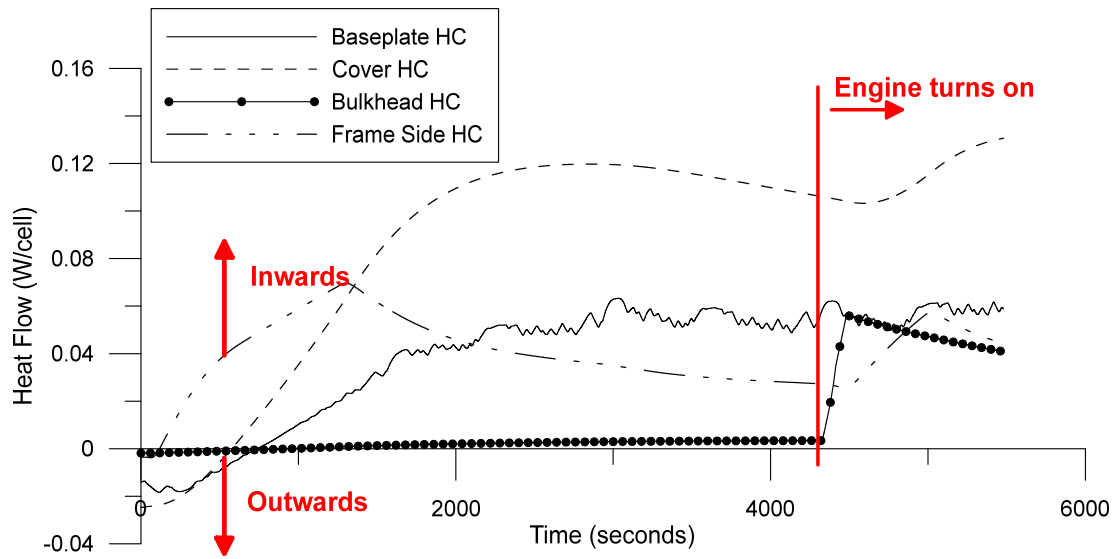
D.19 – Toronto UDDS external component heat flow for FC simulation



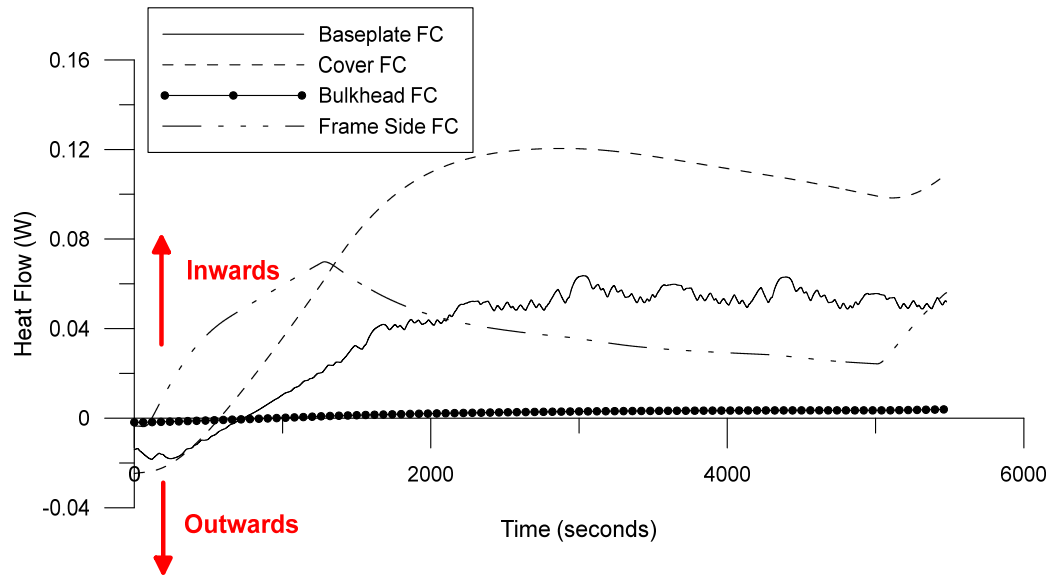
D.20 – San Francisco UDDS external component heat flow for HC simulation



D.21 – San Francisco UDDS external component heat flow for FC simulation



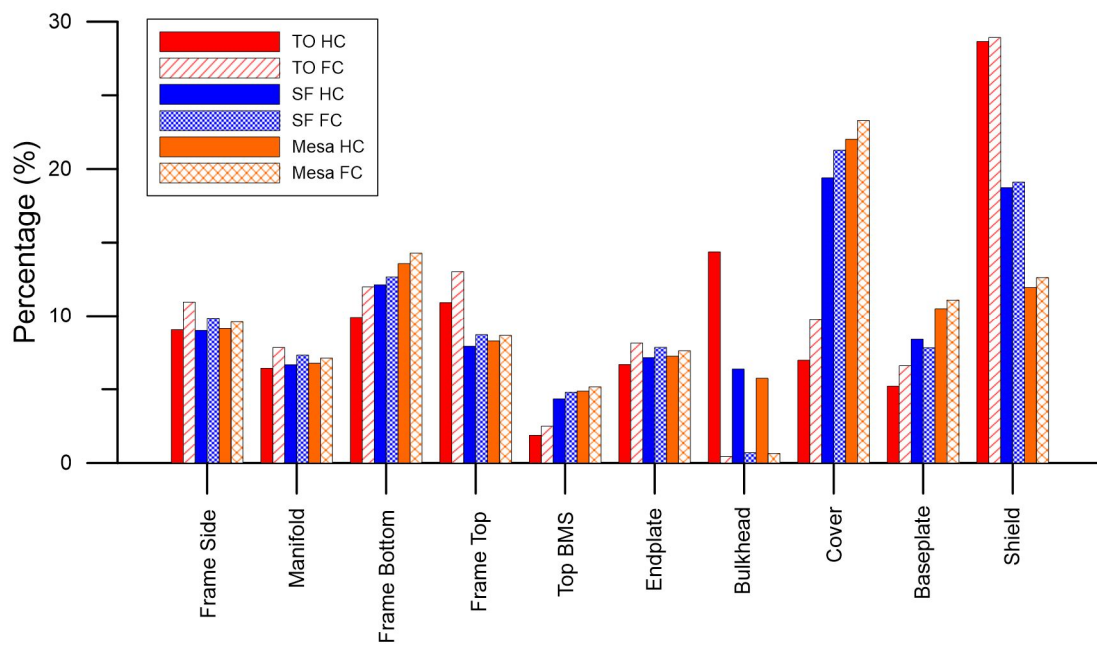
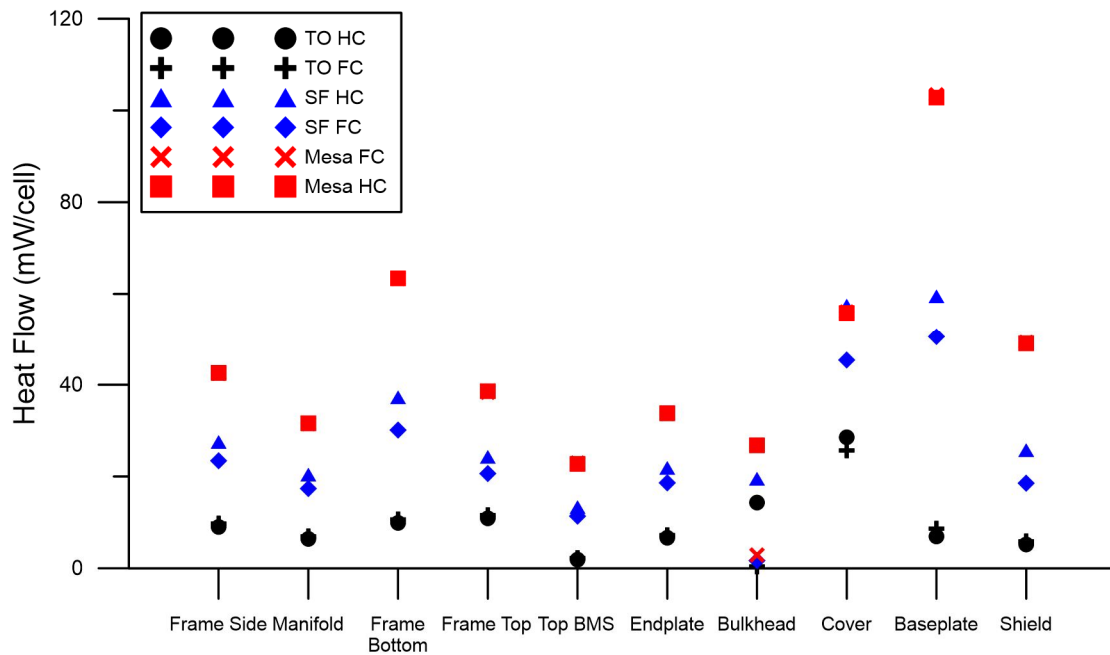
D.22 – Mesa UDDS external component heat flow for HC simulation



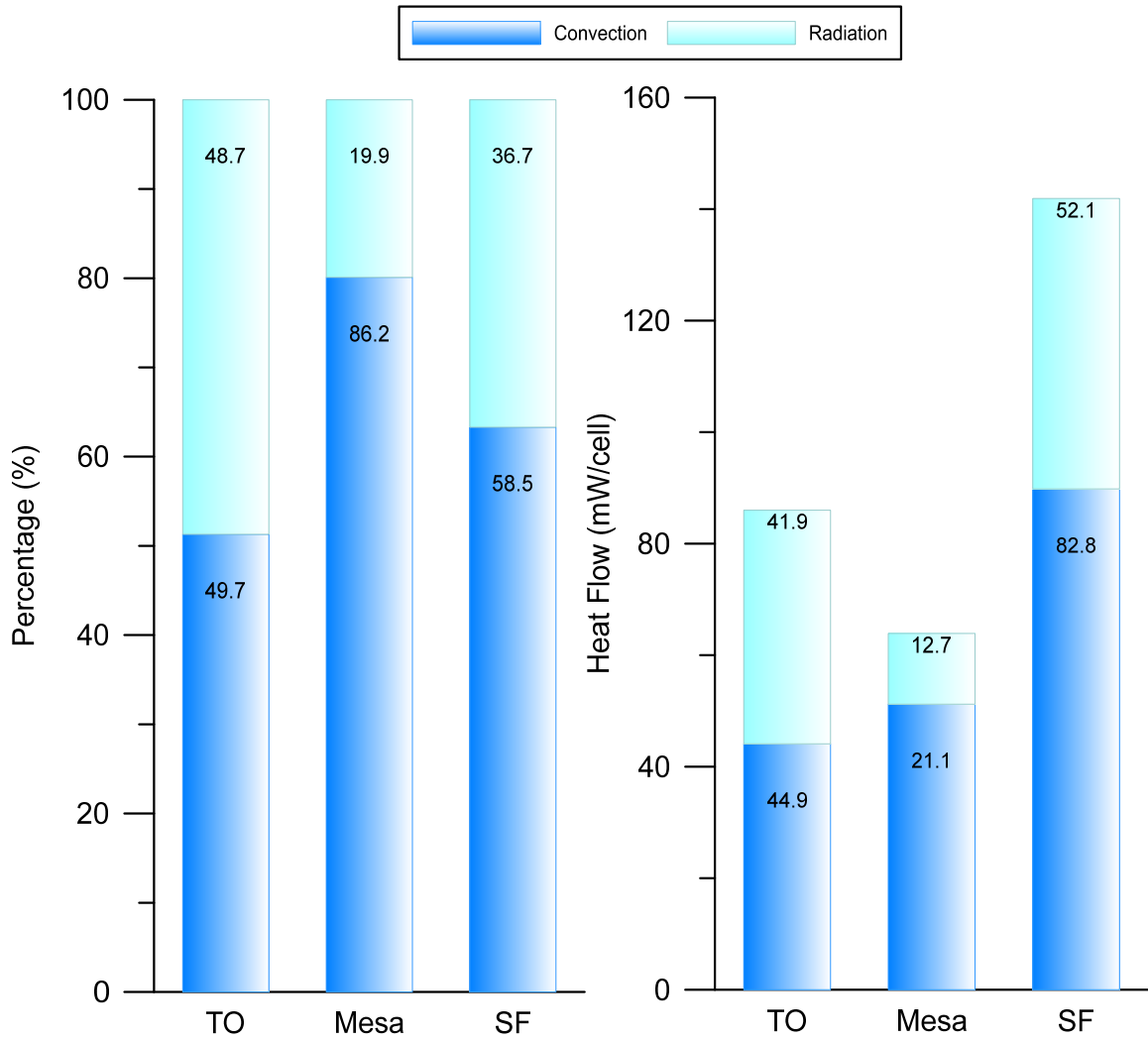
D.23 – Mesa UDDS external component heat flow for FC simulation

D.24 - LA92 Average Heat Flow

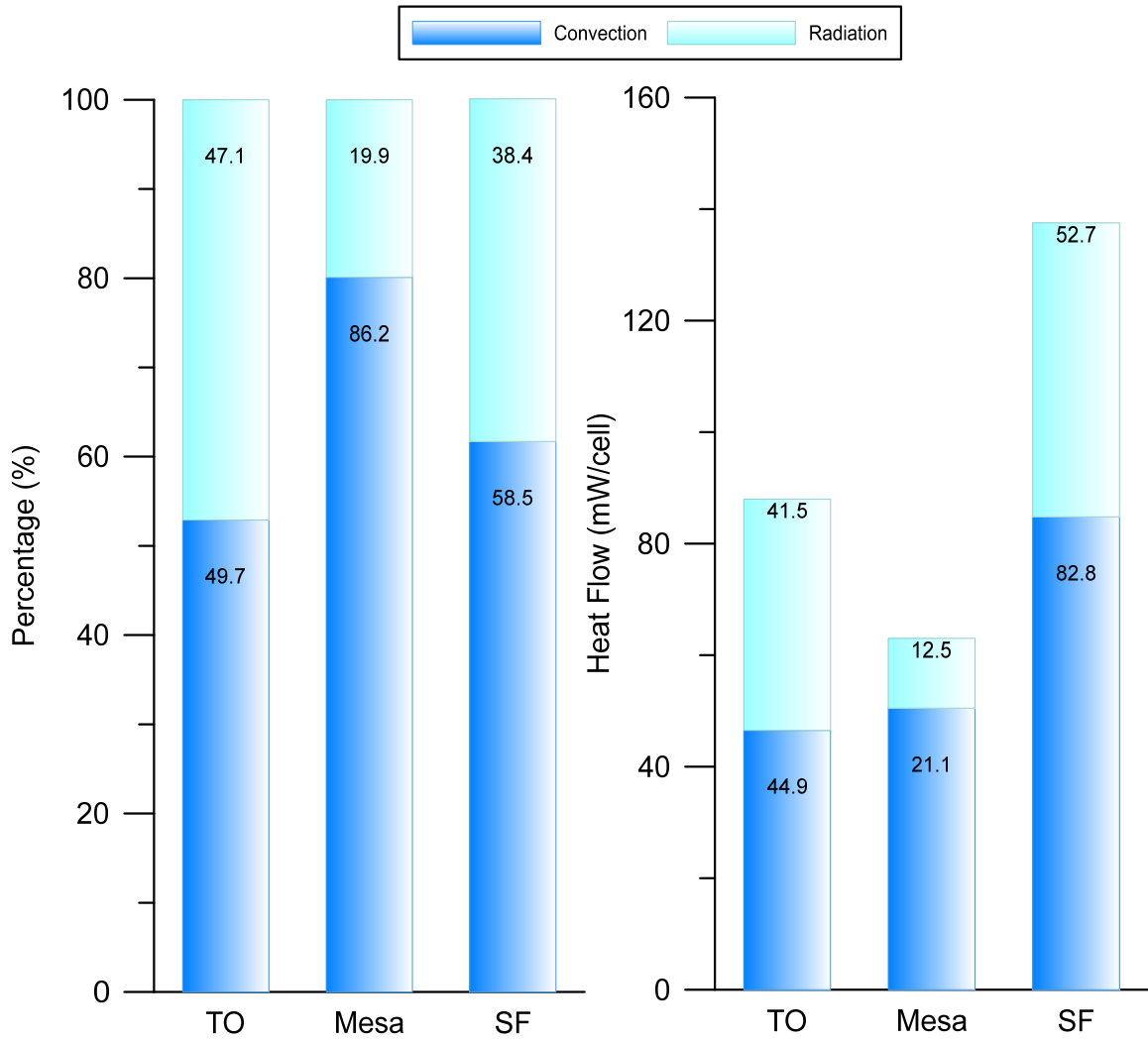
Pack Section	Component	TO HC	TO FC	SF HC	SF FC	Mesa HC	Mesa FC
Interior	Frame Side	9.00	9.74	27.52	23.43	42.59	42.5
	Manifold	6.39	6.94	20.40	17.37	31.59	31.55
	Frame Bottom	9.88	10.65	37.24	30.12	63.40	63.41
	Frame Top	10.88	11.58	24.26	20.64	38.59	38.38
	Top BMS	1.87	2.22	13.32	11.36	22.74	22.92
	Endplate	6.64	7.21	21.86	18.62	33.79	33.73
Exterior	Bulkhead	14.31	0.39	19.50	1.67	26.79	2.89
	Baseplate	6.93	8.63	59.48	50.54	102.81	103.42
	Shield	5.18	5.86	25.73	18.54	49.04	49.24
	Cover	28.54	25.68	57.45	45.41	55.82	56.06



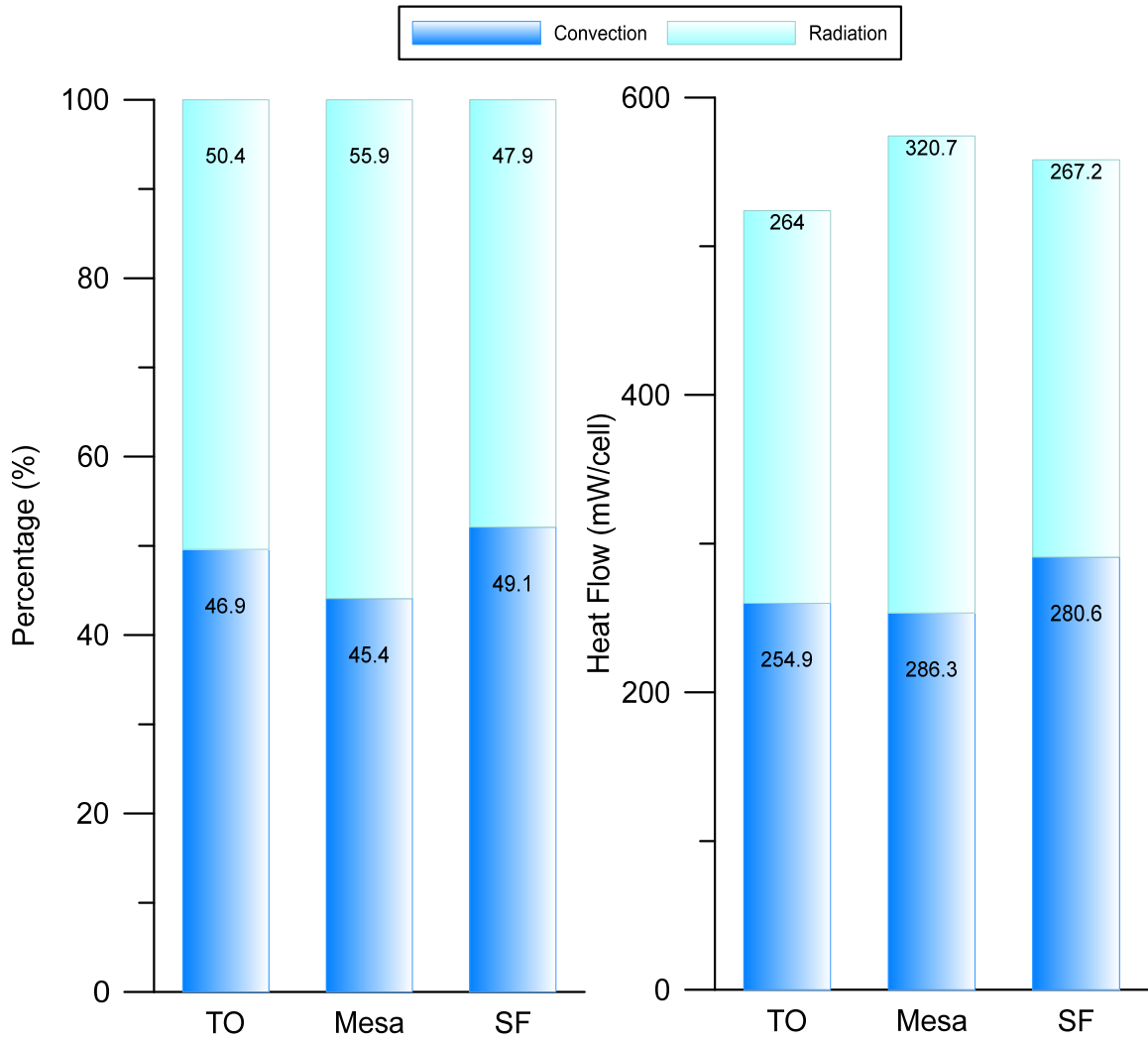
D.25 - LA92 component heat flow percentage



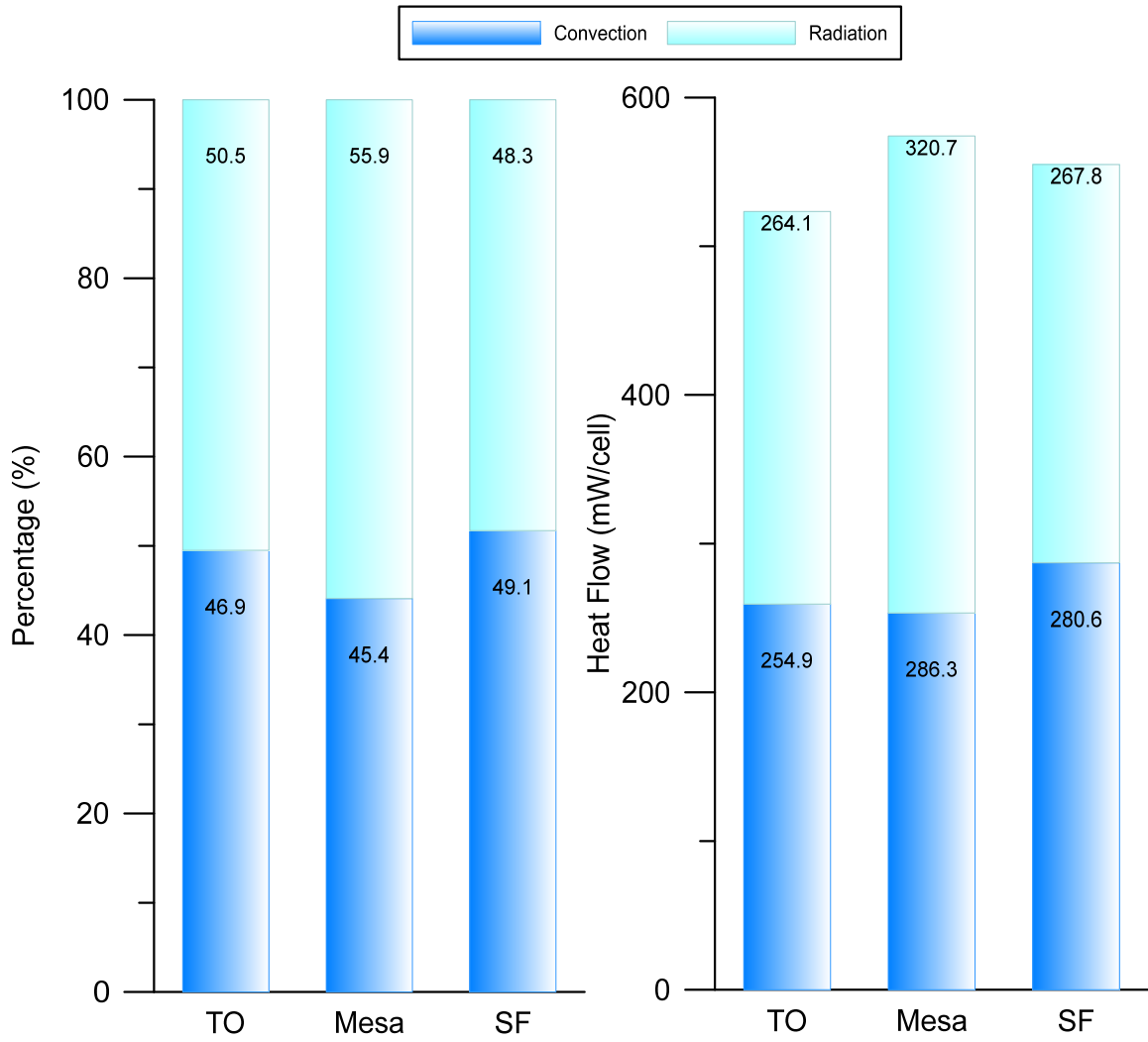
D.26 – HC LA92 shield heat flow percentage (left) and heat flow value (right)



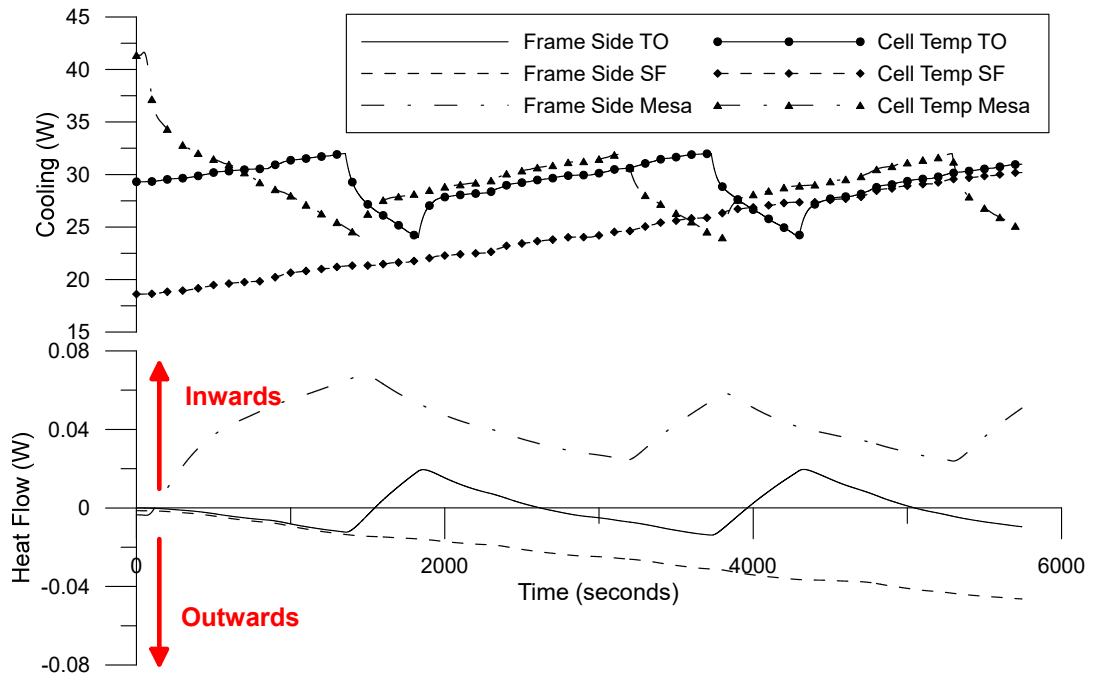
D.27 – FC LA92 shield heat flow percentage (left) and heat flow value (right)



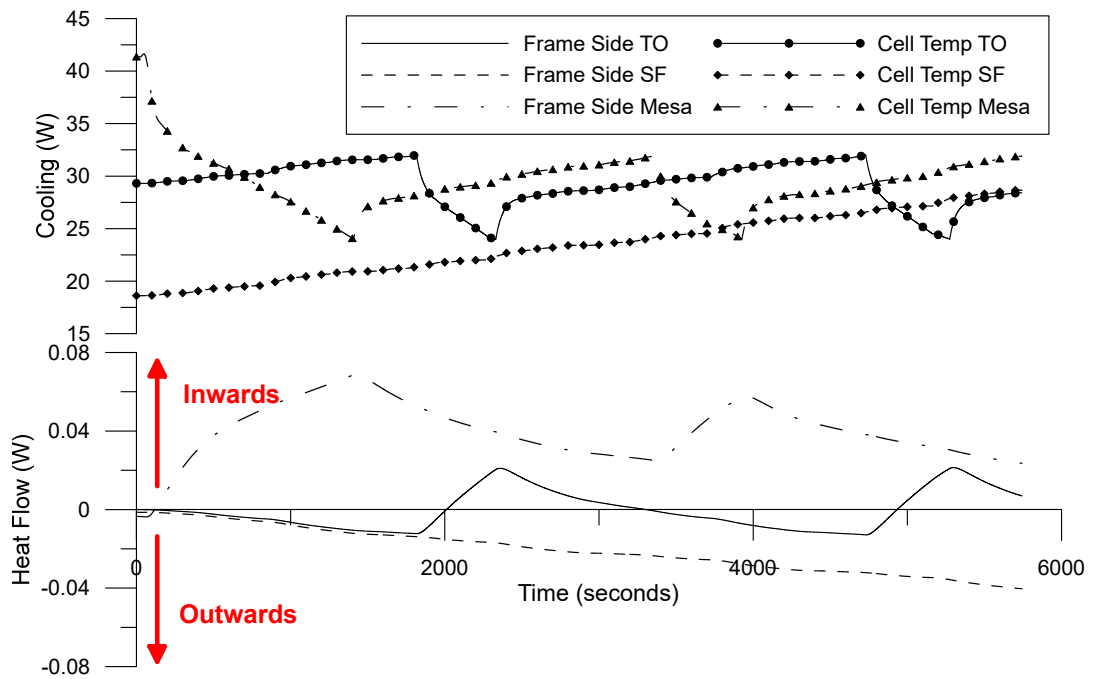
D.28 – HC LA92 shield heat flow percentage (left) and heat flow value (right) at peak solar position



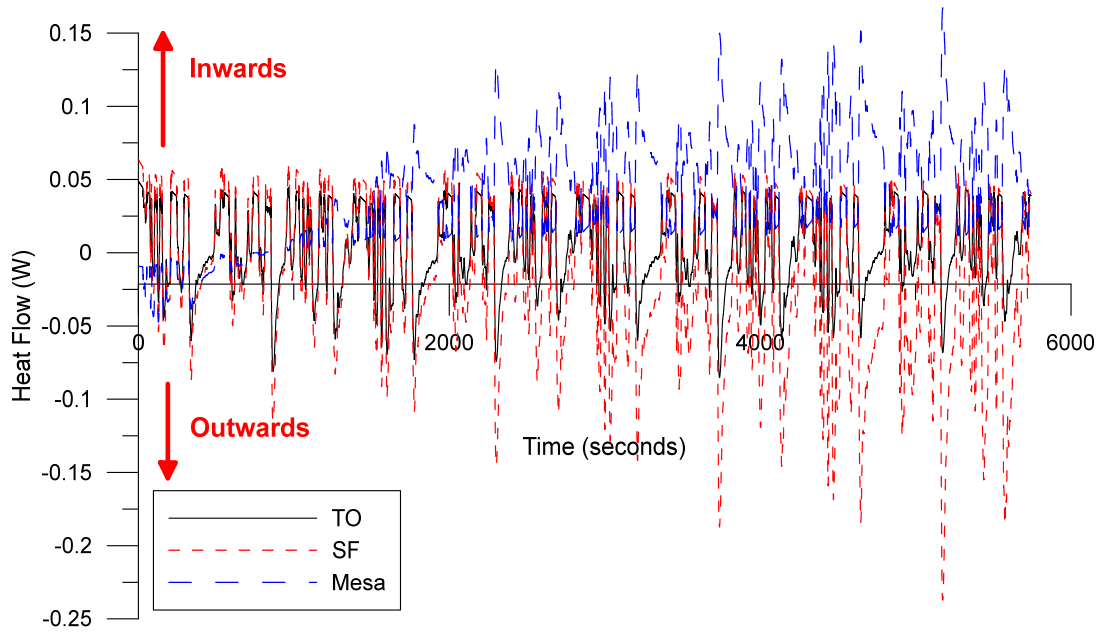
D.29 – HC LA92 shield heat flow percentage (left) and heat flow value (right) at peak solar position



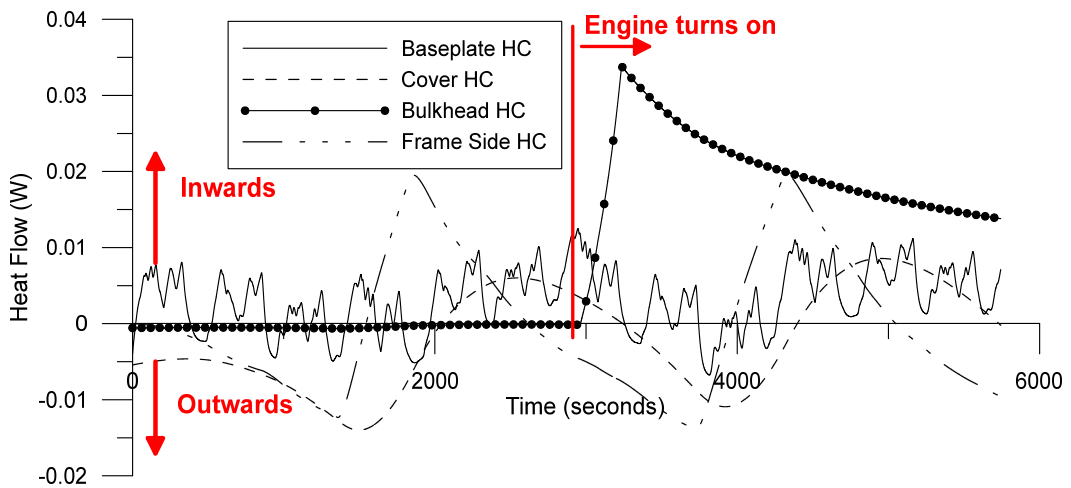
C.30 – LA92 frame side heat flow comparison for HC simulation



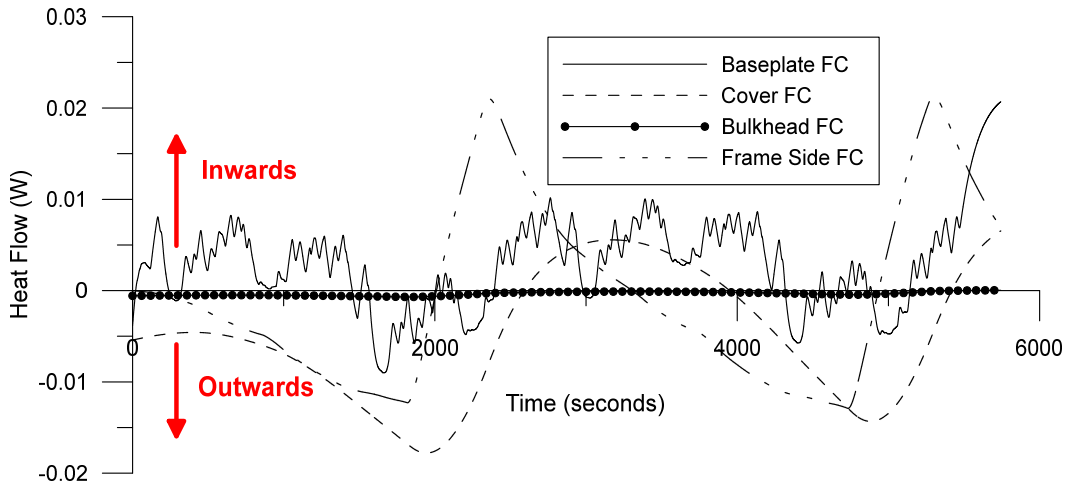
D.31 – LA92 frame side heat flow comparison for FC simulation



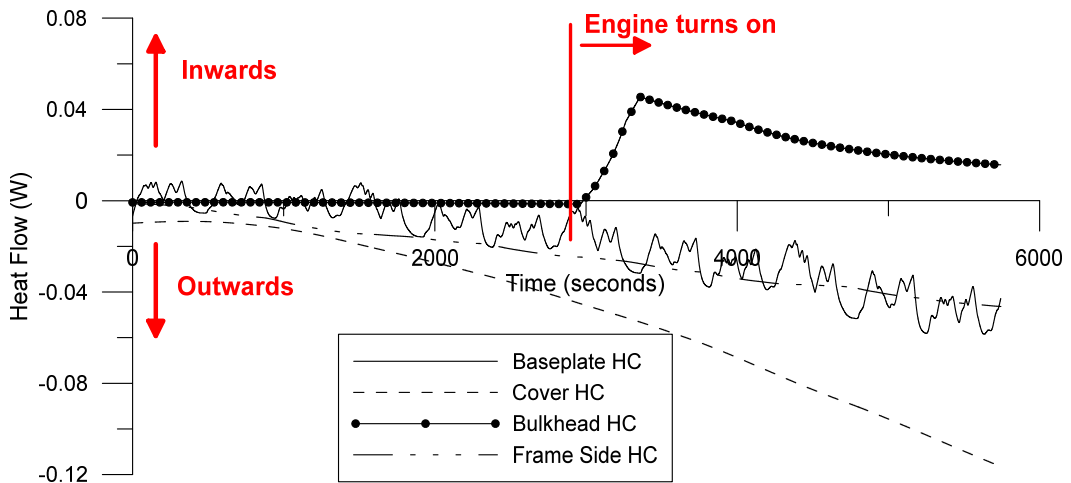
D.32 – LA92 shield heat flows for HC simulations



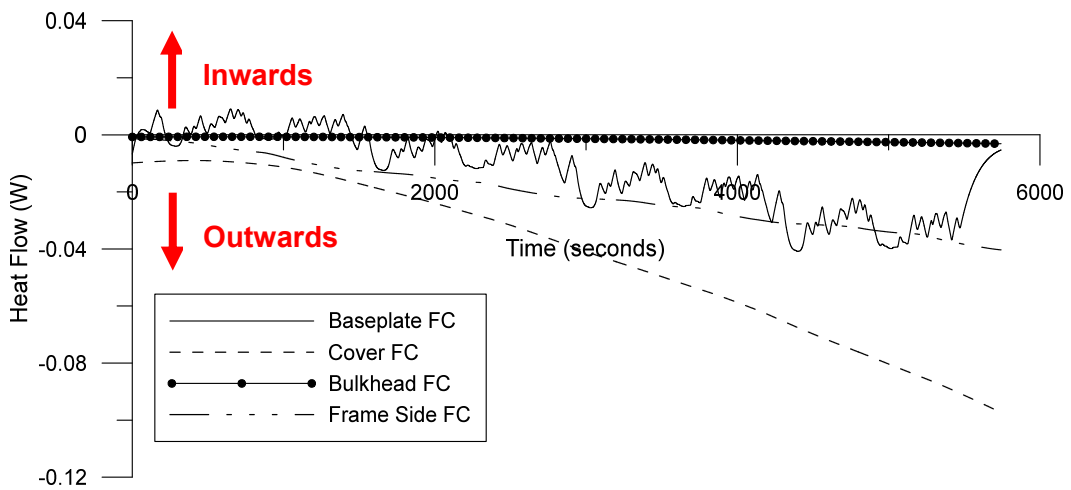
D.33 – Toronto LA92 external component heat flow for HC simulation



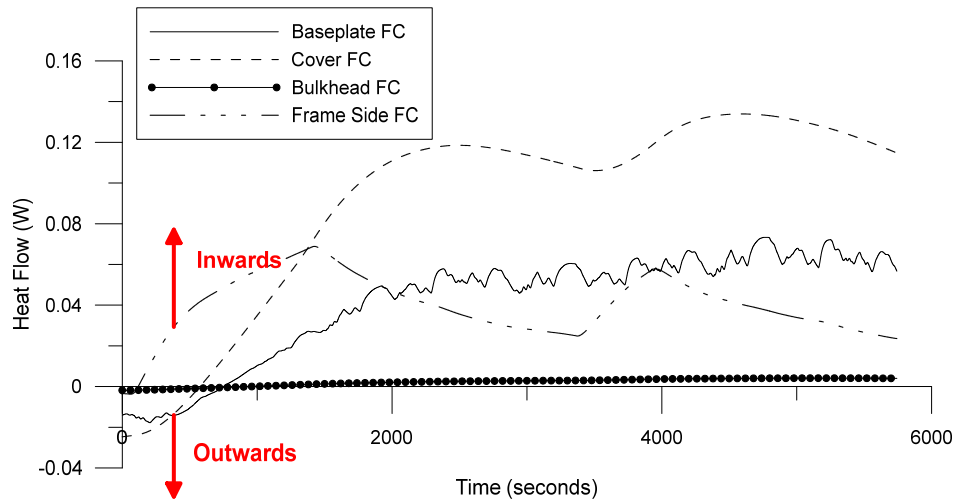
D.34 – Toronto LA92 external component heat flow for FC simulation



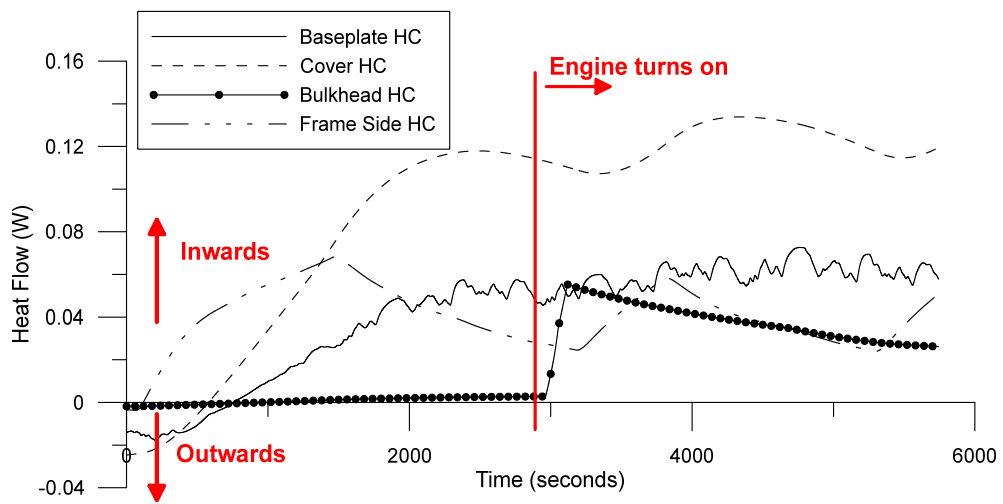
D.35 – San Francisco LA92 external component heat flow for HC simulation



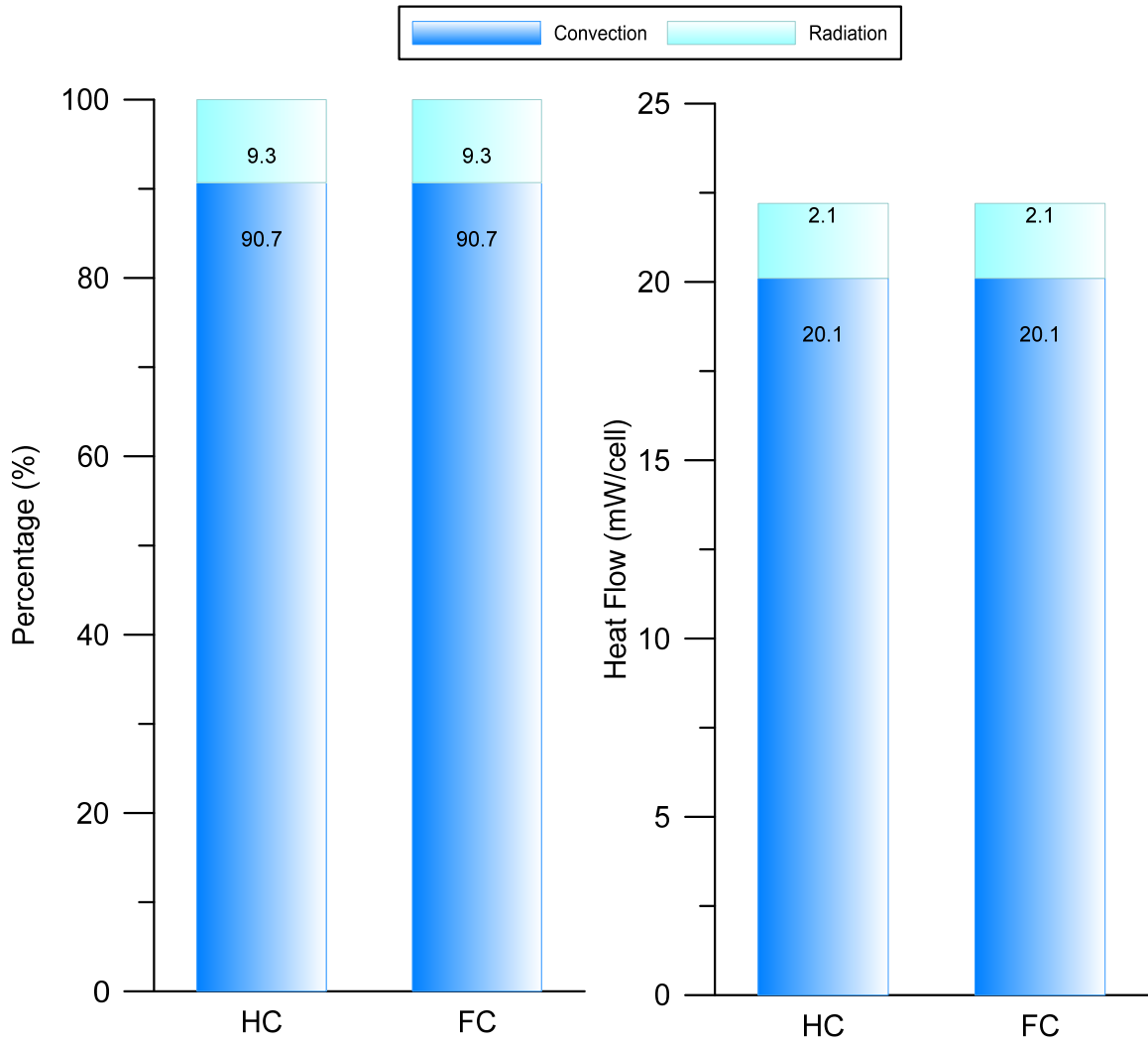
D.36 – San Francisco LA92 external component heat flow for FC simulation



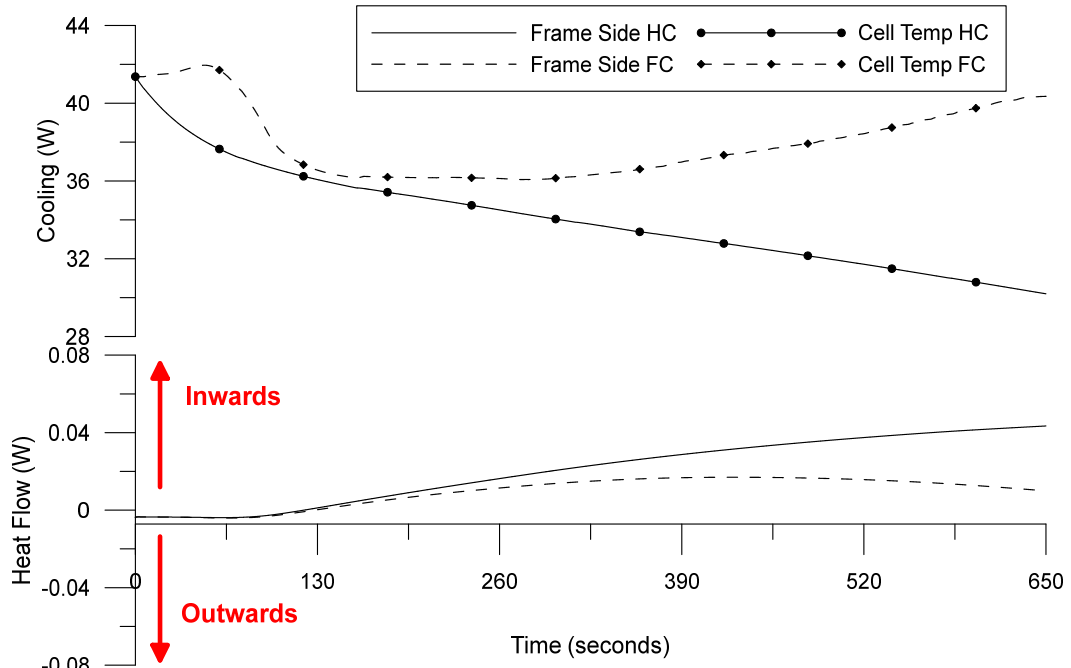
D.37 – Mesa LA92 external component heat flow for HC simulation



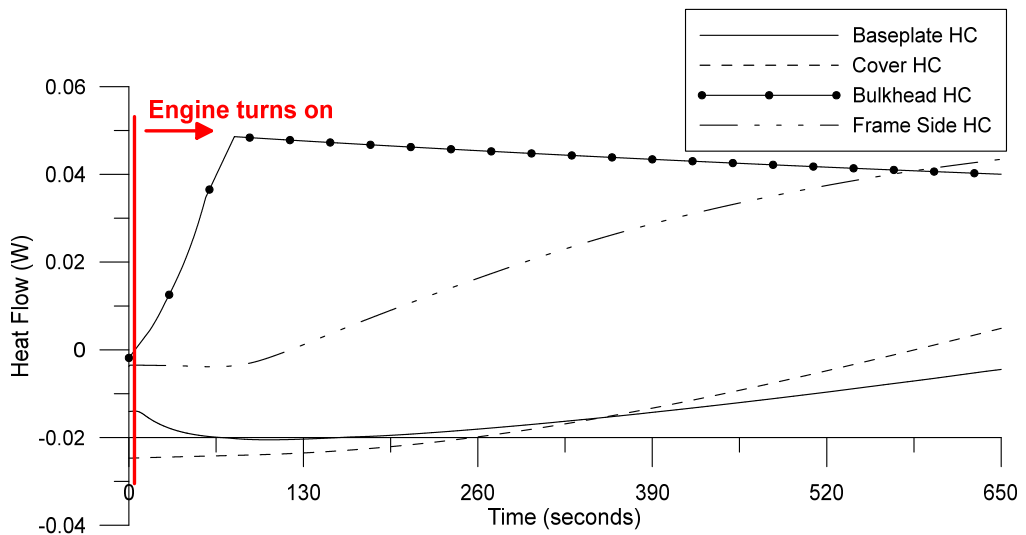
D.38 – Mesa LA92 external component heat flow for FC simulation



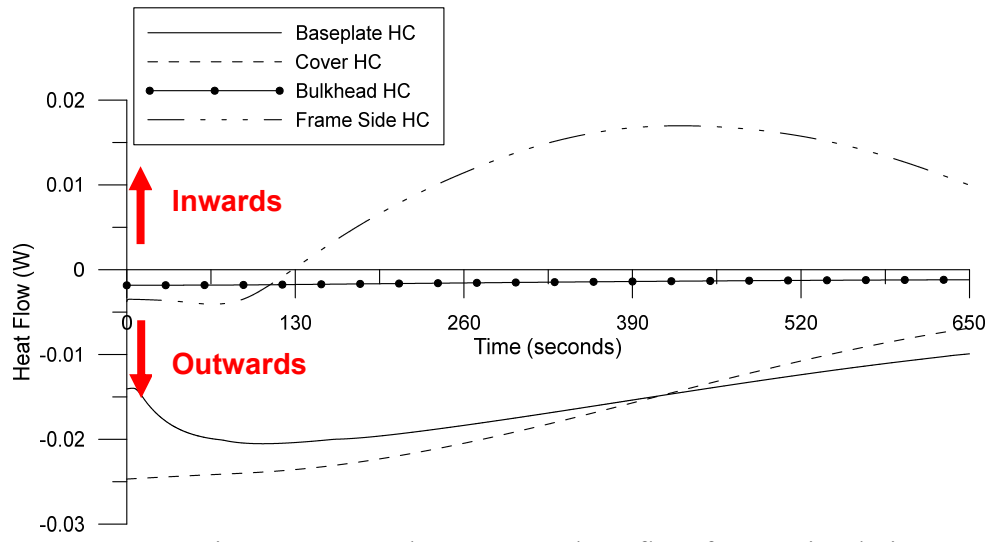
D.39 – Davis Dam shield breakdown for HC and FC simulations



D.40 – Davis Dam frame side heat flow comparison for HC and FC simulations

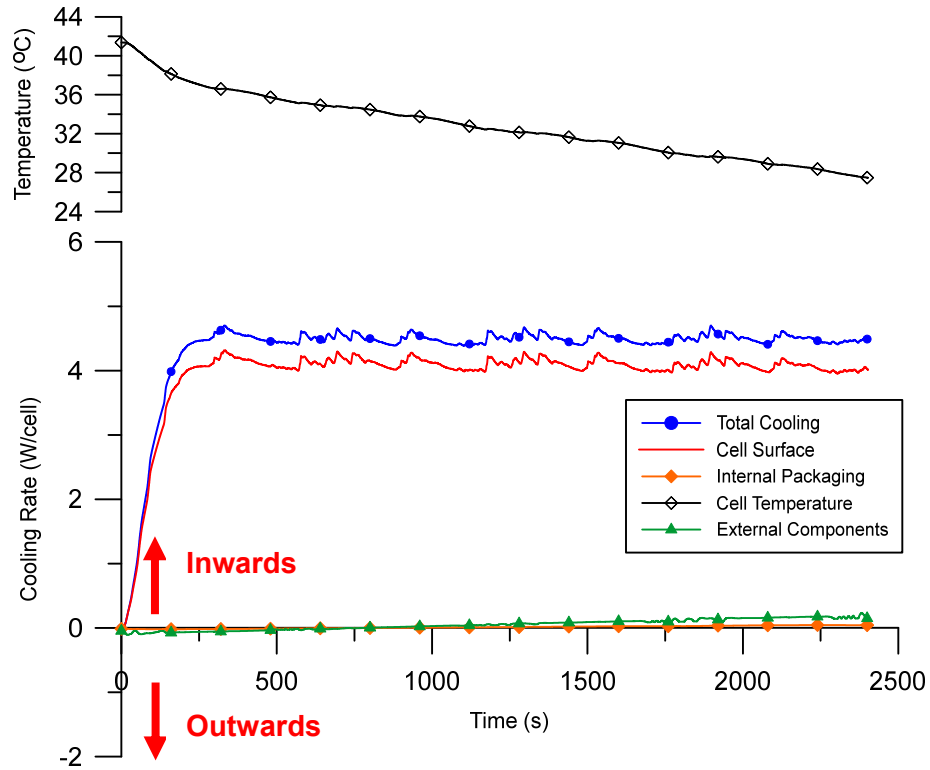


D.41 – Davis Dam external component heat flow for HC simulation

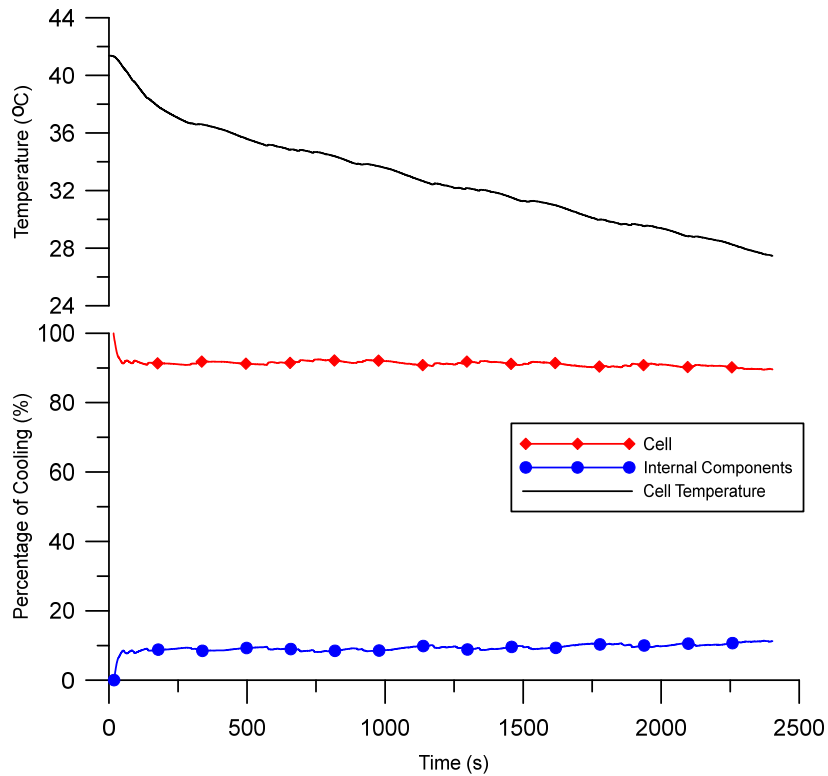


D.42 – Davis Dam external component heat flow for FC simulation

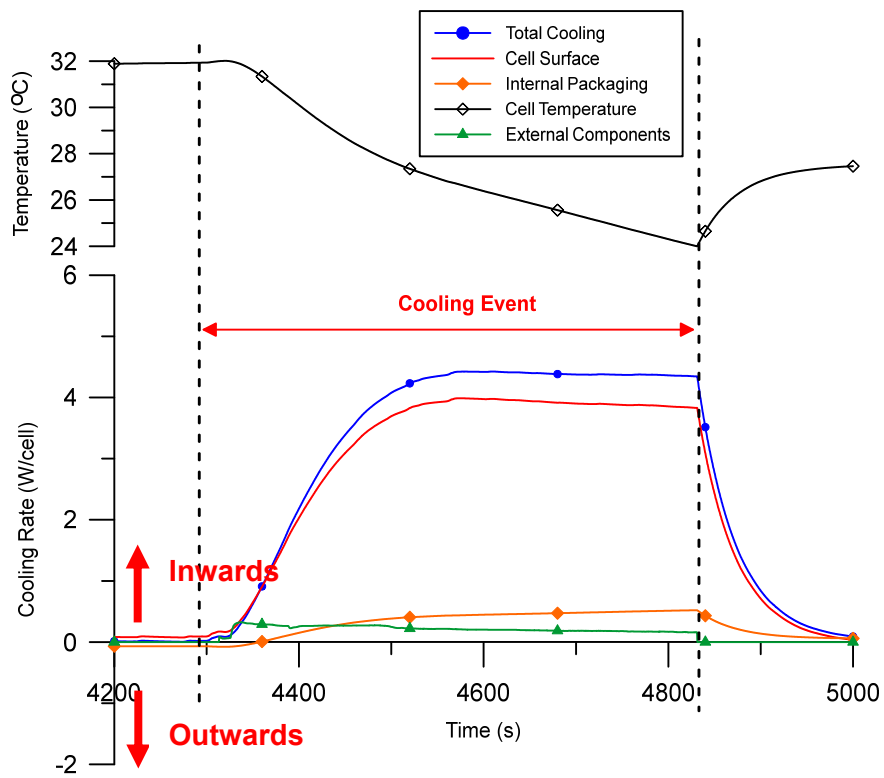
Appendix E - Cooling Performance



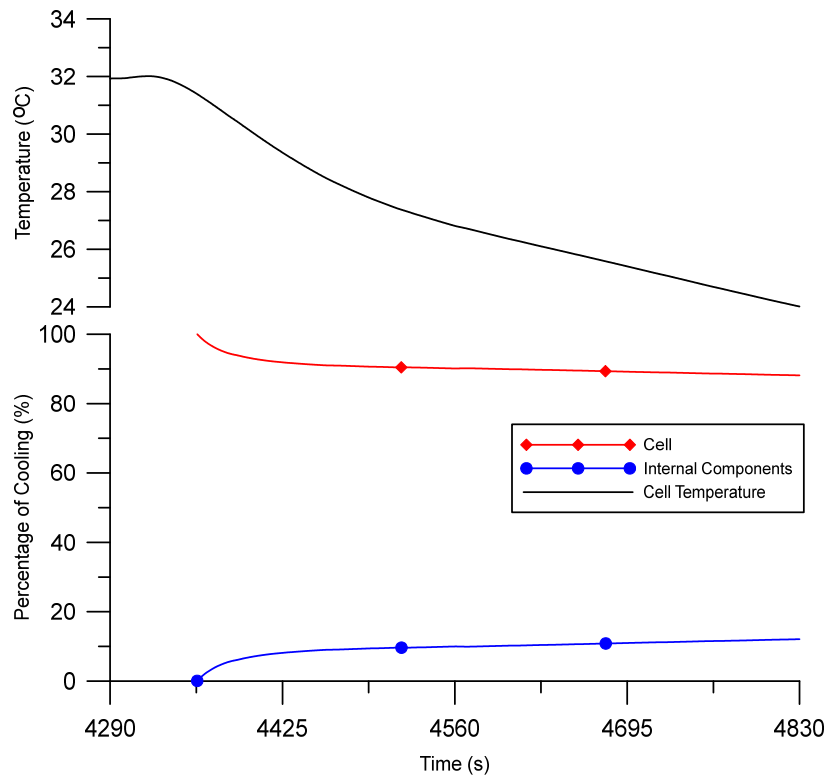
E.1 – US06 Mesa FC cooling effects



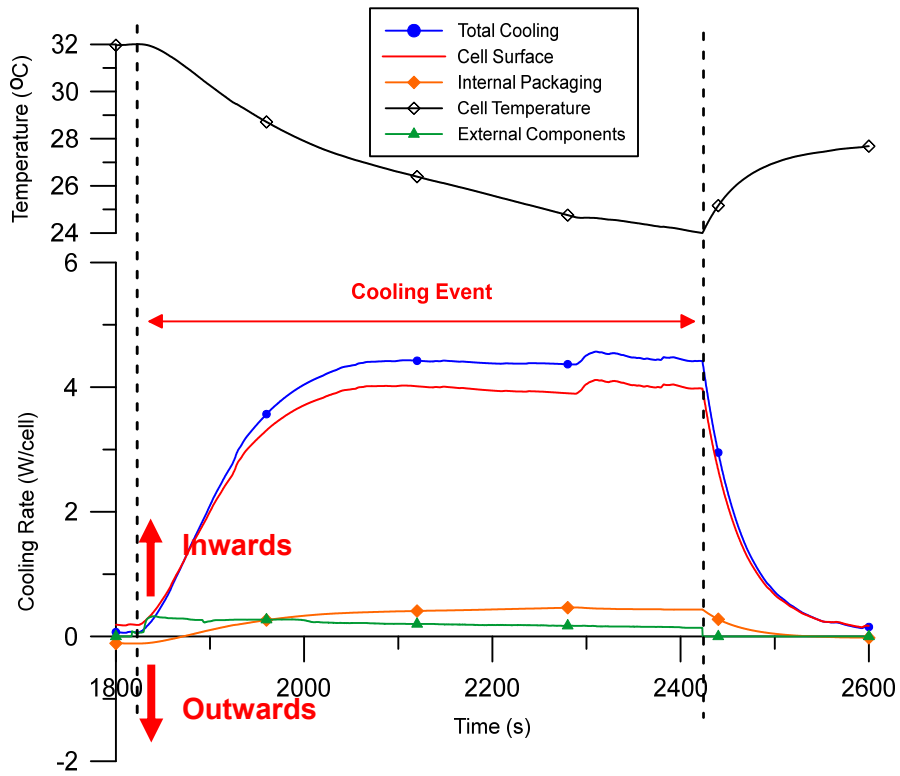
E.2 – US06 Mesa FC cooling percentages



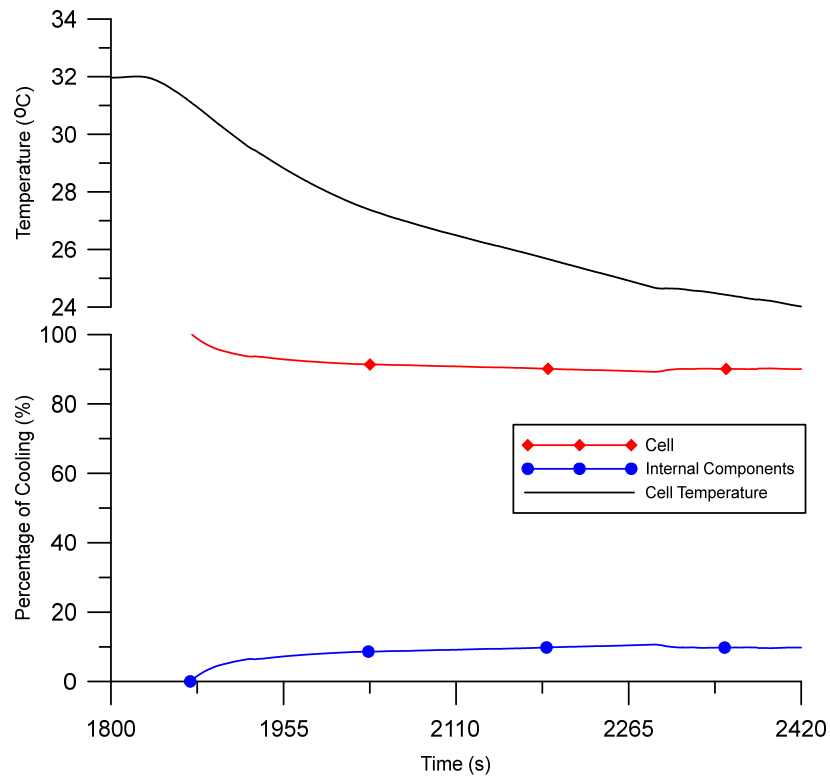
E.3 – UDDS Toronto FC cooling effects



E.4 – UDDS Toronto FC cooling percentages

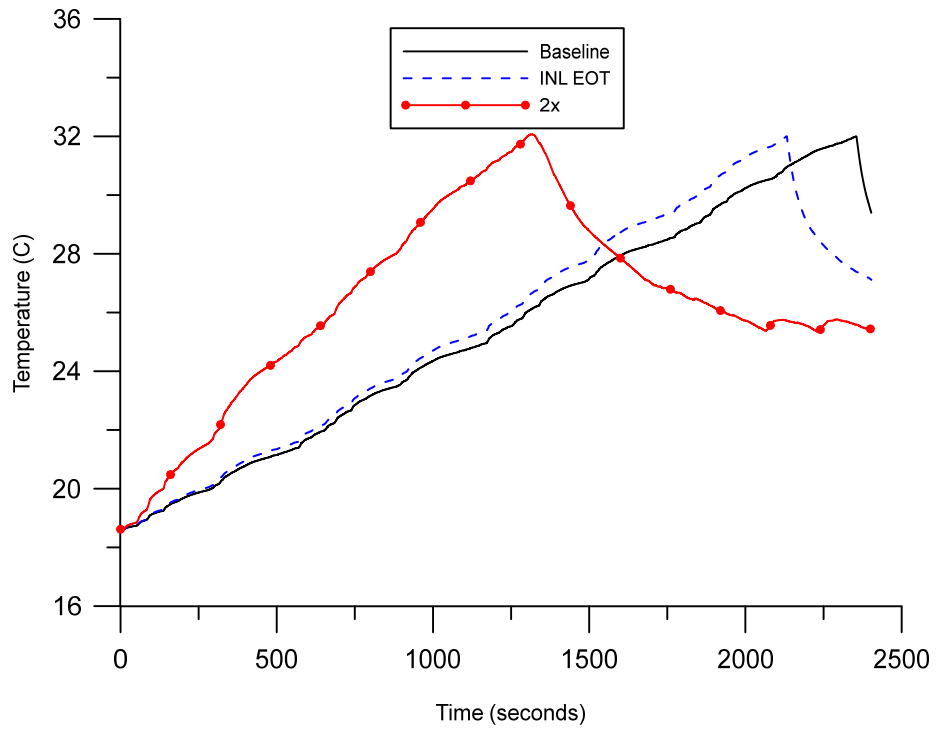


E.5 – LA92 Toronto FC cooling effects

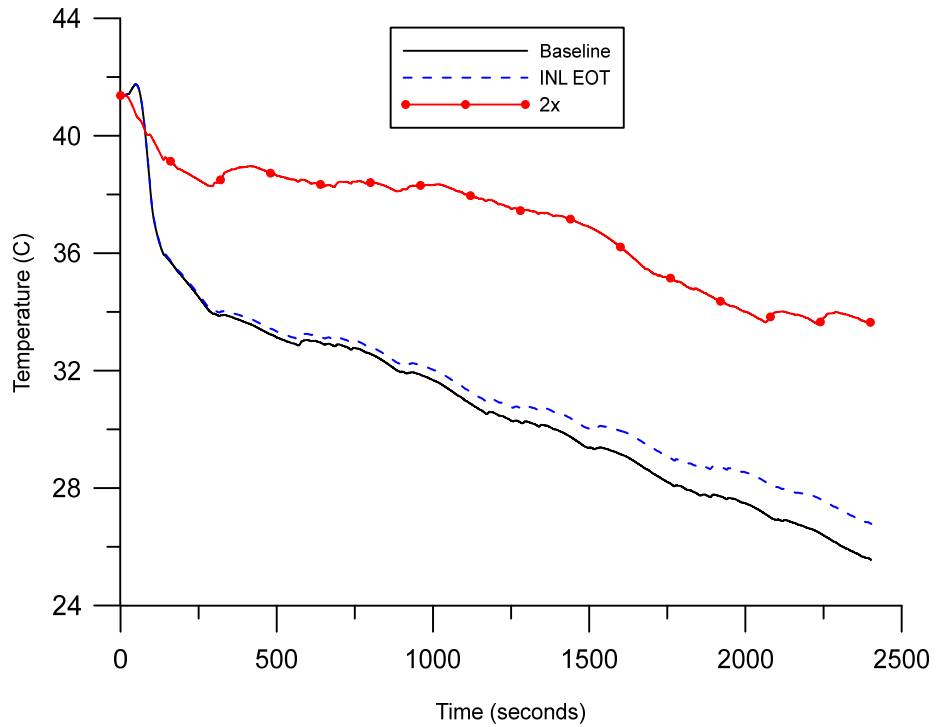


E.6 – LA92 Toronto FC cooling percentages

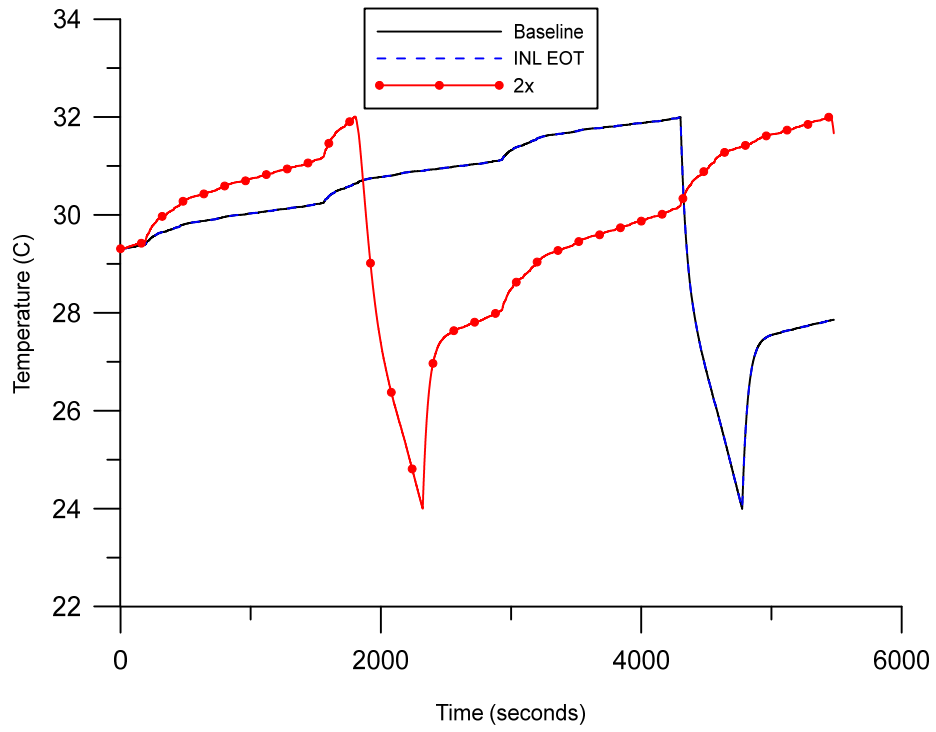
Appendix F - Battery Aging



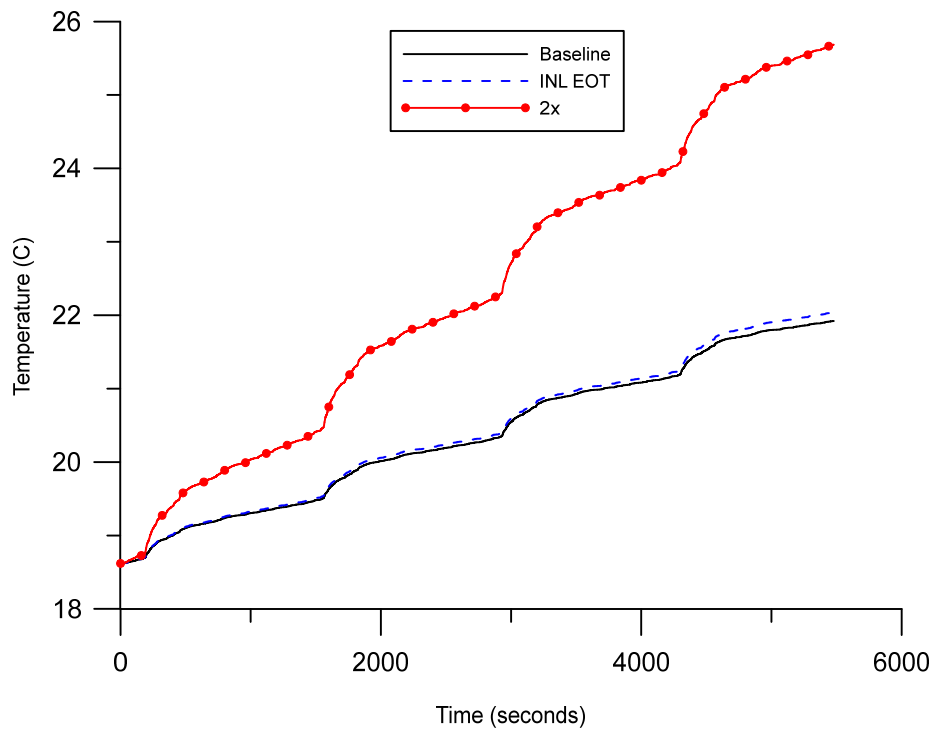
F.1 – US06 San Francisco resistance simulations



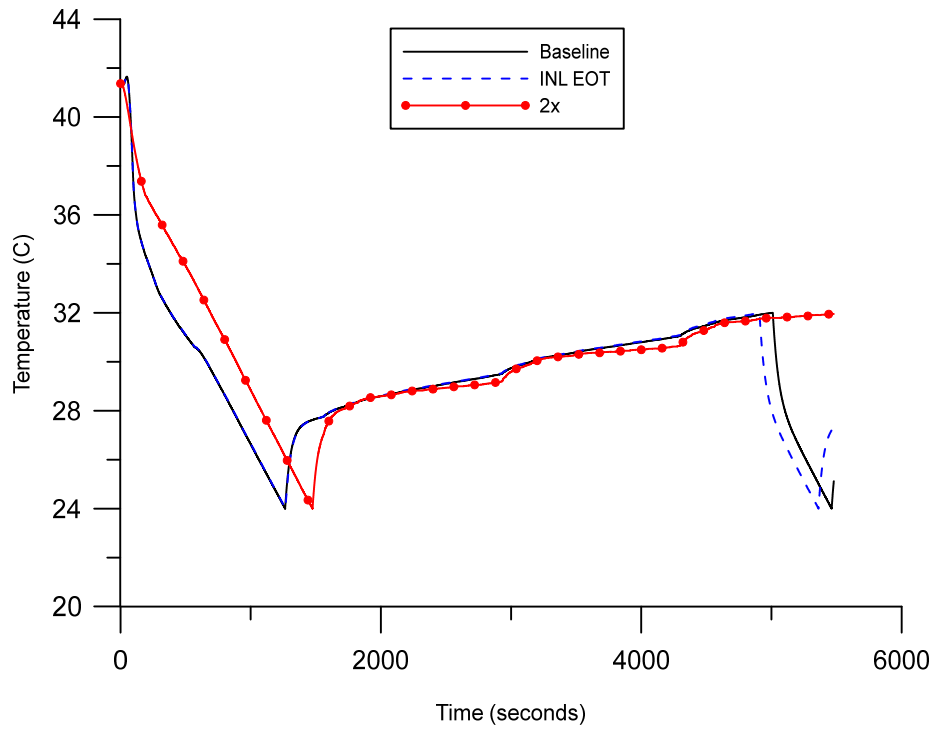
F.2 – US06 Mesa resistance simulations



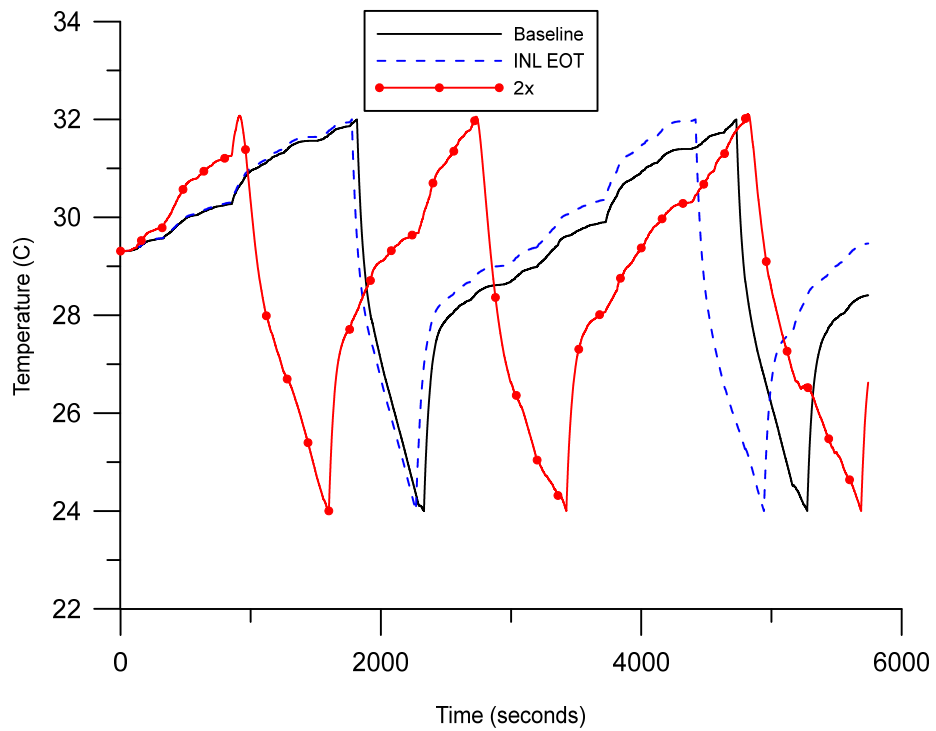
F.3 – UDDS Toronto resistance simulations



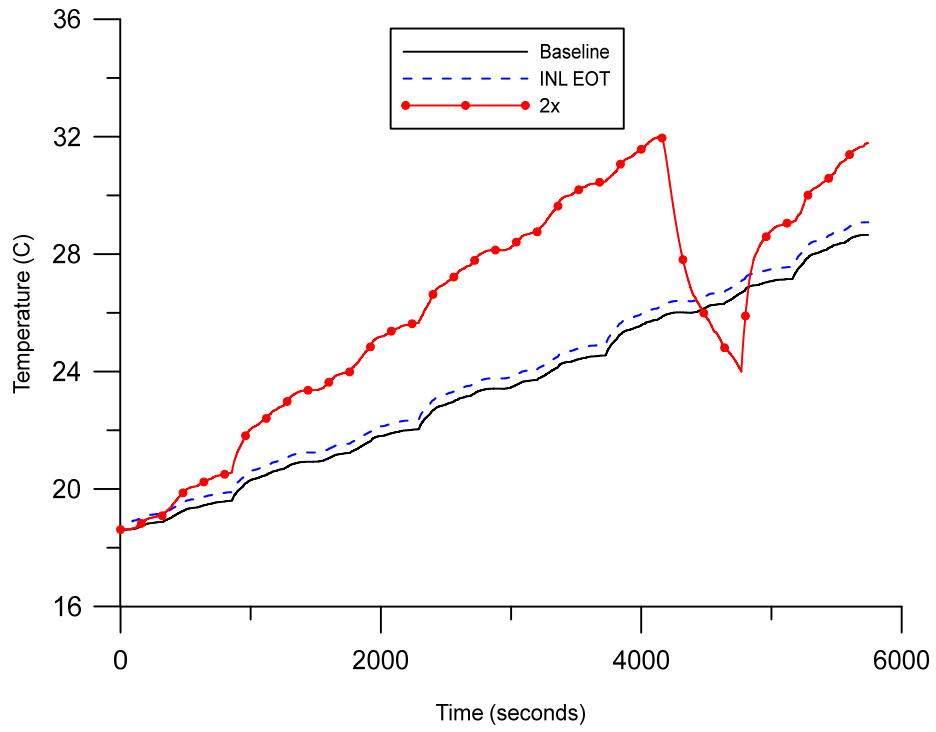
F.4 – UDDS San Francisco resistance simulations



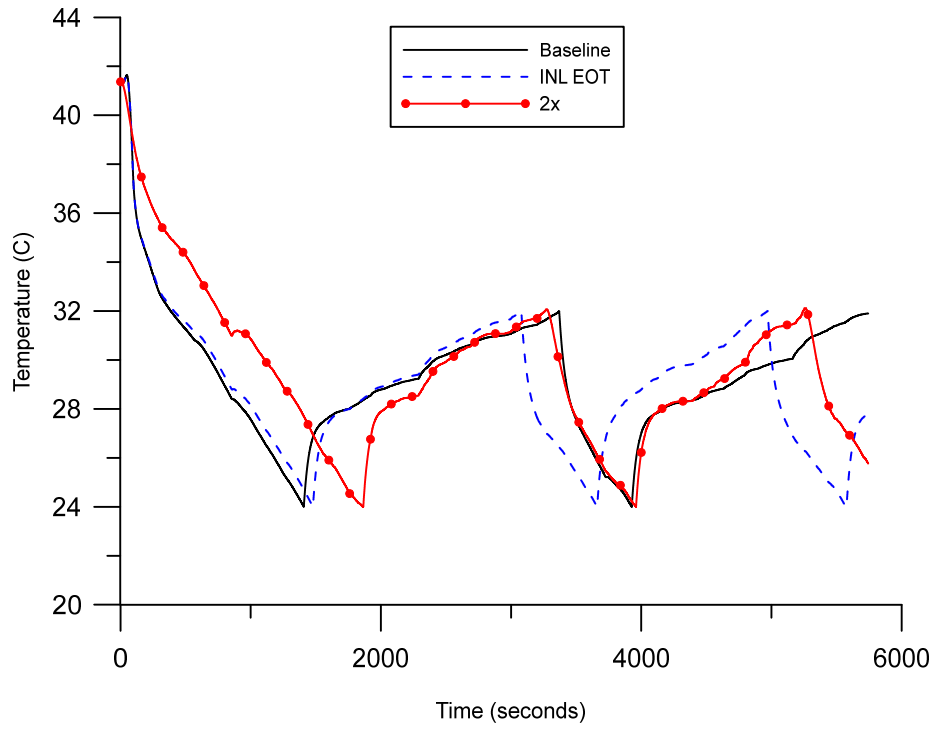
F.5 – UDDS Mesa resistance simulations



F.6 – LA92 Toronto resistance simulations

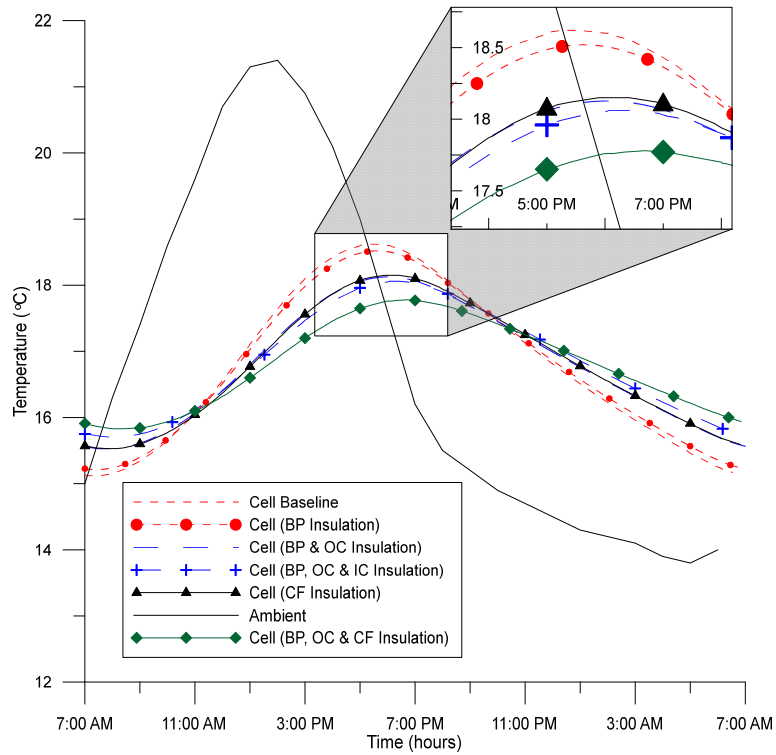


F.7 – LA92 San Francisco resistance simulations

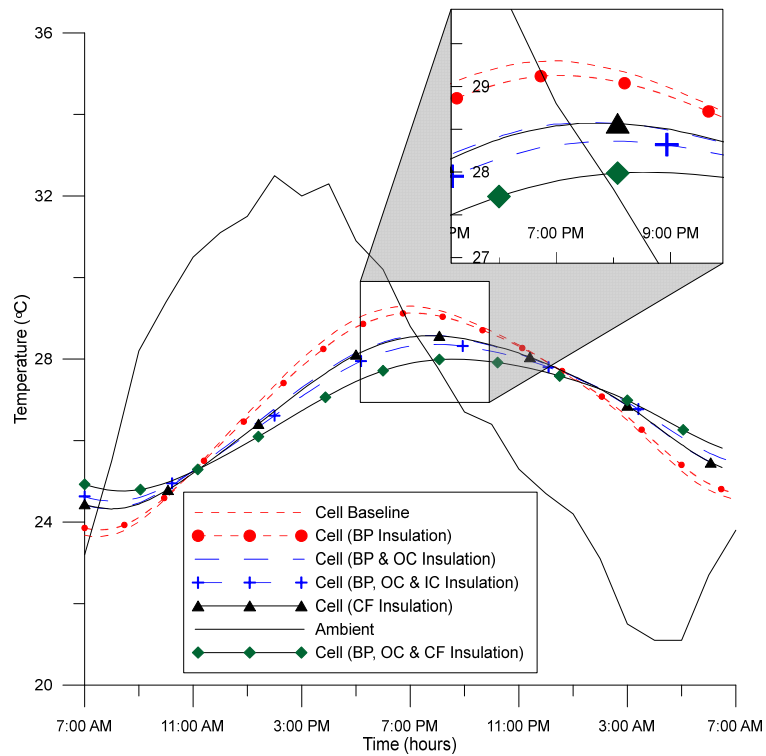


F.8 – LA92 Mesa resistance simulations

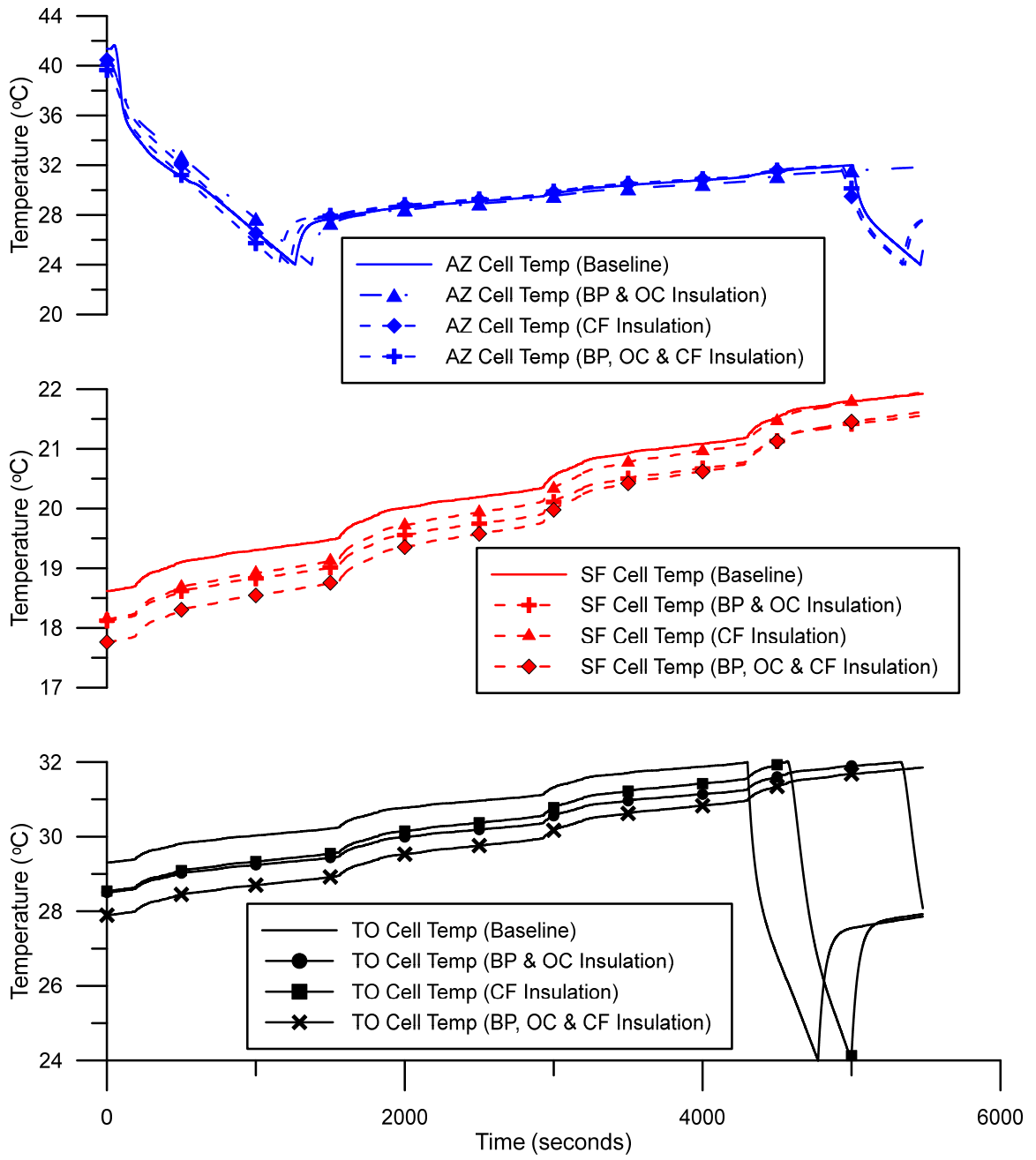
Appendix G – Insulation Addition



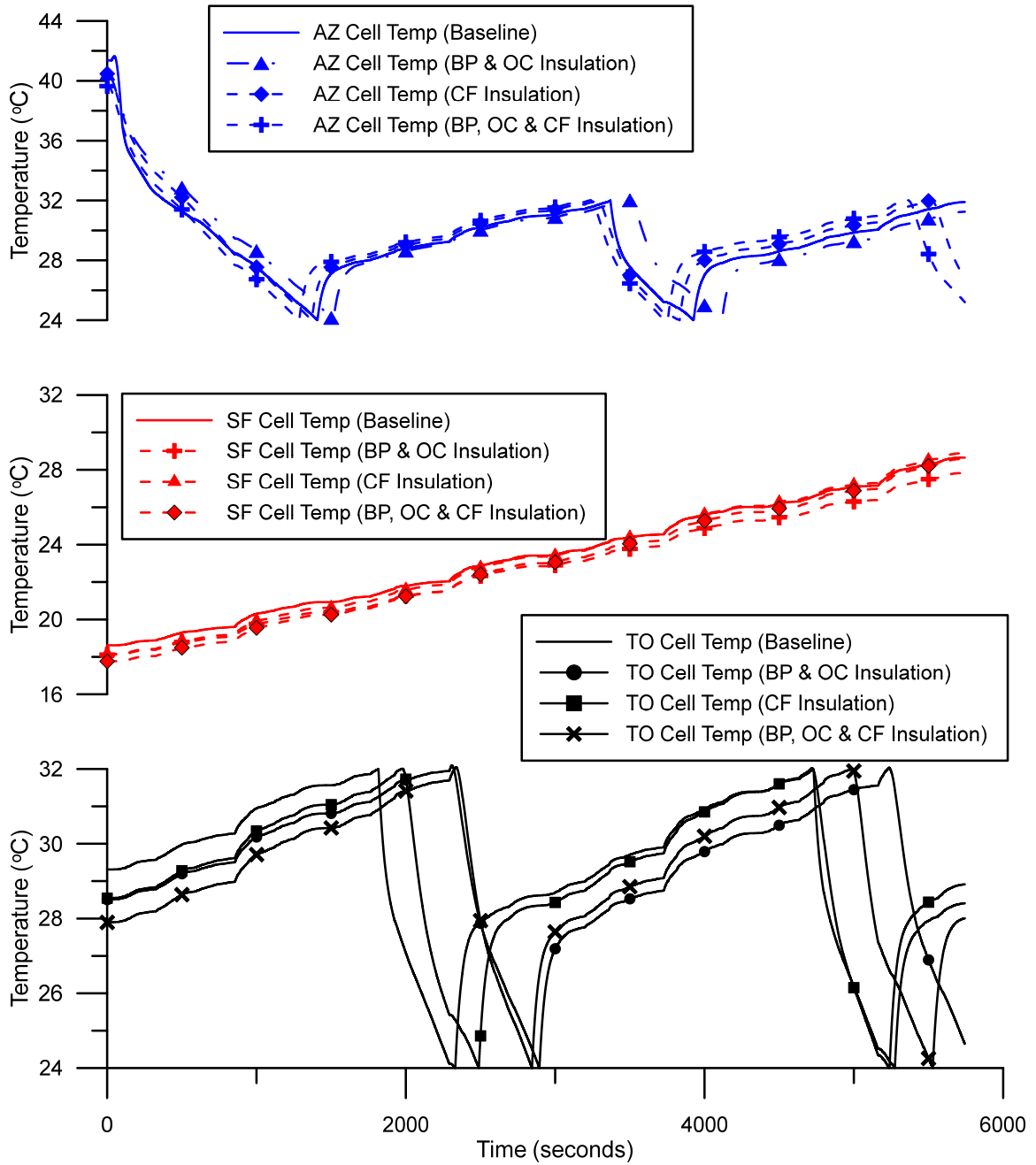
G.1 – San Francisco insulation simulations



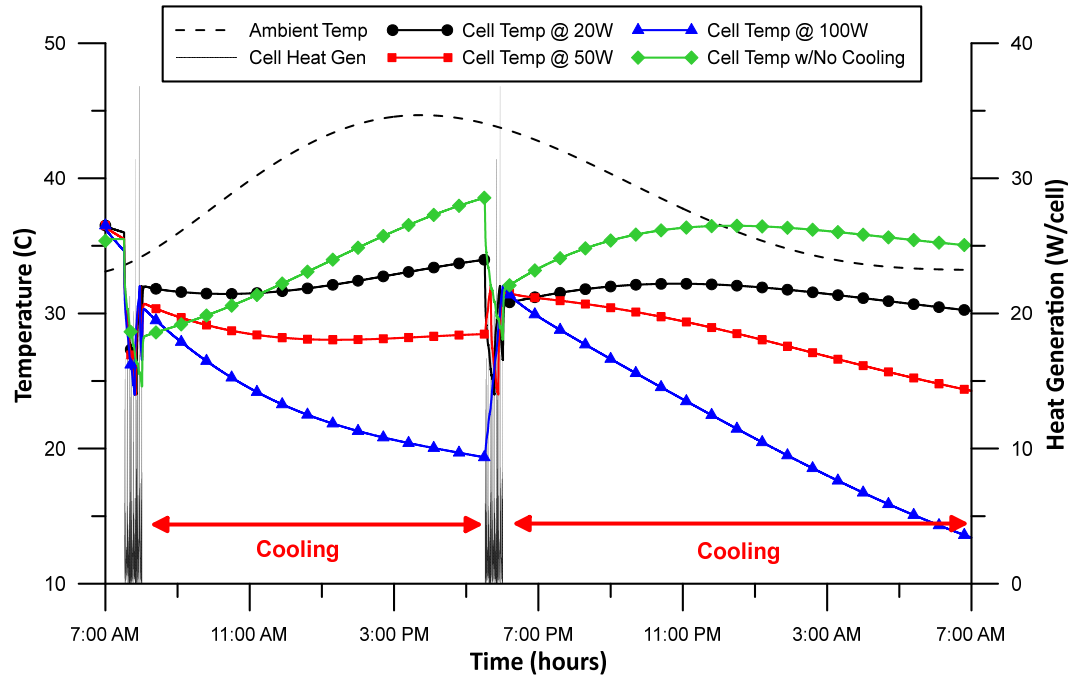
G.2 – Toronto insulation simulations



G.3 – UDDS insulation simulations

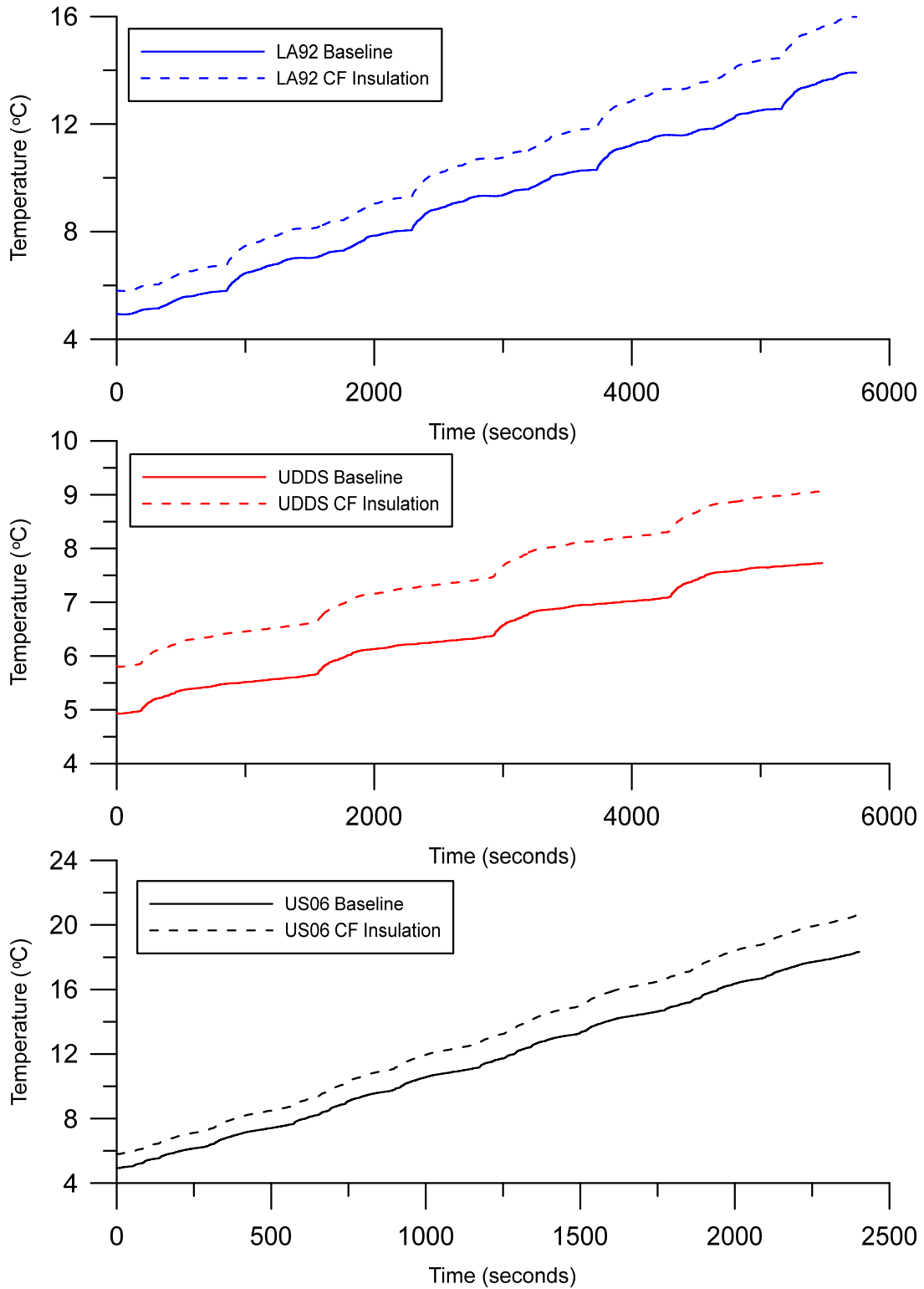


G.4 – LA92 insulation simulations

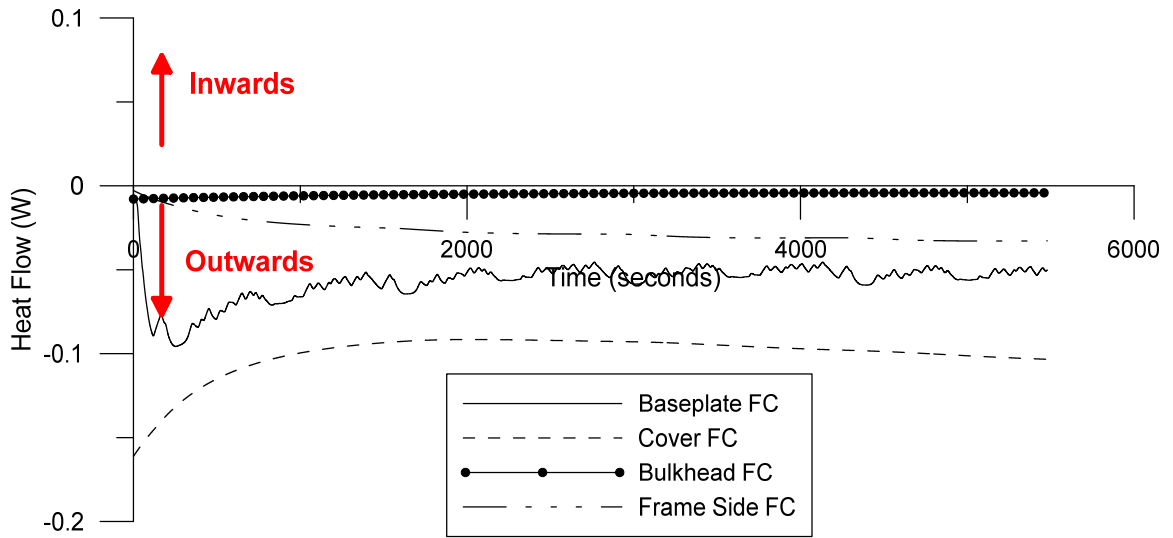


G.5 – 24hr workday simulation with BP-OC insulation and quiescent cooling

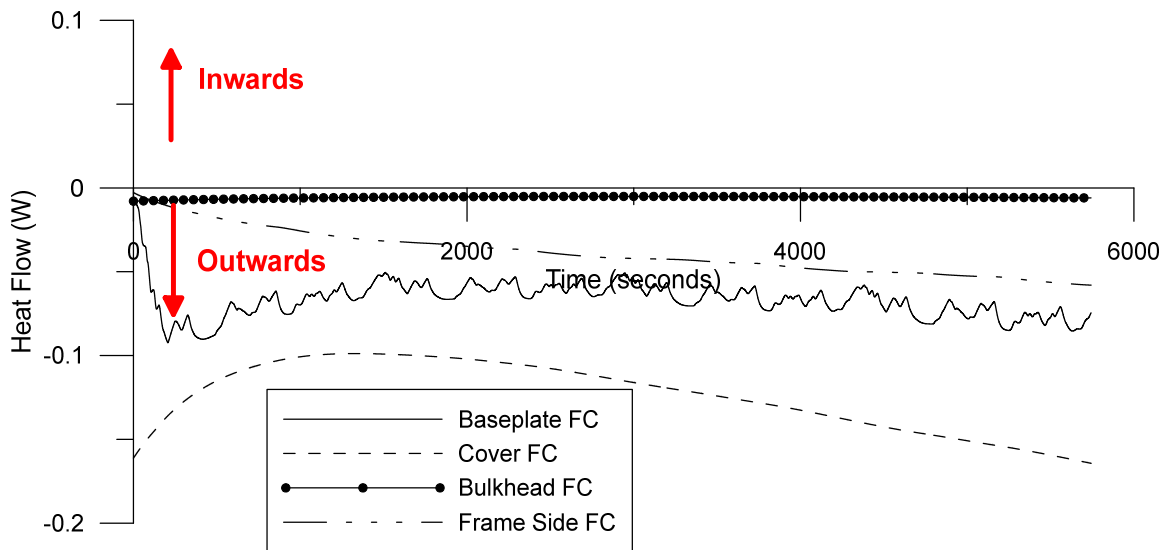
Appendix H – Cold Weather Drive Cycle Simulations



H.1 – LA92 (TOP), UDDS (MIDDLE), US06 (BOTTOM) cold cycle cell temperatures



H.2 – Toronto UDDS external component heat flow for FC cold simulation



H.3 – Toronto LA92 external component heat flow for FC cold simulation